Development of a new Soft Muon Tagger for the Identification of *b* quarks, applied to a Top Quark Pair Production Cross Section Measurement, using the ATLAS Detector at CERN.

Matthew Rose

Department of Physics
Royal Holloway, University of London

A thesis submitted to the University of London for the degree of
Doctor of Philosophy

January 31, 2013

DECLARATION

I confirm that the work presented in this thesis is my own. Where information has been derived from other sources, I confirm that this has been indicated in the document.

Matthew Rose

Abstract

This thesis presents a study of a method for identifying b-jets by searching for "soft" muons produced within them. This method, a so-called Soft Muon Tagger, uses the quality of the match (χ^2_{match}) between tracks left in the inner detector and the muon systems within the ATLAS detector to discriminate between muons within hadronic jets produced by the decay of b quarks, and those within light flavour jets.

The complete characteristics of the tagger are investigated in a detailed study on simulated data. The scale factors between the efficiency of the tagger in simulated and collision data, dependent on the kinematics of the tagged muon, are found using J/ψ decays. These are used in a measurement of the top quark pair production cross section in collision data.

The measurement is performed on data taken during the 2011 run of the LHC, specifically in the lepton+jets top-antitop quark decay channel. A summary of this measurement is presented, and is found to be compatible with theoretical predictions for the cross section at a centre of mass energy of $\sqrt{s} = 7$ TeV, and with published ATLAS and CMS measurements using b-tagging in the lepton+jets channel. The measured cross section is:

$$\sigma_{t\bar{t}} = 165 \pm 2(\text{stat.}) \pm 17(\text{syst.}) \pm 3(\text{lumi.}) \text{ pb}$$

The χ^2_{match}-based soft muon tagger contributes a small b-tagging systematic uncertainty to the cross section measurement compared to measurements performed using lifetime based b-taggers, and has a good signal to background ratio.

Acknowledgements

I would like to thank my supervisor, Dr Veronique Boisvert, for her support and guidance throughout my PhD, and Dr Neil Cooper-Smith for all his help over the last year. I would also like to thank Dr Pedro Teixera-Dias, Dr Glen Cowan and the other staff in the RHUL particle physics group for their willingness to help with any questions I may have had. I am grateful to the Science and Technology Facilities Council for providing the funding that enabled me to complete this PhD and spend an enlightening and enjoyable time at CERN. Thanks must also go to Cathy for all her help in the last year.

To my family, thank you for all your support, especially Clare for putting me up at the beginning and for being a great friend. Thanks must go to Simon, Birdie and Joe for being the most solid mates I could ask for, and to Dan, James, Tom and Rich for making this fun.

Kelly, thank you for your encouragement, reassurance, understanding and help. I genuinely couldn't have done this without you.

Preface

This thesis describes a method of identifying the decays of b quarks in the ATLAS detector at the LHC by identifying the muons produced in their semileptonic decays, using the quality of the match between tracks left in the inner detector and muon systems of ATLAS - specifically the χ^2/Degree of Freedom of this match, or χ^2_{match}. The method is a multivariate selection procedure which includes a χ^2_{match} requirement, and is referred to as a Soft Muon Tagger (SMT).

Chapter 4 describes the LHC and the ATLAS detector in particular detail. An overview of the Standard Model of particle physics is given in Chapter 2. Chapter 3 contains a brief overview of the production and decay modes of the top quark, as well as motivation for its study. Chapter 5 covers the methods of b-jet identification in use at ATLAS, and introduces the SMT with which this thesis is concerned. The performance of the SMT is characterised in Chapter 6, and a collision data/simulation scale factor for the efficiency of the SMT in 2011 data is found in Chapter 7. The SMT is used in a measurement of the top quark pair production cross section in the lepton+jets channel, summarised in Chapter 8, which makes use of the collision data/simulation scale factors.

Section 7.3 and Chapter 8 include content from papers to which I have contributed [1–3]: Section 7.3 is a summary of the mistag rate measurement performed by another member of the joint RHUL-QMUL Soft Muon Tagging group, to which I have been an active contributor over the duration of my PhD studies. This study is complementary to the data/simulation scale factors (see Chapter 7), and is adapted from the χ^2_{match} based soft muon tagger supporting note [1], which is primarily the work of myself and two other authors. Chapter 8 contains a summary of a $t\bar{t}$ cross section measurement in the lepton+jets channel [2, 3], also conducted by the joint RHUL-QMUL Soft Muon Tagging group. My main contribution to this section was to provide the collision data/simulation SMT efficiency scale factors, and the contribution to the total systematic uncertainty of the cross section measurement which arises from their use.

I have also contributed sections on the soft muon tagging efficiency, mistag rate and scale factors to the ATLAS b-tagging note [4] and the “B tagging for Top Physics” supporting note for the 2010 top cross section measurement [5].

Contents

Preface **5**

1 Introduction and Motivation **19**

2 The Standard Model of Particle Physics **21**

2.1 Quantum Electrodynamics 22

2.2 The Weak and Electroweak Interaction 23

2.2.1 The CKM Matrix 23

2.2.2 The Higgs Mechanism 25

2.3 Quantum Chromodynamics 27

3 Top Quark Physics **30**

3.1 Top Quark Production Channels 31

3.2 Decay Modes of the Top Quark 36

3.2.1 Choosing the Lepton+Jets Channel 37

3.3 Motivation for the Study of Top Quark Physics 38

4 The LHC and the ATLAS Detector **40**

4.1 The Large Hadron Collider 40

4.1.1 Accelerating the Beam 40

4.1.2 Event rate and Pile-up 42

4.1.3 The 2011 Dataset, and the LHC Schedule 44

4.2 The ATLAS Detector 47

4.2.1 Inner Detector 48

4.2.2 Calorimetry 54

4.2.3 Muon Spectrometer 57
4.2.4 Magnets 62
4.2.5 Trigger and Data Acquisition 62
4.3 Monte Carlo Simulation 66
4.3.1 Event Generation 66
4.3.2 Detector Simulation 69
4.3.3 Digitisation 70

5 Identifying b-jets, and the Match χ^2 based Soft Muon Tagger 71
5.1 Lifetime based b-tagging 72
5.2 b-tagging performance 75
5.3 Soft Lepton Tagging 76
5.3.1 The $p_{\mathrm{T}}^{\mathrm{rel}}$ based Soft Muon Tagger 77
5.4 The Match χ^2 based Soft Muon Tagger 80
5.4.1 Performance of the χ^2_{match} based Soft Muon Tagger 81
5.4.2 Comparing performance of b-tagging methods 83
5.4.3 SMT Selection Cuts 85
5.4.4 Comparison of Soft Muon Taggers 87

6 Monte Carlo Characterisation of the Match χ^2 based Soft Muon Tagger 89
6.1 Monte Carlo samples and Event Selection 90
6.1.1 Isolation Variables 91
6.2 Branching Ratios 92
6.3 Characterising the b-tagging Efficiency 96
6.3.1 Efficiency of the Individual χ^2_{match} based SMT Cuts 97
6.3.2 Dependence of the b-tagging Efficiency on the p_{T} of b quarks and b-jets 101
6.3.3 Jet Energy Scale 106
6.4 Establishing the Sources of “Fake” Muons 107
6.5 Calibration using Collision Data 109

7 Calibration of the χ^2_{match} based Soft Muon Tagger using $J/\psi \to \mu\mu$ events in Collision Data 110
7.1 Tag and Probe with $J/\psi \to \mu\mu$ 111

7.1.1 Choice of Trigger Requirements for the Tag muon 112
7.1.2 Selection Cuts for Tag and Probe Candidates 113
7.1.3 Kinematic Comparison of Muons from J/ψ and $t\bar{t}$ Decays 116
7.1.4 Background Subtraction 118
7.1.5 Systematic Uncertainties 118
7.1.6 Isolation Dependence 121
7.2 Efficiencies and Scale Factors 128
7.2.1 2010 Data 128
7.2.2 2011 Data 131
7.2.3 Tag and Probe with $Z \to \mu\mu$ 148
7.3 Kinematic Dependence of the SMT Mistag Rate 153

8 The χ^2_{match} based SMT $t\bar{t}$ Cross Section Analysis 156
8.1 The χ^2_{match} based SMT Data/MC Scale Factors 156
8.2 Object and Event Selection 157
8.3 Data Driven Background Determination 159
8.3.1 W+jets Background 159
8.3.2 QCD Multijet Background 160
8.4 Measured b-tagging Efficiencies 161
8.5 Systematic Uncertainties 162
8.6 Results and Conclusion 165
8.6.1 The $t\bar{t}$ Cross Section Measurement 165

9 Conclusions 167

Appendices 169

A CP Violation 169

B Covariance Matrices 170

C Muon and Electron Quality Definitions 172

D Jet Flavour Truth Labelling 174

E Decay Chains of "Fake" Muons **178**

F Uncertainties on Efficiency values **180**

List of Figures

2.1 Feynman diagram of the fundamental QED interaction vertex 22
2.2 Feynman diagrams of the fundamental vertices for weak force interactions . . . 23
2.3 Feynman diagrams of the fundamental QCD interaction vertices 29

3.1 Leading order $t\bar{t}$ production channels. 32
3.2 Single top quark production channels 33
3.3 A summary of public measurements of the $t\bar{t}$ pair production cross section, and the corresponding theoretical expectation 34
3.4 A comparison of current ATLAS $t\bar{t}$ cross section measurements with Tevatron results, and theoretical predictions 35
3.5 Branching fractions of the $t \to Wb$ decay mode 37
3.6 A Feynman diagram of the decay of a pair of top quarks via the lepton+jets channel 38

4.1 A schematic representation of the LHC and its four major experiments 41
4.2 A schematic view of the CERN accelerator complex 42
4.3 Maximum pile-up for any single bunch collision, and the mean maximum for all colliding bunches in 2011 data 44
4.4 Cumulative integrated luminosity by day for 2010 and 2011 pp data collection 46
4.5 Instantaneous and Integrated Luminosity by day in 2011pp data collection . . . 46
4.6 ATLAS data taking efficiency per day 46
4.7 A cut-away view of the ATLAS detector 48
4.8 A schematic view of the signature left by some highly energetic particles passing through the ATLAS detector 49
4.9 A cut-away view of the ATLAS inner detector 50

4.10 Drawing showing the sensors and structural elements traversed by a charged track in the barrel inner detector 51
4.11 Plan view of a quarter-section of the ATLAS inner detector showing each of the major detector elements with its active dimensions and envelopes 52
4.12 A cut-away view of the ATLAS calorimeter system 55
4.13 A cut-away view of the ATLAS muon systems 58
4.14 Plan view of a quarter-section of the ATLAS Muon Spectrometer system, showing the Monitored Drift Tubes (MDTs), Cathode Strip Chambers (CSCs), Resistive Plate Chambers (RPCs) and Thin Gap Chambers (TGCs) 60
4.15 The ATLAS magnet systems 63
4.16 A schematic representation of the ATLAS trigger system 64
4.17 A schematic representation of a pp collision, as simulated by Monte Carlo . . . 67
4.18 Top quark pair production via gluon fusion (s-channel) 69

5.1 Constructing the signed impact parameter 73
5.2 Probability distributions showing compatibility with the primary vertex for jets and tracks within jets, as found using JetProb 74
5.3 LJR as a function of b-jet tagging efficiency for various b-tagging algorithms . 75
5.4 Feynman diagrams of neutral B meson oscillations 76
5.5 An example of the decay of a b quark into a b-jet, containing two soft muons . 77
5.6 A schematic representation of the relative p_{T} of a muon within a b jet, with respect to the p_{T} of the jet axis 78
5.7 Distribution of the transverse momentum relative to the jet axis of muons from b, c and light hadron decays, and fake muons in simulated $t\bar{t}$ events 79
5.8 The χ^2_{match}/DoF distributions of taggable muons in a sample of simulated $t\bar{t}$ data, for both low p_{T} muons and combined muons 82
5.9 b-jet tagging efficiency and light jet rejection factors achieved using a cut on the χ^2_{match} value of a soft muon within the jet 84
5.11 $\Delta R(\mu, \mathrm{jet})$ distributions for simulated $t\bar{t}$ events from simulated dijet events . . . 87
5.12 Light jet rejection as a function of the b-jet tagging efficiency for the χ^2_{match} and $p_{\mathrm{T}}^{\mathrm{rel}}$ based soft muon taggers 88

6.1 Distribution of p_{T} for all muons in the $t\bar{t}$ MC sample 93
6.2 BR of $(t \to b \to \mu)/(t \to b)$, with respect to the p_{T} of the b quark, with and without acceptance cuts on the muon 93
6.3 Comparison of the p_{T} of b quarks produced from $t \to b \to \mu$ decays in the $t\bar{t}$ MC sample, and of the muons produced from $t \to b \to \mu$ 94
6.4 Distribution of the p_{T} of b quarks produced from t decays, and of muons produced from $t \to b \to \mu$ 95
6.5 Inclusive b-tagging efficiency, in percent, for all SMT muons and only those matched to a true muon from $t \to b \to \mu$ 97
6.6 b-tagging efficiencies binned by the p_{T} of the b quark produced via $t \to b$ . . . 100
6.7 b-tagging efficiencies binned by the p_{T} of the closest jet to the b quark produced via $t \to b$ 102
6.8 The ratio of the fraction of jets matched to the b quark in a $t \to b \to \mu$ decay to the fraction of jets matched to all b quarks produced from the decay of a top quark, binned by the p_{T} of the closest jet to the b quark 103
6.9 Comparison of the p_{T} of b quarks with that of their reconstructed jets, for all $t \to b \to \mu$ decays. 104
6.10 Comparison of the p_{T} of b quarks with that of their reconstructed jets, for all $t \to b \to \ell$ decays. 104
6.11 Comparison of the p_{T} of b quarks with that of their reconstructed jets, for all $t \to b$ decays in which the b does not decay to a lepton. 105
6.12 Comparison of the p_{T} of true muons with that of reconstructed muons matched to them, for all muons from $t \to b \to \mu$ decays. 105

7.1 χ^2_{match} distribution of all probe candidates in both 2011 data (periods B-M) and Monte Carlo simulation 116
7.2 Comparison of the distributions of χ^2_{match}, η, ϕ, and p_{T} of probe muons from J/ψ decays in 2011 data (the numerator of the muon reconstruction efficiency), and SMT tagged muons from simulated $t\bar{t}$ decays 117

7.3 Tag and probe invariant mass, showing the fitted composite function (blue), the background fit, with maximum and minimum (dashed lines, maximum and minimum not distinguishable on this scale), the 3σ and 5σ ranges (magenta and green vertical lines respectively), and an approximation of the signal distribution (red) 119
7.4 A cartoon to show the difference between the maximum and minimum background estimations 120
7.5 Isolation energy distributions of probe muons from simulated J/ψ decays, and soft muons from simulated $t\bar{t}$ decays. 122
7.6 Distributions of the number of tracks surrounding the muon for probe muons from simulated J/ψ decays, and soft muons from simulated $t\bar{t}$ decays. 123
7.7 Isolation transverse momentum distributions of probe muons from simulated J/ψ decays, and soft muons from simulated $t\bar{t}$ decays. 124
7.8 ΔR(tag, probe) distributions for probe muons of isolation momenta above and below the beginnings of the bumps observed in the ptcone20, ptcone30 and ptcone40 distributions 126
7.9 Transverse momenta of probe muons of isolation momenta above and below the bumps observed in the ptcone20, ptcone30 and ptcone40 distributions 127
7.10 Comparison of muon reconstruction efficiencies with MCP results, using 2010 data (Crack and Barrel Regions) 129
7.11 Comparison of muon reconstruction efficiencies with MCP results, using 2010 data (Transition and Endcap Regions) 130
7.12 Efficiencies of the SMT χ^2_{match} tagger for a range of 2011 data periods 132
7.13 Muon reconstruction efficiencies with respect to the p_T of the probe, for the Crack regions on side A and C of the detector, using all 2011 data. 133
7.14 Muon reconstruction efficiencies with respect to the p_T of the probe, for the Barrel regions on side A and C of the detector, using all 2011 data. 134
7.15 Muon reconstruction efficiencies with respect to the p_T of the probe, for the Transition regions on side A and C of the detector, using all 2011 data. 135
7.16 Muon reconstruction efficiencies with respect to the p_T of the probe, for the Endcap regions on side A and C of the detector, using all 2011 data. 136

7.17 Muon reconstruction efficiencies with respect to the p_T of the probe, for the Forward regions on side A and C of the detector, using all 2011 data. 137
7.18 χ^2_{match} efficiencies and data/Monte Carlo scale factor with respect to the energy deposited in a cone of various sizes around the probe muon (isolation energy). 138
7.19 χ^2_{match} efficiencies and data/Monte Carlo scale factor with respect to the p_{T} in a cone of various sizes around the probe muon. 139
7.20 χ^2_{match} efficiencies and data/Monte Carlo scale factor with respect to the number of tracks in a cone of various sizes around the probe muon. 140
7.21 χ^2_{match} efficiencies and data/Monte Carlo scale factors with respect to the η and ϕ of the probe muon. 141
7.22 χ^2_{match} efficiencies with respect to the p_T of the probe muon, for the Crack regions on side A and C of the detector, using all 2011 data. 143
7.23 χ^2_{match} efficiencies with respect to the p_T of the probe muon, for the Barrel regions on side A and C of the detector, using all 2011 data. 144
7.24 χ^2_{match} efficiencies with respect to the p_T of the probe muon, for the Transition regions on side A and C of the detector, using all 2011 data. 145
7.25 χ^2_{match} efficiencies with respect to the p_T of the probe muon, for the Endcap regions on side A and C of the detector, using all 2011 data. 146
7.26 χ^2_{match} efficiencies with respect to the p_T of the probe muon, for the Forward regions on side A and C of the detector, using all 2011 data. 147
7.27 Comparison of the p_{T} distributions of probe muons from $J/\psi \to \mu\mu$ and $Z \to \mu\mu$ decays in 2011 data, and truth $t \to b \to \mu$ from simulated $t\bar{t}$ decays 149
7.28 Comparison of muon reconstruction scale factors evaluated using $J/\psi \to \mu\mu$ and $Z \to \mu\mu$ events with respect to the p_T of the probe, for the five $|\eta|$ regions using all 2011 data 151
7.29 Comparison of χ^2_{match} based soft muon tagger scale factors evaluated using $J/\psi \to \mu\mu$ and $Z \to \mu\mu$ events with respect to the p_T of the probe, for the five $|\eta|$ regions using all 2011 data 152
7.30 Mistag rate and data/simulation scale factor of the SMT algorithm as a function of the jet p_T 154

7.31 From the top left to the bottom right, the p_{T}, the χ^2_{match} and the p_{T} relative to the jet axis ($p_{\mathrm{T}}^{\mathrm{rel}}$) of the soft muons in the e+jets channel (left) and μ+jets channel (right) 155

8.1 A Feynman diagram of the decay of a pair of top quarks via the lepton+jets channel. 158

8.2 Data-calibrated and uncalibrated b-jet tagging efficiencies and scale factor, with respect to the p_{T} of the b-jet 162

D.1 Efficiency of matching true b quarks from $t \to b$ and jets of truth flavour 5. . . . 176

D.2 Distribution of ΔR between a jet of truth flavour 5 and the nearest true b quark 177

D.3 Inclusive ε_b^u with respect to jets labelled as truth flavour 5, matched to the reconstructed muon 177

List of Tables

2.1 Fundamental particles of the Standard Model [6] 22

3.1 Production channels of $t\bar{t}$ pairs at various centre of mass energies. 32

3.2 The decay modes and branching fractions of the W bosons within a $t\bar{t}$ decay . . 36

4.1 2011 collision data information 45

4.2 Parameters of the Precision and Trigger chambers of the MS 59

5.1 Comparison of light jet rejection factors produced for the χ^2_{match} and $p_{\text{T}}^{\text{rel}}$ based taggers, when achieving several b-tagging efficiencies 83

6.1 Event selection requirements in the μ+jets channel for a simulated dataset of $t\bar{t}$ events 91

6.2 Comparison of BR (in percent) between measured values and those found in the MC@NLO+Herwig sample of simulated data, for various decays of b quarks producing muons 94

6.3 Efficiency of the individual cuts within the SMT Tagger, without truth matching 98

6.4 Efficiency of the individual cuts within the SMT Tagger, with truth matching . 98

6.5 Truth particles ΔR matched to the SMT muons 107

6.6 Decay chain of muons not from $t \to b$, matched to SMT muons (using the preselected events). 108

6.7 Non muon truth particles matched to SMT muons (using the preselected events). 108

7.1 Data quality requirements included in the muon channel good runs list for all 2011 data 111

7.2 Trigger requirements for both tag and probe candidates, according to 2011 data period . . . 113
7.3 Cuts performed on tag and probe candidates. . . . 114
7.4 Cuts performed on numerator and denominator of SMT tagging efficiency . . . 115
7.5 Trigger requirements for both tag and probe candidates, according to 2010 data period. . . . 128
7.6 Pseudorapidity regions of the ATLAS detector. . . . 131
7.7 Data/MC χ^2_{match} scale factors for 2011 data - uncertainty quoted is statistical + systematic. . . . 148

8.1 W+jets background estimation in the ≥ 3 jet bin, for the e+jets and μ+jets channels 160
8.2 QCD multijet background estimation in the ≥ 3 jet bin, for the e+jets and μ+jets channels . . . 161
8.3 Summary of individual relative systematic uncertainty contributions to the cross section measurement, in percent. . . . 163
8.4 Comparison of signal to background ratios for $t\bar{t}$ cross section measurements performed using SMT and JetProb+SV0 b-tagging algorithms . . . 164
8.5 Observed event yields in the pretag and tagged ≥ 3 jet bin and background estimates with the quadrature sum of the statistical and systematic uncertainties 165

C.1 Definition of loose, medium and tight muon identification cuts, for the Muid and STACO muon reconstruction algorithms. . . . 172
C.2 Definition of variables used for loose, medium and tight electron identification cuts for the central region of the detector ($|\eta| < 2.47$). . . . 173

E.1 The full decay chains of a sample of muons incorrectly tagged as originating from a $t \to b \to \mu$ decay. . . . 179

F.1 Muon reconstruction efficiencies for the Crack region ($0.0 < \eta < 0.1$) of side A of the ATLAS detector . . . 180
F.2 χ^2_{match} efficiencies for the Crack region ($-0.1 < \eta < 0.0$) of side A of the ATLAS detector . . . 181

Chapter 1

Introduction and Motivation

The Large Hadron Collider (LHC) is capable of truly pushing forward the boundaries of physics, and of the knowledge of the human race. One particular area of interest to physicists is that of testing the limitations of the Standard Model of Particle Physics (SM). For many years the SM has been capable of explaining observed interactions, and predicting the existence of new particles. One of the most recent predicted particles to be confirmed is the top quark (t), discovered in 1995 at the Tevatron proton-antiproton collider in the USA [7]. The top quark was only found recently due to the fact that it has a relatively enormous mass, meaning that a collider of hitherto unseen energy was required to produce this quark. Due to the high centre of mass energy at the LHC, the top quark is expected to be produced in large amounts - specifically in pairs of one top and one antitop quark ($t\bar{t}$ pairs). The probability of this occurring in any one particle collision is known as the top quark pair production cross section ($\sigma_{t\bar{t}}$), measured in units of area. At the LHC, most of the interactions produced by the proton–proton (pp) collisions will involve gluon–gluon fusion, which result in $t\bar{t}$ pairs in many cases. Measurement of the $t\bar{t}$ cross section is an important early measurement for the LHC, serving as it does as a powerful validation of the SM, but $t\bar{t}$ production and identification serve another role in the physics program at the LHC - that of probing new physics *beyond* the standard model. Any new physics that has the same decay signature as $t\bar{t}$ pairs will cause an excess in the measured SM $t\bar{t}$ cross section, which is predicted to be $\sigma_{t\bar{t}} = 165^{+11}_{-16}$ pb at a centre of mass energy of $\sqrt{s}$ = 7 TeV [8].

An example of such new physics is the Higgs boson. In some theories of the Higgs field, the boson shares decay modes with the top quark, such as a charged Higgs boson produced from $t \to H^+ b$ and decaying via $H^+ \to c\bar{s}$ [9]. Therefore, an increase in events with the $t \to c\bar{s}b$

signature could indicate not an excess of $t\bar{t}$ pairs decaying via $t \to Wb$, but instead a glimpse of new physics which would be indicated by a second peak in the invariant mass spectrum of the c and $\bar{s}$ jets, in addition to that of the W boson.

The $t\bar{t}$ pair decay modes can be classified in one of three ways, depending on the decays of the W bosons. The W can decay either hadronically into a pair of quarks ($W \to qq$), or leptonically into a lepton and its corresponding neutrino ($W \to l\bar{\nu}_l$). The three categories are "all-hadronic" where both W bosons decay in the first manner, "dilepton" where both decay to a lepton and a neutrino, and "lepton+jets" where one W decays to leptons and one to hadronic jets. The hadron containing the b quark produced from the decay of the top quark decays into a collimated shower of particles, which emanate away from the decay vertex in what is known as a b-jet. Within this b-jet there will often be a muon, which is a relatively long-lived and stable particle, the detection of which can allow us to identify, or "tag" the b-jet (a technique known as "b-tagging"). The momentum of the muon within the b-jet will be lower (also referred to as "softer") than that of a muon produced by the decay of the W boson, and so this method is known as Soft Muon Tagging, or SMT.

Measurements making use of SMT, such as establishing $\sigma_{t\bar{t}}$, can be complementary to measurements made using lifetime based b-tagging techniques as SMT makes use of different properties of the b-jet, and as such is sensitive to different systematic uncertainties. This thesis concerns itself with a new algorithm for the identification of b-jets using their soft muons based on the quality of the muon reconstruction, using the χ^2 per degree of freedom of the match between the track left by a muon in the inner detector of ATLAS and the track left in the muon spectrometer (as explained in Chapter 4). There are other SMT algorithms in use, discussed in Chapter 5, the default algorithm within ATLAS being based on the relative transverse momentum ($p_{\mathrm{T}}^{\mathrm{rel}}$) of the muon to that of the axis of the b-jet. This tagger, by definition, requires the presence of a jet for calibration, whereas a tagger which makes use of the quality of reconstruction of the muon will only require a sample of muons for calibration purposes. The performance of these taggers is compared in Chapter 5.

Chapter 2

The Standard Model of Particle Physics

The Standard Model (SM) of particle physics describes the forces and interactions between the elementary particles of nature. The SM has been developed throughout the 20th century, and with the confirmation of the existence of quarks in the 1970s [10–13] the SM reached its current form. The SM is an amazingly complete description of all currently observable particle interactions, and forms the basis of the general understanding of the interactions of fundamental particles.

The SM incorporates all known elementary particles, which form two distinct groups - fermions (particles of spin-1/2) and bosons (spin-1, except the Higgs with spin-0). These are shown in Table 2.1. The SM contains three generations of leptons and quarks, each of which contain two quarks and two leptons, as indicated in Table 2.1. All the fermions have an antimatter counterpart - in the case of quarks (q), these are antiquarks ($\bar{q}$), each having opposite charge to the quark, and all of which can interact via the strong, weak and electromagnetic forces. The leptons are accompanied by antileptons, also having opposite charge and interacting via the electromagnetic and weak forces. The SM also includes the interactions via the electromagnetic, weak and strong forces, which are said to be mediated by the gauge bosons, the force carriers of the SM.

Table 2.1: Fundamental particles of the Standard Model [6]

Particle Type	Name		Spin	Charge [e]	Mass	Generation
Quarks (Fermions)	up	(u)	1/2	+2/3	1.5 to 3.3 MeV	I
	down	(d)	1/2	-1/3	3.5 to 6.0 MeV	I
	charm	(c)	1/2	+2/3	$1.27^{+0.07}_{-0.11}$ GeV	II
	strange	(s)	1/2	-1/3	105^{+25}_{-35} MeV	II
	top	(t)	1/2	+2/3	1.5 to 3.3 GeV	III
	bottom	(b)	1/2	-1/3	$4.2^{+0.17}_{-0.07}$ GeV	III
Leptons (Fermions)	electron	(e)	1/2	-1	0.511 MeV	I
	e-neutrino	(ν_e)	1/2	0	$\ll 1$ MeV	I
	muon	(μ)	1/2	-1	105.66 MeV	II
	μ-neutrino	(ν_μ)	1/2	0	$\ll 1$ MeV	II
	tau	(τ)	1/2	-1	1776.84 ± 0.27 GeV	III
	τ-neutrino	(ν_τ)	1/2	0	$\ll 1$ MeV	III
Gauge Bosons	photon	(γ)	1	0	0	
	gluon	(g)	1	0	0	
	$W^\pm$		1	± 1	80.398 ± 0.025 GeV	
	W^0		1	0	91.1876 ± 0.0021 GeV	
Higgs Boson	H^0		0	0	$126.0^{\pm 0.4(\text{stat.})}_{\pm 0.4(\text{syst.})}$ GeV [14]	

2.1 Quantum Electrodynamics

The theory of the interactions of particles via the electromagnetic force is Quantum Electrodynamics, or QED. The gauge boson of the electromagnetic force is the photon, which is both massless and has no electric charge, and as such cannot interact with other photons. All charged fermions may take part in electromagnetic interactions. A Feynman diagram of the interaction vertex between photons and fermions is shown in Figure 2.1.

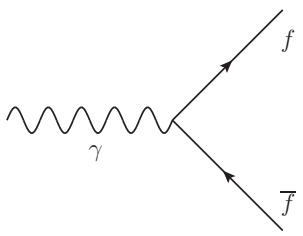

Figure 2.1: Feynman diagram of the fundamental QED interaction vertex. Fermions and antifermions are represented by f and $\bar{f}$, while γ represents the photon.

2.2 The Weak and Electroweak Interaction

The weak force is responsible for most radioactive decay, and allows for the changing of quark flavour via the interaction vertices shown in Figure 2.2(a). The propagators of the weak force are the neutral Z^0 and the charged W^+ and W^- bosons. It is these charged bosons which allow for the flavour changing charged current interactions shown in Figure 2.2(a). Conversely, lepton flavour is conserved at the weak vertices (Figure 2.2(b)).

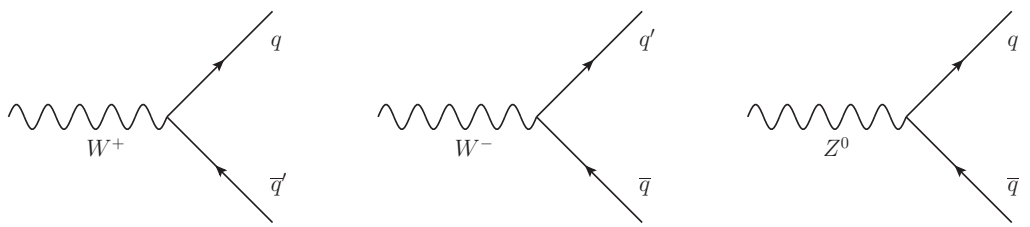

(a) Fundamental vertices for weak interactions involving quarks

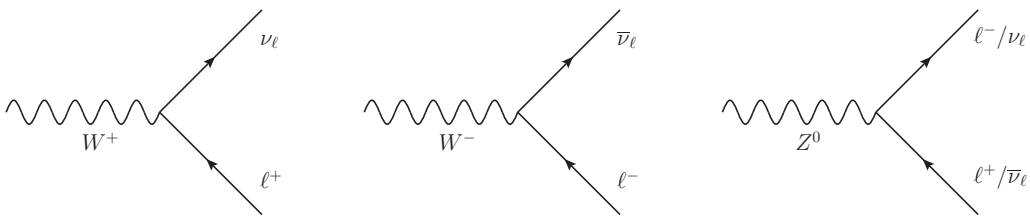

(b) Fundamental vertices for weak interactions involving leptons

Figure 2.2: Feynman diagrams of the fundamental vertices for weak force interactions. Quarks and antiquarks are represented by q and $\bar{q}$ respectively, while $\bar{q}'$ indicates that q and $\bar{q}'$ are of different flavours. Leptons and their neutrinos are shown as ℓ^+, ℓ^-, ν_ℓ and $\overline{\nu}_\ell$.

2.2.1 The CKM Matrix

The relative coupling between quark flavours at the weak interaction vertex is parametrised by the Cabibbo-Kobayashi-Maskawa (CKM) matrix [15, 16], the elements of which are related to the strength of the coupling between the u, c and t quarks and their rotated partners, d', s' and b' - these are superpositions of the d, s and b quarks. The CKM matrix relates the rotated states to the d, s and b physical states as shown in Equation 2.1, and describes their relative coupling, thereby controlling the nine possible flavour changing transformations. The current best values

of the CKM matrix elements are shown in Equation 2.2 [6].

$$\begin{pmatrix} d' \\ s' \\ b' \end{pmatrix} = \begin{pmatrix} V_{ud} & V_{us} & V_{ub} \\ V_{cd} & V_{cs} & V_{cb} \\ V_{td} & V_{ts} & V_{tb} \end{pmatrix} \begin{pmatrix} d \\ s \\ b \end{pmatrix} = V_{CKM} \begin{pmatrix} d \\ s \\ b \end{pmatrix} \tag{2.1}$$

$$V_{CKM} = \begin{pmatrix} V_{ud} & V_{us} & V_{ub} \\ V_{cd} & V_{cs} & V_{cb} \\ V_{td} & V_{ts} & V_{tb} \end{pmatrix} = \begin{pmatrix} 0.97428 \pm 0.00015 & 0.2253 \pm 0.0007 & 0.00347^{+0.00016}_{-0.00012} \\ 0.2252 \pm 0.0007 & 0.97345^{+0.00015}_{-0.00016} & 0.0410^{+0.00016}_{-0.00012} \\ 0.00862^{+0.00026}_{-0.00020} & 0.0403^{+0.0011}_{-0.0007} & 0.999152^{+0.000030}_{-0.000045} \end{pmatrix} \tag{2.2}$$

It can be seen that the couplings between quarks of the same generation (u and d, c and s, t and b) are far larger than those across generations, meaning that flavour changing within generations is favoured compared to the off-diagonal processes in the CKM matrix. Starting with an up quark (u), the probability of u decaying into a down quark (d) is given by $|V_{ud}|^2$. If the three generations of quarks are included, the sum of probabilities for all possible decays is $|V_{ud}|^2 + |V_{us}|^2 + |V_{ub}|^2 = 1$. This is also valid starting with a d decaying to a u quark, combinations of up-type (u, c or t) quark and down-type (d, s or b) quarks, or a W boson decaying to a ud pair. The same matrix element applies regardless of the orientation of the vertices involving charged W bosons shown in Figure 2.2(a), meaning that the coupling at the vertex is the same for $W^+ \to u\bar{d}$, $d \to uW^-$, $u \to dW^+$, $dW^+ \to u$, $u\bar{d} \to W^+$, $uW^- \to d$, and the charge conjugates of these processes. It should be noted that the probability of a top quark decay via the weak interaction involving a bottom quark, such as $t \to Wb$, is ≈ 0.999 given by $|V_{tb}|^2$. The $t \to Wd$ and $t \to Ws$ decays are highly unlikely by comparison. The semileptonic decay of b hadrons, which is of vital importance in the development of the soft muon tagger with which this thesis is concerned, is governed by the V_{ub} and V_{cb} matrix elements - the decay $b \to cW^- \to c\ell\bar{\nu}_\ell$ is dominant as opposed to $b \to uW^- \to u\ell\bar{\nu}_\ell$, as the value of $|V_{cb}|^2$ is a factor of approximately 140 larger than $|V_{ub}|^2$ [6].

The weak interaction also has the unique quality of being able to violate charge-parity (CP) symmetry. The C refers to the effect of replacing particles with their antiparticles, and P refers to the mirror image of the reaction with regards the helicity (the projection of the spin of a particle onto its momentum). CP symmetry proposes that, for particles a and b, the amplitude (M) of a

process $a \to b$ must be the same as the amplitude ($\bar{M}$) of the corresponding antiparticle process $\bar{a} \to \bar{b}$. However, it has been observed that this symmetry can be broken, for example in the decay of neutral Kaons [17]. This is expanded upon in Appendix A.

The so-called "B factories" (such as BaBar at SLAC and Belle at KEK) collided electrons with positrons to produce $e^+e^- \to \Upsilon(4S)$, obtaining pairs of B and $\bar{B}$ mesons from the resulting decay. The study of the decay rates of the B mesons compared to the $\bar{B}$ mesons can give information on the extent of CP violation in these processes. One important experimental goal is the investigation of the extent of CP violation in the early universe, which may explain why the universe appears to be dominated by matter rather than antimatter. If, at the beginning of the universe, the processes producing matter occur at a higher rate than those producing antimatter, then CP symmetry must be violated. The resultant imbalance between matter and antimatter could then accrue over time, resulting in a matter dominated universe.

2.2.2 The Higgs Mechanism

The unification of the weak and electromagnetic forces was first proposed in 1961 by Glashow [18], and developed with Weinberg and Salam [19,20] into a theory for which the three would win the 1979 Nobel prize for physics. It was proposed that, while at low energies the electromagnetic and weak forces can be treated separately, in fact at higher energies (above ≈ 246 GeV) they can be considered to be a single force.

The electroweak interaction theory predicts the existence of four massless bosons, however the three bosons of the electroweak force ($W^{\pm}$ and Z^0) discovered at CERN in 1983 were found to have mass [21]. This discovery breaks the symmetry of the electroweak theory, and so there must be a method of spontaneous electroweak symmetry breaking incorporated into the SM in order to explain the masses of the $W^{\pm}$ and Z^0 bosons. The method suggested by Higgs [22] fulfils this role, predicting another massive boson of spin 0, the "Higgs boson".

The concept of local gauge invariance is a guiding principle of the formulation of the SM. A local gauge invariant theory requires that the Lagrangian[1] of a field theory (such as QED, QCD and Electroweak theory) be invariant under a gauge transformation. This means that if the underlying field variables are subjected to a gauge transformation, the physics of the field (and

[1]The Lagrangian is a mathematical function which summarises the dynamics of a system, defined as the kinetic energy of a system minus its potential energy, as a function of time, spatial coordinates, and the time derivative of these spatial coordinates. The Lagrangian can also be written using functions of these coordinates as the basis.

its observable effects) remains unchanged [23].

The Lagrangian of the current form of the SM, incorporating the Higgs potential, is shown in Equation 2.3. It includes terms relating to the field strength of the strong, weak and electromagnetic forces ($G^a_{\mu\nu}G^{\mu\nu a}, W^a_{\mu\nu}W^{\mu\nu a}$ and $B_{\mu\nu}B^{\mu\nu}$ respectively), the gauge covariant derivative (D_μ), the complex Higgs scalar field (ϕ), the Higgs kinetic terms ($|D_\mu\phi|^2$) and the electromagnetic kinetic terms ($\bar{\psi}D_{mu}\psi$). Finally, the Higgs potential ($V(\phi)$) is added to the SM, as well as mass terms for the fermions ($\lambda\bar{\psi}\psi\phi$) - without the Higgs mechanism these latter terms are not local gauge invariant, however Higgs [22] proposed a way of modifying the SM to preserve local gauge invariance while breaking the symmetry for the vacuum state ("spontaneous symmetry breaking"), allowing for the existence of the massive bosons.

$$\mathcal{L}_{SM} = -\frac{1}{4}\mathrm{G}^{\mathrm{a}}_{\mu\nu}\mathrm{G}^{\mu\nu\mathrm{a}} - \frac{1}{4}\mathrm{W}^{\mathrm{a}}_{\mu\nu}\mathrm{W}^{\mu\nu\mathrm{a}} - \frac{1}{4}\mathrm{B}_{\mu\nu}\mathrm{B}^{\mu\nu} + |\mathrm{D}_\mu\phi|^2 + \bar{\psi}\mathrm{D}_{\mathrm{mu}}\psi - \mathrm{V}(\phi) + \lambda\bar{\psi}\psi\phi \tag{2.3}$$

The Higgs mechanism proposes that at energies above a very high threshold (i.e. those of the very early universe), the masses of the electroweak bosons are negligible compared to their energy, and so the Higgs potential is not required to restore the symmetry of the Lagrangian. However, the symmetry is broken at lower energies and the massive $W^\pm$ and Z^0 bosons interact with a field permeating all space (the Higgs field).The gauge boson of this interaction is the Higgs boson. The LHC operates at the TeV scale, meaning that the Higgs mechanism is required to restore the electroweak symmetry. The coupling of a particle with the Higgs boson is dependent on mass, therefore the Higgs boson is expected to couple most strongly with the top quark, which is by far the most massive of the fundamental particles within the SM.

One extension to the Standard Model which offers an alternative to the neutral SM Higgs boson is the two Higgs-doublet model (2HDM) [24, 25], in which the Higgs field is represented by two doublets of scalar fields, as opposed to the SM Higgs field which consists of a single doublet. 2HDM is used in the Minimal Supersymmetric Standard Model (MSSM), and proposes that one doublet couples to up-type fermions, and the other to down-type. The doublet fields manifest as two charged Higgs bosons ($H^\pm$) and three neutral Higgs bosons (h, H and A). The 2HDM theory permits the decay of the top quark into a charged Higgs boson and a bottom quark, $t \to H^+b$. The $H^+ \to c\bar{s}$ dominates at charged Higgs boson masses of $m_{H^+} \lesssim 130$ GeV, meaning that the charged Higgs boson has the $t \to H^+b \to c\bar{s}b$ signature in common with $t \to Wb \to c\bar{s}b$.

Hence, deviations from the predicted SM $t\bar{t}$ cross section can be indicative of the production of charged Higgs bosons as in the 2HDM model.

A powerful validation of SM Higgs theory has occurred very recently, with the discovery of a boson consistent with the Higgs boson at both ATLAS and CMS at CERN [14, 26] using 2011 data. This discovery does not render the SM complete, however, as the theoretical loop corrections cause the mass of the Higgs boson to diverge, not approaching a limit. This problem needs to be solved, whether by the introduction of a symmetry cancelling the divergences (such as SUSY) or by other means. There is also still work to be done to refine and improve measurements of standard model processes, as well as probing theories beyond the standard model, some of which have observable consequences at the LHC.

2.3 Quantum Chromodynamics

Strong force interactions between "coloured" particles are described by the theory of Quantum Chromodynamics (QCD). Colour, in this context, is just a quantum number which is exchanged in strong interactions, and is a property of gluons and quarks. The chosen colours are red, blue and green (and antired, antiblue and antigreen), as these can be combined to form a colourless state, analogous to the mixing of red, green and blue light to form white light. Quarks take a single colour, while gluons may have a mixture of two colours and anticolours (such as red-antiblue or green-antired). Nine colour-anticolour combinations might naively be expected ($r\bar{g}, r\bar{b}, g\bar{r}, g\bar{b}, b\bar{r}, b\bar{g}, r\bar{r}, g\bar{g}, b\bar{b}$), however there are in fact eight unique colour combinations and eight distinct gluons, meaning that is not possible to add any combination of states to produce any other. The eight colour-anticolour states of the gluon can be shown as in Equation 2.4.

$$\begin{array}{cc} (r\bar{b}+b\bar{r})/\sqrt{2} & i(r\bar{b}-b\bar{r})/\sqrt{2} \\ (r\bar{g}+g\bar{r})/\sqrt{2} & i(r\bar{g}-g\bar{r})/\sqrt{2} \\ (b\bar{g}+g\bar{b})/\sqrt{2} & i(b\bar{g}-g\bar{b})/\sqrt{2} \\ (r\bar{r}-g\bar{g})/\sqrt{2} & (r\bar{r}+g\bar{g}-2b\bar{b})/\sqrt{6} \end{array} \tag{2.4}$$

If the colour states are thought of as column vectors with three elements corresponding to the three colours, then the red, blue and green states can be shown as in Equation 2.5 and the corresponding anticolour states represented as row vectors as shown in Equation 2.6. The consequence of this is that the eight gluon colour states can be represented as the 3×3 matrices

shown in Equation 2.7 [2].

$$r = \begin{pmatrix} 1 \\ 0 \\ 0 \end{pmatrix} \quad g = \begin{pmatrix} 0 \\ 1 \\ 0 \end{pmatrix} \quad b = \begin{pmatrix} 0 \\ 0 \\ 1 \end{pmatrix} \tag{2.5}$$

$$\overline{r} = (1,0,0) \quad \overline{g} = (0,1,0) \quad \overline{b} = (0,0,1) \tag{2.6}$$

$$(r\bar{b} + b\bar{r})/\sqrt{2} = \frac{1}{\sqrt{2}} \begin{pmatrix} 0 & 0 & 1 \\ 0 & 0 & 0 \\ 1 & 0 & 0 \end{pmatrix} \quad i(r\bar{b} - b\bar{r})/\sqrt{2} = \frac{1}{\sqrt{2}} \begin{pmatrix} 0 & 0 & -i \\ 0 & 0 & 0 \\ i & 0 & 0 \end{pmatrix} \tag{2.7}$$

$$(r\bar{g} + g\bar{r})/\sqrt{2} = \frac{1}{\sqrt{2}} \begin{pmatrix} 0 & 1 & 0 \\ 1 & 0 & 0 \\ 0 & 0 & 0 \end{pmatrix} \quad i(r\bar{g} - g\bar{r})/\sqrt{2} = \frac{1}{\sqrt{2}} \begin{pmatrix} 0 & -i & 0 \\ i & 0 & 0 \\ 0 & 0 & 0 \end{pmatrix}$$

$$(b\bar{g} + g\bar{b})/\sqrt{2} = \frac{1}{\sqrt{2}} \begin{pmatrix} 0 & 0 & 0 \\ 0 & 0 & 1 \\ 0 & 1 & 0 \end{pmatrix} \quad i(b\bar{g} - g\bar{b})/\sqrt{2} = \frac{1}{\sqrt{2}} \begin{pmatrix} 0 & 0 & 0 \\ 0 & 0 & -i \\ 0 & i & 0 \end{pmatrix}$$

$$(r\bar{r} - g\bar{g})/\sqrt{2} = \frac{1}{\sqrt{2}} \begin{pmatrix} 1 & 0 & 0 \\ 0 & -1 & 0 \\ 0 & 0 & 0 \end{pmatrix} \quad (r\bar{r} + g\bar{g} - 2b\bar{b})/\sqrt{6} = \frac{1}{\sqrt{6}} \begin{pmatrix} 1 & 0 & 0 \\ 0 & 1 & 0 \\ 0 & 0 & -2 \end{pmatrix}$$

The presence of colour charge means that QCD permits gluons to interact with other gluons, as their colour charges may differ. The fundamental interaction vertices of QCD are shown in Figure 2.3. QCD dictates that all free particles must appear as colourless states, specifically hadrons which are colourless combinations of quarks, antiquarks and gluons. Hadrons can be divided into two classes: mesons, which consist of quark-antiquark ($q\bar{q}$) pairs which must also be a colour-anticolour pair, and baryons, which contain three quarks or antiquarks. Baryons must contain quarks with a combination of red, green and blue (or their anticolours) which mix

[2] These matrices are the Gell-Mann matrices multiplied by a normalising factor of $\sqrt{2}$. These matrices are one possible representation of the generators of the special unitary group called SU(3).

together to be colourless. When a high energy particle is incident on a quark within a hadron, the now separated quarks "hadronise" whereby the separate quarks combine with other partons to form colourless objects.

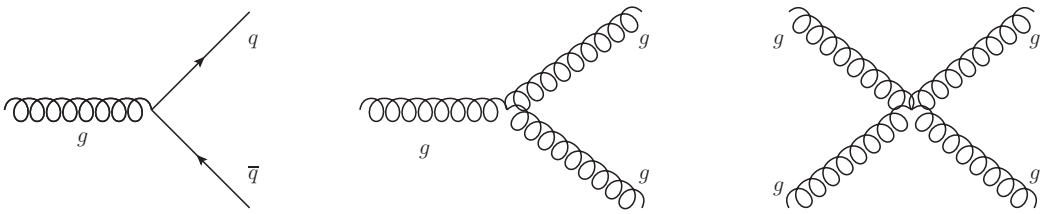

Figure 2.3: Feynman diagrams of the fundamental QCD interaction vertices. Quarks and antiquarks are represented by q and $\bar{q}$ respectively, and the gluon is represented by g.

Chapter 3

Top Quark Physics

The top quark was first proposed by Kobayashi and Maskawa in a paper published in 1973 [16], in which a third generation of quarks was suggested in order to explain CP violation which had been experimentally observed in the decay of Kaons [17]. The third generation was proposed as a weak-isospin doublet [1] of two quarks (in addition to the first two generations, the up and down quarks and the strange and charm quarks). A third generation of leptons was confirmed by the discovery of the τ lepton in 1975 [27], and the prediction was confirmed by the 1977 discovery of the bottom quark (b) [28], one half of the proposed doublet, but the top quark remained elusive for far longer. It was not until 1995 at the Tevatron that the top quark was discovered [7] - the reason for the delay is largely the enormous mass of the top quark; the current world average for the mass of the top quark is $m_t = 173.1 \pm 1.3$ GeV, from Tevatron results [6] - by comparison, this is approximately 40 times the mass of the next most massive quark, the bottom quark (b), and between four and five orders of magnitude larger than the masses of the up and down quarks, the most common of the six SM quarks. The mass of the top quark is approximately equivalent to that of a gold atom. The large mass was not predicted by the original 1973 paper, and meant that a collider of far higher energy than existed at the time of the original prediction was required to produce the top quark.

[1] Such a doublet is a pair of particles expected to behave the same way under interactions with the weak force.

3.1 Top Quark Production Channels

The proton-proton collisions at the LHC will result in either quark-quark or gluon-gluon fusion and scattering, which will produce $t\bar{t}$ pairs from leading order processes as shown in Figure 3.1 [2]. The quarks and gluons shown in Figure 3.1 are partons within the protons colliding within the LHC, and each parton carries a fraction (x_i) of the momentum carried by the proton.

It is relatively simple to calculate the threshold value of x_i required to produce $t\bar{t}$ pairs at both the Tevatron and the LHC. If two colliding partons, i and j, carry x_i and x_j of the centre of mass energy of the collider, $\sqrt{s}$, then one can define $\hat{s}$, the effective centre of mass energy squared, as $\hat{s} = x_i\sqrt{s} \cdot x_j\sqrt{s} = x_i x_j s$. In order to produce $t\bar{t}$ pairs at rest the effective centre of mass energy must be greater than the mass of two top quarks, i.e. $\hat{s} \geq (2m_t)^2$, and so if we assume that the incident partons have symmetric values of x, i.e. $x_i \approx x_j$, the result is as follows:

$$\sqrt{\hat{s}} = \sqrt{x_i x_j s} \approx x_i\sqrt{s} \geq 2m_t \tag{3.1}$$

So the minimum value of x_i required to produce $t\bar{t}$ pairs is

$$x_i \approx \frac{2m_t}{\sqrt{s}} \tag{3.2}$$

This means that the threshold fraction of the proton momentum carried by the partons which produce the $t\bar{t}$ pairs at the Tevatron is 0.18 for $\sqrt{s} = 1.96$ TeV, but only 0.05 at the LHC with $\sqrt{s} = 7$ TeV, or 0.025 at the design energy of $\sqrt{s} = 14$ TeV. The likelihood of a parton possessing the threshold amount of momentum at the Tevatron is higher for u and d valence quarks than for gluons, leading to quark-antiquark ($q\bar{q}$) annihilation being the dominant channel for $t\bar{t}$ production. The Tevatron is a $p\bar{p}$ collider with equal amounts of valence quarks and antiquarks, making $q\bar{q}$ annihilation more likely than in the pp collisions at the LHC. The LHC, by contrast, is a pp collider, meaning that there are no valence antiquarks available for $q\bar{q}$ annihilation. This, in combination with the lower momentum threshold for partons at the LHC, means that gluon fusion dominates and the total $t\bar{t}$ pair production cross section is increased by a factor of over 20 for $\sqrt{s} = 7$ TeV and a factor of more than 100 for $\sqrt{s} = 14$ TeV. While the majority of the momentum within a proton is typically carried by the valence quarks, any of the gluons within the proton may easily have a fraction of the overall momentum in excess of

[2] All Feynman diagrams in this Thesis were produced by the author using JaxoDraw [29].

the small threshold of 0.05. The parton momentum fractions need not have the same value, and the partons may well have differing momenta, therefore production of $t\bar{t}$ pairs at the LHC can therefore involve low-x gluons as well as high-x gluons and valence quarks.

At the LHC, when running at a centre of mass energy of $\sqrt{s} = 7$ TeV, 15% of $t\bar{t}$ pairs are produced from quark-antiquark annihilation (Figure 3.1(a)), with the remaining 85% coming from gluon fusion, as shown in Figures 3.1(b) and 3.1(c). The s-channel has an intermediate gluon which carries all the four-momentum and colour charge of the incoming gluons, while the intermediate particle in the t-channel is either a t or $\bar{t}$ quark, depending on the time ordering of the vertices. These proportions can be compared to those of the Tevatron and the LHC at various centre of mass energies as shown in Table 3.1.

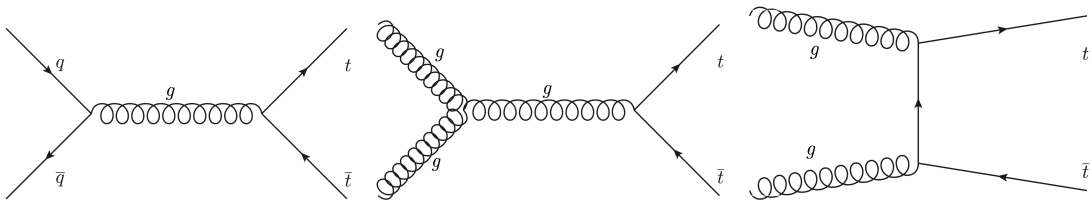

(a) quark-antiquark annihilation (b) gluon fusion (s-channel) (c) gluon fusion (t-channel)

Figure 3.1: Leading order $t\bar{t}$ production channels.

Table 3.1: Production channels of $t\bar{t}$ pairs at various centre of mass energies.

Collider	centre of mass energy	$q\bar{q}$ annihilation	gluon fusion
Tevatron	$\sqrt{s} = 1.96$ TeV	$\sim 90\%$	$\sim 10\%$
LHC	$\sqrt{s} = 7$ TeV	$\sim 15\%$	$\sim 85\%$
LHC	$\sqrt{s} = 8$ TeV	$\sim 12\%$	$\sim 88\%$
LHC	$\sqrt{s} = 14$ TeV	$\sim 10\%$	$\sim 90\%$

The total top quark cross section is one of the most important measurements which can be compared between the LHC and previous top quark results - the top quark has only been observed previously at the Tevatron, and a prediction of the top quark mass was made at the Large Electron-Positron collider at CERN (LEP) [3].

[3]The centre of mass energies achieved at LEP were not sufficient to directly produce top quarks, however it was possible to gather information about the top mass from higher order processes such as radiative corrections to electroweak processes observable at LEP. This led to a top mass prediction of $m_t = 179 \pm 9^{+17}_{-19}$ GeV that was later confirmed by measurements at CDF and D0, serving as a powerful proof of the predictive power of the Standard Model [30].

As a consequence of its large mass, the top quark has a very short lifetime of $\approx 5 \times 10^{-25}$s, shorter than the time required for strong interactions to occur (of the order of 10^{-24}s [6]). This means that unlike other quarks which exist in bound states (hadrons), the top quark lifetime is sufficiently short that there is no time to form hadrons, affording a rare opportunity to study bare top quarks, something which is impossible with the other five less massive quarks.

The LHC makes it possible to study single top quark production, a process first observed at the Tevatron in 2009 [31, 32], with far greater statistics than has previously been possible. Single top quark production is an electroweak process, for which the leading order diagrams are shown in Figure 3.2. Single top production has a cross section approximately half of that of $t\bar{t}$ pairs at the LHC. The cross section for single top quark production at $\sqrt{s} = 7$ TeV with the ATLAS detector has been measured as $\sigma_t = 83 \pm 20$ pb [33], whereas the $t\bar{t}$ cross section has been measured to be $\sigma_{t\bar{t}} = 177^{+18}_{-17}$ pb [34]. Consequently the majority of the top quarks produced will be in the form of $t\bar{t}$.

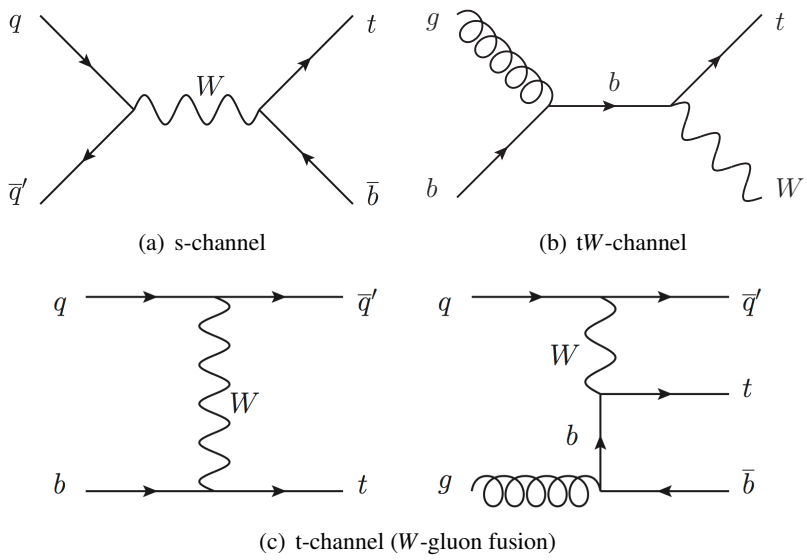

(a) s-channel (b) tW-channel

(c) t-channel (W-gluon fusion)

Figure 3.2: Single top quark production channels .

A summary of the ATLAS measurements of the $t\bar{t}$ pair production cross section, as of May 2012, can be seen in Figure 3.3. The predictions of $\sigma_{t\bar{t}}$ based on simulated data can be seen in Figure 3.4, as well as the values measured by the CDF and D0 experiments at the Tevatron and also the three $t\bar{t}$ decay channels at ATLAS (explained below).

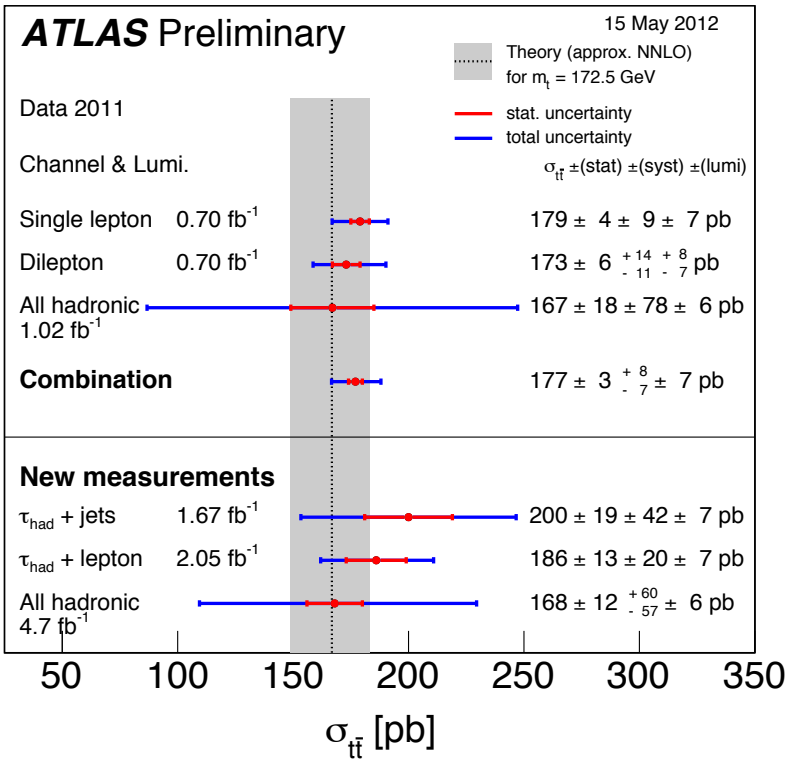

Figure 3.3: A summary of public measurements of the $t\bar{t}$ pair production cross section, and the corresponding theoretical expectation [34].

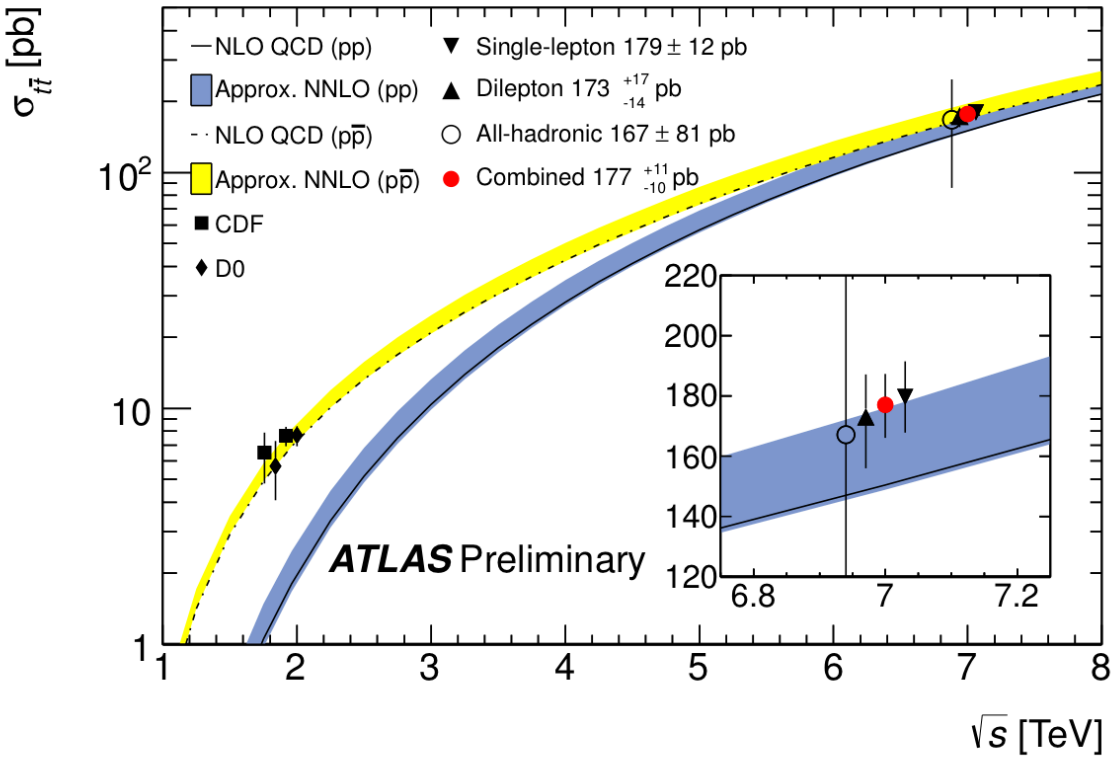

Figure 3.4: A comparison of current ATLAS $t\bar{t}$ cross section measurements with Tevatron results, and theoretical predictions [35].

3.2 Decay Modes of the Top Quark

With the large mass of the top quark well above the production threshold of b quarks and W bosons, $t \to W^+b$ is expected to be the dominant decay mode of the top quark - the branching fraction of $\Gamma(t \to W^+b)$ / $\Gamma(t \to W^+q)$ is measured to be $0.99^{+0.09}_{-0.08}$ [6] [4].

Background processes at the LHC are expected to produce large amounts of hadronic jets, which are expected to mainly consist of "light" jets (originating from the hadronisation of u, d and s quarks) with low transverse energy (E_{T}). Top quark decays, in contrast, are expected to contain energetic b-jets in 99.8% of cases. Therefore, the identification and selection of b-jets can be used to select those events which are likely to have contained a top quark or a $t\bar{t}$ pair. This identification of b-jets is known as "b-tagging", and is explained in detail in Chapter 5.

The b quark produced in the decay of the top quark will itself decay, resulting in a hadronic jet, while the W boson will decay in one of two ways - either the W will decay into a quark and an antiquark [5] or a lepton and its corresponding neutrino. The decay modes of the W bosons are used to differentiate between three different decay channels of $t\bar{t}$ pairs, which are referred to as the "all-hadronic", "lepton+jets" and "dilepton" channels. The decay chains and branching ratios of these channels are shown in Table 3.2 and Figure 3.5.

Table 3.2: The decay modes and branching fractions of the W bosons within a $t\bar{t}$ decay [6]. In this Table, q can refer to any one of the five lighter quarks - the ticks are used to denote that $q\bar{q}'$ refers to a quark and an antiquark which is *not* the antiparticle of the first quark, but instead whichever antiquark may be chosen to conserve the charge of the decaying W boson. The third column shows how these branching fractions are found - the "3" denotes that there are three possible leptons in the decay products, and lepton universality is assumed (i.e. the probability of there being a muon in the decay products is equal to that of an electron or a tau lepton).

		$\Gamma_{\mathrm{channel}}/\Gamma_{\mathrm{total}}$	
W decays to hadrons	$W \to q\bar{q}'$	67.6%	"h"
W decays to leptons	$W^- \to \ell\bar{\nu}_\ell$ or $W^+ \to \bar{\ell}\nu_\ell$	10.8%	"ℓ"
All-Hadronic channel	$t\bar{t} \to W^+bW^-\bar{b} \to q\bar{q}'bq''\bar{q}'''\bar{b}$	45.7%	h^2
Lepton+jets channel	$t\bar{t} \to W^+bW^-\bar{b} \to q\bar{q}'b\ell\bar{\nu}_\ell\bar{b}$ or $\bar{\ell}\nu_\ell bq\bar{q}'\bar{b}$	43.8%	$((3\cdot\ell)\cdot h)\cdot 2$
Dilepton channel	$t\bar{t} \to W^+bW^-\bar{b} \to \bar{\ell}\nu_\ell b\ell\bar{\nu}_\ell\bar{b}$	10.5%	$3\cdot 3\cdot \ell^2$

[4] This represents the probability of a $t \to W^+b$ decay given that the $t \to W^+q$ decay occurs, where $q = d, s, b$.

[5] The W^+ boson will decay to $u\bar{d}$, $u\bar{s}$, $u\bar{b}$, $c\bar{d}$, $c\bar{s}$ or $c\bar{b}$, with decay widths proportional to the corresponding CKM matrix elements squared.

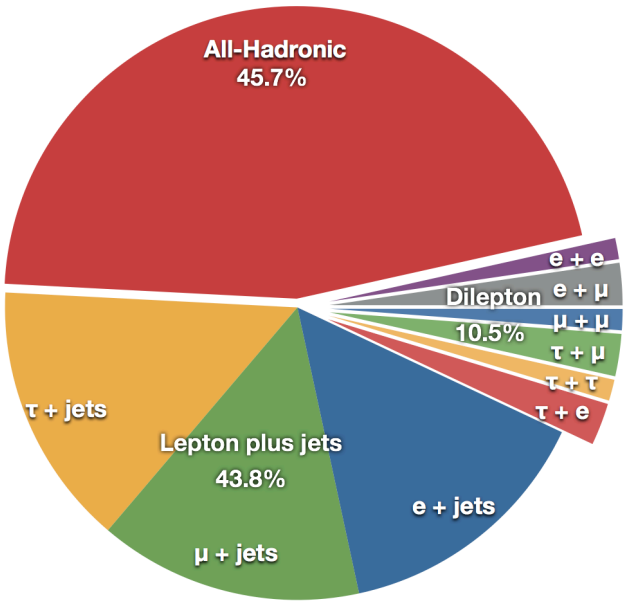

Figure 3.5: Branching fractions of the $t \to Wb$ decay mode.

3.2.1 Choosing the Lepton+Jets Channel

The three channels mentioned in Section 3.2 each have advantages and disadvantages. The all-hadronic channel is the most plentiful, but it is difficult to separate the signal from the high background of hadronic jets from other processes. The dilepton channel has low statistics but also low background compared to the others, while the lepton+jets channel has a high cross section and a distinctive signature, as well as having lower background than the all-hadronic channel. The lepton+jets channel, $t\bar{t} \to b\ell\nu bjj$, where ℓ refers to only muons or electrons, has a combined branching ratio of $\approx 29.2\%$, assuming the same ratios as in Table 3.2. The τ+jets channel is not included as the τ lepton is not a stable final state particle on the time scale of the detector, unlike the other leptons. The branching ratio of $\tau \to (e^-\bar{\nu}_e\nu_\tau$ or $\mu^-\bar{\nu}_\mu\nu_\tau) = 35.24 \pm 0.08\%$ [6]. The τ lepton has sufficient mass to decay into light hadronic jets via the weak interaction, meaning that it does not have the same distinctive signature as the other lepton+jets channels.

The lepton+jets channel has a large cross section and contains one W boson which decays to a lepton (μ or e) and a neutrino, and one which decays to two jets as shown in Figure 3.6. Consequently, the lepton+jets channel has an isolated lepton and some missing transverse energy

($\not{E}_T$, from undetectable neutrinos [6]), allowing $t\bar{t}$ events to be relatively easily identified with reduced background (as compared to the all hadronic and leptonic decay channels) [36]. For these reasons, the lepton+jets channel is chosen for this analysis.

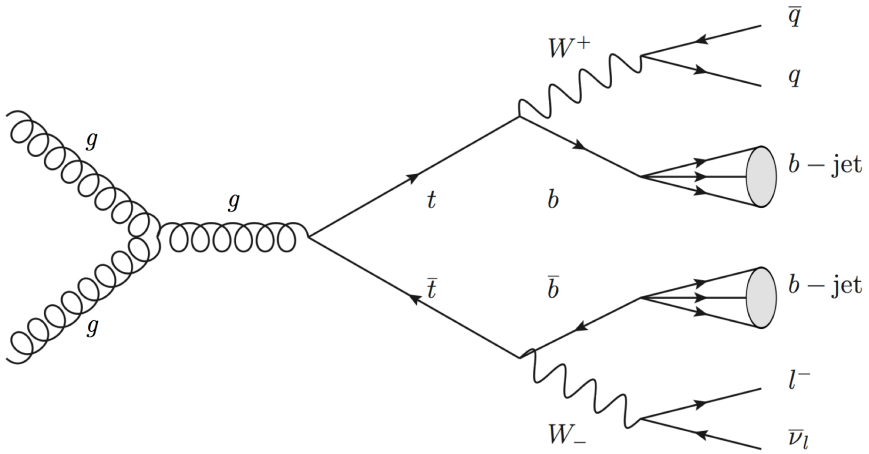

Figure 3.6: A Feynman diagram of the decay of a pair of top quarks via the lepton+jets channel. The decay of the W^- boson into a lepton-antineutrino pair can be seen at the bottom of the diagram, while the W^+ boson decays into a quark-antiquark pair.

3.3 Motivation for the Study of Top Quark Physics

The study of top quark physics at the LHC is important for a number of reasons. To detect the products of $t\bar{t}$ decays makes use of all modules of the ATLAS detector, making such decays useful for calibrating the subdetectors used to provide the information for object reconstruction ("object" referring to reconstructed electrons, muons, photons and jets). Measurement of the $t\bar{t}$ cross section is an important early measurement for the LHC, serving as it does as a powerful validation of the SM, but $t\bar{t}$ production and identification serves another role in the physics program at the LHC - that of searching for new physics *beyond* the standard model.

The particularly large mass of the top quark means that in some theories of the Higgs field, the Higgs boson shares decay modes with the top quark. The 2HDM theory, as mentioned in Section 2.2.2, permits the decay of the top quark into a charged Higgs boson and a bottom quark, $t \to H^+ b$. The $H^+ \to c\bar{s}$ decay is dominant at charged Higgs boson masses of $\lesssim 130$ GeV,

[6] The missing transverse energy is used to estimate the energy of the neutrino produced in $W \to \ell\nu$ decays; it can be found using conservation of momentum in the transverse plane.

meaning that the charged Higgs boson has the $t \to H^+ b \to c\bar{s}b$ signature in common with $t \to Wb \to c\bar{s}b$. Therefore, the existence of a charged Higgs boson could be indicated by an increase in events with the $t \to c\bar{s}b$ signature causing an excess in the measured $t\bar{t}$ cross section (along with a second peak in the invariant mass spectrum of the c and $\bar{s}$ jets in addition to the peak at the mass of the W boson).

Chapter 4

The LHC and the ATLAS Detector

4.1 The Large Hadron Collider

The Large Hadron Collider (LHC) [37,38] is a proton-proton (pp) collider, situated at the European Organisation for Nuclear Research (CERN) which sits astride the Franco-Swiss border on the outskirts of Geneva. The LHC occupies a tunnel 27 km in circumference, at a depth of some 100m beneath ground level, which formerly housed the Large Electron Positron collider (LEP).

The accelerated beams can collide at four interaction points, each of which is in the centre of one of the four main detectors of the LHC. These are ATLAS, ALICE, CMS and LHCb, situated as shown in Figure 4.1. ATLAS (A Toroidal LHC ApparatuS) and CMS (Compact Muon Solenoid) are designed to search for physics beyond the Standard Model, while ALICE (A Large Ion Collider Experiment) and LHCb (Large Hadron Collider beauty experiment) specialise in heavy ion and b quark physics respectively.

4.1.1 Accelerating the Beam

The protons for the LHC are produced from simple hydrogen gas - the electron orbiting the nucleus (in the case of hydrogen, a single proton) is removed using an electric field, and the protons are then guided into the first stage of acceleration, LINAC 2. This is a linear accelerator which uses oscillating electric potentials to accelerate the protons to energies of 50 MeV. The protons are then boosted to 1.4 GeV [1] in the Proton Synchrotron Booster (PSB), the smallest circular accelerator in the sequence. A synchrotron accelerates particles around a loop by varying the

[1] Natural units will be used throughout this thesis, unless otherwise stated.

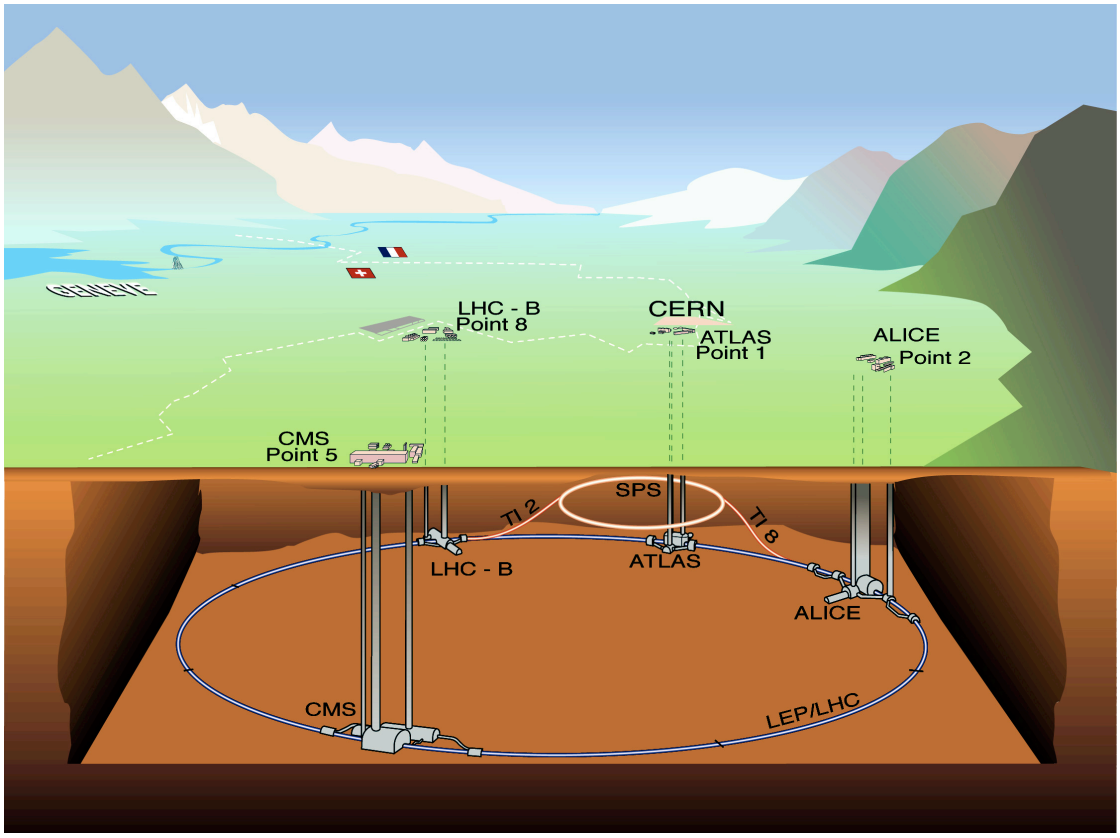

Figure 4.1: A schematic representation of the LHC and its four major experiments [39].

magnetic field which guides the path of the particles as their energy increases [2]. The following stage is the Proton Synchrotron (PS), which accelerates them to 26 GeV, while the penultimate stage is the Super Proton Synchrotron (SPS), which increases the energy to 450 GeV at which point the protons are injected into the LHC. They are accumulated into bunches of approximately 1.15×10^{11} protons, and then accelerated to the desired energy [37] - the LHC has a design energy of 7 TeV per beam ($\sqrt{s} = 14$ TeV [38]). The accelerator complex is shown in Figure 4.2.

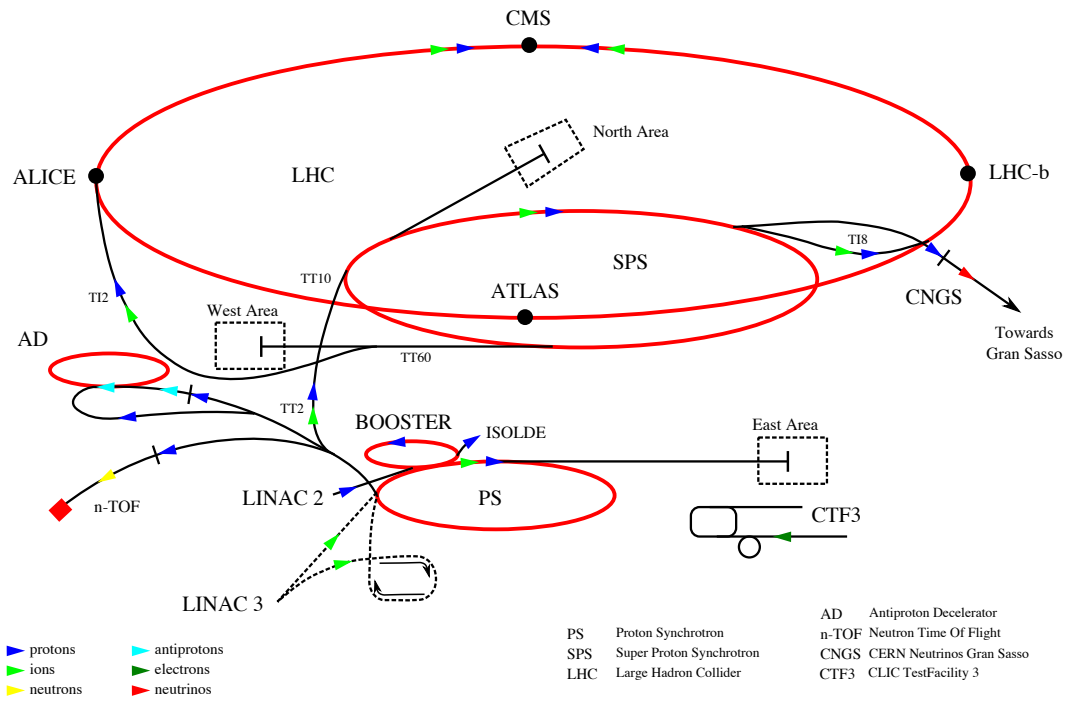

Figure 4.2: A schematic view of the CERN accelerator complex [40].

4.1.2 Event rate and Pile-up

A pp interaction resulting from beam collisions is known as an "event". The number of events per unit time is the event rate, R, which is proportional to $\mathcal{L}$, the instantaneous luminosity of the LHC. $\mathcal{L}$ is a measure of the performance of a particle accelerator, and represents the flux of

[2]Particles of higher energies require stronger magnetic fields to maintain a true path around the synchrotron, compared to those of lower energies.

particles per unit area per unit time. The instantaneous luminosity for a particle collider is found as shown in Equation 4.1, where f is the revolution frequency of the beam, n_b the number of colliding pairs of bunches in the beam, N_1 and N_2 are the number of particles in the two colliding bunches, and A is the cross section of the beam [41].

$$\mathcal{L} = f n_b \frac{N_1 N_2}{A} \tag{4.1}$$

The total number of collisions produced by an accelerator over a period of time is referred to as the integrated luminosity, and expressed in units of inverse area - a convenient unit to use is the barn (b), where $1\text{b}^{-1} = 10^{-28}\text{m}^{-2}$. The rate of a specific process, x, is given by Equation 4.2, where μ_x is the average number of occurrences of process x per bunch crossing and σ_x is the cross section of the process. f and n_b are set by the operating parameters of the LHC itself, and are not process dependent.

$$R = f n_b \mu, \quad R_x = f n_b \mu_x \tag{4.2}$$

$$\mu_x = \sigma_x \frac{N_1 N_2}{A} \tag{4.3}$$

$$R_x = \mathcal{L} \sigma_x \tag{4.4}$$

There are 3564 possible 25 ns “slots” in each LHC fill, which may be occupied by a bunch of protons. Consequently, the minimum possible time separation between proton bunches is 25 ns [41], which is equivalent to approximately 7.5m when travelling at the speed of light. The bunches of protons within the LHC can therefore be crossed at a rate of up to 40 MHz.

Most collisions at the LHC will be inelastic pp collisions, which have a cross section of $\sigma = 79$ mb [42] at the design energy of $\sqrt{s} = 14$ TeV. Apart from the inelastic scattering interactions, the majority of interactions per event can be classed as “soft” interactions, resulting from long range pp interactions with little momentum transferred between partons. These interactions provide a background to harder interactions (scattering processes) and create noise from which it can be difficult to extract the hard signal. As the LHC did not start colliding beams at the full design luminosity, the effect of having multiple events per bunch crossing (known as pile-up) was not expected to be large in early data taking. However, as the luminosity and event rate increase in 2011 data and beyond, pile-up effects are being monitored closely to ensure that

calibrations of the detector take account of the new conditions, and that this potentially serious background to searches for new physics is well understood. During 2011 data taking, instantaneous luminosities of up to $3.65 \times 10^{33}\text{cm}^{-2}\text{s}^{-1}$ were observed by the ATLAS detector - at the end of 2011 data taking, the maximum pile-up in any single collision of bunches was up to 24 [43], while the average number of events across all colliding bunches in a crossing reached a maximum of 17, as can be seen in Figure 4.3.

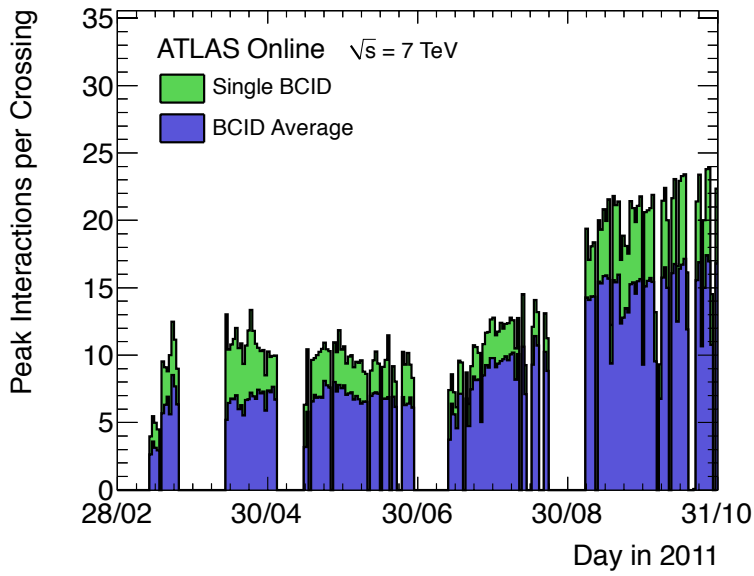

Figure 4.3: Maximum pile-up for any single bunch collision, and the mean maximum for all colliding bunches in 2011 data [43].

4.1.3 The 2011 Dataset, and the LHC Schedule

The LHC is designed to accelerate two counter-rotating beams of protons to $\sqrt{s} = 14$ TeV, however the LHC was not able to produce beams of this energy from the beginning. On the 10th of September 2008 the first proton beam entered the collider, but just 9 days later an unexpected quench occurred in approximately 100 bending magnets, caused by an electronic connection fault between a quadrupole and dipole magnet. This caused approximately 6 tonnes of liquid helium to be released, and the resulting shock wave from the expanding helium was sufficient to dislodge the enormous magnets and cause the quench [44]. This event caused a delay of just over a year, and it was not until the 30th of November 2009 that the LHC was able to circulate beams of 1.18 TeV per beam, breaking the previous record of 0.98 GeV per beam held by the

Tevatron [45]. The LHC ran at 3.5 TeV per beam, with a bunch spacing of 50 ns, from the 30th of March to the 8th of November 2010, and from the 13th of March until the 30th of October 2011, recording 45 pb^{-1} and 5.25 fb^{-1} of data respectively - it is the latter 5.25 fb^{-1} that forms the dataset used for this thesis (the 2010 data is also used for some cross checks).

The 2011 dataset was divided into 11 periods, each consisting of multiple "runs". The periods were also split into numbered blocks, corresponding to different detector conditions - for example, the solenoid and toroid magnetic fields were not switched on during period B1, but both were fully functional during period B2. The dates, number of events and integrated luminosity of the 2011 periods are shown in Table 4.1.

Table 4.1: 2011 collision data information [46, 47].

Period	Runs	Date	Events	Integrated Lumi.
B1:B2	177986-178109	21/03-24/03	36,559,487	12.678 pb^{-1}
D1:D7	179710-180481	14/04-28/04	125,652,340	176.256 pb^{-1}
E1	180614-180776	30/04-03/05	25,772,118	49.927 pb^{-1}
F1:F3	182013-182519	15/05-25/05	64,483,061	149.276 pb^{-1}
G1:G6	182726-183462	27/05-14/06	185,703,386	550.997 pb^{-1}
H1:H4	183544-184169	16/06-28/06	98,041,353	270.281 pb^{-1}
I1:I4	185353-186493	13/07-29/07	132,999,737	391.76 pb^{-1}
J1:J2	186516-186755	30/07-04/08	71,858,810	230.565 pb^{-1}
K1:K6	186873-187815	04/08-22/08	161,887,407	646.715 pb^{-1}
L1:L7	188902-190343	07/09-04/10	281,060,285	1438.07 pb^{-1}
M1:M10	190503-191933	06/10-30/10	242,260,952	1078.12 pb^{-1}

The cumulative integrated luminosity against time for both 2010 and 2011 can be seen in Figure 4.4, with the peak instantaneous and integrated luminosities per day during 2011 data taking shown in Figure 4.5. Figure 4.6 shows the ATLAS data taking efficiency in 2011. The empty bins are due to days on which no stable beams were delivered by the LHC, and correspond to the plateaus in Figure 4.4(b). The efficiency is less than 100% due to factors such as the time taken to ready some ATLAS subdetectors for data taking, and also the occurrence of problems with individual subdetectors which may prevent ATLAS data taking. There are also periods when the LHC runs beams studies and performs a beam dump, during which ATLAS does not record data [43]. The LHC started collisions again in March 2012, operating at 4 TeV per beam until the end of the year. It will then go into shutdown for 20 months for upgrades to allow full energy operation (7 TeV per beam), with reopening planned for late 2014 [48].

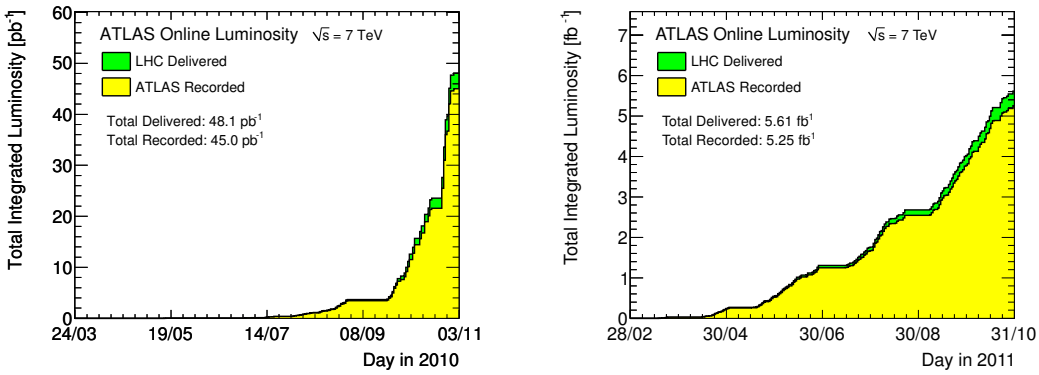

(a) 2010 (b) 2011

Figure 4.4: Cumulative integrated luminosity by day for 2010 and 2011 pp data collection [43].

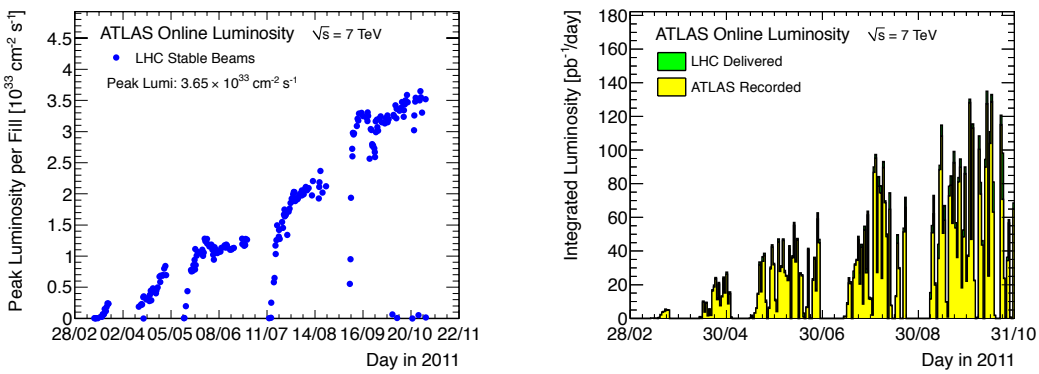

(a) Instantaneous Luminosity (b) Integrated Luminosity

Figure 4.5: Instantaneous and Integrated Luminosity by day in 2011pp data collection [43].

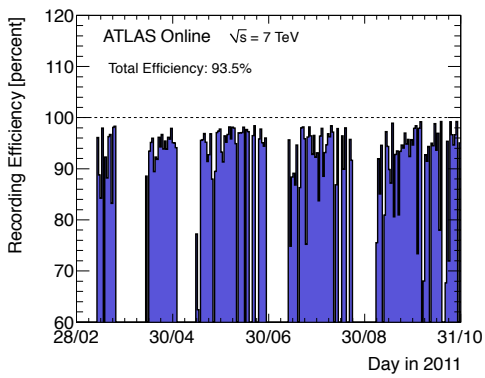

Figure 4.6: ATLAS data taking efficiency per day [43].

4.2 The ATLAS Detector

The ATLAS detector is the larger of the two general purpose detectors at the LHC - it was designed to be able to detect a broad range of new physics signals [42, 49]. As can be seen in Figure 4.7, ATLAS has approximately cylindrical symmetry, with the origin of the coordinate system taken as being the nominal interaction vertex - the point in the beamline which is at the centre of the detector. The z-axis of the detector points along the beamline, with side A of the detector being positive z and side C being negative z. The positive x-axis points towards the centre of the LHC ring. The y axis is perpendicular to these two, with positive y pointing upwards. θ and ϕ correspond to the polar angle from the z axis and the azimuthal angle around the z-axis in the x–y plane respectively. The pseudorapidity, η, is defined as:

$$\eta = -\ln\tan(\theta/2) \tag{4.5}$$

Therefore, side A of the detector also corresponds to positive values of η, and side C to negative values. Regions of the detector with large $|\eta|$ values, (small θ, close to the beamline) are referred to as the forward regions. The cylindrical region with smaller $|\eta|$ values is known as the barrel region of ATLAS - the exact definition of the barrel region varies depending on the geometry of the subdetectors. The distance ΔR in the η–ϕ space is defined as:

$$\Delta R \equiv \sqrt{\Delta\eta^2 + \Delta\phi^2} \tag{4.6}$$

ATLAS consists of four subdetector systems, arranged concentrically in the barrel region from the beamline outwards. These are:

The Inner Detector (ID), which is immersed in a 2 T magnetic field provided by the central solenoid (CS), designed to bend the trajectories of charged particles as they pass through the detector volume.

Electromagnetic and Hadronic Calorimetry Systems (ECal and HCal) which provide energy and position measurements for electromagnetic and hadronic particles respectively.

Muon Spectrometer (MS) for the identification and position measurements of muons.

Toroidal Magnet Systems, which consist of barrel and endcap sections, designed to provide a

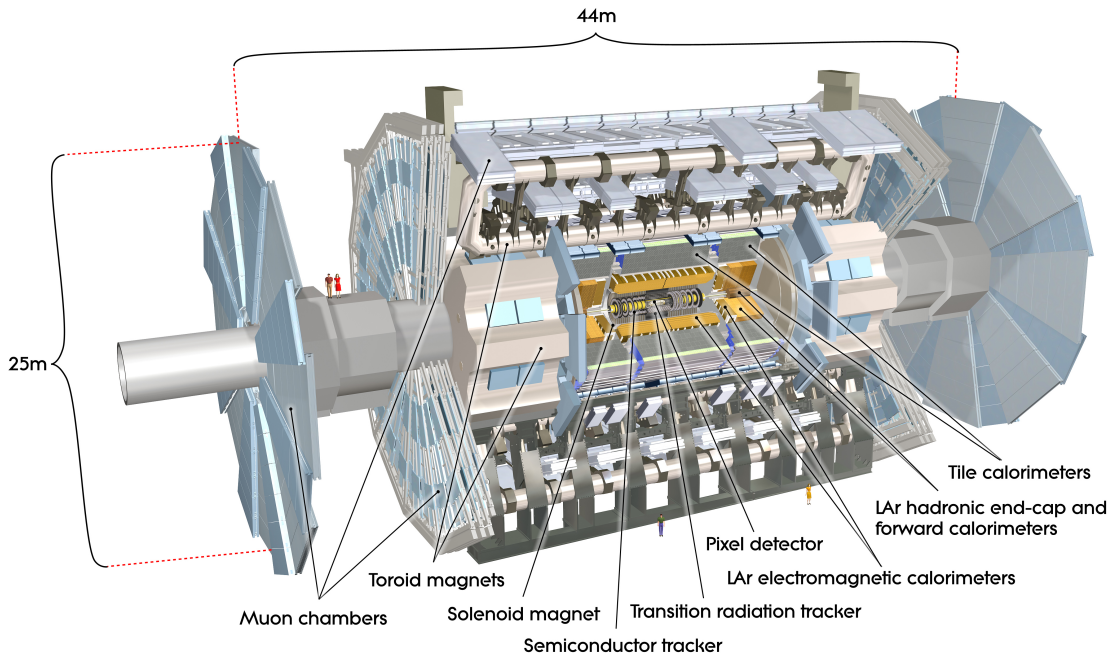

Figure 4.7: A cut-away view of the ATLAS detector. The dimensions of the detector are 25 m in height and 44 m in length. The overall weight of the detector is approximately 7000 tonnes [42].

tangential magnetic field throughout the MS, which is mostly orthogonal to the paths of muons passing through the muon systems.

Each of these subdetectors has a specific role in particle detection. Figure 4.8 shows a schematic view of the signature left by some typical highly energetic particles as they pass through the ATLAS detector - electrons deposit some of their energy in the ID, and the remainder is deposited in the ECal. Photons do not cause a signal in the ID, and hadrons will produce showers of particles deeper in the calorimeter systems, in the HCal. Muons traverse the calorimeters entirely and leave signals in the ID and MS.

4.2.1 Inner Detector

The ID provides measurements of the momentum and position of charged particles passing through it, covering the pseudorapidity range $|\eta| < 2.5$. The ID is immersed in a 2 T magnetic field, generated by the central solenoid. Charged particles passing through a magnetic field are subject to a deflecting force, the strength of which is dependent on the charge and electric field

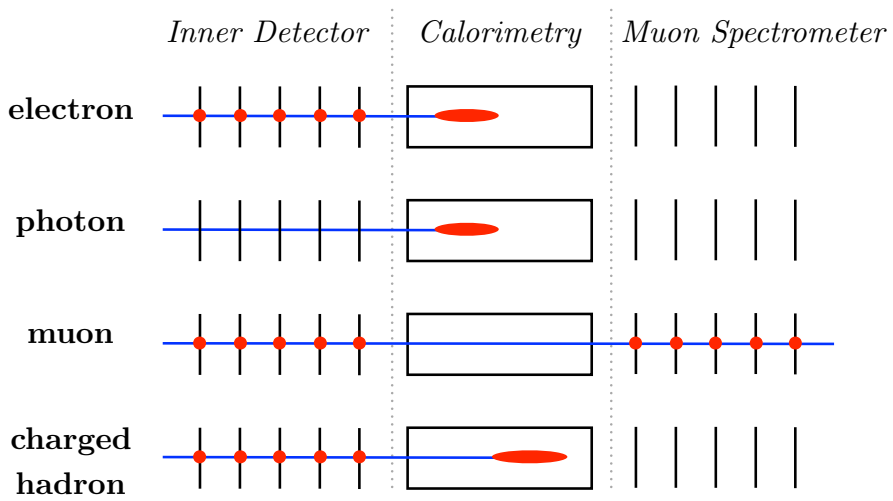

Figure 4.8: A schematic view of the signature left by some highly energetic particles passing through the ATLAS detector. The blue lines represent the path of the particle, from left to right, and the red circles represent a "hit" or signal left in each part of the detector. Adapted from [50].

of the particle. Consequently, the trajectory of such particles through the magnetic field will bend with a radius of curvature proportional to their transverse momentum, allowing a precise measurement of this momentum to take place. In order to achieve the momentum and position resolutions required, high-precision measurements must be made with very fine detector granularity. Three complementary tracking detectors are used to achieve this, arranged concentrically around the beam pipe as shown in Figure 4.9. The detectors are the Pixel detector, Semi-Conductor Tracker (SCT) and the Transition Radiation Tracker (TRT).

Pixel Detector

The silicon Pixel detector is the closest detector to the beam pipe, and provides the most accurate tracking capabilities. When a charged particle passes through a silicon pixel, it creates electron-hole pairs, which then drift towards a readout cathode due to a voltage bias placed across the pixel. The resultant electrical signal, if above a certain threshold, is recorded as a "hit" by the readout systems. The Pixel detector consists of three concentric layers of silicon pixels, as can be seen in Figure 4.10. The innermost layer is called the B-layer, and is particularly important for the identification of b-quarks and photon conversions. Being closest to the interaction point,

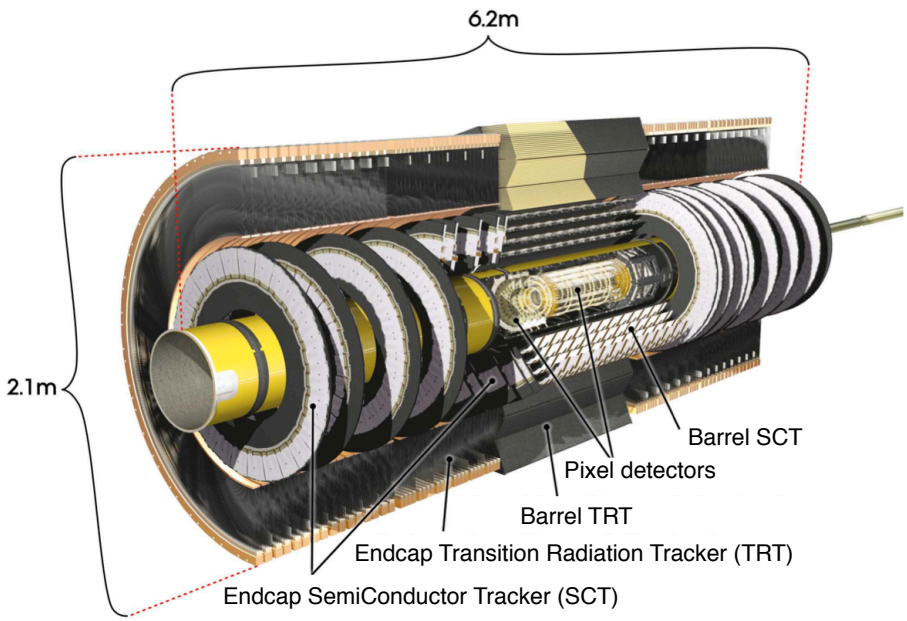

Figure 4.9: A cut-away view of the ATLAS inner detector, adapted from [42].

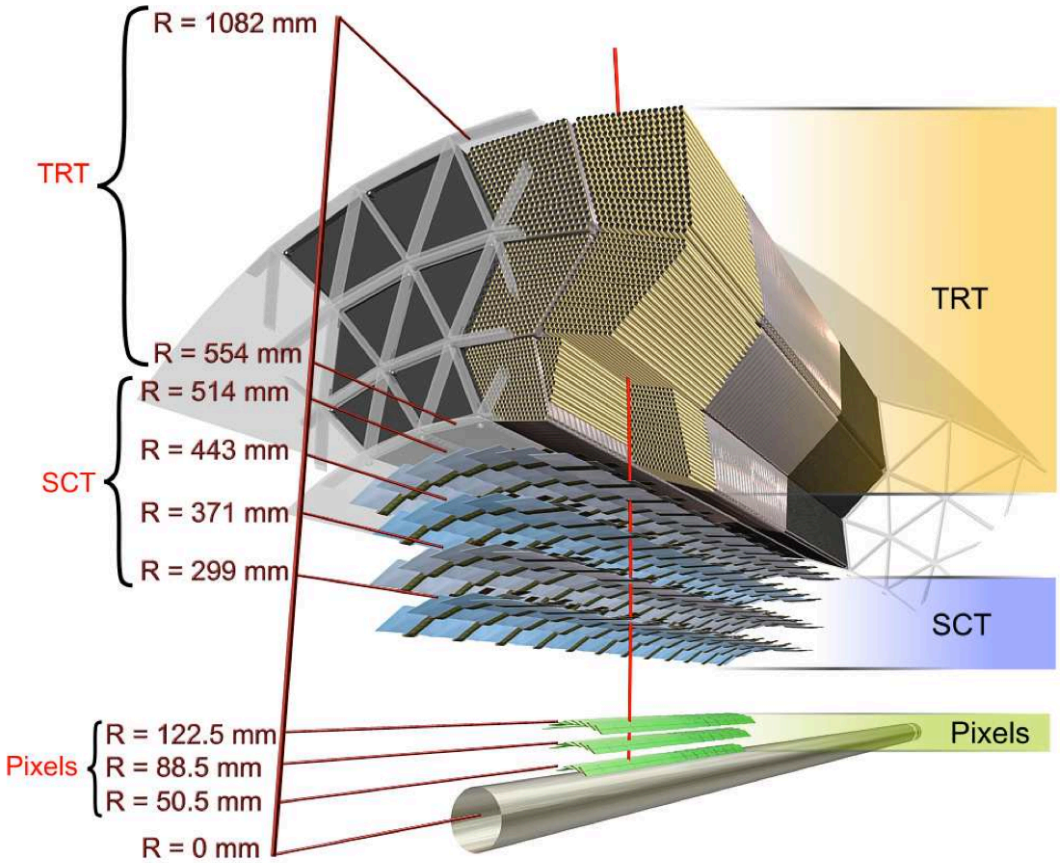

Figure 4.10: Drawing showing the sensors and structural elements traversed by a charged track in the barrel inner detector. The track must pass through the beam pipe, the three concentric layers of the Pixel detector, the four layers of barrel SCT sensors, and approximately 36 straws of 4 mm diameter contained in the barrel TRT modules [42].

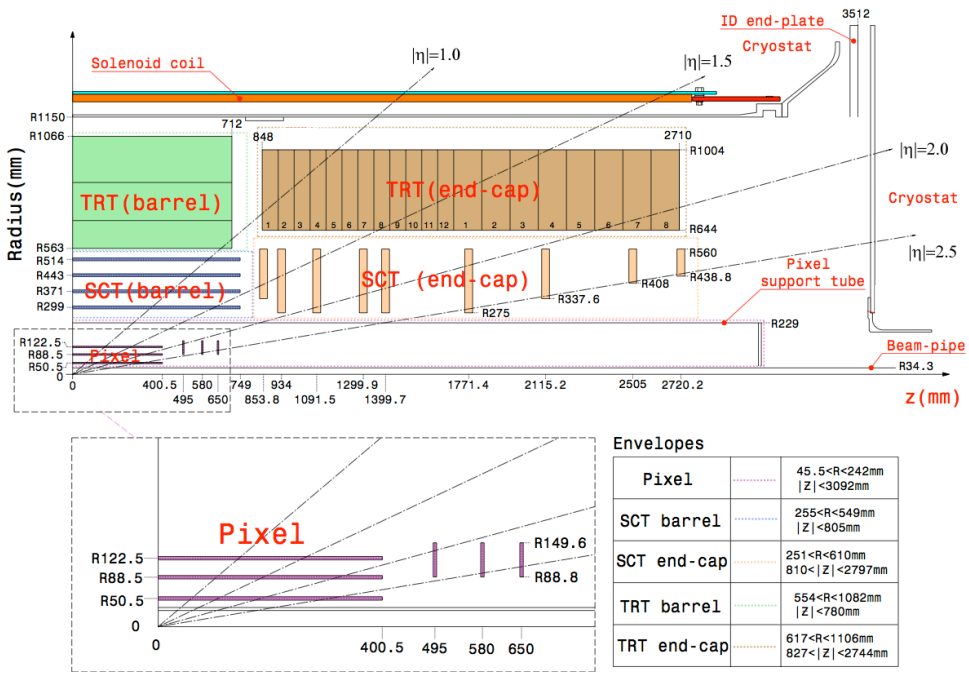

Figure 4.11: Plan view of a quarter-section of the ATLAS inner detector showing each of the major detector elements with its active dimensions and envelopes, adapted from [42].

the B-layer receives the most radiation damage, and consequently it has an expected lifetime of about five years [51]. In order to maintain the performance of the Pixel detector as the B-layer degrades an additional pixel layer has been developed, called the Insertable B-Layer (IBL). This has been developed along with a new beam pipe of smaller radius, providing the extra space required for the additional layer. The current plan is that the IBL will be ready and inserted by September 2013 [52].

The endcap region of the Pixel detector contains three silicon disk layers as can be seen in Figure 4.11. This means that any charged particle which passes through the pseudorapidity range covered by the Pixel detector will produce at least three hits. The Pixel detector has a resolution of 10 μm in $r-\phi$ and 115 μm in the z direction [53], meaning that it is very well suited to detect and identify the secondary vertices caused by b and c quarks and tau leptons (τ); $c\tau_B$, the distance travelled by bottom hadrons based on the speed of light multiplied by their lifetime, is approximately 400–500 μm as τ_B is of the order of a picosecond. For D hadrons (containing c quarks), $c\tau_D \approx$ 20–300 μm, and for τ leptons $c\tau_\tau = 87.11$ μm.

Semi-Conductor Tracker

The SCT is the middle component of the ID, surrounding the Pixel detector. It uses silicon microstrip layers to detect the tracks of charged particles in the same manner as the Pixel detector. The SCT is designed to record up to 8 hits per track, consisting as it does of four layers of modules in the barrel region, while the endcap SCT contains nine disks of modules. Each module is made up of two silicon wafers glued back to back with a 40 mrad stereo rotation, allowing for two dimensional track reconstruction. The resolution of the SCT is 17 μm in $r-\phi$ and 580 μm in z in the barrel region, and 17 μm in $r-\phi$ and 580 μm in r in the endcaps [53].

Transition Radiation Tracker

The TRT is both a transition radiation detector and a straw drift-tube tracker. As shown in Figure 4.10, the TRT is constructed from 73 layers of drift tubes (or "straws") in the barrel, and 160 layers in the endcaps. Each straw is 4 mm in diameter, filled with a mixture of 70% xenon, 27% carbon dioxide and 3% oxygen, and contains a 30 μm anode wire at its centre [53]. A charged particle passing through the straw will leave a trail of electron-ion pairs, which will cascade towards the anode. The resultant electrical signal is then registered as a hit, in much

the same way as in the SCT and Pixel detector. The straws are interweaved with polypropylene fibres, which act as radiators - when relativistic particles cross the boundary from a straw to the polypropylene, the difference in dielectric constant causes them to emit X-rays known as transition radiation. The transition radiation photons are then absorbed by the gas within the tubes, contributing further to the signal collected on the anode. The intensity of the radiation produced is proportional to the Lorentz factor of the particle (γ), where:

$$\gamma = \frac{E}{m} \tag{4.7}$$

Consequently, for a given energy, the TRT can discriminate between particles of differing masses as lighter particles will produce more ionisation than heavier ones. TRT hits are categorised as low or high threshold - particles such as electrons will produce higher levels of transition radiation than hadrons, for example. A typical track will pass through 36 layers of the TRT, as can be seen in Figure 4.10. The TRT is designed to be complementary to the other detectors in the ID - it only offers coverage in the $|\eta| < 2.0$ region of the detector, and only provides spatial information in the $r - \phi$ plane, at a resolution of 130 μm [53]. This lower precision compared to the SCT and Pixel detector is offset by the large number of measurements per track which it provides, and also the large track length contributes significantly to the overall transverse momentum (p_{T}) resolution of the ID. The transverse momentum is defined in the x–y plane of the detector as:

$$p_{\mathrm{T}} = \sqrt{p_x^2 + p_y^2} \tag{4.8}$$

4.2.2 Calorimetry

The Calorimeter system lies outside the CS and the ID, and is designed to contain electrons, photons and hadrons within the dense absorber material and measure their energies. The particles create particle showers in the absorber (*passive*) medium, and the energies of the resulting particles are measured in the sampling (*active*) medium, which lies between layers of absorber - this setup is known as a sampling calorimeter. The energy sampled will be approximately proportional to the energy of the incident particle causing the shower. The calorimeter consists of three sections - the electromagnetic calorimeter (ECal), hadronic calorimeter (HCal) and the forward calorimeter (FCal), arranged as shown in Figure 4.12. The calorimeter systems provide

coverage up to $|\eta| < 4.9$. The ATLAS calorimeter systems are designed to give full ϕ symmetry with no cracks in the azimuthal plane, and also to be as hermetic as possible, allowing for measurement of quantities such as missing energy or momentum which could indicate the presence of neutrinos or other weakly interacting particles which pass undetected through the detector. The thickness of the calorimeter systems is important, so as to contain electromagnetic and hadronic showers and minimise punch-through of particles into the muon systems; the total thickness of active calorimeter in the barrel and endcap regions, in units of interaction length (λ) is $\approx 9.7\lambda$ and 10λ respectively [3].

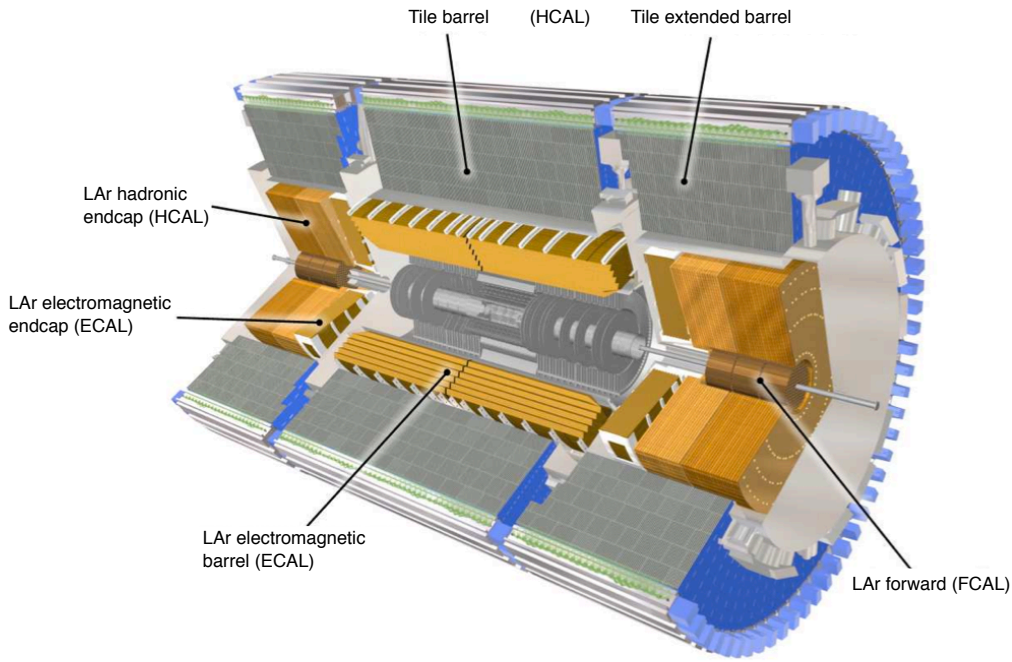

Figure 4.12: A cut-away view of the ATLAS calorimeter system, adapted from [42].

ECal

The ECal is a sampling calorimeter composed of interleaved layers of lead and liquid argon (LAr), which constitute the passive and active layers respectively. Argon is chosen as the active

[3]The interaction length, λ, is the distance over which all but $1/e$ of a number of relativistic charged particles will interact with a material - λ can be used for hadronic interactions as well as electromagnetic. The radiation length, X_0, is the distance over which a high energy lepton or photon loses all but $1/e$ of its energy when traversing a material.

layer due to its stability of response over time and its intrinsic radiation-hardness [42]. Electromagnetic showers are initiated in the dense layers of lead, and these showers ionise the LAr between layers. An applied voltage across the LAr causes the signal to be read out through copper electrodes. Total ϕ coverage is achieved through the folding of the layers of lead and LAr into an accordion geometry. There are four parts to the ECal - a pair of identical endcap modules and a pair of identical barrel modules, which sit back to back apart from a small crack of approximately 4 mm in width at $z = 0$. There is a region between the barrel and endcap modules, in the region $1.37 < |\eta| < 1.52$, which is not used for precision physics as there is a large amount of material in front of the ECal - this region is known as the "crack" region. So as to contain electromagnetic showers as well as possible, the thickness of the ECal is more than 22 radiation lengths (X_0) in the barrel region, and $> 24X_0$ in the endcaps [42]. This implies that the energy of electrons and photons passing through the ECal will be reduced by a factor of $\approx 3.5 \times 10^9$.

HCal

The HCal is a sampling calorimeter designed to measure the energies of hadronic showers, produced in the passive region from incident quarks and gluons. There are two parts to the HCal - a tile calorimeter covers the barrel and extended barrel regions (up to $|\eta| < 1.7$), using plastic scintillator tiles as the active medium and steel as the passive absorber medium. The hadronic endcap calorimeter (HEC) is a sampling calorimeter using LAr and copper as the active and passive media, and covers $1.5 < |\eta| < 3.2$. In the tile calorimeter, hadronic showers initiated in the steel layers cause scintillations in the plastic tiles. The light from these scintillations is then read out by two wavelength shifting fibres, which pass it to photomultiplier tubes, and the resultant electrical signal will be proportional to the energy of the particles which caused the scintillations. The HCal has a total thickness of 7.4λ in the barrel and endcap regions [42].

FCal

The FCal is a LAr sampling calorimeter capable of making both EM and hadronic measurements, constructed as it is of three layers - the first layer uses copper as the absorber, optimised for EM measurements. The two tungsten layers, sitting further from the interaction point, are predominantly used for hadronic measurements. The FCal covers the region $3.1 < |\eta| < 4.9$.

4.2.3 Muon Spectrometer

The outermost component of the ATLAS detector is the Muon Spectrometer. It has been designed to allow the precision measurement of the momenta of muons - although ultimately unstable [4], the muons produced during LHC collisions will survive for longer than it takes to traverse the volume of the detector. Muons tend to be more energetic than electrons (having larger transverse momentum), and so their paths are not as strongly bent in magnetic fields. The bending radius in the ID, r_b, is defined as

$$r_b = \frac{p_{\mathrm{T}}}{qB}$$

where q is the charge of the particle and B is the strength of the magnetic field, meaning that muons do not lose as much energy as electrons through bremsstrahlung (the emission of photons by a charged particle when deflected by a magnetic field). Hence, muons are able to penetrate much further through the detector than other particles. The MS occupies the space outside the calorimeters, and the toroid magnet systems pass through it. The MS can provide precise position and momentum measurements of muons and other charged particles which may have not been well measured in the ID. The MS consists of four parts - two precision chambers, the Monitored Drift Tubes (MDT) and Cathode Strip Chambers (CSC), and two trigger chambers, the Resistive-Plate Chambers (RPC) and the Thin Gap Chambers (TGC) - these can be seen in Figure 4.13, and in more detail in Figure 4.14. The main parameters of the muon chambers are listed in Table 4.2.

As with other parts of ATLAS, the MS is divided into barrel and endcap regions. The magnetic bending in the barrel region ($|\eta| < 1.4$) is provided by the large barrel toroid, as described in Section 4.2.4. In the endcap region ($1.6 < |\eta| < 2.7$), the muon tracks are bent by the endcap toroids, which sit within the ends of the barrel toroids. In the range $1.4 < |\eta| < 1.6$, known as the transition region, magnetic bending is provided by a combination of both endcap and barrel toroids. The barrel region has three layers of chambers, containing both precision and trigger chambers, arranged cylindrically around the beam axis at radii of $r \approx 5$ m, 7.5 m and 10 m. There is a gap in coverage of the barrel MS at $|\eta| \approx 0$, to allow for cabling and services for the solenoid, calorimeters and ID - this gap is in the approximate range $0.04 < |\eta| < 0.08$ depending

[4] The muon has a mean lifetime of approximately 2.2 μs, while the electron has a mean lifetime greater than the age of the universe, meaning that it does not undergo radioactive decay into other particles [6].

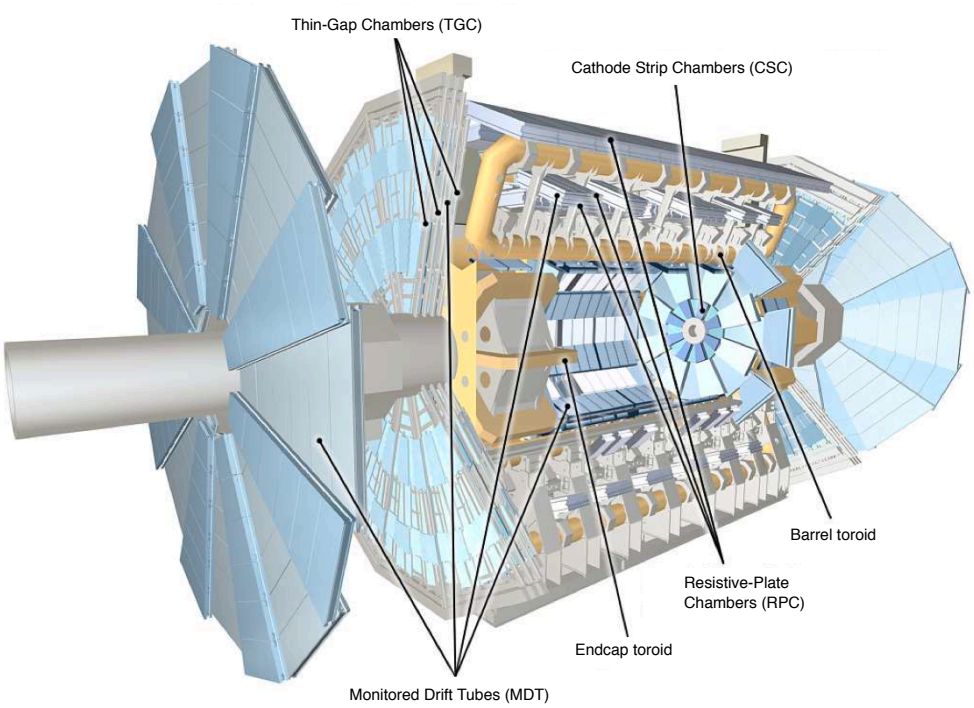

Figure 4.13: A cut-away view of the ATLAS muon systems, adapted from [42].

on where in the detector the gap is measured. The endcap regions have four layers of disks, also containing both types of chambers, arranged perpendicular to the beam at distances of $|z| \approx 7.4$ m, 10.8 m, 14 m and 21.5 m from the interaction point.

Table 4.2: Parameters of the Precision and Trigger chambers of the MS. Adapted from [42].

Monitored Drift Tubes	**MDT**
- Coverage	$\|\eta\| < 2.7$ (innermost layer: $\|\eta\| < 2.0$)
- Number of chambers	1150
- Number of channels	354000
- Function	Precision tracking
Cathode Strip Chambers	**CSC**
- Coverage	$2.0 < \|\eta\| < 2.7$
- Number of chambers	32
- Number of channels	31000
- Function	Precision tracking
Resistive Plate Chambers	**RPC**
- Coverage	$\|\eta\| < 1.05$
- Number of chambers	606
- Number of channels	373000
- Function	Triggering, second coordinate
Thin Gap Chambers	**TGC**
- Coverage	$1.05 < \|\eta\| < 2.7$ (2.4 for triggering)
- Number of chambers	3588
- Number of channels	318000
- Function	Triggering, second coordinate

The Muon Spectrometer is the most vital part of the ATLAS detector as far as the topic of this thesis is concerned - the soft muon tagging algorithm described in Section 5.4 relies upon information from the MS to reconstruct muons from tracks in the detector. Tracks in the ID and MS are used to reconstruct what is known as a “combined” muon, and the quality of the match between the tracks is used in the tagging algorithm as the main discriminant between muons in heavy and light flavour jets.

Precision Chambers

The MDTs are responsible for precision measurement of the track coordinates in the bending direction of the magnetic field (in the r–z plane). They consist of pressurised aluminium drift tubes, each containing a single central tungsten-rhenium wire anode which attracts electrons resulting from ionisation of the gas filling the drift tube, a mix of 93% argon and 7% carbon

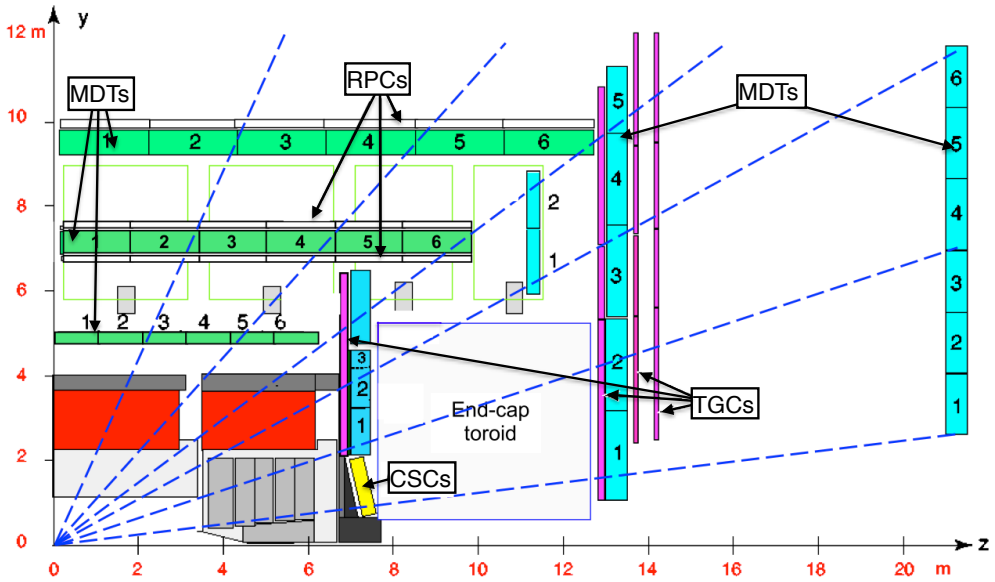

Figure 4.14: Plan view of a quarter-section of the ATLAS Muon Spectrometer system, showing the Monitored Drift Tubes (MDTs), Cathode Strip Chambers (CSCs), Resistive Plate Chambers (RPCs) and Thin Gap Chambers (TGCs). The dashed lines show the paths taken by ideal muons of infinite momentum - these would propagate along straight lines and typically cross three layers of muon chambers. Adapted from [42].

dioxide at a pressure of 3 bar. The precision tracking chambers are built from these single tubes, arranged in alignment with ϕ, such that the central point of each tube is tangential to a circle around the beam axis. 3–4 layers of tubes make up a single chamber - the size of the chambers increases in proportion to r, the radial distance from the beam axis. The cylindrical geometry results in a radial electric field within the MDTs, provided by the toroid magnets - this means that there is little dependence of measurement accuracy on the angle of incidence of a track onto the chamber. The spatial resolution of the MDTs is 80 μm per tube, and 35 μm per chamber [42].

CSCs are used in the innermost layer of the endcaps, due to the high safe operation limit of CSCs compared to MDTs - the highest particle fluxes are expected in the forward direction, and so the first layer of the muon chambers will bear the brunt of this flux. CSCs can operate at fluxes of 1000 $\mathrm{Hz/cm^2}$, while MDTs can only withstand 150 $\mathrm{Hz/cm^2}$ [54]. In contrast to MDTs, CSCs are multi-wire chambers capable of resolving both track coordinates simultaneously. This is achieved by having several layers of wire anodes, which are arranged radially, and two sets of cathode strips, which are arranged parallel and perpendicular to the anode to provide the transverse and precision coordinates of a passing track respectively. The position measurement is found using signals from the two sets of cathodes - signals on the anode wires are not read out. The CSCs have a spatial resolution of 60 μm in the bending direction, but only 5 mm in the non-bending direction. The timing resolution, however, is much better in the CSCs (7 ns per plane as opposed to 700 ns for MDTs), which makes a CSC system especially suitable for regions of high particle densities.

Trigger Chambers

The muon system was designed to be able to trigger on muon tracks, meaning that fast information of coarse resolution is needed to be used by the high level triggers (see Section 4.2.5) - therefore dedicated trigger chambers have been installed capable of delivering track information within nanoseconds of tracks passing through them. RPCs were chosen for this purpose in the barrel region ($|\eta| < 1.05$), which lie in three layers as shown in Figure 4.14, attached to the same support structure as the MDTs. The RPCs are made of two resistive plates, 2 mm apart, between which a potential difference is applied. The gap between plates is filled with a mixture of $C_2H_2F_4$, $\mathrm{Iso-C_4H_{10}}$ and SF_6 [42], and the signal is read out via metal plates attached to the outer faces of the resistive plates.

The TGCs in the endcap region ($1.05 < |\eta| < 2.4$) are multi-wire proportional chambers, like the CSCs. They are called thin gap chambers as the gap between the wires and the cathode is smaller than the gap between wires. The TGCs have better spacial resolution than the RPCs, at 2–6 mm in r and 3–7 mm in ϕ, compared to the RPCs at 10 mm in both z and ϕ. The time resolution of the trigger chambers is 1.5 ns for the RPCs and 4 ns for the TGCs, which is well above the minimum required time resolution of 25 ns (the time between bunch crossings at the design energy and luminosity of the LHC).

4.2.4 Magnets

ATLAS has a large magnet system, consisting of the CS referred to in Section 4.2.1, and three large air-core toroid magnets, shown in Figure 4.15. The magnet systems have been designed to facilitate the bending of the trajectories of charged particles using the minimum amount of material, to minimise the potential for interactions of the particles with the magnets themselves. The CS produces a magnetic field in the positive z direction, producing a bending force in the plane transverse to the beamline.

The toroid system is arranged into two sections, barrel and endcap, providing the magnetic field for the muon systems. Both have eight coils which are arranged radially around the beam axis. The endcap lies within the barrel section at either end, at a rotation of 22.5° with respect to the barrel coils, to provide a radial overlap and optimise the bending power in the region between the two sections. The barrel section provides a magnetic field with a bending power of between 1.5 and 5.5 Tm where $|\eta| < 1.4$, while the endcap toroid provides a bending power of between 1 and 7.5 Tm in the range $1.6 < |\eta| < 2.7$. The bending power is less in the transition region ($1.4 < |\eta| < 1.6$) between the barrel and endcap toroids. The toroidal magnetic field is in the ϕ direction, providing bending in the r–z plane.

4.2.5 Trigger and Data Acquisition

The very high pp interaction rate at full luminosity creates more data than can be stored with existing computing systems. The maximum rate at which data can be written to disk is approximately 300 MB/s, which at a nominal event size of ≈ 1.5 MB gives a maximum rate of ≈ 200 Hz - far below the 40 MHz (or $\approx$ 1GHz, assuming a maximum of 25 events per bunch crossing, with a spacing of 25 ns) event rate expected at the design luminosity of the LHC. It is therefore

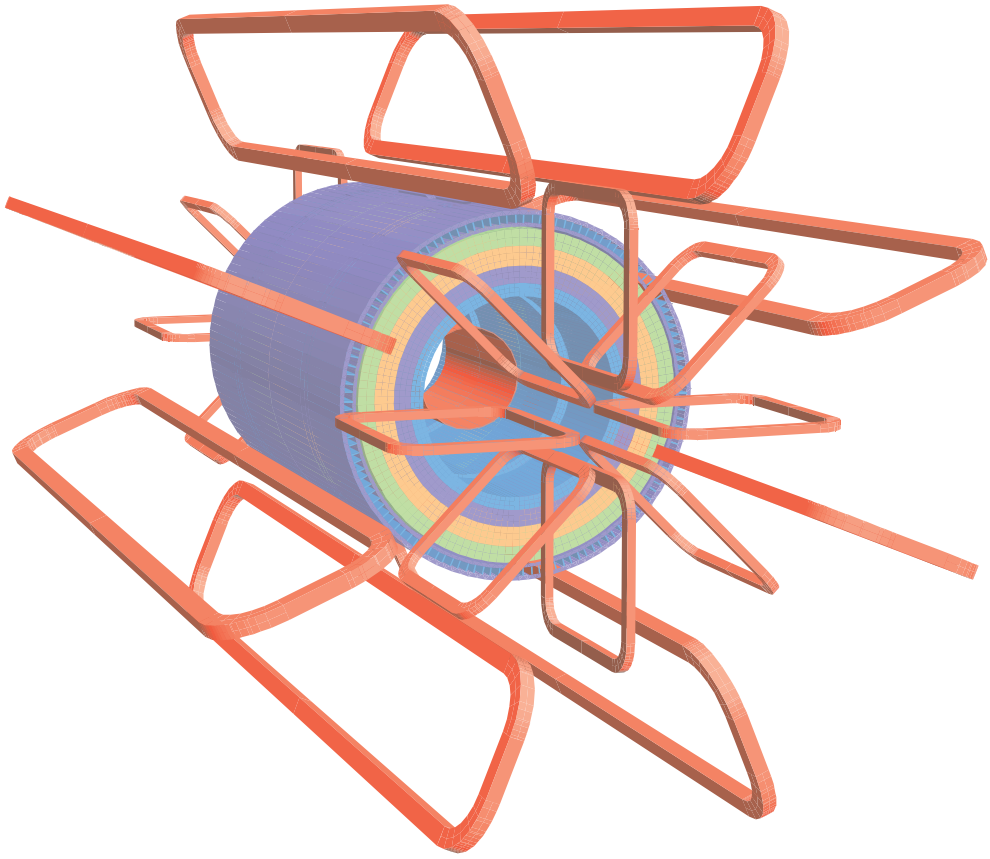

Figure 4.15: The ATLAS magnet systems. The central solenoid is the red cylinder in the middle, surrounded by the Tile calorimeter and the return yoke. The Barrel and Endcap toroids are the larger loops on the outside of the calorimeter [42].

necessary to reduce the rate while retaining as many "interesting" events as possible. The majority of the data produced is not of interest to physics searches (such as minimum bias events [5]), and so the ATLAS Trigger and Data Acquisition System (TDAQ) has been developed to select "interesting" events online, meaning that the selection occurs before the data is stored. The trigger system reduces the recorded interaction rate from $\approx$ 40MHz to $\approx$ 200Hz - minimum bias events are rejected with a factor of 5×10^6, meaning that for each minimum bias event accepted, 5×10^6 are rejected [54].

The TDAQ has three sequential levels: Level 1, Level 2 and Event Filter (L1, L2 and EF respectively), shown in Figure 4.16.

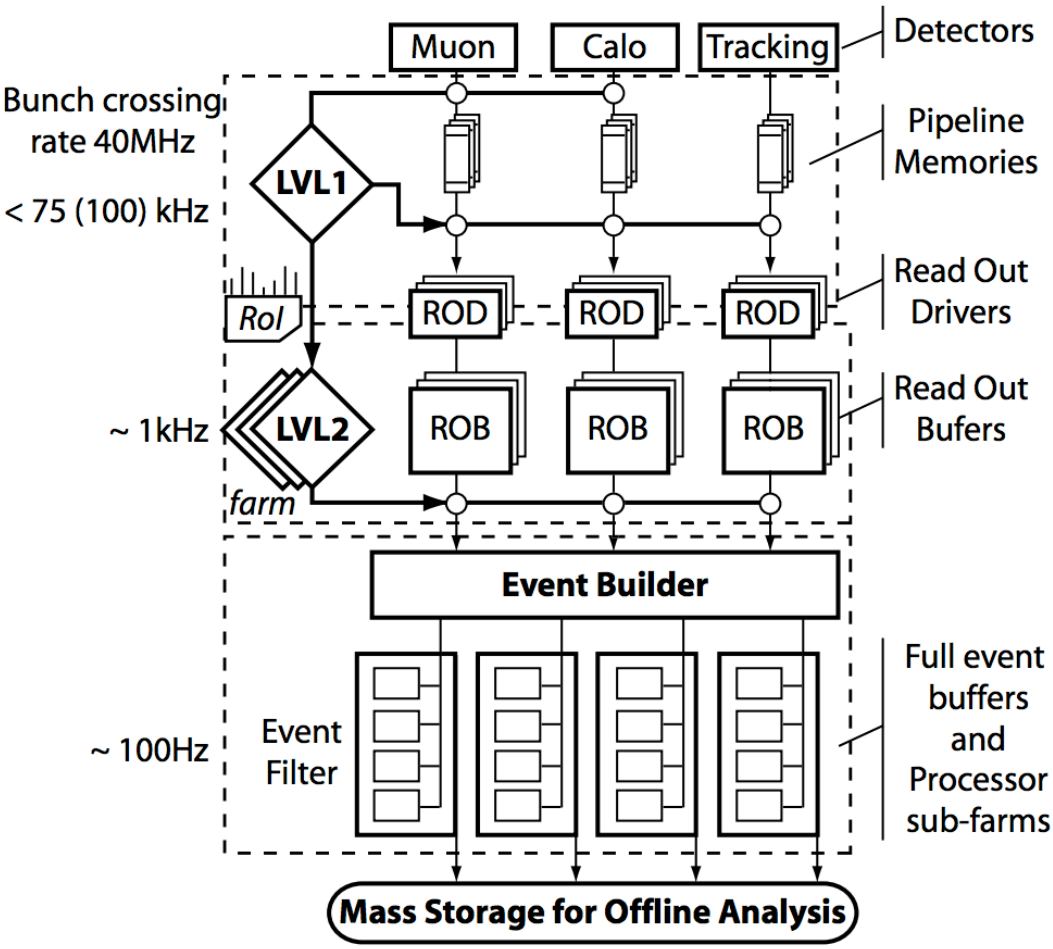

Figure 4.16: A schematic representation of the ATLAS trigger system [55].

[5]Minimum bias events are defined as any inelastic collisions which produce activity in the detector, with no requirements on the kinematics of the event.

The L1 trigger, which is hardware based, performs the initial selection based on reduced granularity information from the TGC and RPC of the MS, and from the ECal, HCal and FCal. The L1 trigger makes selections based on this information within 2.5 μs, and cuts the rate down to 75 kHz. The calorimeter trigger makes use of reduced granularity information from trigger towers [6] to look for objects and events such as high-p_{T} photons, electrons, hadronic decays from τ leptons and hadronic jets [7], as well as those events with large E_{T} or $E_{\mathrm{T}}^{\mathrm{miss}}$, all of which are calculated online. Trigger requirements can also include isolation cones (these will be fully defined in Section 6.1.1) which can be applied to electrons, photons and hadronic decays from τ leptons, providing an idea of how isolated an individual particle is. There is a limit to the number of requirements that may be imposed at one time for a particular object type. The information provided by the TGC and RPC trigger chambers is used to measure the trajectories of muons, while the background contribution from cosmic ray muons is reduced by searching for coincidence between several trigger chambers. The information from the calorimeter and muon systems is passed to the central trigger processor (CTP), which compares the information with predefined selection criteria. If an object passes these criteria, Regions Of Interest (ROIs) are defined which contain spatial and kinematic information about the object. The ROI information is held in readout buffers until it is passed to the L2 triggers.

The ROIs are validated by the L2 triggers, making use of the full granularity of the detector in which they are located. The L2 systems can request further information in validated ROIs, to aid in the identification of particles - through this process the ROIs become global trigger objects, which can eventually become candidate photons, electrons, muons, τ leptons and hadronic jets. The use of ROIs limits the amount of data required by the L2 systems from the detector, as only information from specific geometric regions is requested which reduces the amount of data transferred from the detector to approximately 2% of the total event size. The data is transferred from the detector into a farm of computers which reside next to the ATLAS cavern, which impose further selection criteria onto the ROIs, known as the hypothesis - any ROI which fails the hypothesis is discarded, which results in a further reduction of the rate from 75 kHz to ≈ 2 kHz.

[6] A trigger tower is the analogue sum of the information in a number of cells in the calorimeters, covering an area of approximately 0.1×0.1 in $\Delta\eta \times \Delta\phi$.

[7] Jets are collimated bunches of stable hadrons, which are produced by the hadronisation of partons such as quarks and gluons. Hadronising refers to the process by which hadrons are formed from quarks and gluons - quarks combine with other preexisting quarks such as partons from the original pp collision, and with quark-antiquark ($q\bar{q}$) pairs produced from the vacuum, resulting in jets of hadrons.

The EF system uses offline analysis algorithms to reject further events, performing the final selection of events that will be recorded to disk. Events which have passed the L2 triggers are passed on to the Event Builder (EB), which makes use of the information from L2 and also the full detector information held in the readout buffers to build the event. The event is then passed to the EF where the available latency is 4s per event, allowing more sophisticated event reconstruction algorithms to be applied compared to those used in L1 and L2. It is possible to perform track fitting, vertex reconstruction and photon conversion searches here, often using standard ATLAS algorithms developed for offline use. The EF can access the full detector information (not just that within ROIs), and uses this to apply hypotheses to refine the L2 trigger objects, eventually passing events into different trigger streams depending on which candidate object caused them to pass the trigger [8]. The event rate is now reduced to $\approx$ 200 Hz, which can then be written to storage.

4.3 Monte Carlo Simulation

Before collision data taking using ATLAS began, a large programme of studies using simulated data was undertaken in order to best understand the behaviour of the detector with regards to how objects are reconstructed as they pass through the various subdetectors. Monte Carlo (MC) generators are used to simulate physical processes, and these are then fed through a simulated version of the ATLAS detector and object reconstruction algorithms, returning data in identical format to that returned by ATLAS using collision data taking.

MC generators use combinations of theoretical and empirical models (using data collected from previous experiments) to simulate potential physical processes resulting from the pp collisions within ATLAS. The MC samples of simulated data are produced in a three stage process - the initial event generation, detector simulation and finally digitisation of the data.

4.3.1 Event Generation

The MC generators split an event into constituent parts as shown in Figure 4.17. These parts are parton showering, the hard scattering process, hadronising, hadronic decay, QED-Bremsstrahlung and the underlying event [56].

[8] If an event passes several triggers then the same event can be recorded in multiple trigger streams.

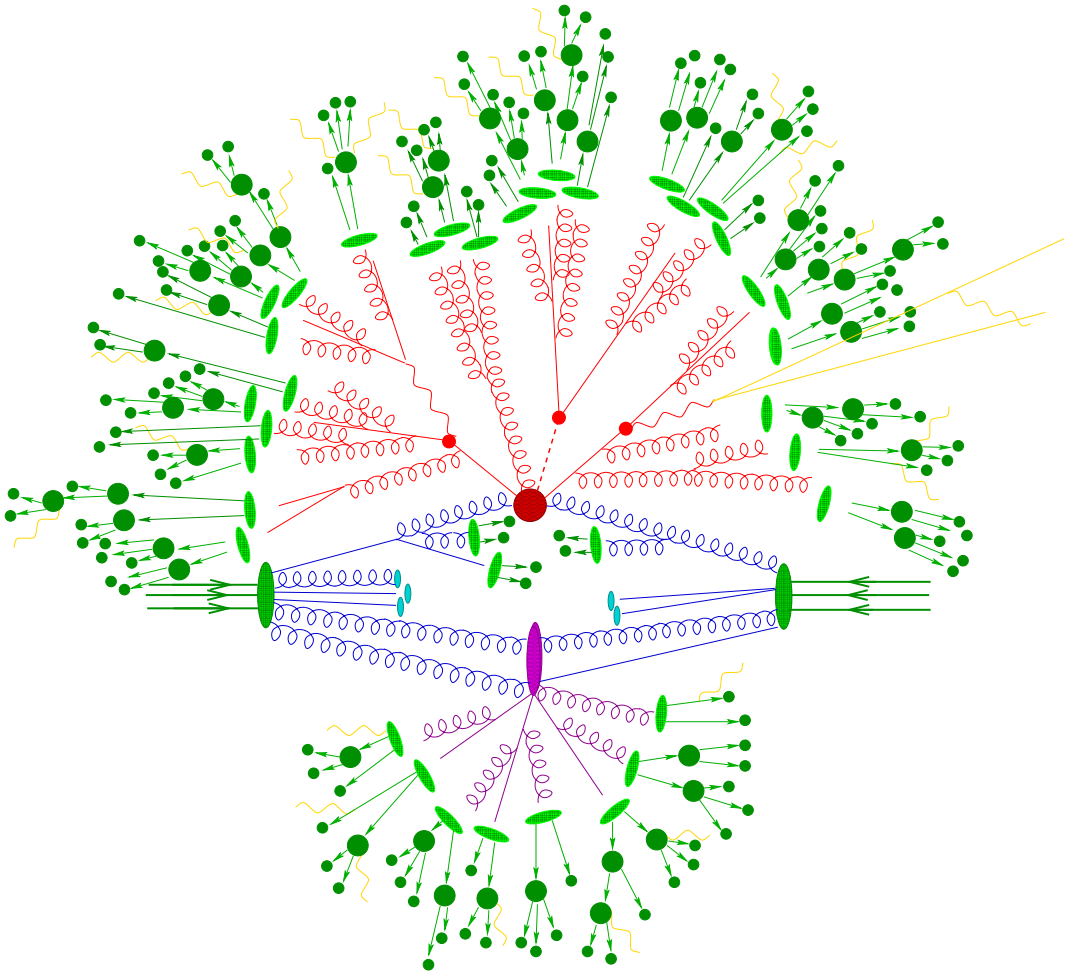

Figure 4.17: A schematic representation of a pp collision, as simulated by Monte Carlo. The incoming protons are represented by the parallel green lines on the left and right. Blue lines represent the parton showering for the initial state, and red lines represent this for the final state. The large red circle shows the hard scattering process, and the hadronising of partons is represented by light green ellipses. Hadronic decay is shown by the dark green lines and circles, and QED-Bremsstrahlung is shown in yellow. Finally, the underlying event is shown in purple [57].

- Parton showering consists of the emission of gluons by coloured partons. A cascade of partons is produced, modelled by perturbation theory above the energy threshold of approximately 1 GeV.

- The hard scattering process is typically theoretically well understood, and also experimentally interesting. The scattering of the colliding partons within the hadron is governed by the parton distribution function (PDF), $f(x_i, Q_i^2)$, which gives the probability of resolving a parton i of momentum fraction x_i within a hadron, via a momentum transfer Q_i^2 between parton i and an incoming particle.

- Hadronising is the confinement of coloured partons into uncoloured hadrons, as referred to in Section 4.2.5. Existing partons combine with other partons remaining from the original pp interaction, and with partons produced from the vacuum as $q\bar{q}$ pairs. The resultant hadrons subsequently decay into stable final state particles, forming hadronic jets.

- QED-Bremsstrahlung is the emission of photons from charged particles, in a similar manner to gluon emission with parton showering, but confined to QED processes.

- The underlying event can refer to the interactions between beam remnants and other soft scattering processes such as minimum bias events.

The various parts of an event can be simulated using different generators, as in some cases one generator is more appropriate for a particular purpose than another. For example, the MC sample of $t\bar{t}$ decays used in Chapter 6 is produced using MC@NLO [58, 59] for simulating the next-to-leading order (NLO) processes, and the Herwig+Jimmy [60, 61] generator for parton showering, while the MC sample of $J/\psi \to \mu\mu$ events used in Chapter 7 is generated using the Pythia generator for both event generation and parton showering [62].

For a particular process, the Feynman diagram with the fewest loops and vertices possible is the tree level (if there are no loops) or leading order (LO) diagram. NLO refers to the next simplest set of diagrams, which have first level corrections added. As an example, Figure 4.18 shows the LO diagram for top quark production from gluon fusion, and some of the NLO radiative loop corrections to this process, which involve the spontaneous emission and absorption of a gluon. LO processes have larger cross sections than NLO or NNLO (next-to-next-to-leading order processes, such as top quark pair production with two radiative corrections), as the cross

section is proportional to the square of the product of the couplings at the vertices, which are < 1.

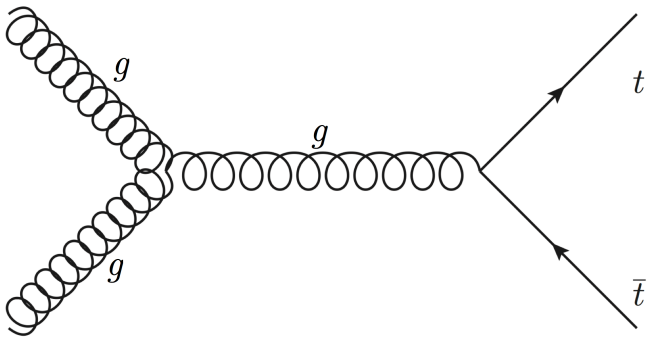

(a) LO top pair production

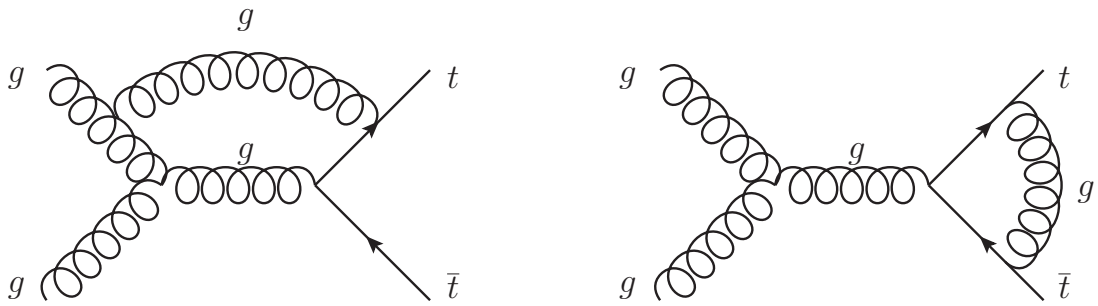

(b) NLO one-loop QCD corrections

Figure 4.18: Top quark pair production via gluon fusion (s-channel). The leading order process and two examples of next-to-leading order processes are shown.

4.3.2 Detector Simulation

The particles generated in the Event Generation stage above are fed into a simulated version of the ATLAS detector, produced using the GEANT4 toolkit [63]. GEANT4 is a software kit for simulating the passage of particles through matter, and is used to model the components of the ATLAS detector. The simulated particles produced in the event generation are passed through the simulated detector, and the resultant information is passed on the the digitisation and object reconstruction phases. The information about the particles produced at the generator level (often referred to as the “truth” information or “truth particles”) is stored as well.

4.3.3 Digitisation

The digitisation stage uses the information from the detector simulation to generate the detector signal, i.e. the voltages and time responses that would be read out of the real ATLAS detector during collision data taking. Object reconstruction algorithms are applied to the resultant data, allowing the reconstruction of objects as referred to in Section 4.2.5. This means that information can be produced in simulation in the same format as that which would be read out of the real ATLAS detector during collision data taking, allowing the same analysis software to be used on both simulated and collision data.

Chapter 5

Identifying b-jets, and the Match χ^2 based Soft Muon Tagger

As referred to in Section 3.2, good rejection of background processes is essential in identifying top quark decays. The high branching ratio of $t \to Wb$ means that the identification and selection of b-jets (b-tagging) can be used to select those events which are likely to have contained a top quark or a $t\bar{t}$ pair. This chapter outlines current b-tagging procedures in use in ATLAS, and introduces the concept of Soft Muon Tagging (SMT) and the χ^2_{match} based SMT algorithm.

The tagging of b-jets at ATLAS is performed using two main techniques, lifetime based taggers and Soft Lepton Taggers (SLT) [1]. Algorithms for b-tagging make use of the unique properties of b-jets, namely their high mass and the relatively long lifetime of b hadrons. This lifetime (τ) is approximately 1.5 ps [64] ($c\tau \approx 450\mu$m), meaning that b hadrons can travel a measurable distance before decaying - the flight length of a b hadron of mass 5 GeV with p_{T} of 50 GeV would be approximately 4.5 mm [2].

The hadronic jets referred to in this analysis correspond to jets of hadrons formed in the decay of quarks, as reconstructed using detector information. The reconstruction of jets is performed using the anti-k_t algorithm, with distance parameter $R = 0.4$ [54, 66]. The anti-k_t algorithm seeks to form conical jets of hadrons using information from the calorimeter systems. The input to the anti-k_t algorithm is topological calorimeter clusters; these are formed by an algo-

[1] The leptons are referred to as "soft" as they have a lower energy distribution compared to those produced from the decay of W bosons, which can be referred to as "hard" leptons.

[2] Using flight length $= c\tau \cdot (p_{\text{T}}/m_B)$, where m_B is the mass of the b hadron [6, 65]

rithm which searches for cells within the calorimeter which have a high signal significance over the expected background, implying that energy from an incident particle has been deposited in these cells. These cells and their neighbouring cells are then added together to form a cluster. If a neighbouring cell is also found to have a high signal significance (but not high enough to trigger the original search), it and its neighbours are added to the topological calorimeter cluster, and so on until no neighbouring cells have a significant signal [67].

5.1 Lifetime based b-tagging

Lifetime taggers rely on the measured distance between primary and secondary vertices, characteristic of long-lived b and c hadrons resulting from the hadronising of b and c quarks. There are a series of successful flavour taggers for high p_{T} jets which have been developed and calibrated by the ATLAS collaboration, allowing for the identification of b and c-jets and the rejection of light jets.

There are three forms of lifetime tagger in use at ATLAS - firstly, a "vertex tagger" (such as SV0) [68] uses a number of well reconstructed tracks with significant impact parameters. The impact parameter is the distance between the interaction (or primary) vertex and the nearest point through which the reconstructed track passes. The vertex tagger then attempts to find a displaced secondary vertex, indicating that a distance has been travelled by the hadron before decaying into other hadrons, resulting in a jet of particles. Those jets produced from the original interaction event will originate from the primary vertex, whereas those produced by the hadronisation of heavy flavour quarks will originate from a displaced vertex, due to the longer lifetime of b and c hadrons.

The IP3D and SV1 taggers create likelihood ratios for a measured variable in a selected jet, and compare these ratios to reference probability distributions obtained from simulated data. The ratio of the probability that a selected jet is a b-jet to the probability that it is a light jet gives the track or vertex weight, which is used to decide whether or not to tag a particular jet as being a b-jet. The measured variables used in IP3D are histograms of the significance of the impact parameter measurements ($d_0/\sigma d_0$ and $z_0/\sigma z_0$). SV1 searches for pairs of tracks originating from the same secondary vertex, and uses their invariant mass, the ratio of the energies of tracks from a particular vertex to the total energy of the jet they are within, and also the number of vertices

to construct a likelihood parameter [68].

A "jet probability" tagger traces the particle tracks within a jet back to the point where they were produced, and determines the probability that a track originated from the primary vertex, based on the signed impact parameter of the jet. This quantity is found by comparing the direction of particles within a jet with the particle from which they decayed (the "parent"). If the track direction is within 90° of the line joining the primary vertex to the point of closest approach of the parent, then the impact parameter is given a positive value. If the angle is greater than 90° then the signed impact parameter will be negative. Figure 5.1 shows a schematic diagram of this definition [69].

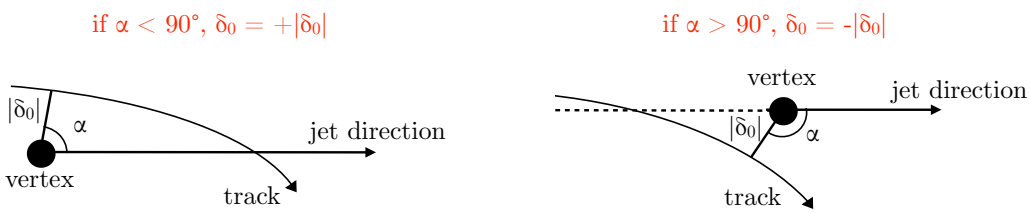

Figure 5.1: Constructing the signed impact parameter. The sign of δ_0, the impact parameter, is based on the angle between the jet direction and the line between the primary vertex and the point of closest approach of the track corresponding to the parent particle.

Jet probability taggers return a value between -1 and 1, with values close to 0 indicating increased likelihood that the track originates from a displaced secondary vertex, and those with an absolute value close to 1 indicating that the track originates from the primary vertex. The track probability distribution for tracks within heavy flavour jets peaks at 0, whereas the distribution for light jets is more evenly spread across the range, as shown in Figure 5.2(a). The probabilities for the tracks within a jet are then combined into a jet probability, shown in Figure 5.2(b). The simulated samples of light and c-jets used to produce Figure 5.2 are "purified" jets - light jets for which a b, c quark or a τ lepton is found within a cone of $\Delta R = 0.8$ around the jet direction are not used to find the performance of the tagger, as there is potential in high jet multiplicity events for tracks from several flavours of decay to be present in the same jet [54]. Therefore such jets are not included in the sample of purified light jets. Purified c-jets do not have a truth level [3] b quark, τ lepton or light jet found within a cone of $\Delta R = 0.8$ around the jet direction.

[3] A "truth level" particle, or "truth particle", refers to a particle produced at the generator level in Monte Carlo, before passing through the simulated detector and object reconstruction processes.

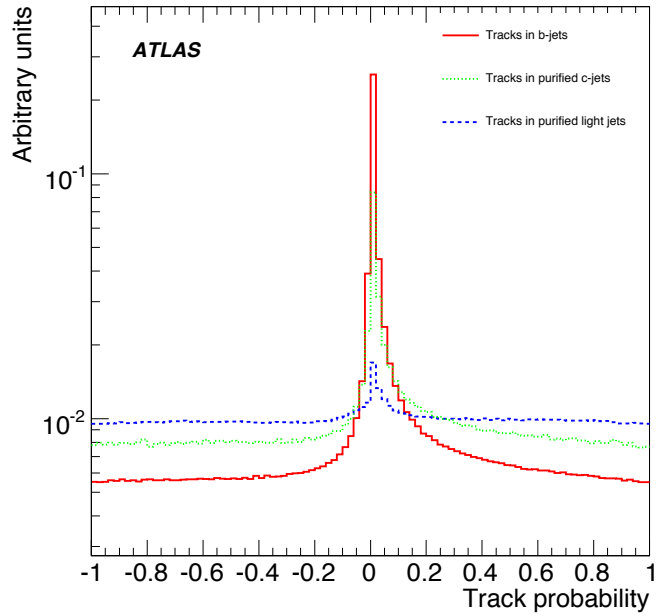

(a) Probability that a track within a jet originates from the primary vertex

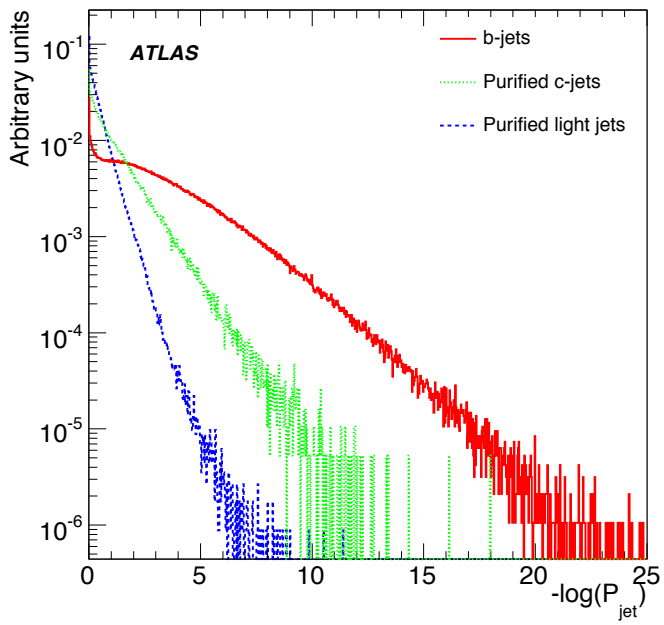

(b) Probability that a jet of tracks originates from the primary vertex

Figure 5.2: Probability distributions showing compatibility with the primary vertex for jets and tracks within jets, as found using JetProb, a jet probability *b*-tagger, produced using simulated data [54].

5.2 Determining the performance of b-tagging algorithms

The performance of b-taggers can be measured by two criteria - the b-jet tagging efficiency (ε_b) and the light jet rejection (LJR). The former is defined as the fraction of taggable true b-jets which are tagged by the b-tagging algorithm - "taggable" jets are good jets which have a high likelihood of being tagged, as they are pure jets which are unlikely to be an incorrectly reconstructed electron or other truth particle. A jet is considered taggable if it has $p_{\text{T}} > 20$ GeV, $|\eta| < 2.5$ and it does not lie within $\Delta R(\text{e}, \text{jet}) < 0.2$ of an electron with $E_{\text{T}} > 25$ GeV, $|\eta| < 2.5$ and isolation energy in a cone of $\Delta R < 0.2$ less than 3.5 GeV.

The mistag rate is the fraction of taggable jets which do not truly originate from the decay of a b hadron, but which are identified by the b-tagger as being b-jets; the LJR is the inverse of the mistag rate, or the number of light jets which are rejected for each light jet that is incorrectly tagged as being a b-jet. Figure 5.3 shows the ε_b and LJR achieved by a selection of b-tagging methods used in ATLAS [70].

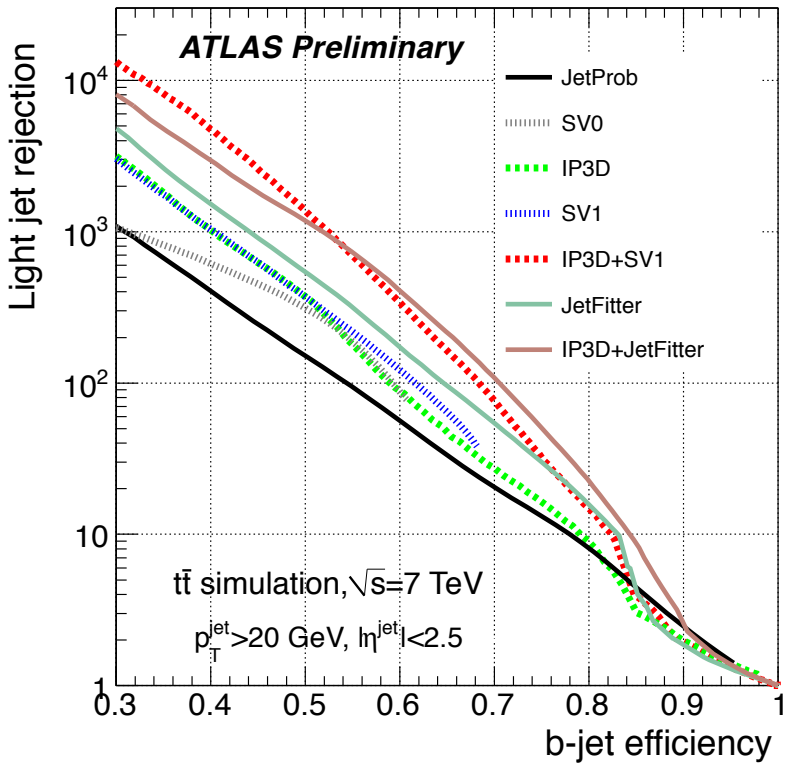

Figure 5.3: LJR as a function of b-jet tagging efficiency for various b-tagging algorithms, based on simulated $t\bar{t}$ events [70].

5.3 Soft Lepton Tagging

Soft Lepton Tagging (SLT) algorithms rely on the identification of a lepton produced from the semileptonic decay of a b or a c quark, rather than looking for a secondary vertex. The term "semileptonic", in this context, refers to a hadron decaying to a lepton-neutrino pair and another hadron.

Hadrons containing heavy flavour quarks can decay into leptons which inherit a relatively low fraction of the quark energy - the branching ratio (BR) for b quarks within b hadrons decaying as $b \to \ell^- \overline{\nu}_\ell X$ is $10.95^{+0.29}_{-0.25}\%$ for muons and $10.86 \pm 0.35\%$ for electrons [6], where X represents any other hadronic products within the b-jet. These low p_{T} leptons can also be produced via $b \to cX \to \ell^+ \nu_\ell X$ and $b \to \bar{c}X \to \ell^- \overline{\nu}_\ell X$, with BRs of $8.02 \pm 0.19\%$ and $1.6 \pm 0.5\%$ respectively for muons [6]. The $b \to \bar{c}X$ decay occurs as the neutral B mesons (B^0 and B^0_s) can oscillate back and forth between the B^0 and $\bar{B}^0$ (or B^0_s and $\bar{B}^0_s$) states, as shown in Figure 5.4. This gives rise to a $\bar{b}$ quark which can then decay into the $\bar{c}$.

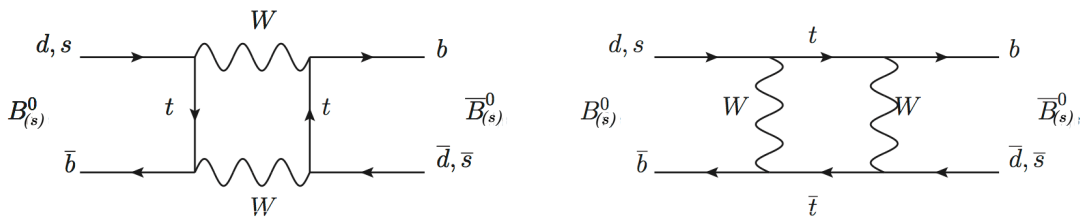

Figure 5.4: Feynman diagrams of neutral B meson oscillations, where the down-type quark in the initial state is the d for the B^0, and s for B^0_s.

There is also a small contribution from $b \to \tau \to \mu$ decays, with a BR of $0.42 \pm 0.04\%$ [6]. This means that in $21.0 \pm 1.0\%$ of decays of b hadrons, a muon is expected to be present in the resultant b-jet (the BR is approximately the same for electrons). In approximately 38% of $t\bar{t}$ decays, therefore, at least one of the hadrons containing b quarks will decay semileptonically [4].

An example of the decay of a b quark into a b-jet containing soft muons, both from $b \to \mu \overline{\nu}_\mu X$ and $b \to cX \to \mu^+ \nu_\mu X$ is shown in Figure 5.5. The soft muons are used instead of the soft electrons as the ATLAS detector reconstructs muons with high purity, and there is a higher incidence of fakes with electrons, which is to say that there is a higher likelihood of light hadrons and other non-electrons being reconstructed as electrons in the calorimetry systems than there is

[4] $1 - (1 - BR(b \dashrightarrow \ell))^2 \approx 0.38$, where $b \dashrightarrow \ell$ indicates all decay modes starting with a b and resulting in a ℓ, regardless of the intermediate particles (if any). The lepton, ℓ, can represent either an electron or a muon.

of misidentifying muons in the MS.

In order to identify the soft muons, they must first be reconstructed. Two muon reconstruction algorithms are used, depending on the momentum of the muon in question. Due to the thickness of the calorimeter systems of the detector, muons with lower momenta (those with p below approximately 5 GeV) do not leave tracks in the outer parts of the MS of the ATLAS detector, and so they can be reconstructed using the ID and inner stations of the MS only (these shall be referred to as low p_{T} muons). Combined muons are reconstructed using information from the ID and all sections of the MS, matching a track in the ID with a track in the MS which has been extrapolated to the beamline.

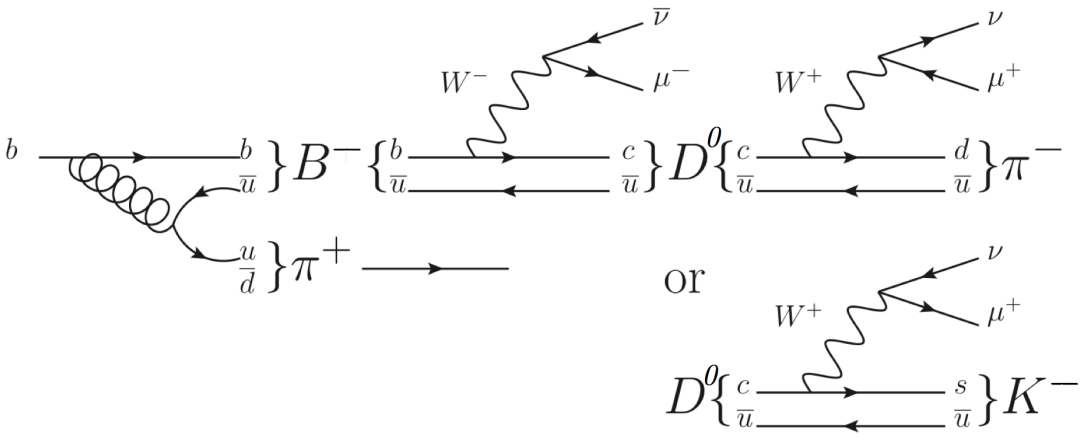

Figure 5.5: An example of the decay of a b quark into a b-jet, containing two soft muons. The resultant hadrons (π^- or K^-) make up part of the b jet. The π^+ in this case is referred to as a fragmentation track, and will originate from the primary vertex, while the soft muon and the π^- or K^- will be traced back to the $D^0 \to W^+\pi^-$ or $D^0 \to W^+K^-$ vertices respectively. This vertex will be displaced from the primary vertex, as the B^- travelled a number of mm before decaying.

5.3.1 The $p_{\text{T}}^{\text{rel}}$ based Soft Muon Tagger

Within SMT there are differing methods of using the signature muon to tag a b-jet. A simple search for the presence of any reconstructed muon in a jet is one approach, and the performance of this can be enhanced by using the $p_{\text{T}}^{\text{rel}}$ of the muon within a jet to discriminate between b-jets and jets from other sources. A cartoon showing the $p_{\text{T}}^{\text{rel}}$ of a muon within a b-jet can be seen in Figure 5.6. The soft muons resulting from the decays of b hadrons tend to have greater values of p_{T} than those originating from light hadron decays, and due to the high mass of b hadrons, muons from direct b decays are more boosted in the plane transverse to the jet

direction, meaning that they will have higher values of $p_{\text{T}}^{\text{rel}}$ than muons produced in light or c-jets - the $p_{\text{T}}^{\text{rel}}$ distributions for direct $b \to \mu\nu X$, sequential $b \to c \to \mu\nu X$, $c \to \mu\nu X$, light hadron $\to \mu\nu X$ decays and fake muons are shown in Figure 5.7 [54].

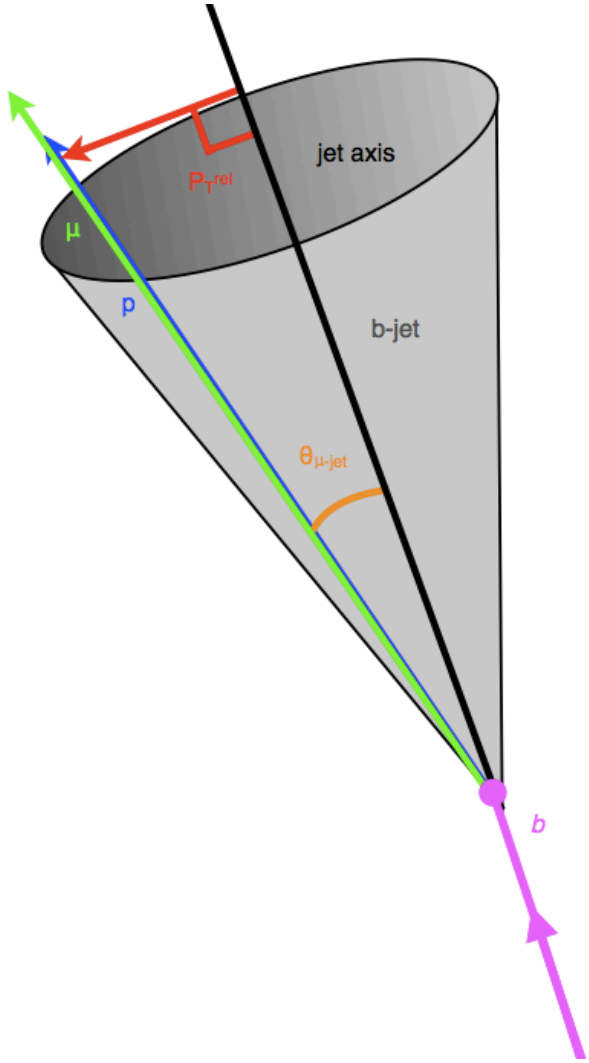

Figure 5.6: A schematic representation of the relative p_{T} of a muon within a b jet, with respect to the p_{T} of the jet axis

The muon, neutrino and quark produced by the semileptonic b decay will proceed with equal probability in all directions in the rest frame of the b, however as the b is boosted in one particular direction the products will also be boosted, and so will form a jet. At low jet p_{T} this will result in a difference in the p_{T} of the jet products with respect to the jet axis, therefore muons resulting from the decay of the heavy b hadrons may have a large $p_{\text{T}}^{\text{rel}}$ [54]. At higher jet energies this effect will become less prominent as the muon $p_{\text{T}}^{\text{rel}}$ becomes very small relative to the overall

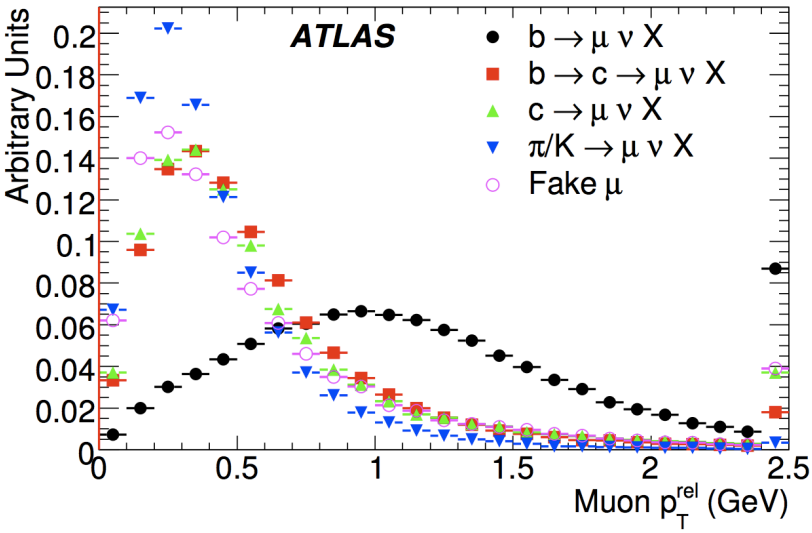

Figure 5.7: Distribution of the transverse momentum relative to the jet axis of muons from b, c and light hadron decays, and fake muons in simulated $t\bar{t}$ events [4]

jet p_T, as all decay products will be more boosted.

The p_T^{rel} tagger makes use of pairs of reconstructed jets and "taggable" muons (which can be either a combined or low p_T muon). Taggable muon, in this case, means that the muon satisfies the following criteria:

- ΔR (between jet axis and muon) < 0.5
- Impact parameter of muon with respect to the primary vertex, $|d_0| < 4$ mm
- Muon $p_T > 4$ GeV
- Match χ^2/degree of freedom (χ^2_{match}) < 10

The requirement that the muon p_T be greater than 4 GeV greatly reduces the mistagging rate of the SMT, by removing most muons produced from the decays of light hadrons (such as π and K mesons), with a comparatively small reduction in the efficiency of the tagger. The requirement on $|d_0|$ is imposed to reduce the contribution from long-lived hadrons [5], which can produce a secondary vertex at larger distances from the primary vertex. Also this removes contributions from interactions with the material of the beam pipe itself. The requirement on χ^2_{match} has been found

[5] Hadrons such as K and π mesons, and Σ and Ξ baryons have lifetimes longer than the B and D mesons, but short enough that they are able to decay within the detector volume.

to reduce the contribution from fake muons in simulated data while not significantly reducing the efficiency of selecting true muons [54].

Once the μ-jet pairs have been established, the $p_{\text{T}}^{\text{rel}}$ of the pair is used to find the likelihood ($p_{\text{T}}^{\text{rel}}$ weight) of the muon being a soft muon from a b decay, based on Monte Carlo simulated $p_{\text{T}}^{\text{rel}}$ distributions. The jet is consequently tagged (or not) as a b-jet. The $p_{\text{T}}^{\text{rel}}$ weight threshold can be set to achieve different operating points of b-tagging efficiency.

The $p_{\text{T}}^{\text{rel}}$ algorithm is used within ATLAS to calibrate lifetime based b-taggers, however the χ^2_{match} based soft muon tagger described in Section 5.4, which is the main topic of this thesis, is used for a measurement of the $t\bar{t}$ cross section.

5.4 The Match χ^2 based Soft Muon Tagger

Another method of SMT, proposed in [71] (hereafter referred to as "the 2010 study"), makes use of the quality of the match between the tracks left by a muon in the MS and ID of the ATLAS detector. Specifically, the χ^2/degree of freedom of the match (χ^2_{match}) is used as a discriminating variable between b-jets, c-jets and light jets. This variable is shown in Equation 5.1 and defined (for combined muons) as the difference between the MS and ID track parameters, $\mathbf{T}_{\text{MS}}$ and $\mathbf{T}_{\text{ID}}$ respectively, weighted by their combined covariance matrices, $\mathbf{C}_{\text{MS}}$ and $\mathbf{C}_{\text{ID}}$. The track parameters in question are the perigee parameters η, ϕ, p_{T}, d_0 and z_0, as shown in Equation 5.2.

$$\chi^2_{\text{match}} = (\mathbf{T}_{\text{MS}} - \mathbf{T}_{\text{ID}})^T (\mathbf{C}_{\text{MS}} + \mathbf{C}_{\text{ID}})^{-1} (\mathbf{T}_{\text{MS}} - \mathbf{T}_{\text{ID}}) \tag{5.1}$$

$$\mathbf{T}_{\text{MS or ID}} = \begin{pmatrix} \eta \\ \phi \\ p_{\text{T}} \\ d_0 \\ z_0 \end{pmatrix}_{\text{MS or ID}} \tag{5.2}$$

The covariance matrices are formed as shown in Equation 5.3 [72], containing the measurement uncertainties on the track parameters, $T_i - \langle T_i \rangle$, where T_i represents the measured values of the 5 elements of the vector of track parameters and $\langle T_i \rangle$ is the expected value of T_i. The source of the measurement uncertainties is the limited resolution of the detector components.

$\mathbf{C}_{\text{MS}} + \mathbf{C}_{\text{ID}}$ is shown in full in Appendix B.

$$\mathbf{C}_{ij} = (T_i - \langle T_i \rangle)(T_i - \langle T_j \rangle) \tag{5.3}$$

The χ^2_{match} value is expected to prove useful in identifying heavy flavour jets because light hadrons (such as the π and K mesons) decaying in flight, either within the ID or between the ID and MS, can produce a genuine muon which leaves a high quality track in the MS but does not produce a continuous track through the ID and MS. The emission of an undetectable neutrino in the production of the muon causes a kink in the track, due to conservation of momentum. Another source of fake muons (non muons detected by tracks in the MS and ID systems) is hadronic punch-through events, caused by hadrons passing through the calorimeters or interacting with the material of the detector. Such events produce showers of particles, some of which can be reconstructed as muons. As the interactions can take place in between the MS and ID, the quality of match between the tracks in these systems is likely to be poor when compared with true muons found within the heavy flavour jets produced by the decay of b hadrons.

The studies performed in the 2010 study and quoted here define the χ^2_{match} SMT method as having the same requirements for a taggable muon as the $p_{\text{T}}^{\text{rel}}$ based SMT algorithm, but additionally requiring that the χ^2_{match} pass a tightened cut compared to the $\chi^2_{\text{match}} < 10$ mentioned in Section 5.3.1.

5.4.1 Performance of the χ^2_{match} based Soft Muon Tagger

The χ^2_{match} distributions for various flavours of jets within a Monte Carlo simulated sample of $t\bar{t}$ events is shown in Figure 5.8, for both low p_{T} and combined muons as defined in Section 5.3.1.

As can be seen, the χ^2_{match} distribution for combined muons seems to show more b-jet discriminating power of the χ^2_{match}variable than for low p_{T} muons. This is due to the difference in how the combined and low p_{T} tracks are established - low p_{T} muons make use of tracks in the ID and at most three coordinates from the MS (see the description of the layout of the MS in Section 4.2.3, and Figure 4.14 in the same section). By contrast, combined muons make use of many more spatial coordinates from the entire MS system. The result of this is an increased proportion of “fake” muons in the sample of low p_{T} muons. “Fake” muons are tracks reconstructed as muons within jets which, when compared with the truth information from simulation, do not correspond to muons produced at the generator level (“true” muons) - by this it is meant that no

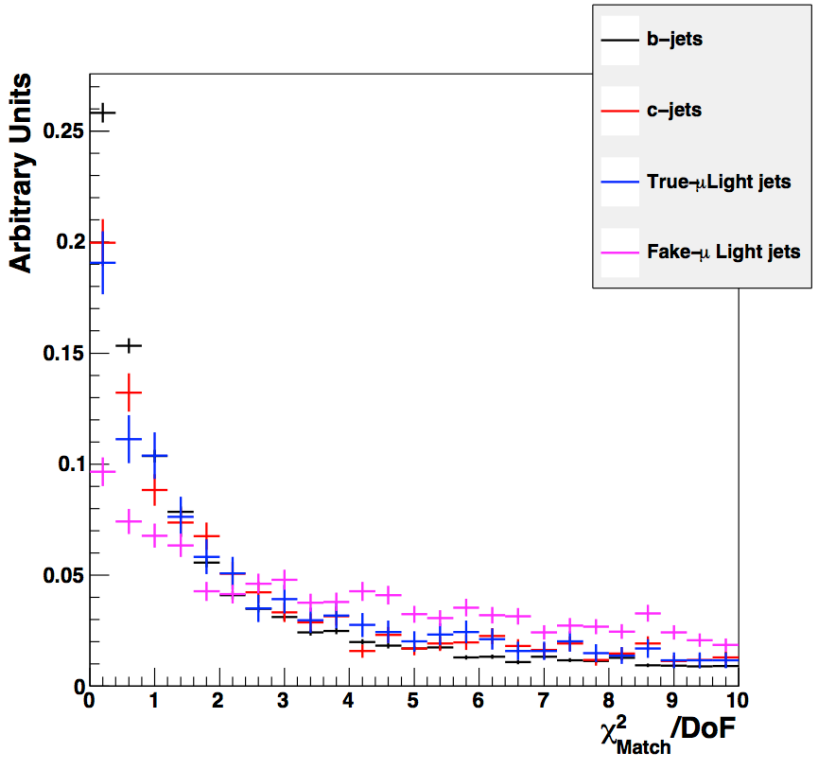

(a) χ^2_{match}distribution for taggable muons reconstructed using low p_{T} methods.

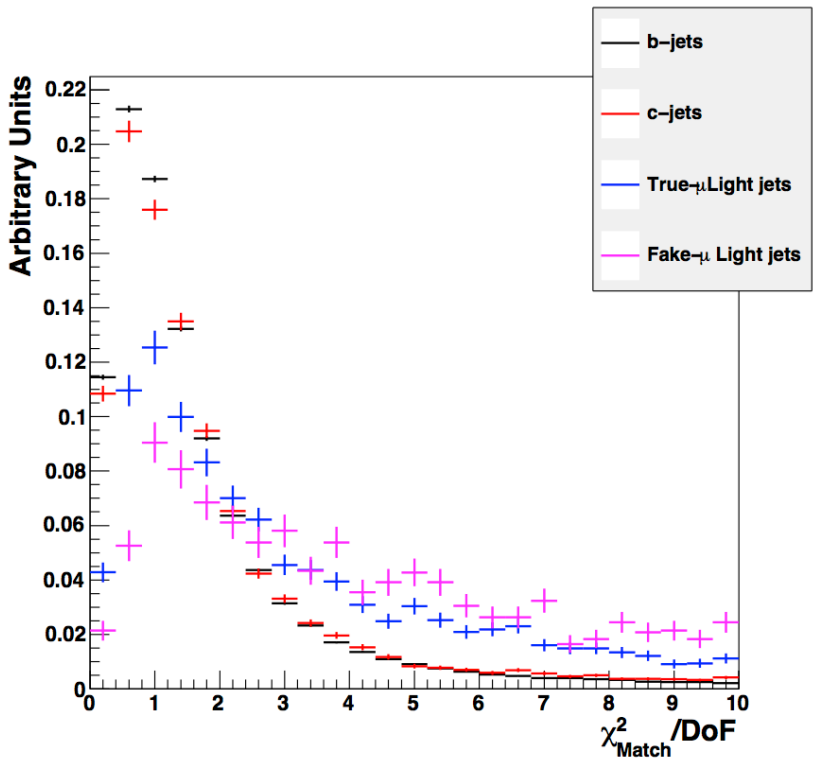

(b) χ^2_{match}distribution for taggable combined muons.

Figure 5.8: The χ^2_{match}/DoF distributions of taggable muons in a sample of simulated $t\bar{t}$ data, for both low p_{T} muons and combined muons [71].

true muon is found within $\Delta R < 0.01$ of the reconstructed muon.

The difference in the discriminating power of χ^2_{match} in combined and low p_{T} muons is borne out when studies of the ε_b and LJR are performed using the χ^2_{match} variable as the determinant. Keeping ε_b at an operating point of 10% for these studies, the achievable LJR is found - an LJR of 350 ± 5 is found when using both combined and low p_{T} muons, whereas an LJR of 470 ± 9 is achieved when using combined muons only. These LJR values are achieved using a χ^2_{match} cut of $\chi^2_{\text{match}} < 2.5$ and $\chi^2_{\text{match}} < 3.2$ respectively in order to keep the b-tagging efficiency at the operating point of 10%. Consequently, the requirement is made that the taggable muon should be a combined muon for optimum performance of the χ^2_{match} tagger - in all future references to the χ^2_{match} tagger, it should be assumed that a cut of $\chi^2_{\text{match}} < 3.2$ is being used as the discriminant. The LJR and ε_b values achieved for various cuts on χ^2_{match} are shown in Figure 5.9, and the cuts implemented in order to achieve various b-tagging efficiencies are shown in Table 5.1.

Table 5.1: Comparison of light jet rejection factor produced for the χ^2_{match} and $p_{\text{T}}^{\text{rel}}$ based taggers, when achieving several b-tagging efficiencies [71].

	$p_{\text{T}}^{\text{rel}}$ based tagger		χ^2_{match} based tagger	
ε_b	$p_{\text{T}}^{\text{rel}}$ weight $>$	LJR	χ^2_{match} weight $<$	LJR
8 %	3.7	790 ± 19	1.8	740 ± 17
9 %	3.4	585 ± 12	2.3	595 ± 12
10 %	3.14	430 ± 8	3.2	470 ± 9
11 %	2.93	310 ± 5	6.0	330 ± 5

5.4.2 Comparing performance of b-tagging methods

It has been demonstrated in Monte Carlo simulations of $t\bar{t}$ data that at an operating point of $\varepsilon_b = 10\%$ (taking the branching ratio of $b \to (c \to)\mu$ into account), LJR values of 430 ± 8 and 470 ± 9 can be achieved using the $p_{\text{T}}^{\text{rel}}$ and χ^2_{match} based soft muon taggers respectively [71]. As the BR of $b \dashrightarrow \mu$ is only $21.0 \pm 1.0\%$, the maximum ε_b that can be achieved by a SMT algorithm is also $21.0 \pm 1.0\%$. This should be noted when comparing performance of b-tagging algorithms - for example, the operating point of the $p_{\text{T}}^{\text{rel}}$ tagger in this instance is approximately 48% of the maximum possible value of ε_b. As shown in Figure 5.3, the LJR achieved for the JetProb tagger for an operating point of $\varepsilon_b = 48\%$ is approximately 180, significantly lower than the rejection achieved by the soft muon taggers.

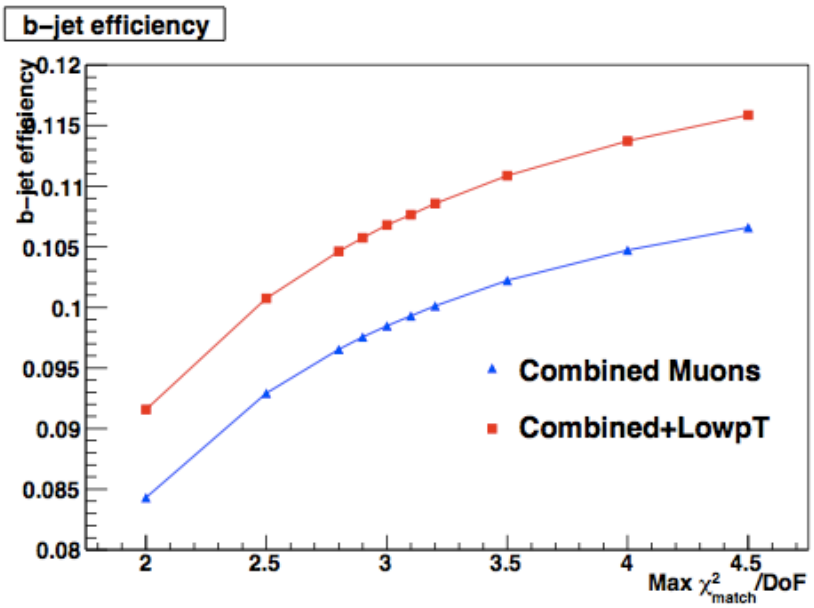

(a) b-jet tagging efficiency found using a cut on the χ^2_{match} value of a soft muon within the jet.

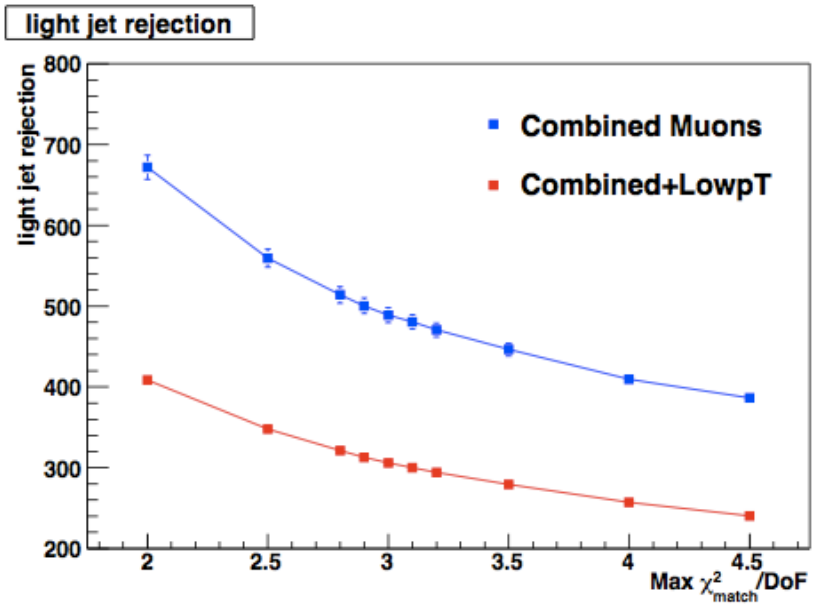

(b) Light Jet Rejection found using a cut on the χ^2_{match} value of a soft muon within the jet.

Figure 5.9: b-jet tagging efficiency and light jet rejection factors achieved using a cut on the χ^2_{match} value of a soft muon within the jet. Two categories of soft muons were used - combined muons only, and combined+low p_{T} muons [71].

5.4.3 SMT Selection Cuts

The Monte Carlo studies in the 2010 study make only the most basic of requirements on the jet and muon used for the χ^2_{match} based tagger. In order to use the muon for flavour tagging of a jet on a sample of collision data, further requirements must be put in place. The selections include those used for the $p_{\text{T}}^{\text{rel}}$ based tagger, with the addition of muon quality recommendations from the Muon Combined Performance (MCP) group [73] and specific cuts optimised for the χ^2_{match} tagger. The MCP quality cuts are put in place to take into account the conditions of the silicon systems in the ID - if the extrapolated muon track passes through a dead area of the detector, then it is treated as if a hit has occurred in this region [73].

The STACO algorithm used for reconstructing muons performs a statistical combination of the MS track, extrapolated to the beamline, with a corresponding track in the ID. There is a requirement that the χ^2 of this pair of tracks be below 100. If multiple ID tracks are matched with the MS track, only the ID track with the smallest ΔR with the extrapolated MS track will be used [74].

The selections are the following:

- Muon collection and type:
  1. The STACO collection of reconstructed muons is used
  2. Combined muon, in order to have a valid χ^2_{match} value
- MCP quality cuts:
  1. N(B layer hits) $>$ 0, if B layer hits are expected on the muon track
  2. N(Pixel hits) + N(crossed dead Pixel sensors) $>$ 1
  3. N(SCT hits) + N(crossed dead SCT sensors) $>$ 5
  4. N(Pixel holes) + N(SCT holes) $<$ 3
  5. If $|\eta| < 1.9$:
     - N(TRT hits) + N(TRT outliers) $>$ 5
     - N(TRT outliers)/[N(TRT hits) + N(TRT outliers)] $<$ 0.9
  6. If $|\eta| \geq 1.9$ and N(TRT hits) + N(TRT outliers) $>$ 5:
     - N(TRT outliers)/[N(TRT hits) + N(TRT outliers)] $<$ 0.9

- Flavour tagger specific cuts:

  1. $p_{\text{T}} > 4$ GeV
  2. $|d_0| < 3$ mm
  3. $|z_0 \cdot \sin(\theta)| < 3$ mm
  4. $\Delta R(\mu, \text{jet}) < 0.5$: in case of ambiguities, the muon is only associated with the closest jet

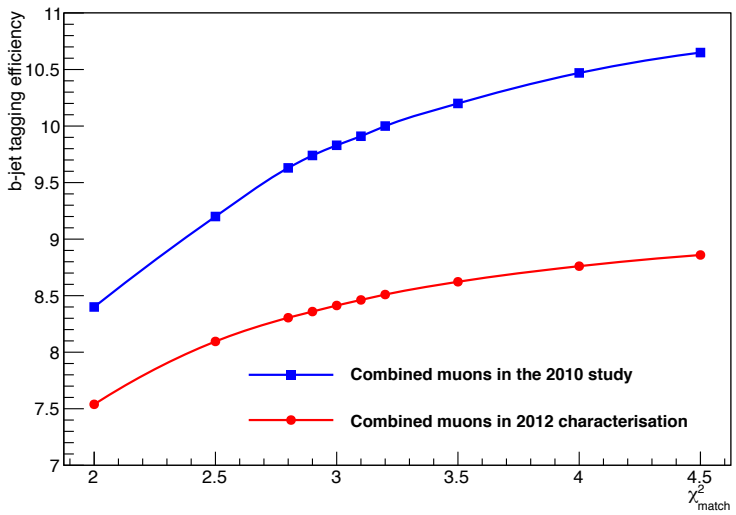

Figure 5.10: Comparison of b-jet tagging efficiencies found in the 2010 study [71] and the characterisation in Chapter 6 of this thesis, for various cuts on the χ^2_{match} value of a soft muon within the jet.

Figure 5.10 shows a comparison of the b-tagging efficiencies found in the 2010 study [71], and those found in Chapter 6 of this thesis. The reduction of the efficiency is due to the additional cuts placed on the soft muons and jets as the precise definition of the tagger has been refined.

The impact parameter requirements ($|d_0|$ and $|z_0 \cdot \sin(\theta)|$) are added to remove tracks which may be produced by the interaction of products of the collision hard scattering process with the material of the detector, and also to suppress tracks from hadronic interactions. The $|z_0 \cdot \sin(\theta)|$ cut is also effective in suppressing tracks from different vertices at high instantaneous luminosity. The $\Delta R(\mu, \text{jet}) < 0.5$ cut is needed in order to include most b-jets - it is chosen because while the anti-k_t algorithm used for jet clustering [54] defines the radius of a jet cone as $\Delta R < 0.4$, if only the soft muons within this radius are considered, 6% of b-jets would be excluded, as can be seen in Figure 5.11.

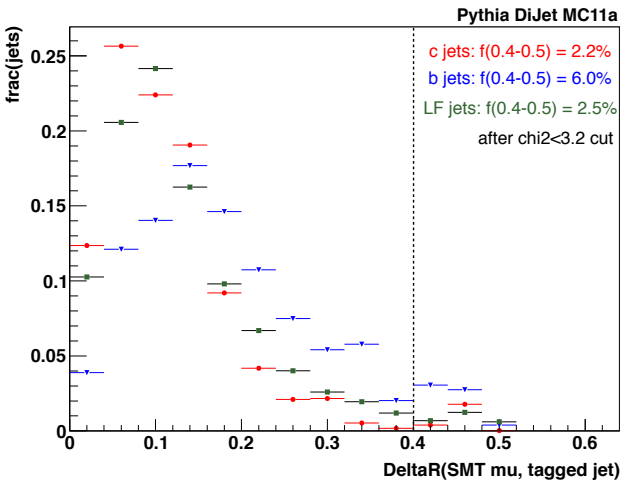

Figure 5.11: $\Delta R(\mu,\text{jet})$ distributions for simulated $t\bar{t}$ events from simulated dijet events. The fraction of jets contained in the ring between $\Delta R(\mu,\text{jet})$=0.4 and $\Delta R(\mu,\text{jet})$=0.5 is also displayed for the three flavours of jet, after all other tagger selections have been made [1]. It can be seen that the expansion of the maximum $\Delta R(\mu,\text{jet})$ to 0.5 includes proportionally more b-jets than c or light jets.

5.4.4 Comparison of Soft Muon Taggers

Studies on simulated data comparing the $p_{\text{T}}^{\text{rel}}$ and χ^2_{match} based soft muon taggers find the performances overall to be similar in terms of ε_b and LJR - Figure 5.12 shows the performance of the two taggers, and also of the $p_{\text{T}}^{\text{rel}}$ tagger with the additional requirement that the muon be a combined muon to see if this affects the performance.

It can be seen that the effect of the combined muon requirement on the $p_{\text{T}}^{\text{rel}}$ based tagger is negligible. It was also found that the χ^2_{match} based tagger performed better at higher values of jet E_{T}; $p_{\text{T}}^{\text{rel}}$ shows strong dependence on jet E_{T}, and at higher E_{T} values there is little difference between the $p_{\text{T}}^{\text{rel}}$ distributions for b-jets and light jets meaning that the discriminating power of a $p_{\text{T}}^{\text{rel}}$ based tagger is lessened [71]. The χ^2_{match} distribution, however, shows no systematic dependence on the E_{T} of the jet, implying a better discriminating power at high jet E_{T} than that of the $p_{\text{T}}^{\text{rel}}$ based tagger. The studies mentioned so far in this section have been exclusively performed on a simulated sample of $t\bar{t}$ data, and calibration in collision data is essential before the χ^2_{match} tagger can be used in a $t\bar{t}$ pair production cross section measurement, or be used for other analyses requiring jet flavour tagging.

The χ^2_{match} tagger has advantages over the $p_{\text{T}}^{\text{rel}}$ based tagger in terms of calibration with

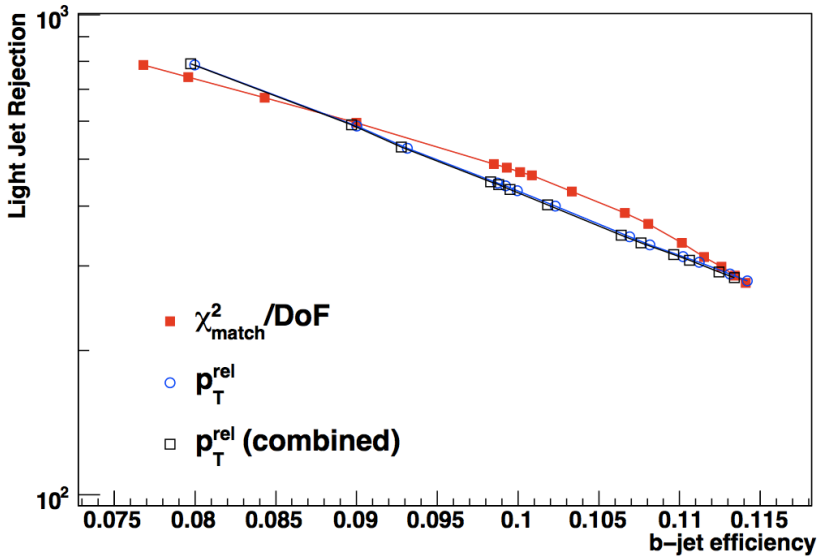

Figure 5.12: Light jet rejection as a function of the b-jet tagging efficiency for the χ^2_{match} and p_T^{rel} based soft muon taggers. The performance of the p_T^{rel} tagger using only combined muons is also shown [71].

collision data. As p_T^{rel} is a property of a muon within a jet, a jet is required for calibration. As a consequence of this, the performance of the tagger is dependent on the quality of the jet reconstruction, as well as that of the muon. The χ^2_{match} of the muon is a property of the muon alone, and so a sample of muons is required to perform calibrations with collision data. This does not pose a problem as there are large statistics samples containing isolated muons available in early data, such as $J/\Psi \to \mu\mu$ and $Z \to \mu\mu$. A detailed study of the efficiency of the χ^2_{match} based tagger and of determining the scale factor between collision and simulated data is performed, and the results can be seen in Chapter 7.

Chapter 6

Monte Carlo Characterisation of the Match χ^2 based Soft Muon Tagger

To help with understanding the χ^2_{match} based soft muon tagger presented in the previous chapter, a study of the characteristics of the tagger was undertaken. The first stage of this study is to reproduce and complement the initial study [71], in light of the fact that the initial study did not include the final list of requirements for the tagger, shown in Section 5.4.3. In this section the event selection is explained, and the performance of individual requirements within the tagger is investigated, as well as the dependence of the b-tagging efficiency on the transverse momenta of true b quarks and reconstructed jets. The sources of all reconstructed muons incorrectly tagged as originating from b-jets (these are referred to as "fakes") are found by matching of the reconstructed muons to truth particles in the simulated dataset.

As an example of characterising the tagger, if one assumes that in a sample of 100 b-jets one has 20 soft muons, 10 of which are selected by the soft muon tagger, then it is possible to look at the characteristics of the tagged and untagged muons and jets, to see if there are obvious reasons why some soft muons were not tagged, and why some particles which are not soft muons are tagged as being so.

Characterising the χ^2_{match} based soft muon tagger involves investigating which events and particles pass the constituent selection cuts. The first stage is to establish the "truth" information related to the actual content of the simulated dataset - how many $t\bar{t}$ events are generated, and of these how many decay to b quarks, and in turn how many of these produce muons in the final state of the decay and what other decay products are produced. In this context, "truth" refers

to the simulated particles produced at generator level, i.e. before the reconstruction algorithms have produced entities such as jets and reconstructed muons. This allows decay chains and branching ratios (BRs) to be found, and permits investigation of any dependences of the BRs on the particle characteristics.

6.1 Monte Carlo samples and Event Selection

In order to investigate the characteristics of the χ^2_{match} based soft muon tagger, a dataset of three million Monte Carlo simulated top-antitop quark pairs was produced ("the $t\bar{t}$ MC sample"). The μ+jets channel is investigated here, as it has high statistics and the presence of the muon is required to check the efficacy of the veto of the hard muon from the W boson in the $t \to Wb$ decay, as mentioned below. The simulated data sample used for the characterisation studies was produced using MC@NLO [58, 59] for simulating the next to leading order (NLO) processes, and the Herwig+Jimmy [60, 61] generator for parton showering [75].

The μ+jets channel event selection requires that the event passes the requirements listed in Table 6.1 [76]. These event selection criteria look to select only events in which the $t\bar{t}$ pair has decayed via $t \to W^+b \to q\bar{q}(b\text{-jet})$ and $\bar{t} \to W^-\bar{b} \to \ell\bar{\nu}(\bar{b}\text{-jet})$, or the charge conjugates of these decays. The event selection here is the same as that used for the $t\bar{t}$ cross section measurement summarised in Chapter 8 - although $t\bar{t}$ decaying via the μ+jets channel will result in 4 jets, requiring that 3 good jets are present reduces the systematic uncertainty related to the jet energy scale (explained in Section 6.3.3), while still excluding the dilepton channel. Of the 3 million $t\bar{t}$ events subjected to the event selection, 569999 pass all nine requirements - these events will be referred to as "the preselected sample" in this chapter. The efficiency of the event selection is therefore 19.0% of all simulated events.

The requirements for a jet to be classed as "good" are that it must have $p_{\text{T}} > 25$ GeV and jet vertex fraction > 0.75, meaning that at least 75% of the p_{T} of the jet must be traceable to a single vertex [1]. Muons must be combined muons (as defined in Section 5.3.1) passing the

[1]The jet vertex fraction (JVF) is the fraction of the total p_{T} of a jet carried by tracks traceable to each primary vertex within an event, i.e. if all tracks originating from one vertex (A) were shared equally between two jets (1 and 2), but the tracks from a second vertex (B), having the same total p_{T}, were contained within one jet (2), then JVF (1,A) = 1 as all the p_{T} contained in jet 1 is in tracks originating from vertex A, however JVF (1,B) = 0 as no tracks originate from vertex B. JVF (2,A) = 1/3 as 1/3 of the p_{T} in jet 2 is held by tracks from vertex B, and JVF (2,B) = 2/3 as 2/3 of the p_{T} in jet 2 came from vertex B.

Table 6.1: Event Selection requirements in the μ+jets channel for a simulated dataset of $t\bar{t}$ events. When the event selection is performed on the $t\bar{t}$ MC sample, 569999 events pass all nine requirements.

Cut	Requirement
0	Event passes correct triggers (`EF_mu18_medium1` or `EF_mu18`)
1	Primary Vertex has at least 4 tracks
2	At least one muon
3	Exactly one muon
4	No good electrons
5	Require trigger matching
6	Remove events with e/μ overlap
7	Reject the event if there is a `LooseBad` jet
8	At least two good jets
9	At least three good jets

"tight" selection [2], and be found within the $|\eta| < 2.5$ range. Overlap removal is performed by removing events in which a selected electron and muon share the same reconstructed track in the inner detector (the reconstructed electron and muon tracks are separated by $\Delta R < 0.01$). If the muon has indeed been produced by the decay of a W boson, it is expected to be isolated, and so a requirement is made that the reconstructed muons pass isolation requirements [3] and that the muons be separated from any good jet by at least $\Delta R = 0.4$. The electron+jets event selection used for the $t\bar{t}$ cross section analysis in Chapter 8 is similar, except that exactly one good electron and no good muons are required. The event selection is covered in more detail in Section 8.2. An additional veto is applied to the invariant mass of the muon from the decay of the W boson and the SMT muon coming from the tagged b-jet in the μ+jets channel to remove contributions from Υ and Z decaying to $\mu^+\mu^-$. The mass vetoes applied are 8 GeV $\leq m_{\mu\mu} \leq$ 11 GeV and 80 GeV $\leq m_{\mu\mu} \leq$ 100 GeV respectively.

6.1.1 Isolation Variables

Used as a measure of the isolation of a particle, etcone20 is the transverse energy deposited in the calorimeter in a cone of $\Delta R < 0.2$ around the particle, which is assumed to occupy a cone of $\Delta R < 0.1$ within this outer cone. The other isolation measures used in this thesis are: etcone30 and etcone40, which are equivalent to etcone20 but use cones of $\Delta R < 0.3$ and 0.4 respectively;

[2] The definitions of the quality cuts for electrons and muons can be found in Appendix C.

[3] Specifically, the muons are required to have etcone20$<$ 4 GeV and ptcone30$<$ 2.5 GeV, as will be defined in Section 6.1.1.

ptcone20, ptcone30 and ptcone40, which are the sums of the transverse momenta of all tracks of $p_{\text{T}} > 1$ GeV in cones of the same three sizes around a particle; nucone20, nucone30 and nucone40, which are the numbers of tracks found in the cones around the particle.

6.2 Branching Ratios

The BR of $b \dashrightarrow \mu$ is expected to be $21.0 \pm 1.0\%$, as shown in Section 5.3. Approximately half of the muons are expected to be produced from direct $b \to \mu$ decays, and half from sequential $b \to c \to \mu$. The BR is defined as the number of muons produced from $t \to b \to \mu$ decays, divided by the number of b quarks produced from $t \to b$. The BR is also found using only those muons which have $p_{\text{T}} > 4$ GeV and $|\eta| < 2.5$, which are said to pass the muon acceptance cuts. Muons are only reconstructed in the $|\eta| < 2.5$ region due to the coverage of the ID. The p_{T} requirement reflects the very low reconstruction efficiency below 4 GeV, caused by energy deposition in the calorimeter systems which lie in between the MS and ID. Low p_{T} muons do not have sufficient momentum to traverse the calorimeter systems and leave tracks in the MS, allowing a combined muon to be reconstructed. This cut is also put in place as is greatly reduces the contribution of muons from background light-jet decays - the p_{T} distributions of true "soft" muons (from $t \to b \to \mu$ decays), "hard" ($t \to W \to \mu$) and all other muon sources ("background") are shown in Figure 6.1. The cut at 4 GeV greatly enhances the proportion of soft and hard muons in the sample while dramatically reducing the background.

The two BRs are shown in Figure 6.2 - the mean BR across all p_{T} with no acceptance cuts is $21.48 \pm 0.04\%$, which agrees with the expected number of $21.0 \pm 1.0\%$ [6]. In the $t\bar{t}$ cross section analysis using the χ^2_{match} based soft muon tagger (discussed in Chapter 8), the individual BRs in simulation are reweighted so that they agree with the world averages quoted by the PDG [6]. However, as the BR found here is inclusive of all decay channels ($b \to \mu$, $b \to c \to \mu^+$, $b \to \bar{c} \to \mu^-$ and $b \to \tau \to \mu$), the ratio between the simulation and world average BR is $1.00 \pm 0.05\%$ [2], so the reweighting has little effect on the inclusive $b \dashrightarrow \mu$ BR. The simulation and world average BRs are shown in Table 6.2.

When the p_{T} and $|\eta|$ muon acceptance requirements are imposed a dependence is observed with respect to the p_{T} of the b quark. The BR is low at low b quark p_{T} values, rising towards the expected ratio at higher values of the quark p_{T}. This can be explained as the majority of

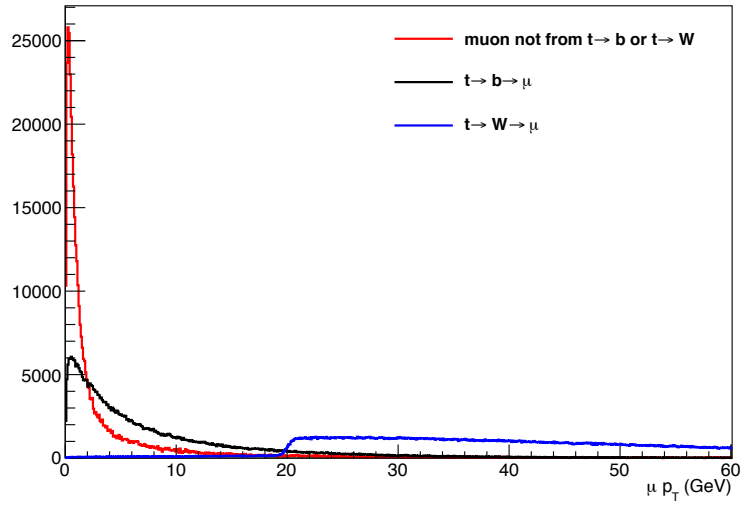

Figure 6.1: Distribution of p_{T} for all muons in the $t\bar{t}$ MC sample. The integrals of the distributions have been scaled to be equal to one another below 60 GeV.

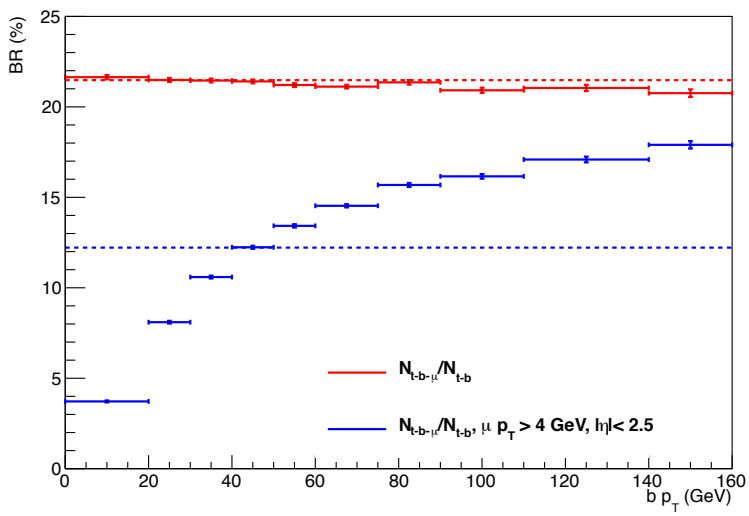

Figure 6.2: BR of $(t \to b \to \mu)/(t \to b)$, with respect to the p_{T} of the b quark, with and without acceptance cuts on the muon. The dashed lines represent the mean values across all p_{T}.

Table 6.2: Comparison of BR (in percent) between measured values and those found in the MC@NLO+Herwig sample of simulated data for various decays of b quarks producing muons . "PDG" indicates [6].

Source	PDG	MC@NLO+Herwig	Ratio
$b \to \mu$	$10.95 \pm 0.29\%$	$9.57 \pm 0.03\%$	1.14 ± 0.03
$b \to \tau \to \mu$	$0.42 \pm 0.04\%$	$0.70 \pm 0.02\%$	0.60 ± 0.06
$b \to c \to \mu^+$	$8.02 \pm 0.19\%$	$8.24 \pm 0.03\%$	0.97 ± 0.02
$b \to \bar{c} \to \mu^-$	$1.60 \pm 0.50\%$	$2.51 \pm 0.02\%$	0.64 ± 0.20
Total BR	$21.0 \pm 1.0\%$	$21.0 \pm 0.1\%$	1.00 ± 0.05

muons from b quarks with lower p_{T} values will not pass the muon acceptance cut, with this effect lessening as the b quark p_{T} increases. Above 70 GeV there are far fewer events, but most muons have p_{T} in excess of the muon acceptance requirement, as shown in Figures 6.3 and 6.4.

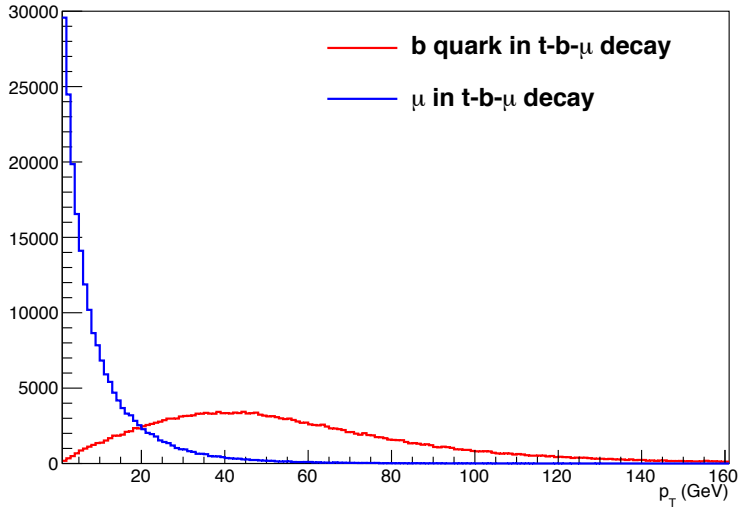

Figure 6.3: Comparison of the p_{T} of b quarks produced from $t \to b \to \mu$ decays in the $t\bar{t}$ MC sample, and of the muons produced from $t \to b \to \mu$

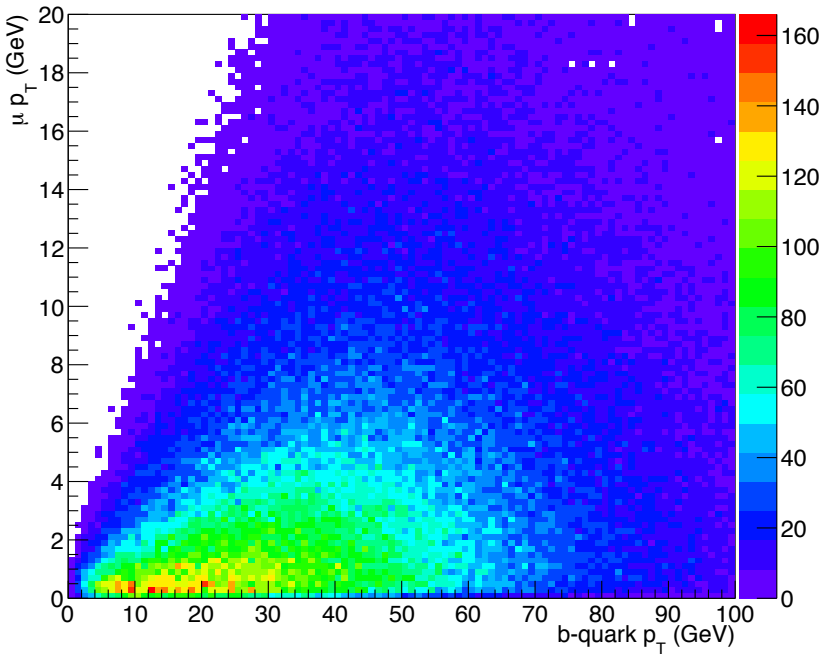

Figure 6.4: Distribution of the p_{T} of b quarks produced from t decays, and of muons produced from $t \to b \to \mu$

6.3 Characterising the b-tagging Efficiency

The b-tagging efficiency discussed in Chapter 5 is the most important characteristic of the performance of the soft muon tagger. In order to find the b-tagging efficiency in a simulated event, firstly all muons produced as the result of $t \to b \to \mu$ decays are identified using the Monte Carlo truth record. Next, any SMT reconstructed jets are identified and the kinematic variables of the reconstructed muon within the tagged jet are stored. The "unmatched" b-tagging efficiency (ε_b^u) is defined as the ratio of all SMT tagged muons to the total number of $t \to b \to \mu$ decays - it assumes that all SMT tagged muons do in fact originate from $t \to b \to \mu$ (Equation 6.1).

To find the "matched" b-tagging efficiency (ε_b^m), the SMT reconstructed muons are compared with those found in the truth record - the reconstructed tagged muon is said to be matched with the truth muon if the ΔR between them is less than 0.01. These matched SMT muons make up the numerator in Equation 6.3. In the event that there is more than one truth muon in an event, the truth muon closest to the tagged muon is selected. In the Monte Carlo $t\bar{t}$ sample used, the maximum number of $t \to b \to \mu$ observed in a single event is two, as might be expected from two top quarks decaying via the μ+jets channel.

The inclusive b-tagging efficiencies ($\varepsilon_{b,incl}$) take into account the BR of $b \to \mu$, meaning that the denominator of the efficiencies is the number of $t \to b$ decays. The unmatched and matched inclusive b-tagging efficiencies, $\varepsilon_{b,incl}^u$ and $\varepsilon_{b,incl}^m$ (Equations 6.2 and 6.4), correspond to the mean values across all b quark p_{T} shown in Figure 6.5. The difference between $\varepsilon_{b,incl}^u$ and $\varepsilon_{b,incl}^m$ can be accounted for by the fact that some SMT muons do not correspond to truth muons from $t \to b \to \mu$ - the sources of these "fake" SMT muons are investigated in Section 6.4. Using the preselected events defined in Section 6.1, the following b-tagging efficiencies are found:

$$\varepsilon_b^u = \frac{\text{Number of SMT reconstructed muons}}{\text{Number of true muons from } t \to b \to \mu} = 39.63 \pm 0.10\% \tag{6.1}$$

$$\varepsilon_{b,incl}^u = \frac{\text{Number of SMT reconstructed muons}}{\text{Number of true } b \text{ quarks from } t \to b} = 8.51 \pm 0.03\% \tag{6.2}$$

$$\varepsilon_b^m = \frac{\text{Number of SMT muons matched to truth muons}}{\text{Number of true muons from } t \to b \to \mu} = 33.41 \pm 0.10\% \tag{6.3}$$

$$\varepsilon_{b,incl}^m = \frac{\text{Number of SMT muons matched to truth muons}}{\text{Number of true } b \text{ quarks from } t \to b} = 7.18 \pm 0.02\% \tag{6.4}$$

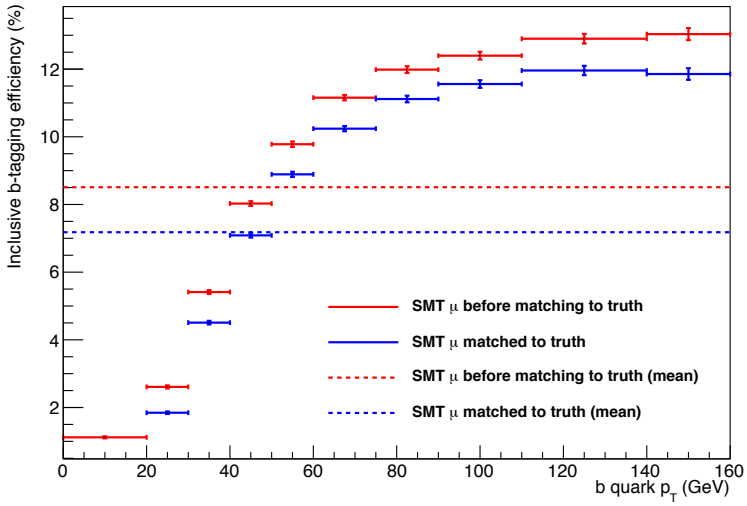

Figure 6.5: Inclusive b-tagging efficiency, for all SMT muons and only those matched to a true muon from $t \to b \to \mu$. The dashed lines represent the mean values across all p_{T}.

6.3.1 Efficiency of the Individual χ^2_{match} based SMT Cuts

The efficiencies of the cuts which make up the χ^2_{match} based soft muon tagger are found by applying them individually to the reconstructed muons. The cuts applied, in order, are:

1. Does the reconstructed muon pass the MCP quality cuts?
2. Is the reconstructed muon not within $\Delta R < 0.01$ of a vetoed muon from $t \to W \to \mu$?
3. If the tagged jet is to be matched to truth information, both the following must be satisfied:
   - Is there a reconstructed muon within $\Delta R < 0.01$ of the true muon from $t \to b \to \mu$?
   - Is there a good jet within $\Delta R < 0.4$ of the b quark?
4. Is the $\Delta R(\text{reco } \mu, \text{jet}) < 0.5$?
5. Does the reconstructed muon have $p_{\text{T}} > 4$ GeV and $|\eta| < 2.5$?
6. Is the reconstructed muon $|d_0| < 3$mm and $|z_0 \cdot \sin\theta| < 3$mm?
7. Is the reconstructed muon $\chi^2_{\text{match}} < 3.2$?

The results of these cuts on the preselected events are shown in Table 6.3 in the case where all reconstructed muons are considered as potential SMT muons, and Table 6.4 for the case

where the muon and b quark in the $t \to b \to \mu$ decay are matched to reconstructed muons and jets before the cuts are applied. A comparison is made between the number of reconstructed muons that pass all the individual cuts and the SMT tagged reconstructed muon, which has been tagged within the event selection code. This serves as a cross check that the SMT is implemented correctly. The expectation is that the number of reconstructed muons passing stage (7) above will be equal to the number of reconstructed muons within soft muon tagged jets. The highlighted efficiencies in Tables 6.3 and 6.4 correspond to those shown above in Equations 6.1 to 6.4.

Table 6.3: Efficiency of the individual cuts within the SMT Tagger, without truth matching. The uncertainties on the efficiencies quoted here are statistical only.

Cut	% of previous	% of $t \to b \to \mu$	% of $t \to b$
All $t \to b$ in dataset			100.00
All $t \to b \to \mu$ in dataset	21.48	100.00	21.48
Reco. muon passes MCP quality cuts	90.48	90.48	19.43
Reco. muon is not matched to a vetoed $t \to W \to \mu$	99.84	90.34	19.40
$\Delta R(\text{reco}\ \mu, \text{jet}) < 0.5$	56.86	51.37	11.03
Reco. muon $p_{\text{T}} > 4$ GeV and $\lvert\eta\rvert < 2.5$	84.48	43.40	9.32
Reco. muon $\lvert d_0\rvert < 3$mm and $\lvert z_0 \cdot \sin\theta\rvert < 3$mm	99.72	43.28	9.29
Reco. muon $\chi^2_{\text{match}} < 3.2$	91.57	39.63 ± 0.10	8.51 ± 0.02
All SMT tagged muons (ε_b^u)		$\mathbf{39.63 \pm 0.10}$	$\mathbf{8.51 \pm 0.02}$

Table 6.4: Efficiency of the individual cuts within the SMT Tagger, with truth matching. The uncertainties on the efficiencies quoted here are statistical only.

Cut	% of previous	% of $t \to b \to \mu$	% of $t \to b$
All $t \to b$ in dataset			100.00
All $t \to b \to \mu$ in dataset	21.48	100.00	21.48
Reco. muon passes MCP quality cuts	90.48	90.48	19.43
Reco. muon is not matched to a vetoed $t \to W \to \mu$	99.84	90.34	19.40
$\Delta R(\text{good jet}, b \text{ from } t \to b) < 0.4$		69.46	14.92
$\Delta R(\text{reco}\ \mu, \mu \text{ from } t \to b \to \mu) < 0.01$		57.54	12.36
$\Delta R(\text{jet}, b) < 0.4$ and $\Delta R(\text{reco}\ \mu, \mu) < 0.01$	49.59	44.80	9.62
$\Delta R(\text{reco}\ \mu, \text{jet}) < 0.5$	96.65	43.30	9.30
Reco. muon $p_{\text{T}} > 4$ GeV and $\lvert\eta\rvert < 2.5$	84.69	36.67	7.88
Reco. muon $\lvert d_0\rvert < 3$mm and $\lvert z_0 \cdot \sin\theta\rvert < 3$mm	99.69	36.56	7.85
Reco. muon $\chi^2_{\text{match}} < 3.2$	91.38	33.41 ± 0.10	7.18 ± 0.02
SMT tagged muons matched to $t \to b \to \mu$ (ε_b^m)		$\mathbf{33.41 \pm 0.10}$	$\mathbf{7.18 \pm 0.02}$

The effects of the individual cuts on ε_b^m can be seen in Figure 6.6, which shows the efficiency of matching a reconstructed muon to the muon from $t \to b \to \mu$, and the efficiency when the reconstructed muon is required to pass some of the cuts listed above. The reconstructed muon and the jet within which it is found have been matched to truth muons and b quarks respectively before the other cuts are applied, so the explicit effects of the $\Delta R(\text{reco}\ \mu, \text{jet}) < 0.5$ requirement, the $t \to W \to \mu$ veto and the MCP quality cuts are not shown in these plots.

It can be seen that the largest reduction in efficiency from the muon only cuts is due to the muon p_{T} and $|\eta|$ requirements, as these have the largest effect on the low p_{T} muons coming from lower p_{T} b quarks, as shown in Figure 6.4. The $|\eta|$ part of this requirement has a minimal effect, as all reconstructed muons lie in the $|\eta| \leq 2.5$ region by definition. Tables 6.3 and 6.4 show that $< 85\%$ of matched and unmatched reconstructed muons pass the combined p_{T} and $|\eta|$ requirements.

The impact parameter requirements have very little effect indeed, excluding $\approx 0.3\%$ of the reconstructed muons passing the muon acceptance cuts. The impact parameter cuts are tightened to $|d_0| < 2\text{mm}$ and $|z_0 \cdot \sin\theta| < 2\text{mm}$ to verify that these cuts have very little effect (the tighter cut is removed before the χ^2_{match} cut is applied).

The $\chi^2_{\text{match}} < 3.2$ requirement, the final and most important part of the soft muon tagger, rejects approximately 8% of the muons passing the previous requirements. The p_{T} and impact parameter cuts have already removed a large amount of the background to the soft muon signal, removing most low p_{T} muons from the decay of light hadrons and restricting the impact parameter range to that of the flight length ($c\tau$) of b and c hadrons. The χ^2_{match} cut serves to further reduce the contribution from both true and fake muons from light jets, as was shown in Figure 5.8(b).

The increased gradient in the lower p_{T} region and the overall reduction in efficiency of Figure 6.6(b) when compared to Figure 6.6(a) can be attributed to the shape of the BR curve in Figure 6.2, when the muon acceptance cuts are put in place. This shape, when multiplied by the curves in Figure 6.6(a), leads to the curves seen in Figure 6.6(b).

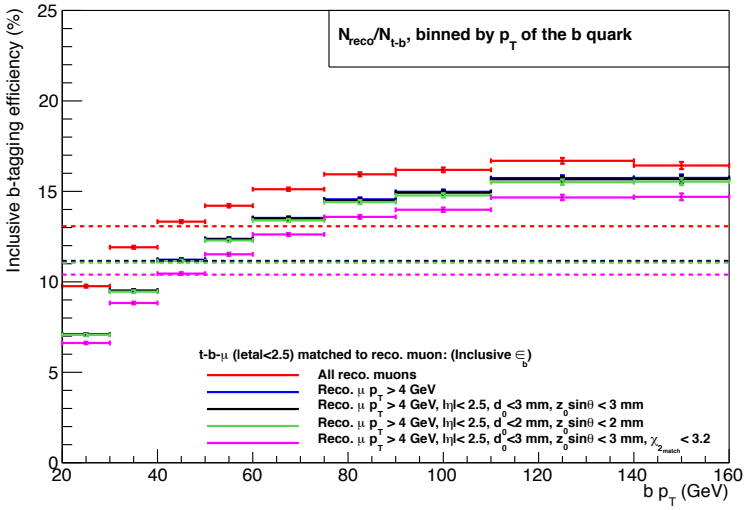

(a) Inclusive ($N_{\text{reco}\,\mu}/N_{t\to b}$)

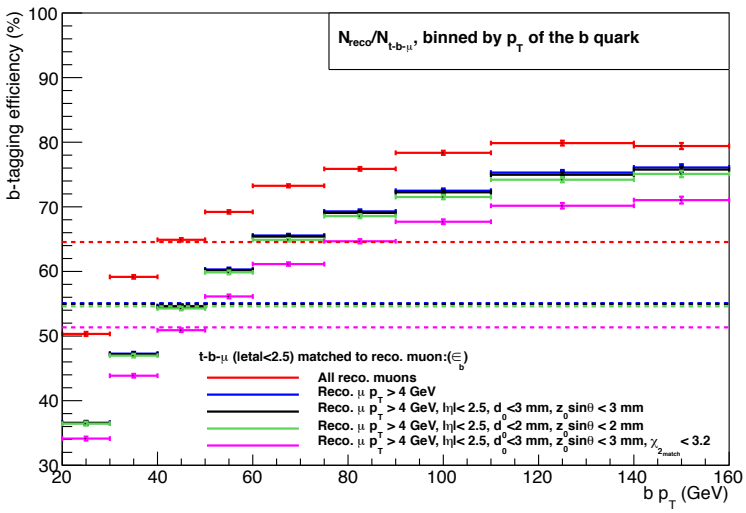

(b) $N_{\text{reco}\,\mu}/N_{t\to b\to\mu}$

Figure 6.6: b-tagging efficiencies binned by the p_{T} of the b quark produced via $t \to b$. The dashed lines represent the mean values across all p_{T}.

6.3.2 Dependence of the b-tagging Efficiency on the p_{T} of b quarks and b-jets

The χ^2_{match} based soft muon tagger is intended for use in any situation where the identification of b-jets is required, and in other analyses the p_{T} distribution of the jets may be different to that of the b-jets produced in the decay of $t\bar{t}$ pairs. It is therefore important to investigate the dependence of the b-tagging efficiency on the p_{T} of the reconstructed b-jet.

Figure 6.7 shows the impact of the same cuts as applied in Figure 6.6, however in this case the requirement is made that a "good" jet be found within $\Delta R < 0.4$ of the b quark (the truth b quarks in the denominators of the efficiencies, either all b quarks from $t \to b$ or the b quarks in the $t \to b \to \mu$ decay). Only 69.46% of b quarks are matched to good jets, as seen in Table 6.4. This is in part due to the fact that all b quarks matched to jets with $p_{\text{T}} < 25$ GeV are excluded by the good jet requirement.

The distributions of the b-tagging efficiencies with respect to the p_{T} of the b quark and to that of the reconstructed jet matched to the b quark (Figure 6.7) are quite different; to understand this variation it is necessary to look at the efficiency of the reconstruction algorithms to reconstruct a jet from a true b quark ($\varepsilon^{(b,\text{jet})}_{\text{match}}$), meaning the percentage of true hadronic jets produced from the decay of b quarks which are reconstructed as b-jets. The b-tagging efficiencies are subject to $\varepsilon^{(b,\text{jet})}_{\text{match}}$. This efficiency is found both for the b quarks in $t \to b \to \mu$ decays and for all b quarks produced from the decay of a top quark.

The ratio of these efficiencies, with respect to the jet p_{T}, is effectively a combination of the BR($t \to b \to \mu$)/($t \to b$) and the b-jet reconstruction efficiency. This ratio, shown in Figure 6.8, can be applied to the distributions in Figure 6.6(b) to produce those in Figure 6.7(a). In the same way, the mean value of ε_b with respect to the p_{T} of the b quark can be multiplied by the mean value of the ratio of efficiencies, which approximately gives the mean value of $\varepsilon_{b,incl}$ with respect to the p_{T} of the reconstructed jet matched to the b quark [4]:

$$\begin{aligned} \varepsilon_b \text{ w.r.t. } p_{\text{T}}(b) \times \frac{\varepsilon^{(b,\text{jet})}_{\text{match}} \text{ for } t \to b \to \mu}{\varepsilon^{(b,\text{jet})}_{\text{match}} \text{ for } t \to b} &\approx \varepsilon_{b,incl} \text{ w.r.t. } p_{\text{T}}(\text{jet}) \\ 52.42 \pm 0.10\% \times 19.70 \pm 0.04\% = 10.32 \pm 0.14\% &\approx 10.70 \pm 0.08\% \end{aligned} \tag{6.5}$$

[4] ε_b w.r.t. $p_{\text{T}}(b)$, $\varepsilon_{b,incl}$ w.r.t. p_{T}(jet) and the ratio of $\varepsilon^{(b,\text{jet})}_{\text{match}}$ for $t \to b \to \mu$ to that for $t \to b$ correspond to the red dashed lines in Figures 6.6(b), 6.7(a) and 6.8 respectively.

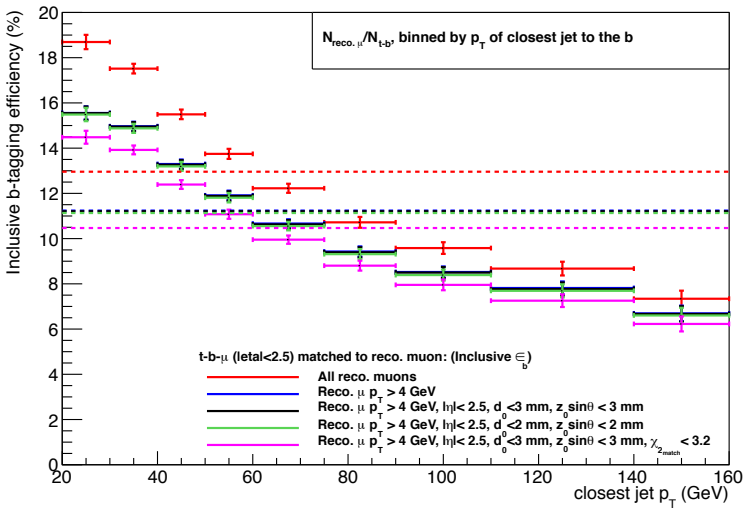

(a) Inclusive ($N_{\text{reco}\,\mu}/N_{t\to b}$)

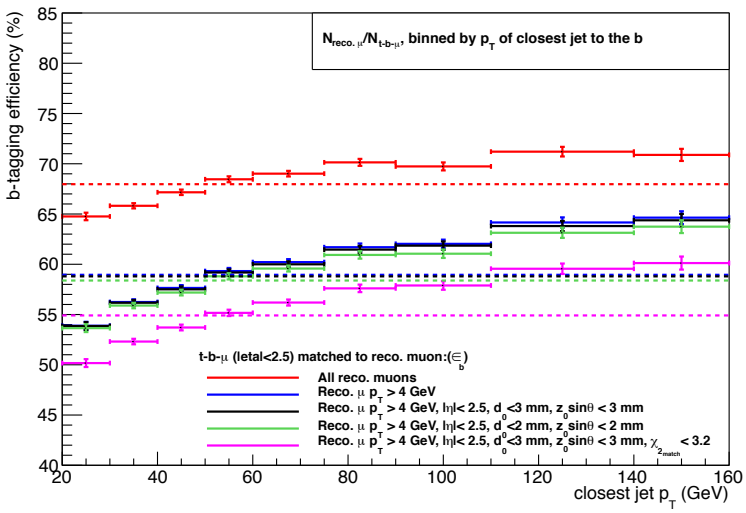

(b) $N_{\text{reco}\,\mu}/N_{t\to b\to\mu}$

Figure 6.7: b-tagging efficiencies binned by the p_{T} of the closest jet to the b quark produced via $t \to b$. The dashed line represents the mean value across all p_{T}.

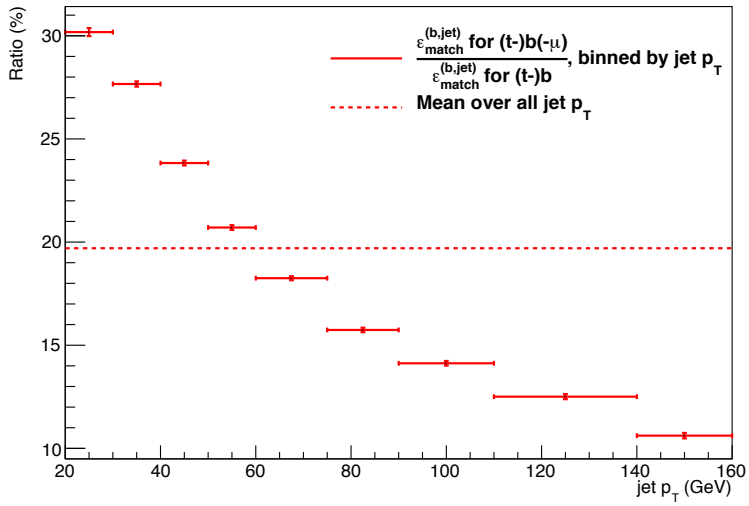

Figure 6.8: The ratio of the fraction of jets matched to the b quark in a $t \to b \to \mu$ decay to the fraction of jets matched to all b quarks produced from the decay of a top quark, binned by the p_{T} of the closest jet to the b quark. This is effectively a combination of the BR$(t \to b \to \mu)/(t \to b)$ and the b-jet reconstruction efficiency. The dashed lines represent the mean values across all p_{T}.

Comparing Figures 6.2 and 6.8, it can be seen that if the BR is found using the reconstructed jets instead of the true b quarks, the trend is reversed, in that the ratio of $t \to b \to \mu$ decays to all $t \to b$ decreases with p_{T}. The reason for this difference is that in $t \to b \to \mu$ decays the jet p_{T} is often lower than that of the b quark, and there is poor resolution in the p_{T} matching as can be seen in Figure 6.9. The resolution is improved in the case of all $t \to b \to \ell$ decays (Figure 6.10), and also when it is required that the $t \to b$ decay does not result in a lepton, as shown in Figure 6.11. The dashed lines indicate the points where the p_{T} of the jet is equal to that of the b quark, and are included to show the bias in the reconstructed p_{T}. The p_{T} of the reconstructed jet is expected to be lower than that of the true b quark in the case of the semileptonic b decay, as there is a neutrino produced which is a source of missing E_{T} and is not reconstructed as part of the jet. For comparison, Figure 6.12 shows that in the case of reconstructing the muons, the p_{T} of the truth muons is well reconstructed.

The result of this is that while the overall efficiency across all b quark p_{T} does not vary greatly from the efficiency over all jet p_{T}, the efficiency in the individual bins of each efficiency can show large differences, as the same reconstructed muons matched to truth muons could be placed in different p_{T} bins in each of the two plots.

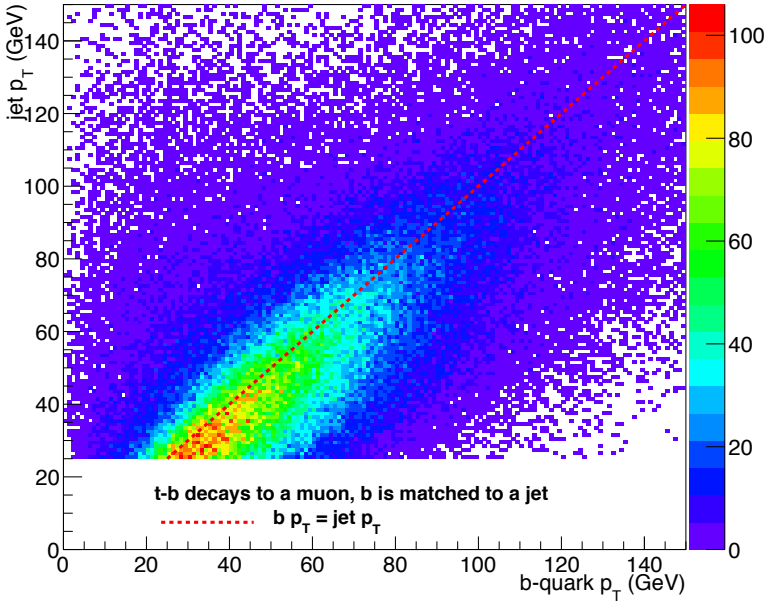

Figure 6.9: Comparison of the p_{T} of b quarks with that of their reconstructed jets, for all $t \to b \to \mu$ decays.

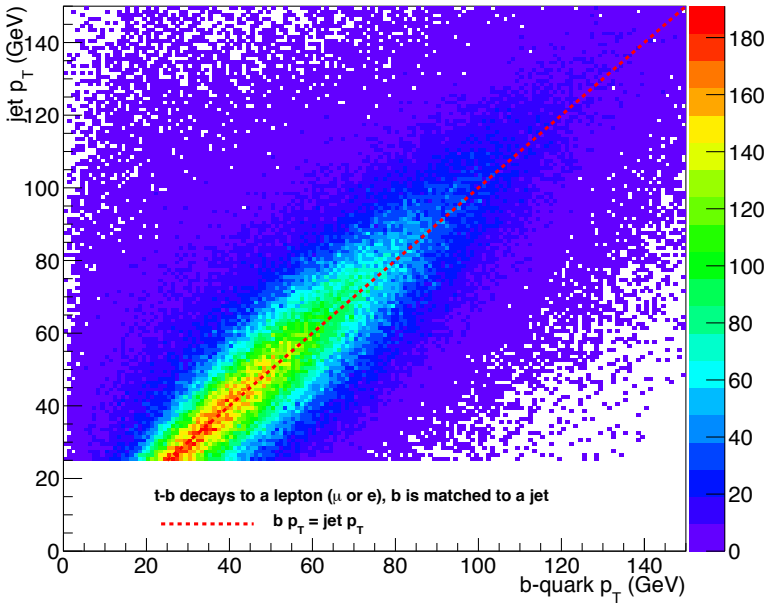

Figure 6.10: Comparison of the p_{T} of b quarks with that of their reconstructed jets, for all $t \to b \to \ell$ decays.

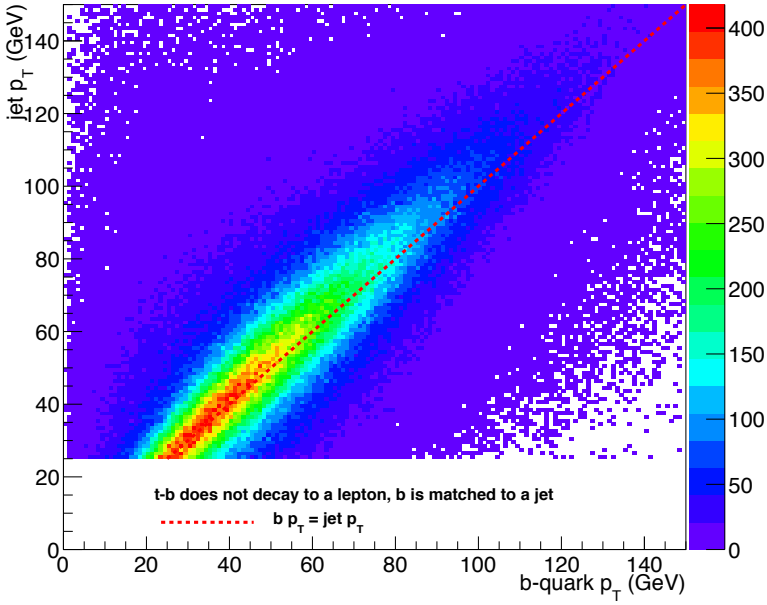

Figure 6.11: Comparison of the p_{T} of b quarks with that of their reconstructed jets, for all $t \to b$ decays in which the b does not decay to a lepton.

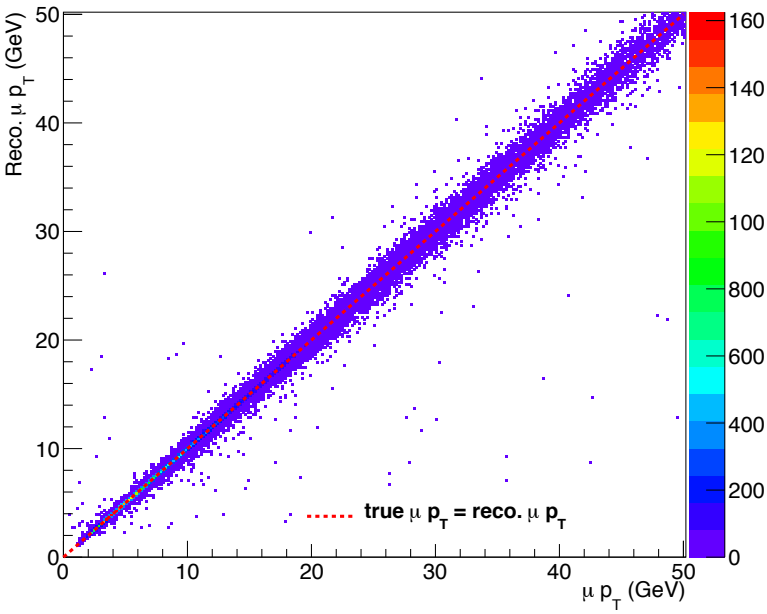

Figure 6.12: Comparison of the p_{T} of true muons with that of reconstructed muons matched to them, for all muons from $t \to b \to \mu$ decays.

There is a reconstruction agorithm used within ATLAS which attempts to label jets with the flavour of the truth particle from which they originate. This is not used in the characterisation of the χ^2_{match} based SMT, but Appendix D contains a brief description of the labelling method, and the dependence of $\varepsilon_{b,incl}$ found using jets labelled as originating from b quarks.

6.3.3 Jet Energy Scale

The difference in the p_{T} of b quarks and jets is related to the Jet Energy Scale (JES) calibration. In the reconstruction process, there are some detector effects which cause the energy of a hadronic jet to be inaccurately modelled [77], which results in the energy of the reconstructed jet being lower than that of the truth jet. The JES is found using simulated data and applied to reconstructed jets so that the jet energy accurately reflects the energy of the stable truth particles in the ATLAS detector. The JES is calibrated to give a correct measurement of the average energy across the entire detector, and must be independent of other events occurring within the detector at the same time (pile-up). In the EM+JES calibration scheme [77] the JES calibration is found using the ECal response to events at the electromagnetic (EM) energy scale, and this is then calibrated in data to find the correction factor. The central value of the correction is found from simulation at hadronic jet energies, and the correction factor found at the EM scale is applied to the reconstructed energy of jets based on their energy and pseudorapidity.

The reconstructed jets used in the characterisation of the χ^2_{match} based SMT have had the b-jet specific JES applied, however the JES only corrects jet energies so that the average b-jet energy across an event is correct. In ATLAS, a specific JES correction for semileptonic b decays is not yet available, and the fact that the resultant b-jet contains a neutrino means that the corrected jet energies will still be underestimates of the true b-jet energies. A correction factor can be found [4] by comparing the p_{T} of truth particles to the calorimeter response (i.e. the reconstructed jet p_{T}) to all b-jets and to those including a $b \to \mu\nu$ decay. This correction is applied in Section 8.4, but not used in the characterisation.

6.4 Establishing the Sources of "Fake" Muons

In Section 6.3, the truth matching was mentioned - after the matching takes place, it is important to establish the source of those reconstructed muons which are incorrectly tagged by the χ^2_{match} based SMT ("fakes"). In a similar manner to the matching of tagged muons with true muons from $t \to b \to \mu$ decays, if there is no true $t \to b \to \mu$ muon within $\Delta R < 0.01$ of the SMT muon then the SMT muon will be matched to the nearest true muon from any source within $\Delta R < 0.01$, which counts as a fake. The source of this fake can then be established. In the case where there is no true muon within the $\Delta R < 0.01$ cone around the SMT muon, the nearest truth Monte Carlo particle is chosen. The only remaining option is that there is no truth particle at all within $\Delta R < 0.01$. The SMT muons are matched to truth particles as shown in Table 6.5.

Table 6.5: The SMT muons are ΔR matched to truth particles in the simulated data sample.

Particle matched to the SMT muon, and the source of that particle	% of all SMT muons
True muons from $t \to b \to \mu$	83.9
True muons from other sources	10.2
Non-muons (π, K etc.)	5.7
No truth particle within $\Delta R < 0.01$	< 0.2

The true muons from non $t \to b$ sources are found to be distributed as shown in Table 6.6. The main source of fakes is the decay of $t \to W \dashrightarrow \mu$, constituting 89.54% of all true muons not from $t \to b \to \mu$ which are matched to SMT muons. Decays of $t \to W \dashrightarrow \mu\bar{\nu}_\mu$ with no hadrons in the decay chain account for 28.84% of fakes, with a small number of cases (just over 4% of all fakes) in which the W decays to a τ lepton before decaying to the muon, via the chain $W \to \tau\bar{\nu}_\tau \to \mu\bar{\nu}_\mu\nu_\tau\bar{\nu}_\tau$. The decay of $t \to W \to X_c \to \mu\bar{\nu}_\mu$ makes up 60.70%. In these cases the muon has been correctly tagged as being from the decay of a heavy flavour hadron, however the origin of this jet is not a b. The same is true for the small remainder (10.47%), which are muons produced from the decay of $X_b \to \mu$ and $X_c \to \mu$, where the X_b and X_c hadrons have been produced from the partons in the original collision within the event [5], with no top quark or W boson in the decay chain.

Of the 5.9% of the SMT tagged muons which are not matched to a truth muon, the vast ma-

[5] Table E.1 in Appendix E shows the full decay chain of a sample of each of the channels shown in Table 6.6. This is included as a verification that the method used to identify the sources of mistagged muons is doing so correctly.

Table 6.6: Decay chain of muons not from $t \to b$, matched to SMT muons (using the preselected events).

Decay chain of muon	Number	% of all true μ (non $t \to b \to \mu$)	% of all fakes
All μ not from $t \to b \to \mu$	9533	100.00	62.45
$t \to W \to X_c \to \mu$	5786	60.70	37.91
$t \to W \to \mu$	2749	28.84	18.01
$X_c \to \mu$	464	4.87	3.04
$X_b \to \mu$	312	3.27	2.04
$X_b \to X_c \to \mu$	198	2.08	1.30
$t \to X_c \to \mu$	24	0.25	0.16

Table 6.7: Non muon truth particles matched to SMT muons (using the preselected events).

Particle	Number of particles	% of all true non μ	% of all fakes
All SMT μ not matched to truth μ	5732	100.00	37.55
π^+ or π^-	4136	72.16	27.09
K^+ or K^-	1315	22.94	8.61
photon	40	0.70	0.26
p or $\bar{p}$	23	0.40	0.15
s baryon	6	0.10	0.04
K^0_S	6	0.10	0.04
K^0_L	3	0.05	0.02
No particle matched to SMT μ	203	3.54	1.33

jority (95.1%) are matched to π^+, π^-, K^+ or K^- and only 78 SMT muons (1.3%) are matched to other true particles, shown in Table 6.7. The majority of these events can be explained by hadronic punch-through; this is a phenomenon whereby some hadrons interact late in their journey through the detector, interacting with the detector material and producing showers of particles which progress through to the MS. Also not all hadrons are stopped in the HCal, and some then go on to leave tracks in the MS meaning that they are reconstructed as muons instead of hadrons. In 3.54% of cases in which the SMT muon cannot be matched to a truth muon, there is in fact no true final state particle within $\Delta R < 0.01$ of the tagged muon.

6.5 Calibration using Collision Data

The studies performed in this section make use of a simulated dataset of $t\bar{t}$ events, effectively a sample of signal events only. As such, the characterisation presented here is of limited use in terms of analysis on collision data, as the detector simulation in Monte Carlo is not perfect and cannot be relied upon exclusively for efficiency and performance values. What is required is calibration of the χ^2_{match} based soft muon tagger using data to find the efficiency and mistag rates, which can then be used in conjunction with simulation to find a data/MC scale factor which can be applied to the simulated events. Calibration of the efficiencies in simulated and collision data is described in detail in Chapter 7, while a brief overview of work on the mistag rate is given in Section 7.3.

Chapter 7

Calibration of the χ^2_{match} based Soft Muon Tagger using $J/\psi \to \mu\mu$ events in Collision Data

The characterisation of the χ^2_{match} algorithm in Chapter 6 makes use of a simulated version of the ATLAS detector and its reconstruction capabilities. The simulation can not be relied upon to perfectly reproduce conditions within the detector, and so the muon reconstruction and the effect of the χ^2_{match} requirement must be calibrated using collision data.

As mentioned in Section 5.4.4, one of the advantages of the χ^2_{match} algorithm over other soft muon tagging methods is that the presence of a jet is not required in order to measure the χ^2_{match} of a muon. Consequently, the χ^2_{match} efficiency can be measured using samples of isolated muons, such as those produced in the decays of $J/\psi \to \mu\mu$ and $Z \to \mu\mu$. As χ^2_{match} is a characteristic of combined muons only, it is necessary to find the muon reconstruction efficiency before the χ^2_{match} soft muon tagging efficiency can be determined. Collision data/Monte Carlo simulation scale factors for these efficiencies are also measured, which are required in order to find the $t\bar{t}$ cross section. The efficiencies and scale factors are found using a tag and probe method, as described in Section 7.1.

Software, Collision Data and Simulated samples

The tag and probe method used here is based on a modified version of existing software packages, developed for use in the analysis in [78], running in the ATHENA software framework.

For the analysis of 2011 data, the dataset used is composed of those luminosity blocks from the Muons stream of collision data which are included in the chosen Good Runs List (GRL) as recommended by the Muon Combined Performance Group. The GRL includes only those luminosity blocks where all relevant parts of the detector were operational (the toroid, SCT, etc.). The exact requirements of the GRL are listed in Table 7.1.

The 2011 autumn processing of periods "B2" to "M" is used, corresponding to data taken between the 22nd of March and the 30th of October (see Table 4.1) [1]. The simulated data sample (Monte Carlo) contains 5 million direct $J/\psi \to \mu\mu$ events, generated using the Pythia generator [62]. For all simulated data, at the generator level a requirement is made that the absolute value of the pseudorapidity ($|\eta|$) of the muons be less than 2.5, and that the transverse momentum (p_T) must be greater than 4 GeV - these are the muon acceptance cuts defined in Section 6.2.

Table 7.1: Data quality requirements included in the muon channel good runs list for all 2011 data [46].

GRL Requirement	Description
ptag `data11_7TeV`	Dataset name contains project tag `data11_7TeV`
DQ `global_status`	ATLAS status is ready for data taking
DQ `atlsol`	Solenoid is on and current is stable
DQ `atltor`	Toroid magnet is on and current is stable
DQ `trig_muo`	Muon triggers are running
DQ `cp_mu_mmuidcb`	No known issues with the muid muon reconstruction algorithm
DQ `cp_mu_mstaco`	No known issues with the STACO muon reconstruction algorithm
DQ `idvx`	ID vertex finding algorithms are running
DQ `idbs`	Good beam spot data is available, no known issues
DQ `lumi`	Offline luminosity is OK, luminosity values are reliable

7.1 Tag and Probe with $J/\psi \to \mu\mu$

A tag and probe method has been chosen to measure the muon reconstruction efficiency in both simulated and collision data. This method probes the efficiency of selection criteria, or

[1] Period "B1" is not included as the Toroidal magnetic field was not switched on, so the entire period does not meet the requirements of the GRL.

an algorithm, by making use of the decay products of particles such as Z, J/ψ and Υ (a meson composed of a $b\bar{b}$ pair). These are able to decay into, in the case of J/ψ mesons, two leptons. The branching fractions of $J/\psi \to \mu^+\mu^-$ or e^+e^- are $5.93 \pm 0.06\%$ and $5.94 \pm 0.06\%$ respectively [6]. However, $\approx 73\%$ of J/ψ mesons decay to gluons and the remaining 13.5% decay via virtual photons to hadrons - there are no other known decays which contain a prompt muon, meaning that the detection of one muon in a decay implies the existence of another, with a mass such that the invariant mass of the pair of muons is close to that of the J/ψ. One well reconstructed muon per decay is selected using strict quality cuts, and labelled as the tag muon. As it is likely that there is another muon present in the decay products, the selection of the other muon can be very loose - for example just looking for a track in the inner detector, rather than in both MS and ID. The loosely defined muon is called the probe candidate.

The performance of a selection algorithm is then tested by finding what proportion of the probe candidates are selected by the algorithm. The number of tag and selected probe pairs, divided by the total number of tag and probe pairs, gives the efficiency of the selection.

7.1.1 Choice of Trigger Requirements for the Tag muon

In order to be selected as the tag muon, a candidate particle must pass at least one of the trigger chains [2] listed in Table 7.2 - the reconstructed tag muon must pass through the $\eta - \phi$ region of the MS in which the trigger muon was found (the Region Of Interest, or ROI). The nomenclature of the triggers can be explained as follows - the EF in the names refers to the Event Filter. As explained in Section 4.2.5, the EF uses offline analysis algorithms to reject events which do not pass their selection criteria. In the case of the `EF_mu13_MG_medium` trigger, in accordance with the ATLAS trigger chain naming conventions, the requirements are that the p_{T} of the trigger muon passes a threshold of 13 GeV, reconstructed using the MuonGirl algorithm that requires a track in the ID to be matched to a track segment in the internal muon trigger chambers of the MS. Finally, the "medium" muon identification cuts are applied at the EF. The `EF_mu4T_Trk_JPsi` trigger chain requires the presence of a reconstructed muon with p_{T} greater than 4 GeV, and the muon identification threshold is higher at Level 1 than the non "`T`" version of the trigger ("`_tight`" would have the same meaning) [79]. It also requires that there is an ID track in the event which, when combined with the muon, has an invariant mass between 2850 GeV and 3350 GeV

[2] A trigger chain is an event filter trigger which relies upon an event having already passed specific L1 and L2 triggers.

(approximately the mass of the J/ψ, ± 250 GeV) [46]. EF_mu6_Trk_JPsi_loose, by comparison, has a wider mass window of 2600 MeV $< m_{\text{inv}} <$ 3600 MeV, meaning that when seeking to identify J/ψ pairs, while the former trigger chain made it difficult to fit the background function [3] due to the narrow window around the J/ψ peak, when used in conjunction with the looser chain the window is sufficiently wide to permit an estimate of the background using the sidebands on either side, allowing this to be subtracted in the signal region around the mass of the J/ψ.

The trigger chains are chosen in order to ensure no bias in our preselection in favour of combined muons - triggers such as EF_2mu4_Jpsimumu and EF_2mu4T_Jpsimumu which preselect a pair of muons are not used, as this is likely to bias the reconstruction efficiency by preselecting two reconstructed muon tracks as opposed to a combined muon and an ID only track.

Table 7.2: Trigger requirements for both tag and probe candidates, according to 2011 data period

Period	Run Number	Trigger requested
B2, D & E	$\leq$ 180776	EF_mu13_MG, EF_mu13, EF_mu18_MG, EF_mu18, EF_mu4_Trk_Jpsi
F2-F3	$\leq$ 182519	EF_mu13_MG, EF_mu13, EF_mu18_MG_medium, EF_mu18_medium, EF_mu18_MG, EF_mu18, EF_mu4_Trk_Jpsi
G-K	$\leq$ 187815	EF_mu13_MG, EF_mu13, EF_mu18_MG_medium, EF_mu18_medium, EF_mu18_MG, EF_mu18, EF_mu4_Trk_Jpsi, EF_mu6_Trk_Jpsi_loose
L	$\leq$ 190343	EF_mu13_MG, EF_mu13, EF_mu18_MG_medium, EF_mu18_medium, EF_mu18_MG, EF_mu18, EF_mu4T_Trk_Jpsi, EF_mu6_Trk_Jpsi_loose
M	$\leq$ 191933	EF_mu13_MG, EF_mu13, EF_mu18_MG_medium, EF_mu18_medium, EF_mu18_MG, EF_mu18, EF_mu4T_Trk_Jpsi, EF_mu6_Trk_Jpsi_loose

7.1.2 Selection Cuts for Tag and Probe Candidates

To find the muon reconstruction efficiency, first the tag muons must be selected. In addition to the reconstruction and trigger conditions mentioned above, the tag muon is required to pass the cuts listed in Table 7.3 [4]. The momentum requirements are imposed due to the limited ability of the detector to reconstruct combined muons at low momentum (p) and p_{T}, as such muons are unlikely to be of sufficient energy to traverse the calorimeter systems and leave tracks in the muon spectrometer as mentioned in Section 5.3.1. Similarly the ID only covers the region $|\eta| < 2.5$, so it is required that muons lie within this limit.

[3] The background subtraction method is covered in detail in Section 7.1.4.

[4] These cuts are adapted from the Muon Reconstruction Efficiency note [78] to allow simple comparison with the results in that note as a crosscheck of our reconstruction efficiency results in 2010 data.

The impact parameters d_0 and z_0 are the distances of closest approach of the reconstructed ID track to the primary vertex, in the transverse and longitudinal planes respectively. The d_0 significance is defined as $|d_0/\sigma(d_0)|$, where σ is the standard deviation of the distribution of values of d_0. The z_0 significance is similarly defined. These impact parameter requirements are necessary in order to increase the likelihood of detecting a prompt J/ψ, which is more likely to originate from the primary vertex. Prompt J/ψ particles are produced directly from the proton-proton collision, or from the decay of heavier charmonium states, whereas non-prompt J/ψ are produced from the subsequent decay of b hadrons [80].

Table 7.3: Cuts performed on tag and probe candidates.

Tag muon	Probe candidate
$\lvert\eta\rvert < 2.5$	
Must be a Combined muon	ID Track required
$p_{\text{T}} > 4$ GeV	$p > 3$ GeV
$\lvert d_0\rvert < 0.3$mm	2 GeV $\leq m_{inv}$(tag & probe) $\leq$ 4 GeV
$\lvert z_0\rvert < 1.5$mm	Opposite charge to tag
d_0 significance < 3	ΔR (tag & probe) < 3.5
z_0 significance < 3	Common vertex: $\chi^2 < 6$

The probe candidate is only required to have a good ID track [5] associated with it, and to have a momentum greater than 3 GeV. In order to make a tag and probe pair, it is required that the invariant mass of the pair lies within $\approx \pm 1$ GeV of 3096.916 ± 0.011 MeV, the mass of the J/ψ meson [6]. Also the probe must have the opposite charge to the tag, and lie within $\Delta R < 3.5$ (i.e. in the same hemisphere of the detector) - as the J/ψ meson will be in motion when it decays, the decay products will be moving in the same direction as the J/ψ with respect to the primary vertex. Finally, a requirement is made that the paths of the tag and probe can be fitted to a common vertex, with a $\chi^2/\text{DoF} < 6$. In the high multiplicity conditions of an LHC collision event, an ID track may pass the selection criteria for more than one tag. The common vertex requirement is added to ensure that each tag forms only one unique pair with a probe.

Probes which are combined muons are called "muonprobes". The ratio of tag and muon-probe pairs to tag and probe pairs (after subtracting background events) will therefore give the combined muon reconstruction efficiency ($\varepsilon_{\text{reco}}$), as shown in Equation 7.1. Similarly, in order to test the performance of the χ^2_{match} based soft muon tagger, the ratio of those tag and muonprobe

[5] A good ID track passes the MCP quality cuts mentioned in Section 5.4.3.

pairs which pass the χ^2_{match} tagger cuts (Soft Muon Tagged, or SMT, candidates) to all tag and muonprobe pairs will give the efficiency of the SMT tagger (ε_{SMT}), as shown in Equation 7.2. The muonprobe is therefore the numerator of the reconstruction efficiency, and the denominator of the χ^2_{match} based SMT efficiency. The selection requirements of the χ^2_{match} based tagger on the muon are shown in Table 7.4 - these are discussed in Section 5.4.3. The "Jet only" cuts are not applied to the muons, but are included here for completeness. The efficiencies found using collision data and Monte Carlo samples can then be compared, in order to find the scale factor between the two.

$$\varepsilon_{\text{reco}} = \frac{N^{J/\psi}_{\text{muonprobe}}}{N^{J/\psi}_{\text{probe}}} \tag{7.1}$$

$$\varepsilon_{SMT} = \frac{N^{J/\psi}_{\text{SMT}}}{N^{J/\psi}_{\text{muonprobe}}} \tag{7.2}$$

$$\left(\begin{array}{rcl} N^{J/\psi}_{\text{probe}} & = & \text{Number of } J/\psi \text{ reconstructed from tag and probe pairs} \\ N^{J/\psi}_{\text{muonprobe}} & = & \text{Number of } J/\psi \text{ reconstructed from tag and muonprobe pairs} \\ N^{J/\psi}_{\text{SMT}} & = & \text{Number of } J/\psi \text{ reconstructed from tag and muonprobe pairs,} \\ & & \text{the muonprobe passes the } \chi^2_{\text{match}} \text{ tagger cuts} \end{array}\right)$$

Table 7.4: Cuts performed on numerator and denominator of SMT tagging efficiency

Muonprobe	SMT tagged candidate
All probe cuts passed	
Must be a Combined muon	
	$p_{\text{T}} > 4$ GeV
	$\lvert d_0 \rvert < 3$mm
	$\lvert z_0 \cdot \sin\theta \rvert < 3$mm
	$\chi^2_{\text{match}} < 3.2$

Jet only cuts
$\Delta R(\mu_W, \mu_{SMT}) > 0.01$
jet track multiplicity > 3 or jet EM fraction < 0.8

The χ^2_{match} distribution of all probe candidates in both collision data and Monte Carlo simulation is shown in Figure 7.1 - while there is a difference in the exact shape of the distributions,

this can be corrected for by a data/simulation scale factor. Also the exact shape of the distribution is unimportant, as the important value is the efficiency of the cut at $\chi^2_{\text{match}} = 3.2$. When the total integral of the simulated dataset is scaled to be equal to that of the collision data, 95.9% of probe candidates in collision data pass the χ^2_{match} cut, compared with 96.3% in simulated $J/\psi \to \mu\mu$ decays, so the efficiency of the cut is very similar in spite of the difference in shape. The shapes of the distributions above the χ^2_{match} cut do not differ greatly, as can be seen from the fact that the data/simulation ratio in the lower plot becomes approximately constant at higher values of χ^2_{match}.

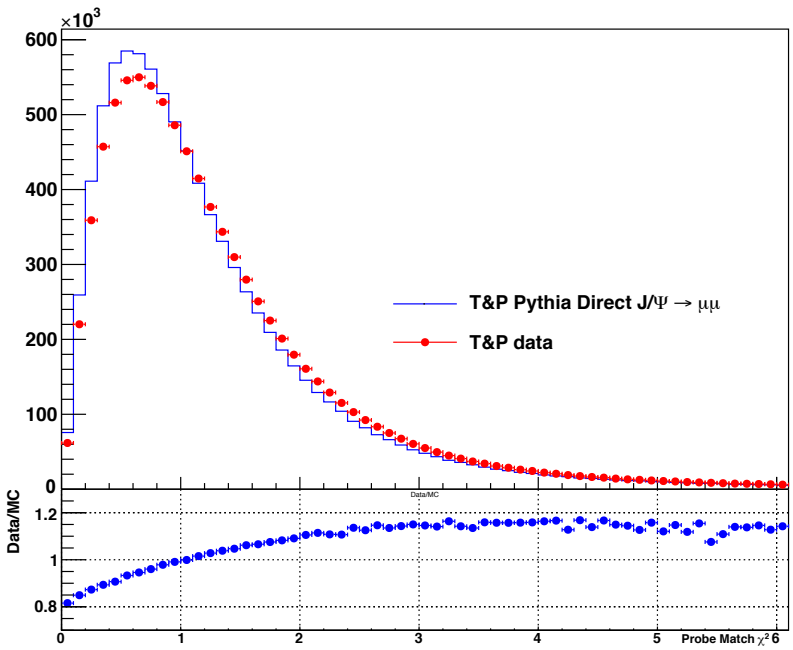

Figure 7.1: χ^2_{match} distribution of all probe candidates in both 2011 data (periods B-M) and Monte Carlo simulation. The integral of the Monte Carlo distribution has been scaled to be equal to that of data, and the lower plot shows the ratio of data/Monte Carlo entries in each bin.

7.1.3 Kinematic Comparison of Muons from J/ψ and $t\bar{t}$ Decays

The χ^2_{match} distributions of the probe muons selected using the tag and probe method on $J/\psi \to \mu\mu$ decays in collision data and that of the SMT tagged muons produced from $t \to b \to \mu$ decays in $t\bar{t}$ simulation are shown in Figure 7.2(a). The shapes of the distributions are similar, suggesting that the χ^2_{match} can be used as a tagging discriminant on both samples. Figure 7.2(b) demonstrates that the p_{T} distributions of the probe muon in collision data and of the SMT tagged muon produced from a simulated $t \to b \to \mu$ decay are quite different.

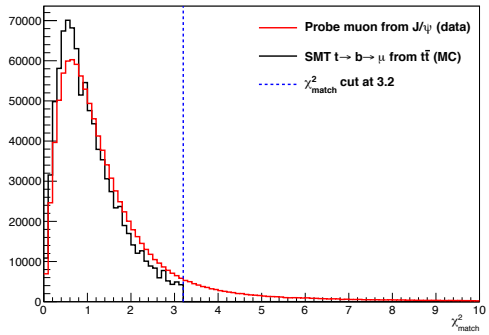

(a) Distribution of χ^2_{match} for probe muons from J/ψ decays and soft muon tagged truth $t \to b \to \mu$ from $t\bar{t}$ decays (integral normalised below $\chi^2_{\text{match}} = 3.2$)

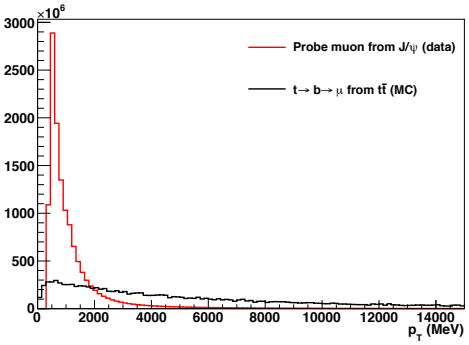

(b) Distribution of p_{T} for probe muons from J/ψ decays and truth $t \to b \to \mu$ from $t\bar{t}$ decays

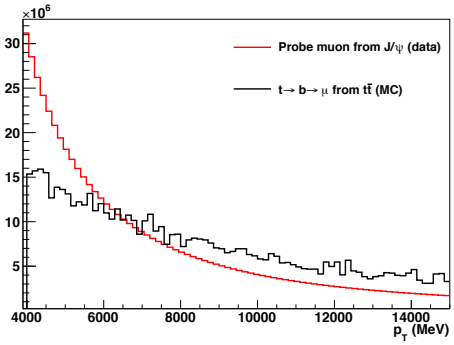

(c) Distribution of p_{T} for probe muons from J/ψ decays and truth $t \to b \to \mu$ from $t\bar{t}$ decays (integral normalised above 4 GeV)

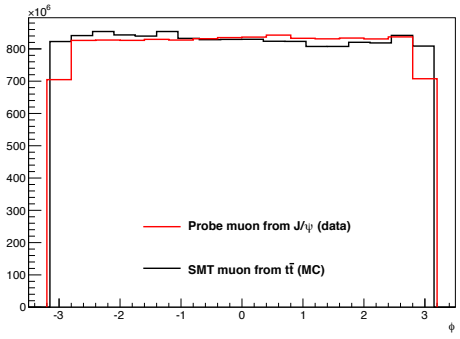

(d) Distribution of ϕ for probe muons from J/ψ decays and SMT tagged truth $t \to b \to \mu$ from $t\bar{t}$ decays

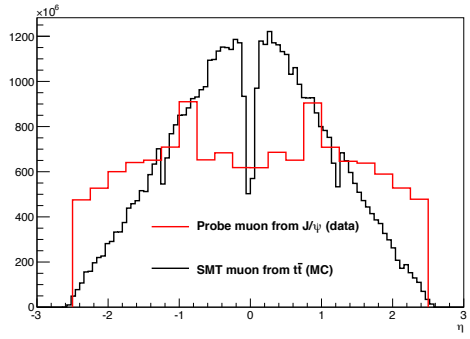

(e) Distribution of η for probe muons from J/ψ decays and SMT tagged truth $t \to b \to \mu$ from $t\bar{t}$ decays

Figure 7.2: Comparison of the distributions of χ^2_{match}, η, ϕ, and p_{T} of probe muons from J/ψ decays in 2011 data (the numerator of the muon reconstruction efficiency), and muons from simulated $t\bar{t}$ decays (either SMT tagged or from true $t \to b \to \mu$ decays). The integral of the J/ψ data is scaled to be equal to that of the $t\bar{t}$ dataset.

As can be seen in Figure 7.2(c), where the integrals of the two plots are normalised above $p_{\text{T}} = 4$ GeV, above 10 GeV the J/ψ sample begins to suffer from relatively poor statistics. For this reason, a tag and probe method is used on a sample of $Z \to \mu\mu$ decays, allowing the analysis to be extended further into the higher muon p_{T} range. The ϕ distributions are similar (Figure 7.2(d)), but the pseudorapidity shown in Figure 7.2(e) differs in shape. The poor reconstruction of muons in the Crack and Transition regions of the detector can be clearly seen in the SMT tagged muon distribution, due to the non-uniform magnetic field in the Transition between endcap and central toroid magnets, and the reduced sensitivity in these regions due to there being fewer modules in the MS capable of detecting muons.

7.1.4 Background Subtraction

In the invariant mass range between 2.5 and 3.6 GeV, a composite function consisting of a quadratic plus Gaussian shape is fitted to the invariant mass distribution, an example of which can be seen in Figure 7.3. Initially, when using early 2010 data, a linear function was fitted to the background but as more data became available and the statistical uncertainty on the efficiency decreased, it was found that a quadratic function was much better at describing the background shape. The mean of the Gaussian part of the composite function is expected to lie close to 3.097 GeV, the invariant mass of the J/ψ. In the region within 3σ of this mean (within which 99.73% of the signal events would lie, if the distribution were a perfect Gaussian), the quadratic background is integrated and subtracted from the actual number of events in the bins in this range, *not* from the integral of the composite function - consequently the number of signal events is not sensitive to the exact signal shape. The remainder is then taken as the signal, and in the case of tag and probe pairs this number is the denominator of Equation 7.1, shown above. In the case of tag and muonprobe pairs, the signal is the numerator of Equation 7.1 and the denominator of Equation 7.2.

7.1.5 Systematic Uncertainties

The total uncertainty on the reconstruction and χ^2_{match} based efficiencies is taken as being the statistical uncertainty on the efficiency calculation, the uncertainty on the fit used to estimate the background in the signal region of the invariant mass plots and the fit uncertainty on the efficiency, added in quadrature.

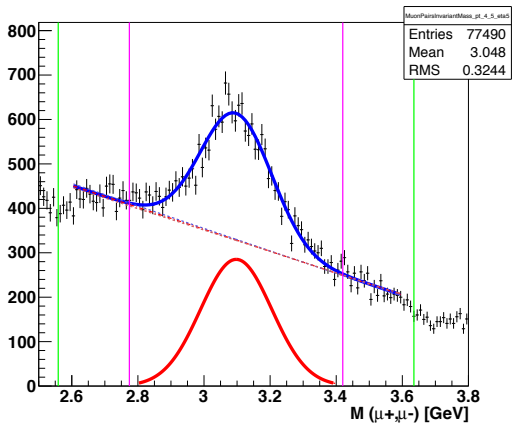

(a) Tag and probe Invariant Mass, probe is an ID track

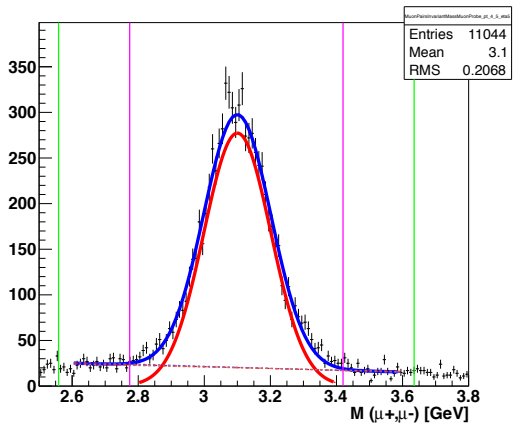

(b) Tag and probe Invariant Mass, probe is a combined muon

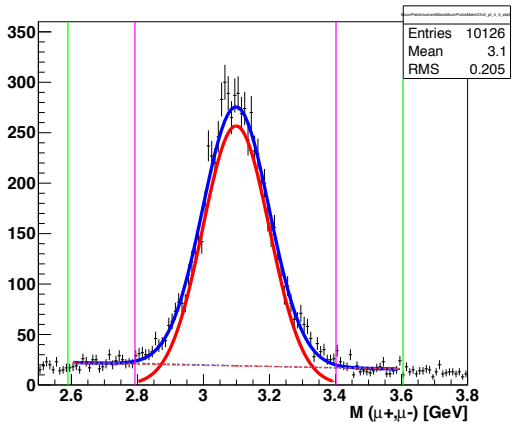

(c) Tag and probe Invariant Mass, probe passed SMT requirements

Figure 7.3: Tag and probe invariant mass, showing the fitted composite function (blue), the background fit, with maximum and minimum (dashed lines), the 3σ and 5σ ranges (magenta and green vertical lines respectively), and an approximation of the signal distribution (red). This plot is made using all 2011 data, for probe muons with 4 GeV $< p_T <$ 5 GeV, in the Forward region of side A of the detector.

The difference in the efficiency calculated using the 3σ and 5σ ranges ($\varepsilon_{5\sigma} - \varepsilon_{3\sigma}$) is taken as the fit uncertainty on that efficiency. Having fixed the mean and σ of the Gaussian to define the signal range, the background estimate is varied between its maximum and minimum values, shown in Figure 7.3 by the blue and brown dotted lines. The quadratic background, expressed as $q = ax^2 + bx + c$, has three uncertainties; those on the coefficients of the quadratic term (a) and the linear term (b) and the uncertainty on the intercept at $x = 0$, c. The maximum and minimum background functions are found by varying a, b and c between their minimum and maximum values, e.g. $a_{\text{min}} = a - \Delta a$ and $a_{\text{max}} = a + \Delta a$. These were combined as follows: $q_{\text{min}} = a_{\text{min}}x^2 + b_{\text{max}}x + c_{\text{min}}$, and $q_{\text{max}} = a_{\text{max}}x^2 + b_{\text{min}}x + c_{\text{max}}$. Figure 7.4 shows an exaggerated example of the effect of the background uncertainties, which cannot be clearly seen in Figure 7.3.

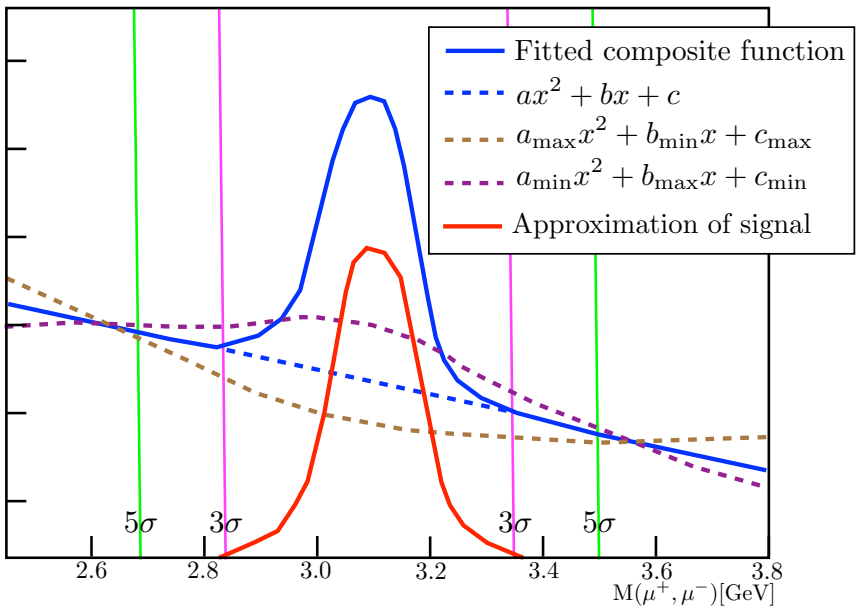

Figure 7.4: A cartoon to show the difference between the maximum and minimum background estimations, shown as the brown and purple dashed lines respectively.

The difference in the efficiencies calculated using the signal value from these different backgrounds ($\varepsilon_{\text{bkgmax}} - \varepsilon_{\text{bkgmin}}$) is taken as the systematic uncertainty on the background fit. There is also a binomial uncertainty on each efficiency, calculated as shown in Equation 7.3. These three uncertainties are added in quadrature to find the total uncertainty on the efficiency measurement, as represented in Equation 7.4. The statistical uncertainty is typically the largest of the three uncertainties considered - Appendix F contains a sample of the uncertainties of the reconstruction

and χ^2_{match} efficiencies, specifically for the Crack region of side A of the detector.

$$\Delta\varepsilon_{stat} = \sqrt{\frac{\varepsilon(1-\varepsilon)}{(N^{J/\psi}_{\text{probe}} \text{ or } N^{J/\psi}_{\text{muonprobe}})}} \tag{7.3}$$

$$\Delta\varepsilon = \sqrt{(\Delta\varepsilon_{stat})^2 + (\varepsilon_{5\sigma} - \varepsilon_{3\sigma})^2 + (\varepsilon_{\text{bkgmax}} - \varepsilon_{\text{bkgmin}})^2} \tag{7.4}$$

7.1.6 Isolation Dependence

As the soft muons in a $t\bar{t}$ event are buried within a b-jet, they have a very different isolation profile to those produced from a J/ψ. Consequently, the dependence of the χ^2_{match} scale factors on isolation is investigated. Nine isolation variables were chosen for this investigation - the first of these is the energy deposited in the calorimeter in a cone of three different sizes around the central muon [6] - the cones have opening angles of 0.2, 0.3 and 0.4, and the corresponding variables are called etcone20, etcone30 and etcone40 respectively. The other isolation variables are the number of tracks (nucone20, nucone30 and nucone40) and the p_{T} (ptcone20, ptcone30, ptcone40) found in the same cones. As expected, the variables which use larger cones tend to show more events, and extend to higher values simply because they encompass a greater volume.

Figures 7.5 to 7.7 show the isolation distributions for probe muons from J/ψ decays and soft muons from $t\bar{t}$ decays. The high statistics available in 2011 data, along with the increased pile-up compared to earlier data, allow the isolation dependence of the data/simulation scale factors to be evaluated over a large isolation range as there are an increased number of muons with higher isolation energies (meaning that the muons themselves are less isolated). Figures 7.5 to 7.7 show the distributions for simulated J/ψ events only, as the upper limit on the isolation range is dictated by the available Monte Carlo simulation statistics at high values of isolation energy, momentum or track multiplicity. Figure 7.5(c) shows the same distribution as Figure 7.5(a) on a logarithmic scale, and it can be seen that it should be possible to find a scale factor measurement in the higher isolation energy regions up to and including the range relevant to $t\bar{t}$ events, depending on which isolation variable is considered.

[6] The central muon is taken to occupy a cone of opening angle 0.1 in the centre of these larger cones, meaning that, for example, etcone20 corresponds to the energy deposited in a cone of opening angle between 0.1 and 0.2.

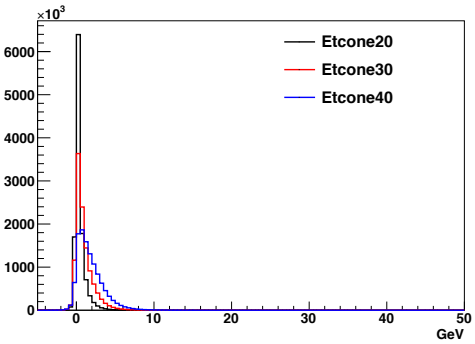

(a) Isolation energy of probe muons from simulated J/ψ decays

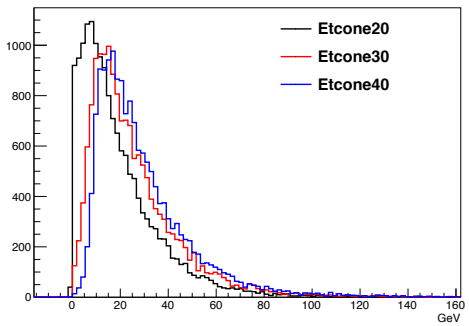

(b) Isolation energy of simulated $t\bar{t}$ soft muons

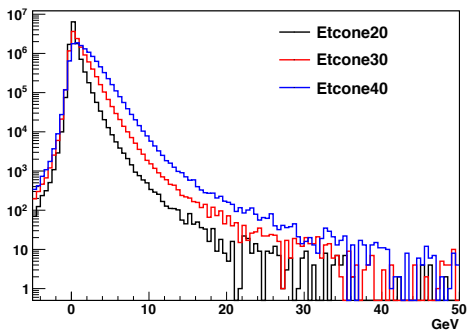

(c) Isolation energy of probe muons from simulated J/ψ decays, on a logarithmic scale

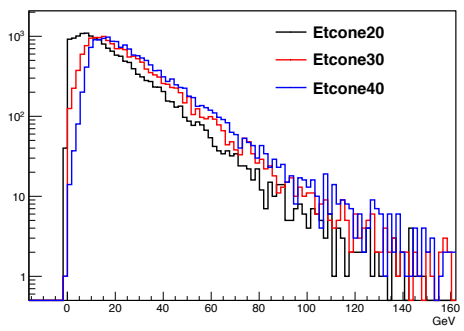

(d) Isolation energy of simulated $t\bar{t}$ soft muons, on a logarithmic scale

Figure 7.5: Isolation energy distributions of probe muons from simulated J/ψ decays, and soft muons from simulated $t\bar{t}$ decays.

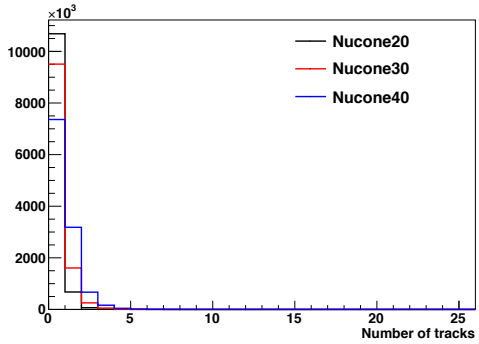

(a) Tracks in cone around probe muons from simulated J/ψ decays

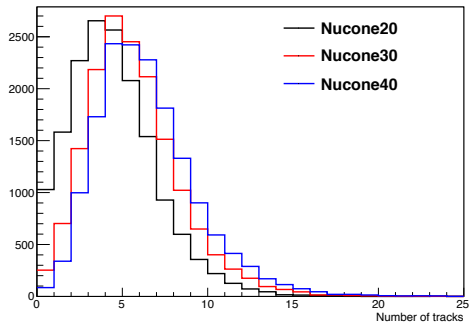

(b) Tracks in cone around simulated $t\bar{t}$ soft muons

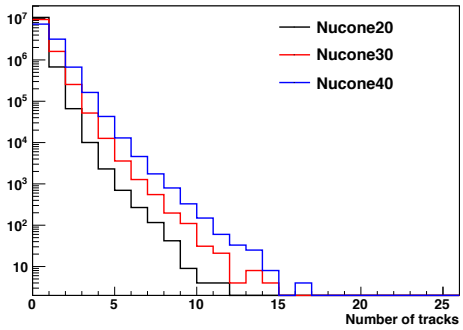

(c) Tracks in cone around probe muons from simulated J/ψ decays, on a logarithmic scale

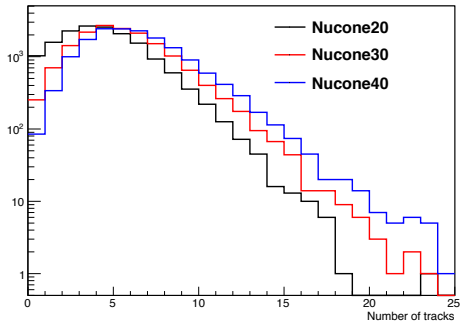

(d) Tracks in cone around simulated $t\bar{t}$ soft muons, on a logarithmic scale

Figure 7.6: Distributions of the number of tracks surrounding the muon for probe muons from simulated J/ψ decays, and soft muons from simulated $t\bar{t}$ decays.

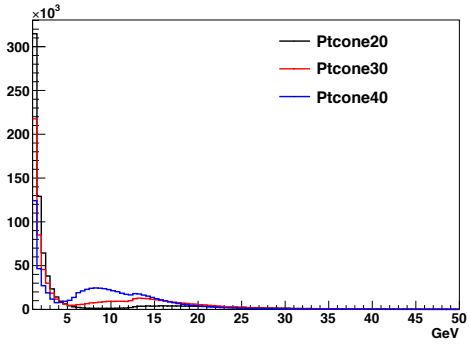

(a) Isolation transverse momentum of probe muons from simulated J/ψ decays

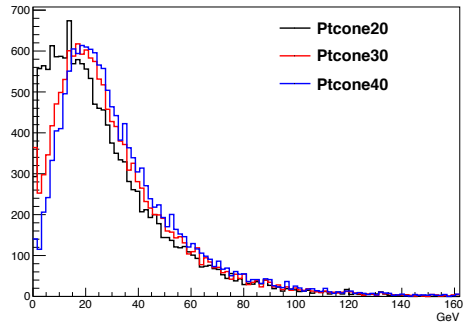

(b) Isolation transverse momentum of simulated $t\bar{t}$ soft muons

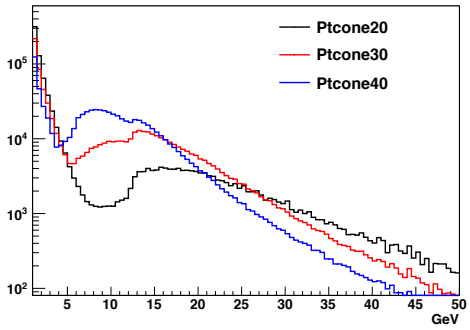

(c) Isolation transverse momentum of probe muons from simulated J/ψ decays, on a logarithmic scale

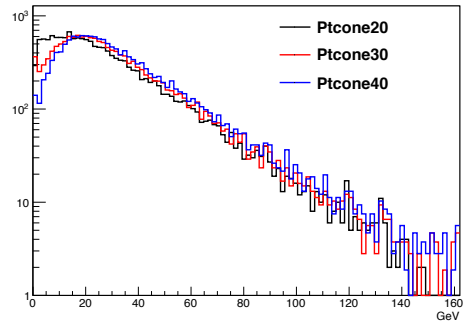

(d) Isolation transverse momentum of simulated $t\bar{t}$ soft muons, on a logarithmic scale

Figure 7.7: Isolation transverse momentum distributions of probe muons from simulated J/ψ decays, and soft muons from simulated $t\bar{t}$ decays.

The Effect of Tag and Probe Proximity on Isolation Momentum

The distributions shown in Figures 7.7(a) and 7.7(c) have an interesting feature - where an exponential decrease in the number of probe muons is expected with increasing isolation momentum, a bump is observed at slightly different values for ptcone20, ptcone30 and ptcone40. This feature is investigated by dividing the sample of simulated $J/\psi \to \mu\mu$ decays into two parts for each variable - those with isolation momenta above and below the bump, which is taken as beginning at 10 GeV, 6 GeV and 4 GeV for ptcone20, ptcone30 and ptcone40 respectively.

The ΔR between the tag and probe muons (ΔR(tag,probe)) is investigated for these samples, producing the plots shown in Figure 7.8. It can be seen that the probe muons with isolation momenta above the beginning of the bump correspond to the cases where the tag muon lies within the isolation cone of the probe, which causes the value of the isolation momentum to be increased. While there is a sharp decline at the edge of the isolation cone, the distributions in Figure 7.8 show that a small proportion of the probe muons (the contribution is almost invisible in Figures 7.8(a), 7.8(c) and 7.8(e)) with ptcone20 > 10 GeV lie outside the $\Delta R < 0.2$ cone, as is the case for the other isolation momentum measurements and their respective ΔR cones. On a logarithmic scale it can be seen that the contribution from probe muons of isolation momenta above the bump threshold that lie outside the isolation cone is higher for larger cones, as the momentum threshold is lower. The tag and probe are more likely to lie closer to one another in cases where the J/ψ itself has high p_{T}, meaning that the decay products will be more collimated than in cases where the J/ψ has lower p_{T}. This can be seen in Figure 7.9 - as expected, the p_{T} of the probe muon is higher in cases where the isolation momentum is above the bump. As the cone is bigger for ptcone40 than ptcone30 and ptcone20, the J/ψ need not be as boosted for the tag and probe muons to both lie within the cone, and the probe p_{T} is correspondingly lower.

If two ID tracks lie very close to one another, a reduction in performance of the tagger might be expected as the tag and probe tracks become harder to uniquely identify. However, we do not see this effect, and the data/simulation scale factor found in Section 7.2.2 below (shown in Figure 7.19) is intended to compensate for discrepancies between any such effect in the collision and simulated data. Soft muons produced in $t \to b \to \mu$ decays are unlikely to be found very close to one another, so if the calibration in data were to be performed again the $J/\psi \to \mu\mu$ decays could be divided into those in which ΔR(tag, probe) is above and below a minimum value (the size of the isolation cone), so as to better reflect the conditions found in $t\bar{t}$ decays.

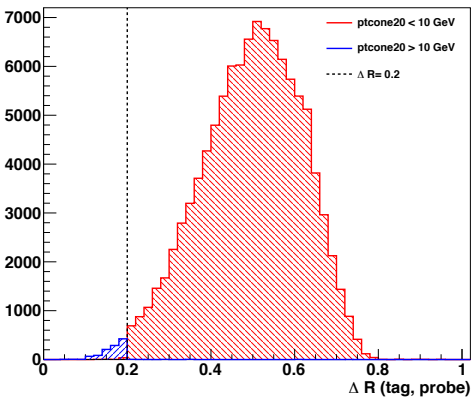

(a) ΔR(tag, probe) for probe muons with ptcone20 above and below 10 GeV

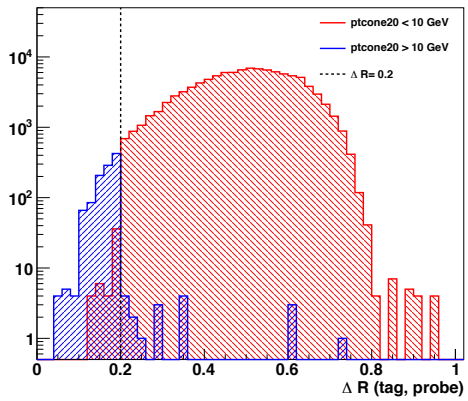

(b) ΔR(tag, probe) for probe muons with ptcone20 above and below 10 GeV, on a logarithmic scale

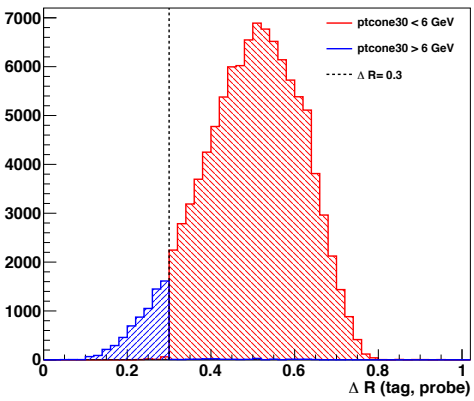

(c) ΔR(tag, probe) for probe muons with ptcone30 above and below 6 GeV

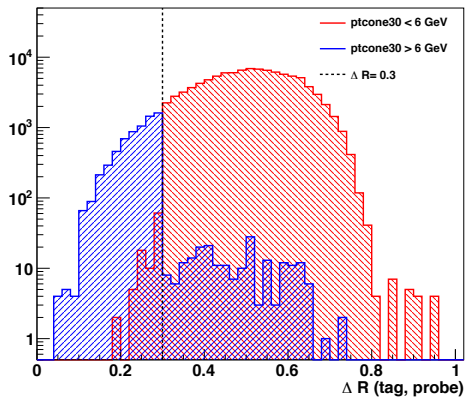

(d) ΔR(tag, probe) for probe muons with ptcone30 above and below 6 GeV, on a logarithmic scale

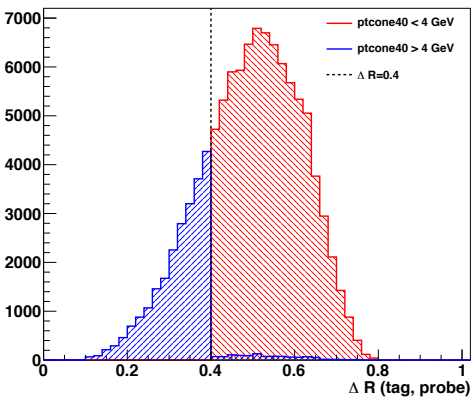

(e) ΔR(tag, probe) for probe muons with ptcone40 above and below 4 GeV

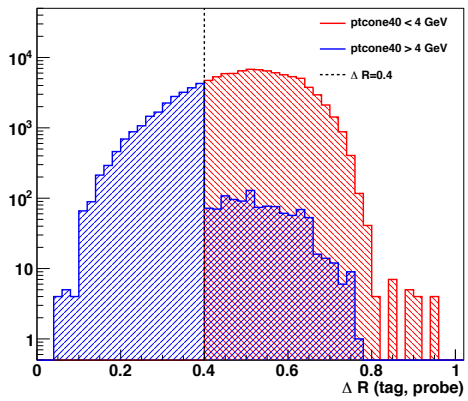

(f) ΔR(tag, probe) for probe muons with ptcone40 above and below 4 GeV, on a logarithmic scale

Figure 7.8: ΔR(tag, probe) distributions for probe muons of isolation momenta above and below the beginnings of the bumps observed in the ptcone20, ptcone30 and ptcone40 distributions.

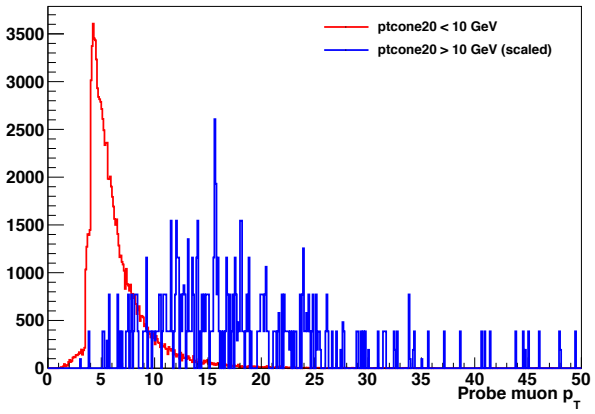

(a) p_T of probe muons with ptcone20 above and below 10 GeV

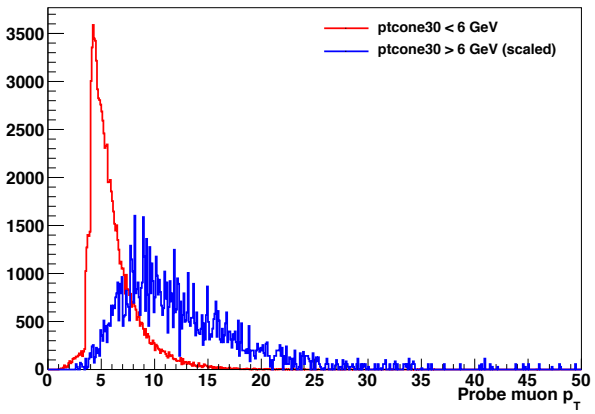

(b) p_T of probe muons with ptcone30 above and below 6 GeV

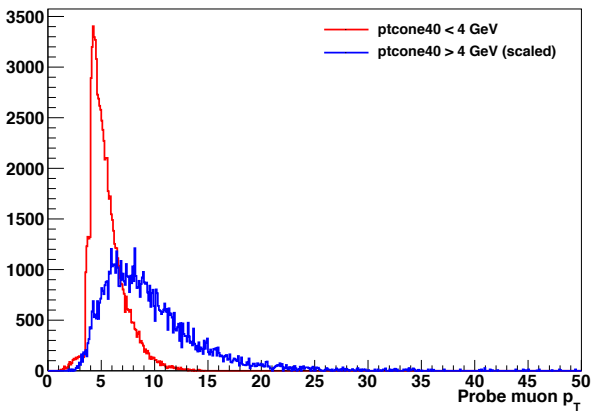

(c) p_T of probe muons with ptcone40 above and below 4 GeV

Figure 7.9: Transverse momenta of probe muons of isolation momenta above and below the bumps observed in the ptcone20, ptcone30 and ptcone40 distributions. The integral of the distribution with isolation momenta below the bump has been scaled to be equal to the distribution above the bump, for ease of visual comparison.

7.2 Efficiencies and Scale Factors

The tag and probe analysis was performed on 2010 collision data, as shown in Section 7.2.1, which allowed a cross-check of our results with those given in [78]. This was a necessary precursor to the 2011 analysis, to serve as a validation of the methods used to find the efficiencies and scale factors.

7.2.1 2010 Data

The collision data sample used to find the reconstruction efficiency for comparison with the results in [78] is comprised of those luminosity blocks from the Muons stream which are included in the chosen Good Runs List (GRL), for periods "E" to "I" of 2010 collision data. This represents an integrated luminosity of 35.5 pb^{-1}. The Monte Carlo simulated data sample consists of 1 million direct $J/\psi \to \mu\mu$ events.

The tag candidate is required to pass any one of the triggers listed in Table 7.5 - the dimuon trigger, `EF_mu4_Trk_JPsi`, is not used for 2010 data as it only accepts muons within 250 GeV either side of the J/ψ mass (3.097 GeV), as mentioned in Section 7.1.1, which results in a narrow sideband region to the the invariant mass distribution, meaning that it is difficult to estimate the background contribution in the signal region - see Section 7.1.4 for the background subtraction method.

Table 7.5: Trigger requirements for both tag and probe candidates, according to 2010 data period.

Period	Run Number	Trigger requested
E	$\leq$ 161948	`EF_mu4_MG`, `EF_mu4`, `EF_mu6_MG`, `EF_mu6`
F	$\leq$ 162882	`EF_mu4_MG`, `EF_mu4`, `EF_mu6_MG`, `EF_mu6`, `EF_mu10_MG`, `EF_mu10`
G1-G4	$\leq$ 165818	`EF_mu6_MG`, `EF_mu6`, `EF_mu10_MG`, `EF_mu10`
G5-H	$\leq$ 166964	`EF_mu10_MG`, `EF_mu10`, `EF_mu13_MG`, `EF_mu13`
I	$\leq$ 167844	`EF_mu13_MG`, `EF_mu13`, `EF_mu13_MG_tight`, `EF_mu13_tight`

The reconstruction efficiencies for 2010 data were compared with the results quoted in [78] by the Muon Combined Performance group, and found to agree within uncertainties. These comparisons are shown in Figures 7.10 and 7.11, for a selection of the five $|\eta|$ regions corresponding to different parts of the muon systems in the ATLAS detector, as described in Table 7.6.

The reconstruction efficiency at low p_{T} is lower due to the fact that such muons lose momentum while passing through the material of the detector, with a typical muon losing $\approx$ 3 GeV

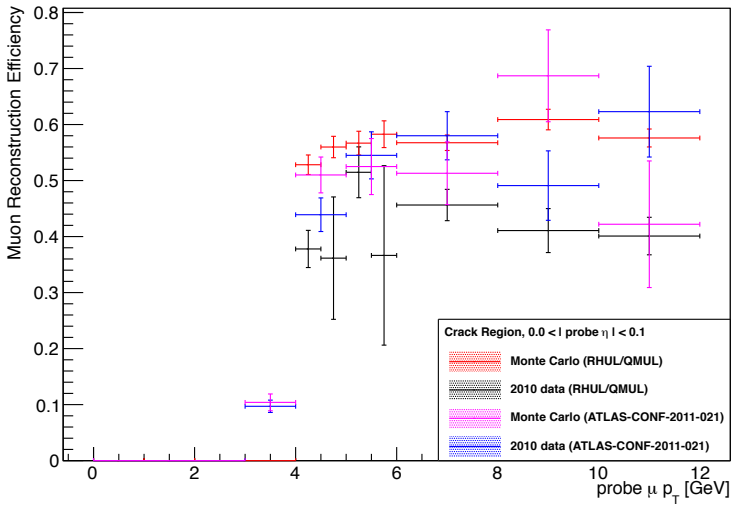

(a) Muon reconstruction efficiencies in the Crack region.

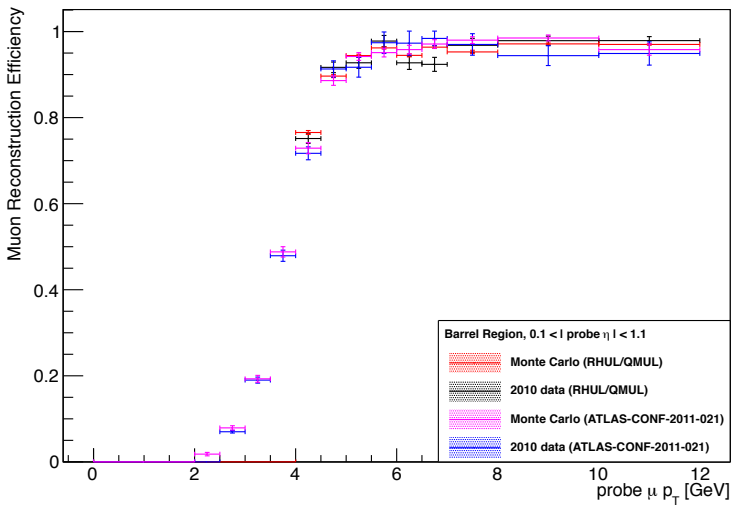

(b) Muon reconstruction efficiencies in the Barrel region.

Figure 7.10: Comparison of muon reconstruction efficiencies with MCP results, using 2010 data (Crack and Barrel Regions). The error bars on the Monte Carlo simulated data points (red and purple) show only the statistical uncertainty, while those on the collision data (black and blue) represent the statistical and systematic uncertainties added in quadrature. The efficiencies measured in this analysis (red and black) are compared with those found in [78] (purple and blue).

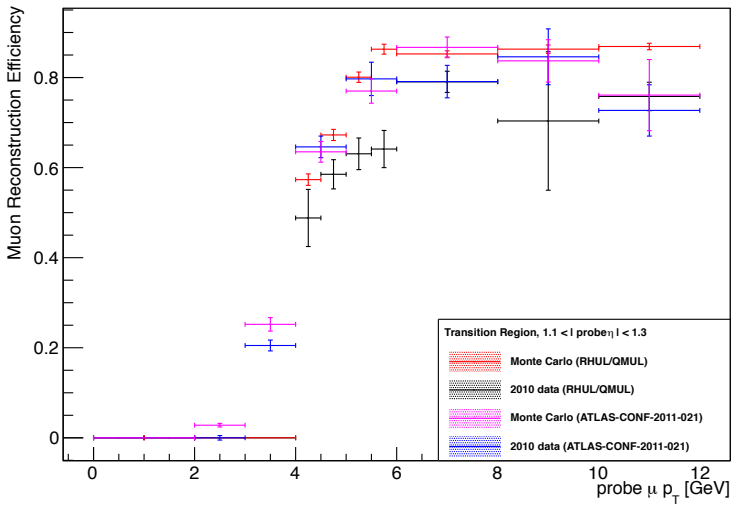

(a) Muon reconstruction efficiencies in the Transition region.

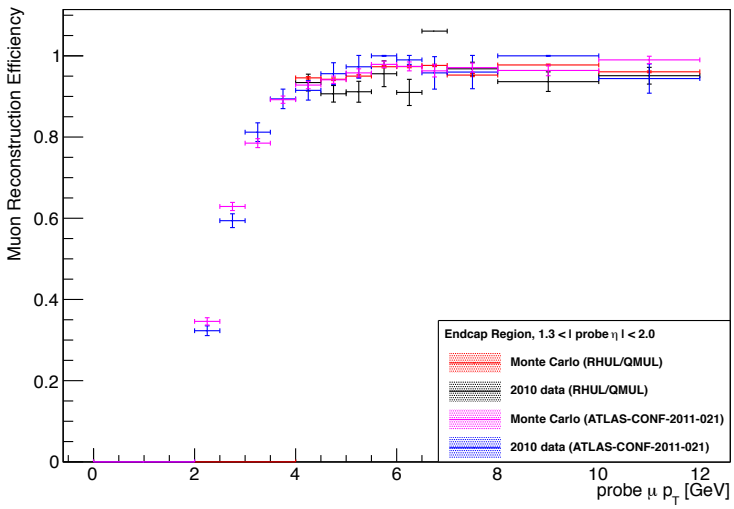

(b) Muon reconstruction efficiencies in the Endcap region.

Figure 7.11: Comparison of muon reconstruction efficiencies with MCP results, using 2010 data (Transition and Endcap Regions). The error bars on the Monte Carlo simulated data points (red and purple) show only the statistical uncertainty, while those on the collision data (black and blue) represent the statistical and systematic uncertainties added in quadrature. The efficiencies measured in this analysis (red and black) are compared with those found in [78] (purple and blue).

before reaching the MS. This means that it is often not possible to reconstruct low p_{T} muons which have left tracks in the ID. The lower efficiencies in the Crack and Transition regions are also expected, as there is a volume for the passage of services and cabling in the Crack region, resulting in fewer modules in the MS, and thus the tracking capability is reduced. Similarly, the Transition region between Barrel and Endcap suffers from non-uniform chamber configuration and magnetic field, lying as it does at the intersection of the magnetic fields produced by the Barrel and Endcap toroids (as shown in Figure 4.15).

As the reconstruction efficiencies and data/simulation scale factors were found to be in agreement with those quoted in [78], it was deemed reasonable to extend the analysis of the χ^2_{match} tagger to 2011 data.

Table 7.6: Pseudorapidity regions of the ATLAS detector.

$\lvert\eta\rvert$ range	Name
$0.0 < \lvert\eta\rvert < 0.1$	Crack
$0.1 < \lvert\eta\rvert < 1.1$	Barrel
$1.1 < \lvert\eta\rvert < 1.3$	Transition
$1.3 < \lvert\eta\rvert < 2.0$	Endcap
$2.0 < \lvert\eta\rvert < 2.5$	Forward

7.2.2 2011 Data

The tag and probe analysis was repeated on 2011 collisions, allowing for the efficiencies to be found using a much larger dataset. Due to the difference in pile-up (as shown in Figure 4.3) and detector conditions from period to period in 2011, it was deemed necessary to investigate any period dependence - the overall χ^2_{match} tagging efficiency was found for all periods, and a selection of these periods representing a spread across the entirety of 2011 data was chosen. These efficiencies are shown in Figure 7.12. The largest and smallest values for each efficiency lie within the uncertainty of each measurement, and so it is reasonable to claim that the different detector conditions under which each period of data was collected do not have an effect on the χ^2_{match} efficiency. It was therefore decided to combine all of the 2011 periods into one dataset and find the dependence on other variables, with no necessity for separate scale factors to be used depending on the period.

In 2011 data the detector was divided into 10 η regions, as opposed to the 5 $|\eta|$ regions in

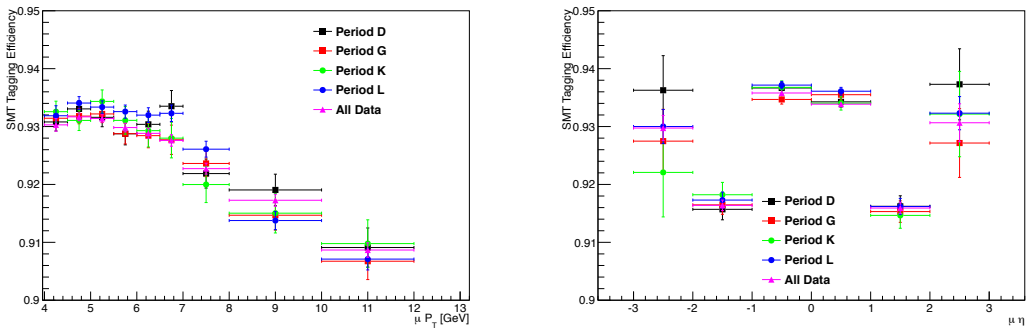

(a) χ^2_{match} efficiencies with respect to the p_T of the probe (b) χ^2_{match} efficiencies with respect to the pseudorapidity of the probe

Figure 7.12: Efficiencies of the SMT χ^2_{match} tagger for a range of 2011 data periods

2010. These regions correspond to the five regions in Table 7.6, but split into side A ($\eta > 0$) and side C ($\eta < 0$) of the detector. The dependences of the reconstruction efficiencies on the p_{T} of the probe muon, as found in 2011 data, are shown in Figures 7.13 to 7.17.

As mentioned in Section 7.2.1, the reduced reconstruction efficiencies at the lowest transverse momenta ($p_{\text{T}} \lesssim 4$ GeV) are expected, as these muons are unlikely to leave tracks in the MS due to having already deposited most of their energy in the calorimeter systems. The Crack and Transition regions of the detector also have comparatively low reconstruction efficiencies due to the non-uniform magnetic field in the Transition between endcap and central toroid magnets, and the reduced sensitivity in these regions due to there being fewer modules in the MS capable of detecting muons.

The increased integrated luminosity available in 2011 data allowed the dependence of the collision data/MC scale factor on the isolation variables to be extended to higher values, as shown in Figures 7.18, 7.19 and 7.20. The upper limit on the isolation range is restricted by the Monte Carlo sample in use, meaning that while efficiencies could be found using collision data for higher isolation values, it is not possible at this time to produce scale factors above the ranges shown. This is because the background subtraction methods cannot accurately fit and subtract the background with low statistics, so we cannot find the J/ψ signal. In all cases the data/Monte Carlo scale factor found is flat across the isolation range, meaning that no dependence on the isolation of the probe muon is observed.

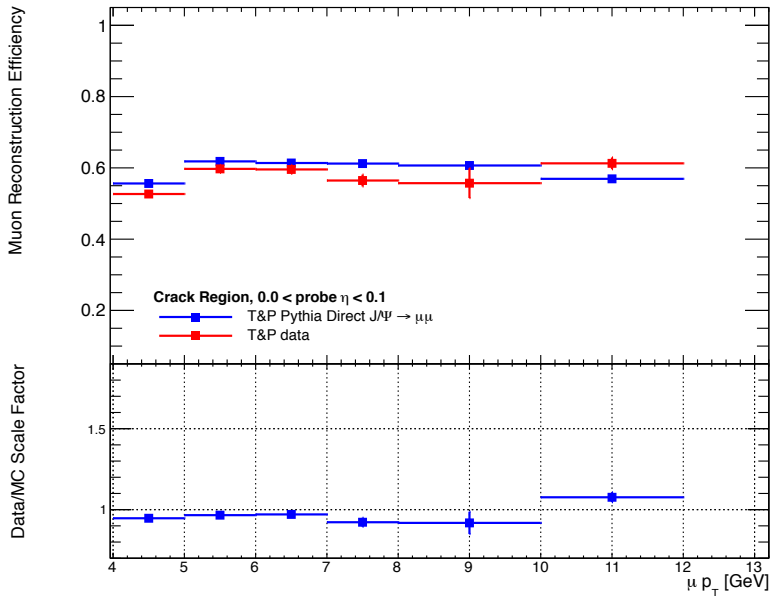

(a) Crack η region, side A

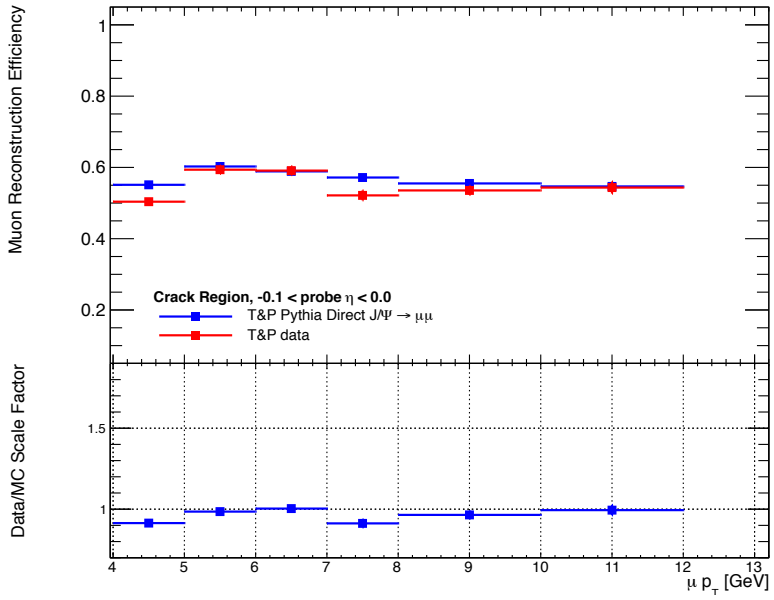

(b) Crack η region, side C

Figure 7.13: Muon reconstruction efficiencies with respect to the p_T of the probe, for the Crack regions on side A and C of the detector, using all 2011 data.

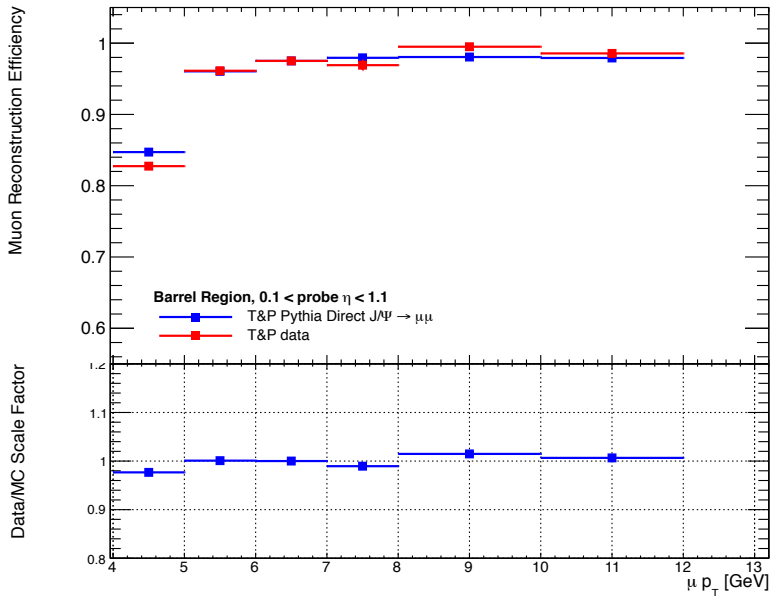

(a) Barrel η region, side A

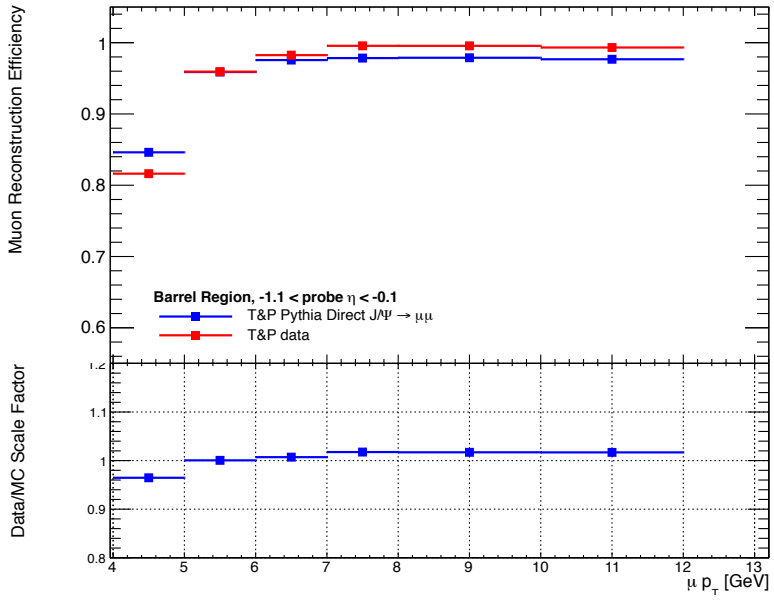

(b) Barrel η region, side C

Figure 7.14: Muon reconstruction efficiencies with respect to the p_T of the probe, for the Barrel regions on side A and C of the detector, using all 2011 data.

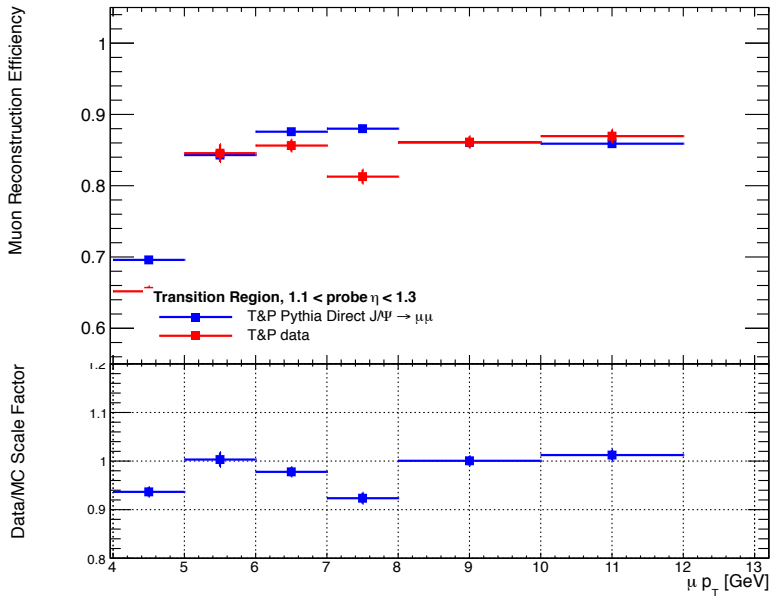

(a) Transition η region, side A

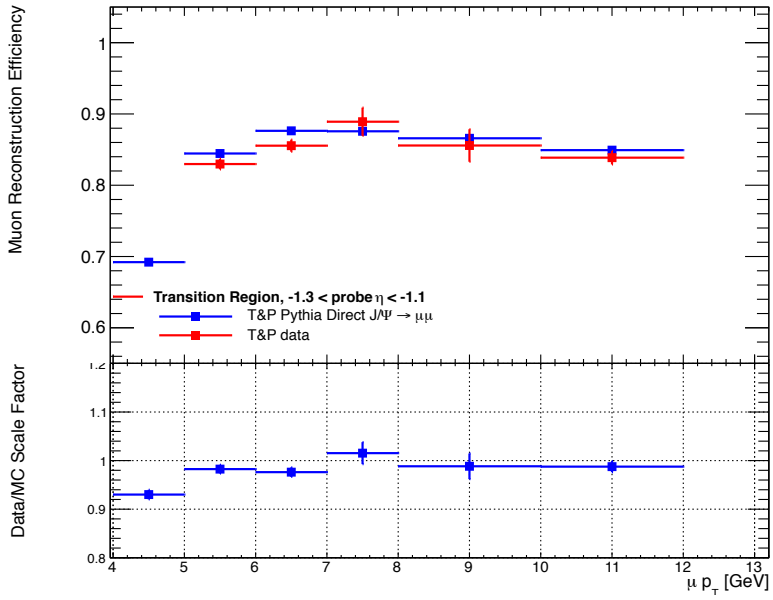

(b) Transition η region, side C

Figure 7.15: Muon reconstruction efficiencies with respect to the p_T of the probe, for the Transition regions on side A and C of the detector, using all 2011 data.

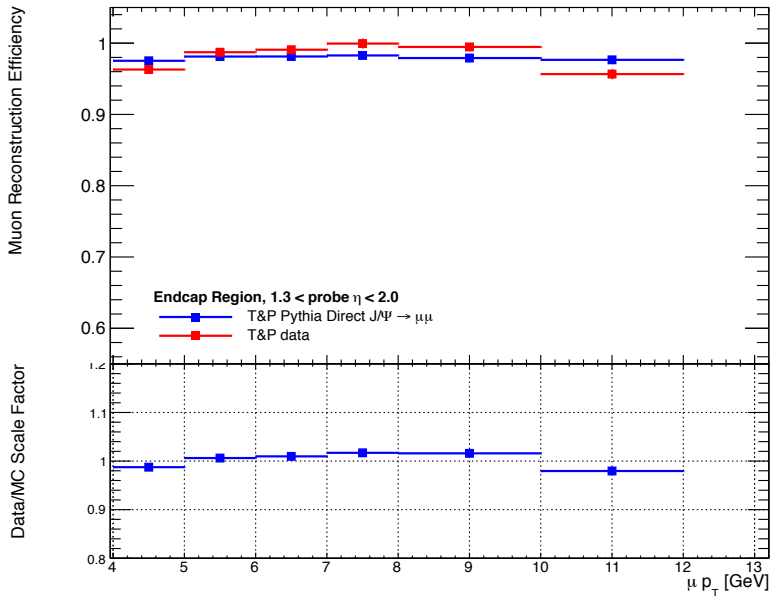

(a) Endcap η region, side A

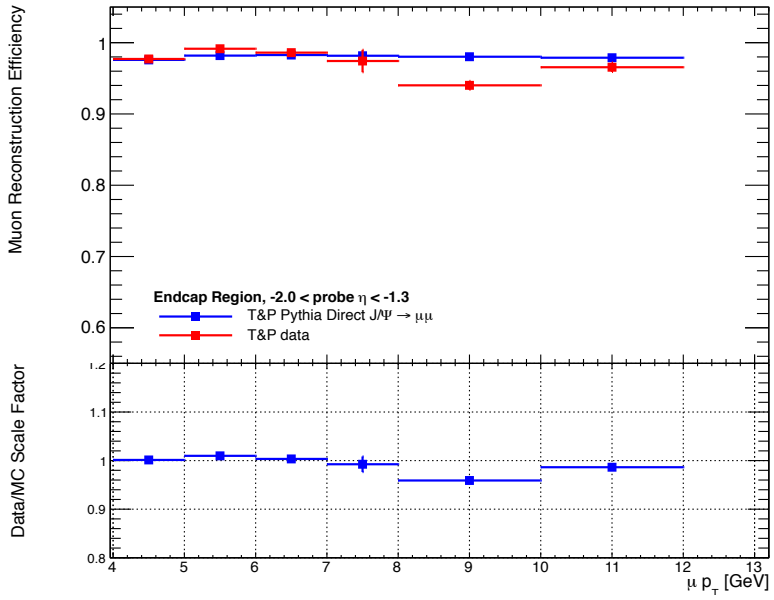

(b) Endcap η region, side C

Figure 7.16: Muon reconstruction efficiencies with respect to the p_T of the probe, for the Endcap regions on side A and C of the detector, using all 2011 data.

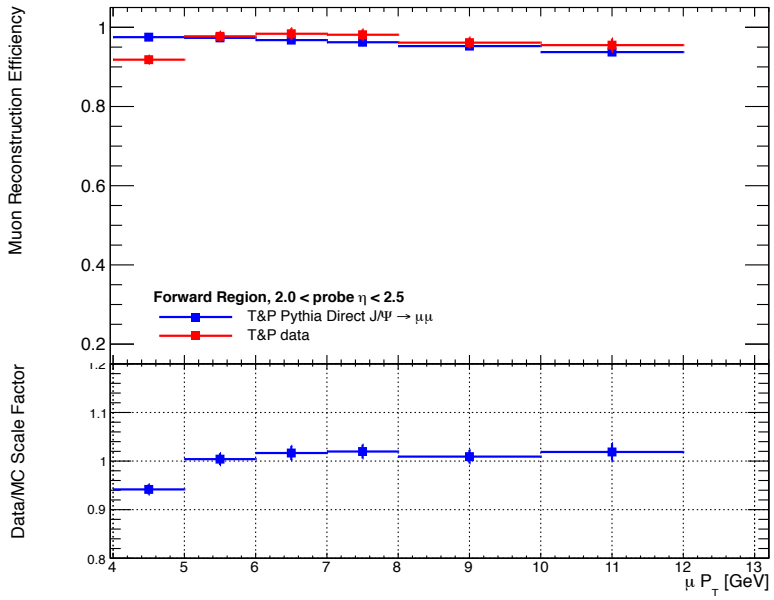

(a) Forward η region, side A

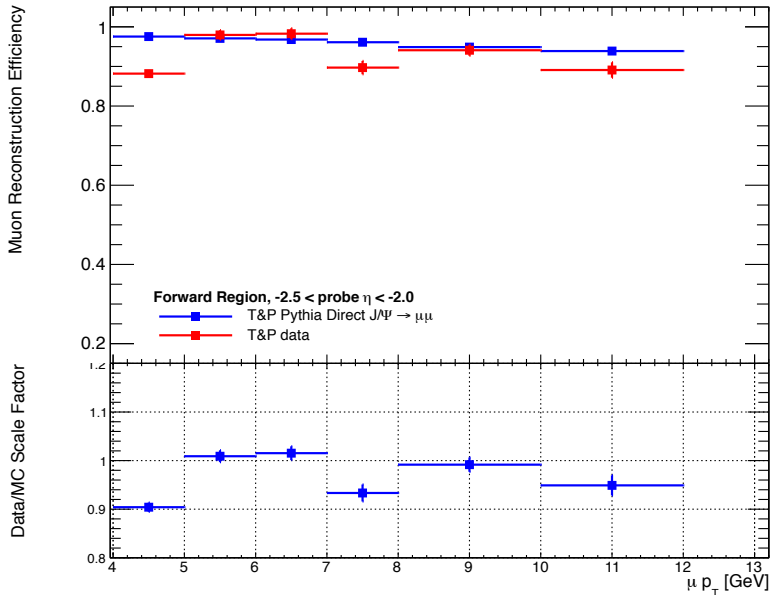

(b) Forward η region, side C

Figure 7.17: Muon reconstruction efficiencies with respect to the p_T of the probe, for the Forward regions on side A and C of the detector, using all 2011 data.

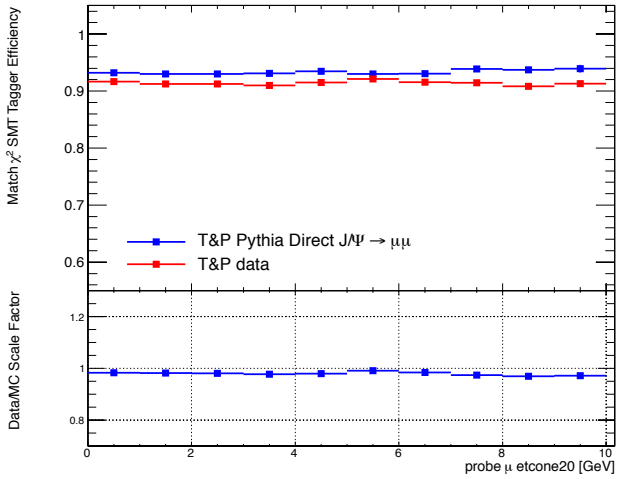

(a) “etcone20”

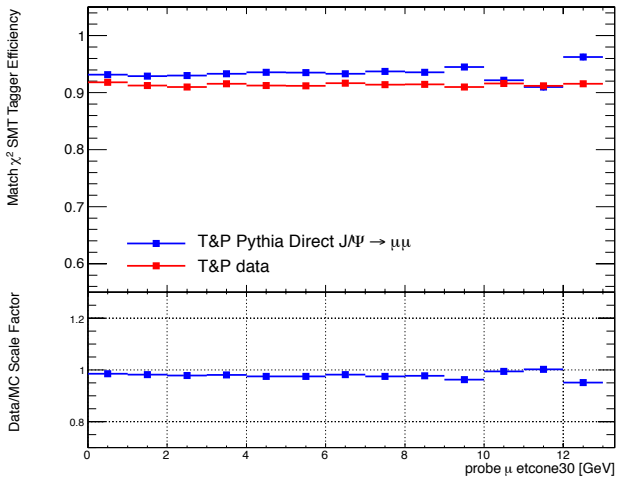

(b) “etcone30”

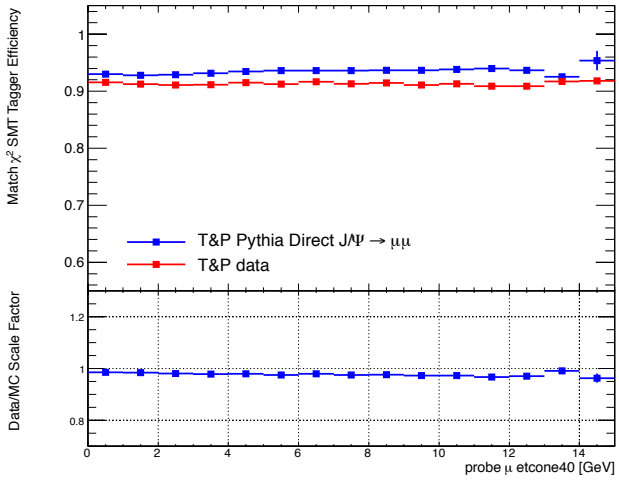

(c) “etcone40”

Figure 7.18: χ^2_{match} efficiencies and data/Monte Carlo scale factor with respect to the energy deposited in a cone of various sizes around the probe muon (isolation energy).

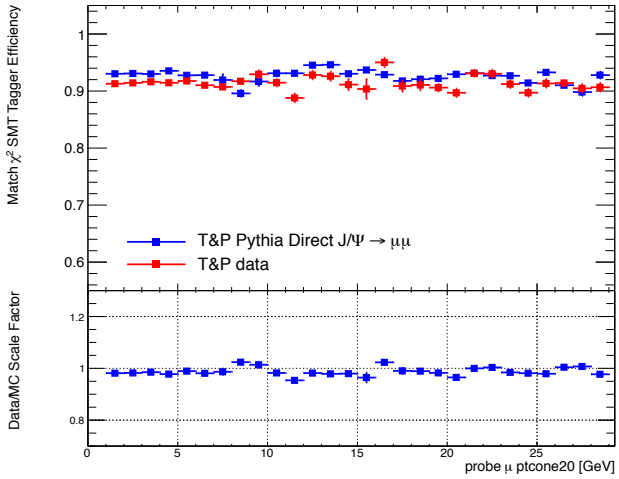

(a) "ptcone20"

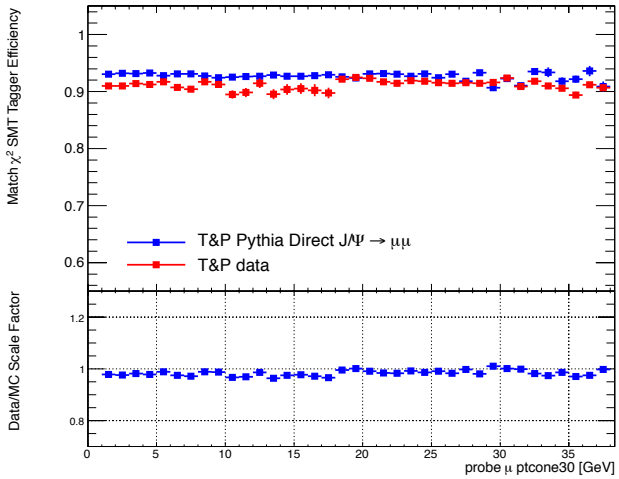

(b) "ptcone30"

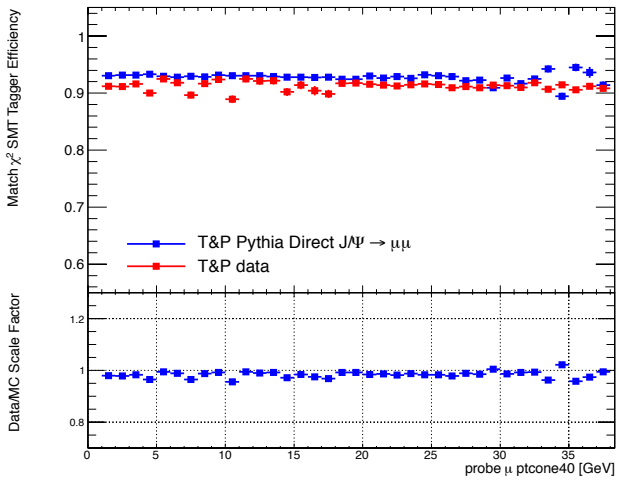

(c) "ptcone40"

Figure 7.19: χ^2_{match} efficiencies and data/Monte Carlo scale factor with respect to the p_{T} in a cone of various sizes around the probe muon.

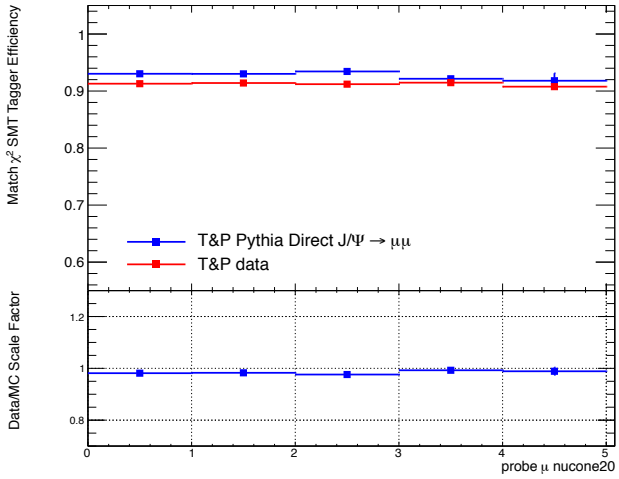

(a) " nucone20"

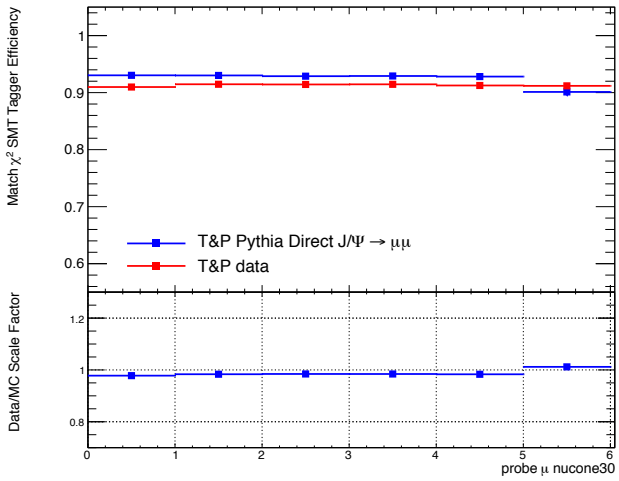

(b) "nucone30"

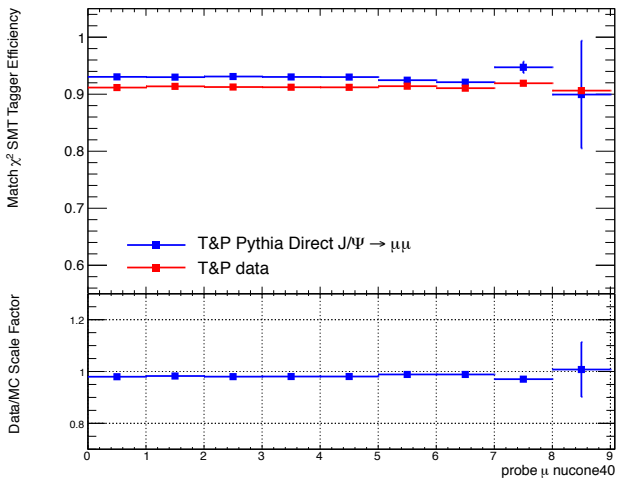

(c) "nucone40"

Figure 7.20: χ^2_{match} efficiencies and data/Monte Carlo scale factor with respect to the number of tracks in a cone of various sizes around the probe muon.

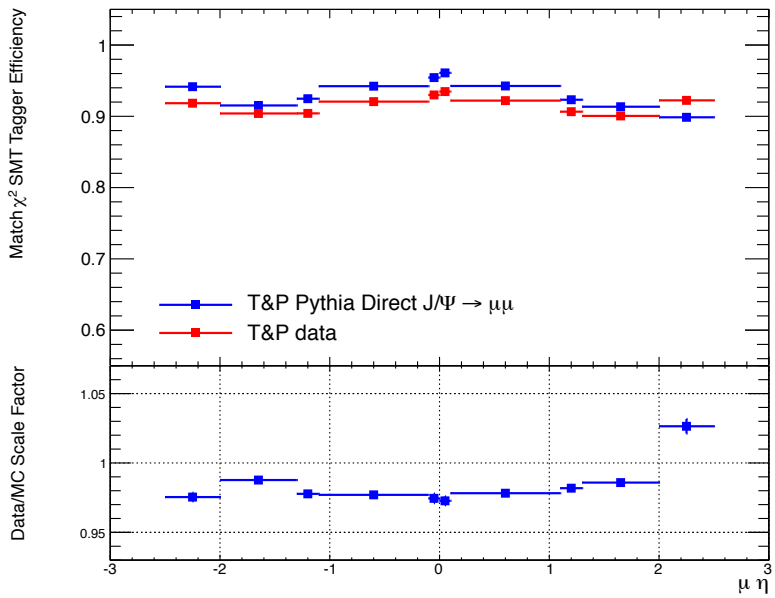

(a) χ^2_{match} efficiencies and scale factor with respect to the η of the probe muon

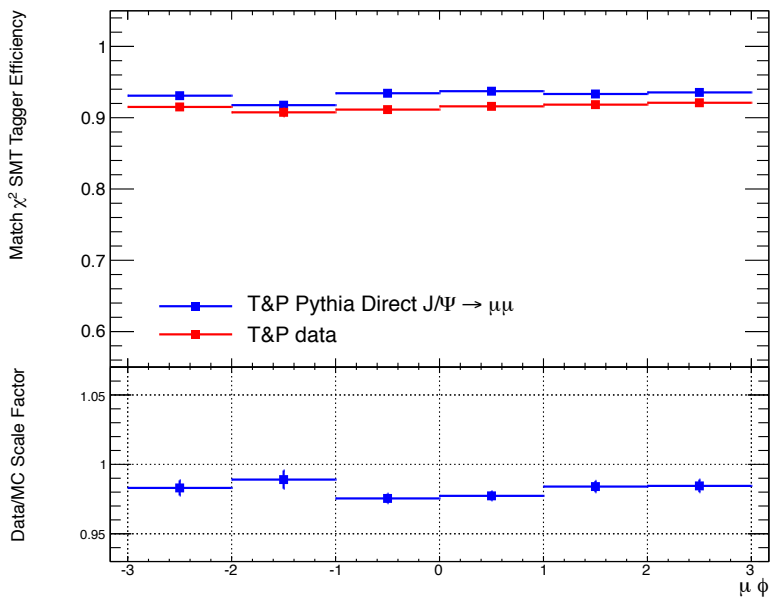

(b) χ^2_{match} efficiencies and scale factor with respect to the ϕ of the probe muon

Figure 7.21: χ^2_{match} efficiencies and data/Monte Carlo scale factors with respect to the η and ϕ of the probe muon.

The dependence on the spatial variables of the detector is shown in Figure 7.21. The scale factor exhibits no strong dependence on ϕ. With respect to the pseudorapidity of the probe, two things are observed - firstly that there is an asymmetry in the dependence, and secondly that there seems to be a structure to it, as can be seen in Figure 7.21(a).

The large difference that can be seen between the χ^2_{match} efficiency in the Forward regions of side A and side C of the detector is seen in the Monte Carlo simulation but not in the collision data. It represents a drop in efficiency of up to $\approx 10\%$ at higher muon p_{T}. It is also observed in Monte Carlo studies of $Z \to \mu\mu$. Discussions within the MCP group have led to the belief that this is a symptom of a problem with the CSC digitisation model in the simulation - the issue is also observed in the Muid chain (an alternative method of muon reconstruction to the STACO chain used in this analysis) and is confirmed by independent observations of experts in the Muon Combined Performance group. This problem is corrected for by the data/MC scale factor, and so it is necessary to split the scale factor into side A and C, as opposed to just having a scale factor binned by the five regions of $|\eta|$.

The p_{T} dependence of the χ^2_{match} tagging scale factor was investigated in the ten η regions of the detector. The resulting plots are shown in Figures 7.22 to 7.26, from which it is clear that a single scale factor across the entire range of p_{T} and η values would be inappropriate. A large difference is seen between the scale factors for the χ^2_{match} based tagger in the Forward regions in side A and side C of the detector (positive and negative η respectively), as shown in Figure 7.26. It was decided that scale factors should be produced binned by both p_{T} and η - the η bins are the ten described above, and the p_{T} bins chosen are from 4-5 GeV, 5-6 GeV, 6-7 GeV, 7-8 GeV, 8-10 GeV and 10-12 GeV.

The scale factors are shown in Table 7.7, along with their associated uncertainties. The uncertainties on the scale factors (ΔSF) are calculated using the total uncertainties on the efficiencies, as mentioned in Section 7.1.5. ΔSF is found as shown in Equation 7.5, where the efficiency and uncertainty values for collision data or Monte Carlo simulation are represented by $\varepsilon_{\text{data}}$, $\Delta\varepsilon_{\text{data}}$, ε_{MC} and $\Delta\varepsilon_{\text{MC}}$.

$$\Delta\text{SF} = \frac{\varepsilon_{\text{data}}}{\varepsilon_{\text{MC}}}\sqrt{\left(\frac{\Delta\varepsilon_{\text{data}}}{\varepsilon_{\text{data}}}\right)^2 + \left(\frac{\Delta\varepsilon_{\text{MC}}}{\varepsilon_{\text{MC}}}\right)^2} \tag{7.5}$$

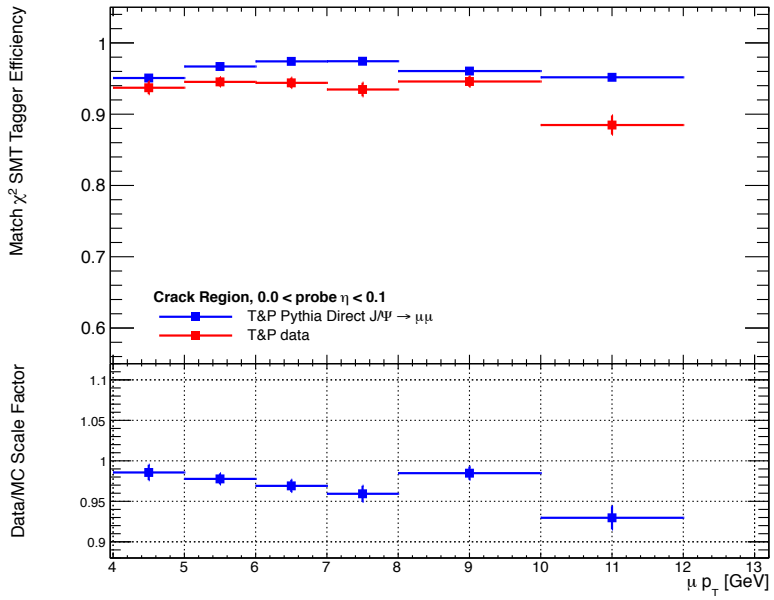

(a) Crack η region, side A

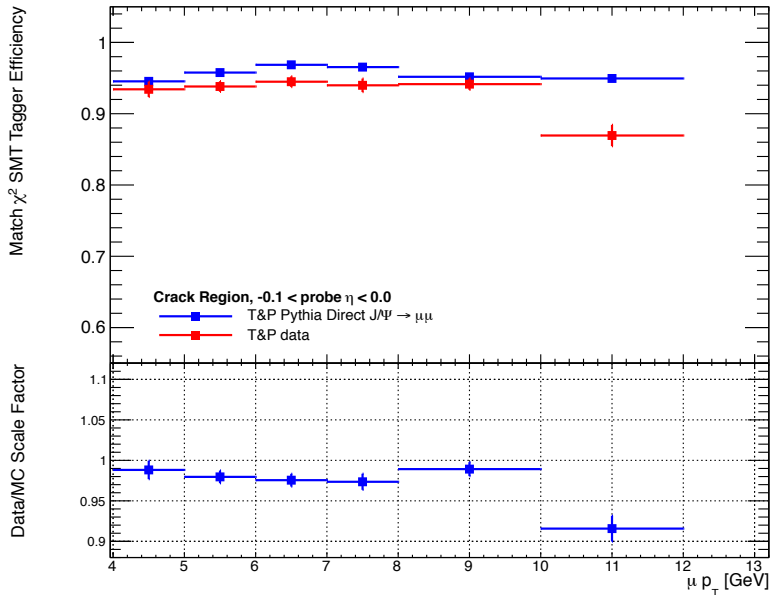

(b) Crack η region, side C

Figure 7.22: χ^2_{match} efficiencies with respect to the p_T of the probe muon, for the Crack regions on side A and C of the detector, using all 2011 data.

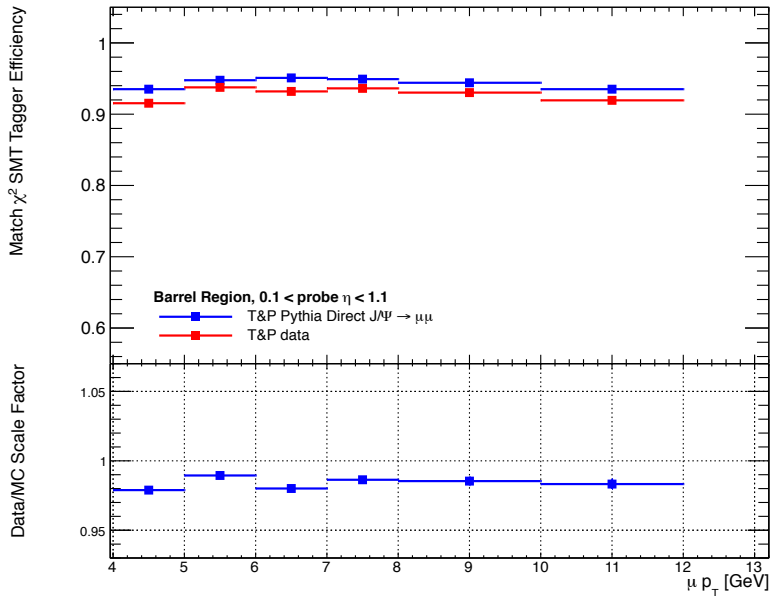

(a) Barrel η region, side A

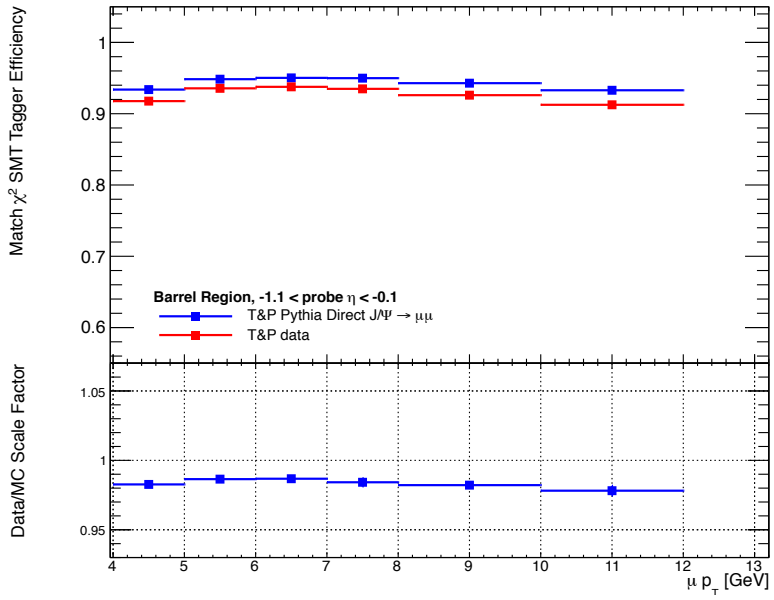

(b) Barrel η region, side C

Figure 7.23: χ^2_{match} efficiencies with respect to the p_T of the probe muon, for the Barrel regions on side A and C of the detector, using all 2011 data.

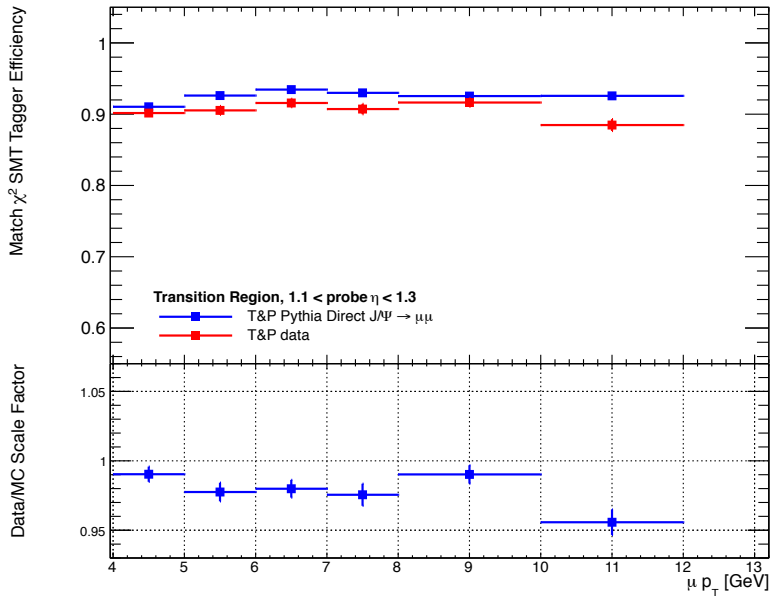

(a) Transition η region, side A

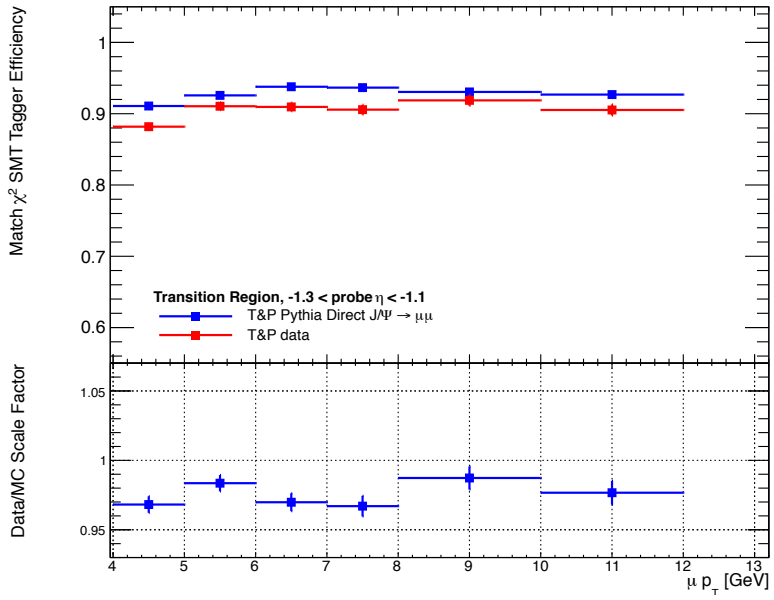

(b) Transition η region, side C

Figure 7.24: χ^2_{match} efficiencies with respect to the p_T of the probe muon, for the Transition regions on side A and C of the detector, using all 2011 data.

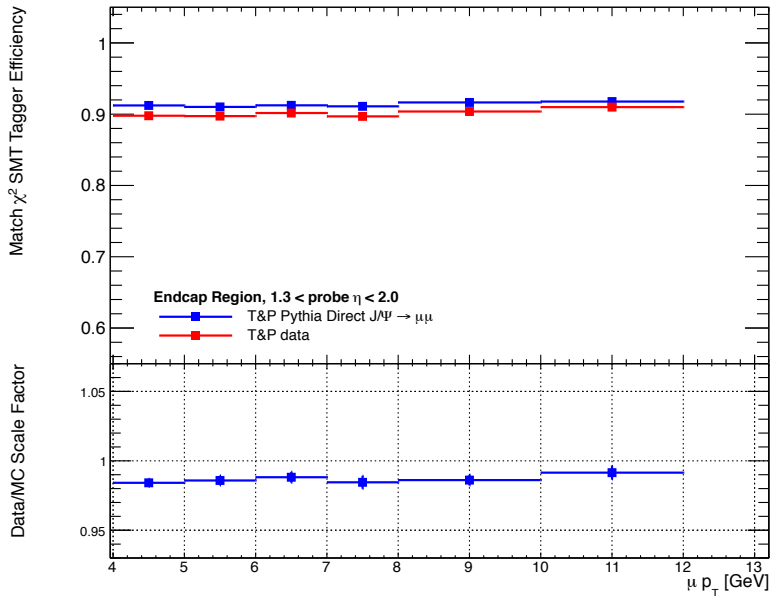

(a) Endcap η region, side A

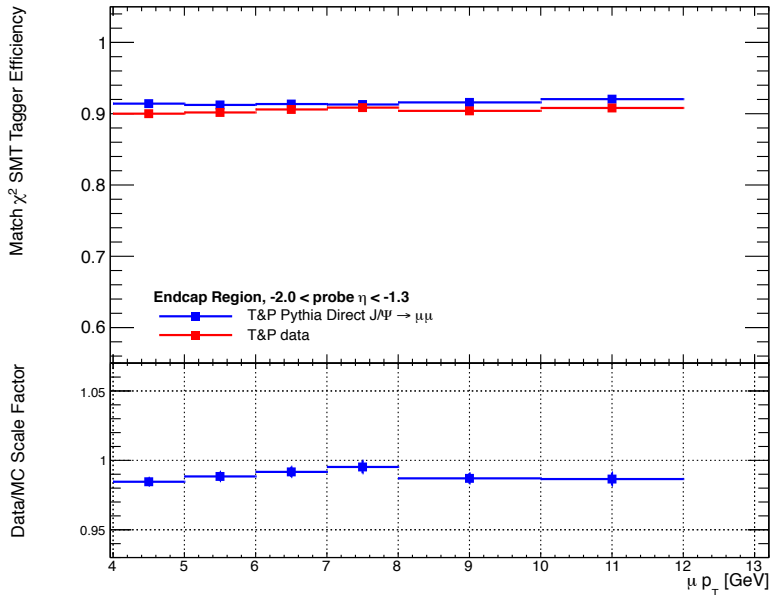

(b) Endcap η region, side C

Figure 7.25: χ^2_{match} efficiencies with respect to the p_T of the probe muon, for the Endcap regions on side A and C of the detector, using all 2011 data.

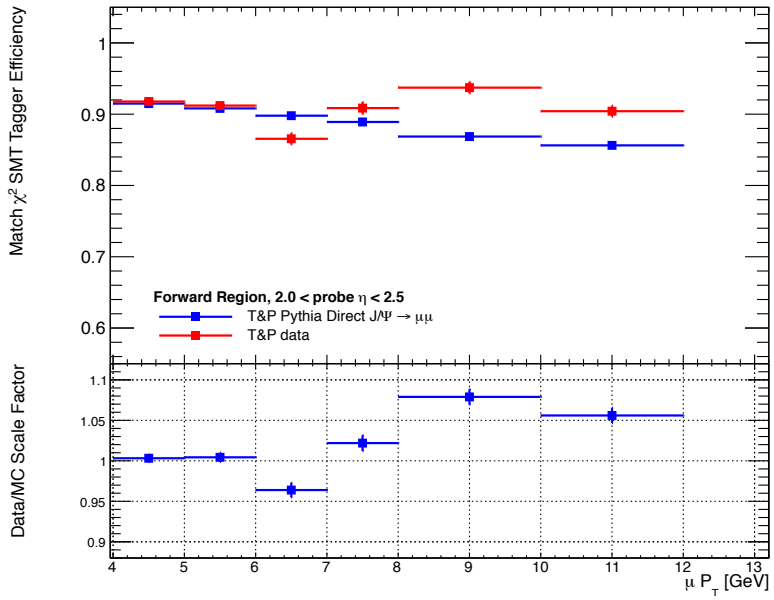

(a) Forward η region, side A

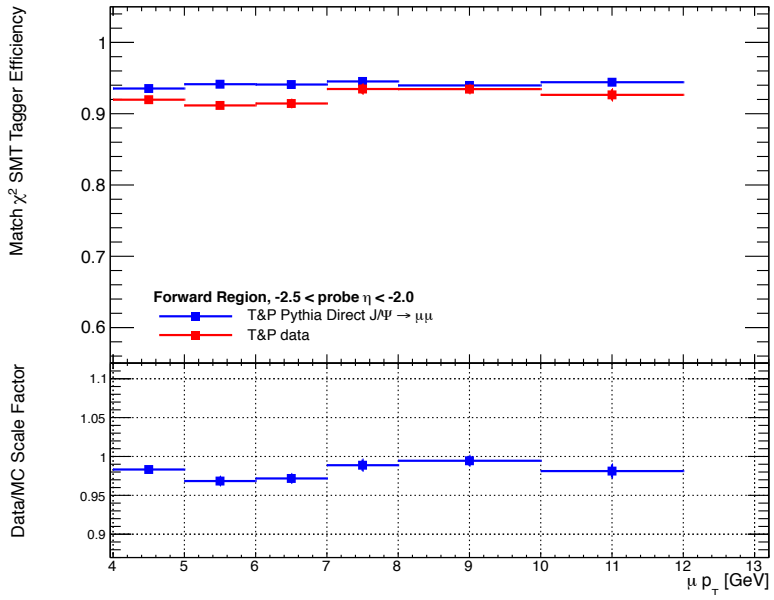

(b) Forward η region, side C

Figure 7.26: χ^2_{match} efficiencies with respect to the p_T of the probe muon, for the Forward regions on side A and C of the detector, using all 2011 data.

Table 7.7: Data/MC χ^2_{match} scale factors for 2011 data - uncertainty quoted is statistical + systematic.

Side A ($\eta > 0$)					
p_{T} range	Crack	Barrel	Transition	Endcap	Forward
4-5 GeV	0.986 ± 0.010	0.979 ± 0.002	0.990 ± 0.005	0.984 ± 0.003	1.003 ± 0.005
5-6 GeV	0.978 ± 0.007	0.989 ± 0.002	0.978 ± 0.007	0.986 ± 0.004	1.004 ± 0.006
6-7 GeV	0.969 ± 0.008	0.980 ± 0.002	0.980 ± 0.006	0.988 ± 0.004	0.964 ± 0.009
7-8 GeV	0.959 ± 0.010	0.986 ± 0.003	0.976 ± 0.008	0.985 ± 0.005	1.022 ± 0.010
8-10 GeV	0.985 ± 0.008	0.985 ± 0.003	0.990 ± 0.007	0.986 ± 0.004	1.079 ± 0.010
10-12 GeV	0.930 ± 0.014	0.983 ± 0.003	0.956 ± 0.009	0.991 ± 0.005	1.056 ± 0.009
Side C ($\eta < 0$)					
p_{T} range	Crack	Barrel	Transition	Endcap	Forward
4-5 GeV	0.988 ± 0.011	0.983 ± 0.002	0.968 ± 0.006	0.985 ± 0.003	0.983 ± 0.005
5-6 GeV	0.980 ± 0.008	0.986 ± 0.002	0.984 ± 0.006	0.988 ± 0.003	0.968 ± 0.006
6-7 GeV	0.976 ± 0.008	0.987 ± 0.002	0.970 ± 0.006	0.992 ± 0.004	0.972 ± 0.006
7-8 GeV	0.974 ± 0.010	0.984 ± 0.003	0.967 ± 0.007	0.995 ± 0.005	0.989 ± 0.007
8-10 GeV	0.989 ± 0.009	0.982 ± 0.003	0.987 ± 0.008	0.987 ± 0.004	0.994 ± 0.006
10-12 GeV	0.916 ± 0.016	0.978 ± 0.004	0.977 ± 0.009	0.987 ± 0.005	0.981 ± 0.009

7.2.3 Tag and Probe with $Z \to \mu\mu$

In order to cover a larger muon p_{T} range than is possible using $J/\psi \to \mu\mu$ alone, extending further into the range appropriate for the muons in $t\bar{t}$ decays, the tag and probe study was extended to use $Z \to \mu\mu$ events. As shown in Figure 7.27, muons produced in $Z \to \mu\mu$ decays have a much harder p_{T} distribution than those from $J/\psi \to \mu\mu$. The data to simulation scale factors obtained for higher p_{T} muons using the $Z \to \mu\mu$ tag and probe method can be applied to muons in the same manner as those found from $J/\psi \to \mu\mu$. More detail on the $Z \to \mu\mu$ scale factors is available in [1].

The recommendation of the MCP group [73] is that the muon reconstruction scale factors obtained from $Z \to \mu\mu$ events should be extrapolated down to low muon p_{T}, rather than finding muon reconstruction scale factors using $J/\psi \to \mu\mu$ events. As a check of the appropriateness of this decision, scale factors found using the two methods are compared in the overlapping region in muon p_{T}. This overlap between the scale factors is shown in Figure 7.28, for the entire η range and for the Crack, Barrel, Transition, Endcap and Forward $|\eta|$ regions of the MS. The scale factor recommended by the MCP [73] group, referred to here as the "prescribed" scale factor, is also added to Figures 7.28(b) to 7.28(f) - as an overall scale factor for all data periods is not provided, the prescribed scale factors plotted here are the per-period scale factors,

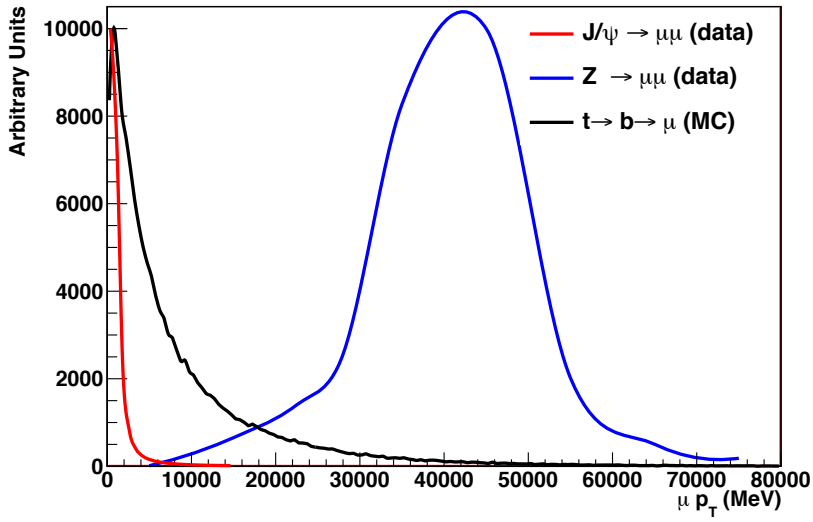

Figure 7.27: Comparison of the p_{T} distributions of probe muons from $J/\psi \to \mu\mu$ and $Z \to \mu\mu$ decays in 2011 data, and truth $t \to b \to \mu$ from simulated $t\bar{t}$ decays. The distributions have been scaled for easy visual comparison.

weighted by luminosity and averaged over all periods, and should be taken as approximations for comparison with the values found using $J/\psi \to \mu\mu$ and $Z \to \mu\mu$. Consequently, while the scale factor obtained using $J/\psi \to \mu\mu$ does not agree well with the MCP scale factors in the Crack region, neither does the scale factor obtained from $Z \to \mu\mu$ upon which the MCP scale factor is based [7]. The Crack region covers the smallest $|\eta|$ range and has the lowest number of events (hence the large uncertainties on the points in Figure 7.28(b)).

While the scale factors and uncertainties shown in blue in Figure 7.28 are only an approximation of the prescribed reconstruction scale factors, it is surprising that there is not better agreement between these and the scale factors obtained directly from $Z \to \mu\mu$ decays. It is expected they would agree within uncertainties. Also, the extrapolation of the $Z \to \mu\mu$ scale factors to low muon p_{T} but with increased uncertainties can be called into question, as in the Barrel, Transition, Endcap and Forward regions the majority of the scale factors found using J/ψ decays lie within the uncertainty of the prescribed scale factor, but themselves have vastly reduced uncertainties. It follows that analyses which make use of the prescribed scale factors may there-

[7]The muon reconstruction scale factors are taken from the muon efficiency corrections software package, which is used for applying scale factors to muons in simulated data to better reflect the reconstruction efficiencies found using collision data. This software is recommended for use by the MCP group and written by Marco Vanadia, who also provided the $Z \to \mu\mu$ scale factors in this analysis, using the same data samples for the reconstruction and χ^2_{match} scale factors.

fore be subject to artificially inflated uncertainties which propagate through to affect their final results. This has been brought to the attention of members of the MCP group.

Figure 7.29 shows the χ^2_{match} data/simulation scale factors obtained using $J/\psi \to \mu\mu$ and $Z \to \mu\mu$, and the overlap between the two. These were used to provide scale factors for the reweighting of simulated data when using the χ^2_{match} soft muon tagger in other analyses. The muon p_{T} range of $4 < p_{\text{T}}(\mu) < 12$ GeV is provided using $J/\psi \to \mu\mu$, and $Z \to \mu\mu$ is used to find the scale factor for 12 GeV $< p_{\text{T}}(\mu) <$ 7 TeV. The scale factors found using the two methods can be seen to be consistent in the region of overlap.

Of the results found in this chapter, the collision data/MC χ^2_{match} scale factors in the $J/\psi \to \mu\mu$ muon p_{T} range (shown in Table 7.7) are used in the $t\bar{t}$ cross section analysis described in Chapter 8. In the higher muon p_{T} range, the χ^2_{match} scale factors found using $Z \to \mu\mu$ are used. These scale factors are applied to tagged muons in the analysis depending on the p_{T}, η and ϕ values of the muons.

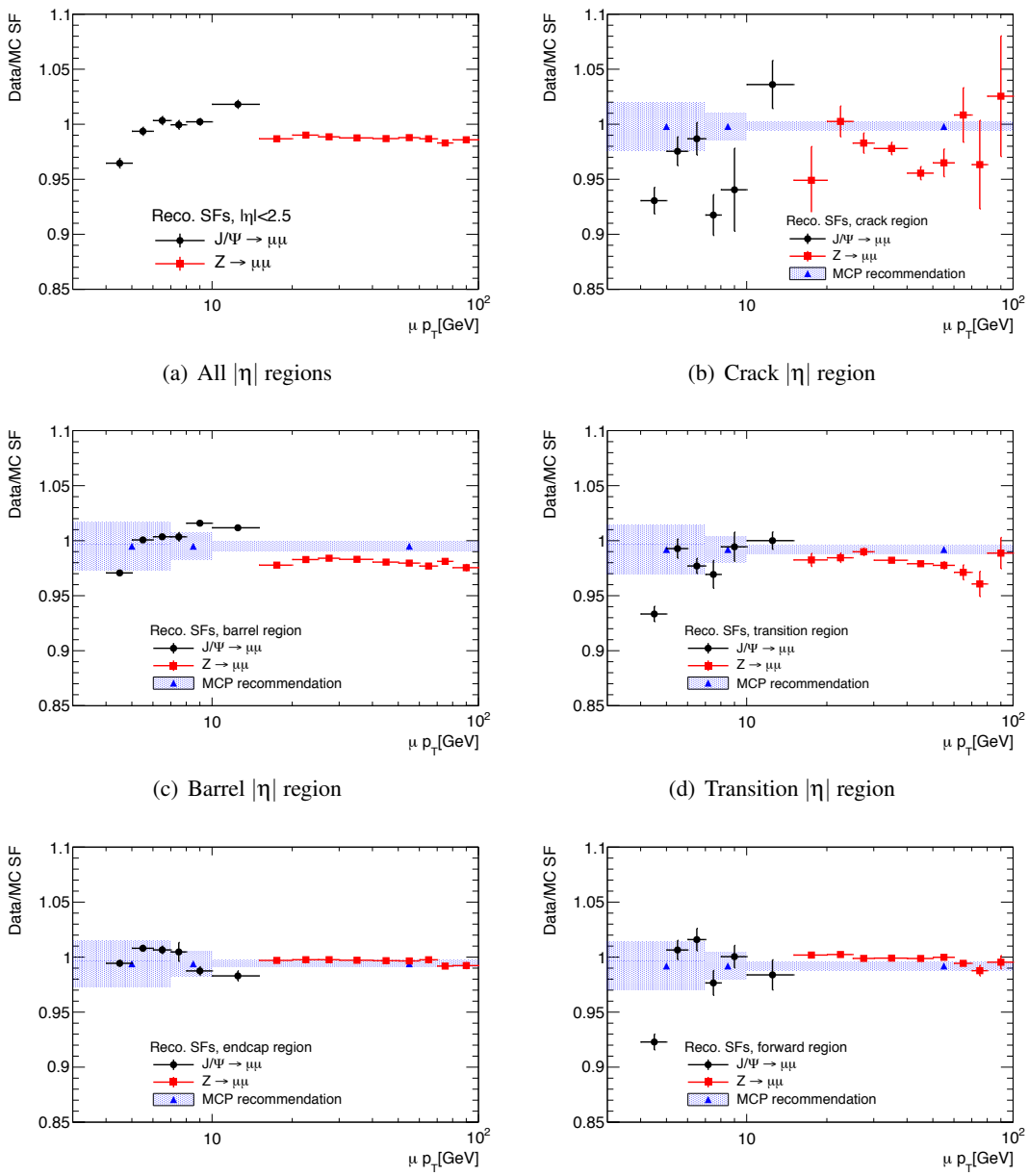

(a) All $|\eta|$ regions

(b) Crack $|\eta|$ region

(c) Barrel $|\eta|$ region

(d) Transition $|\eta|$ region

(e) Endcap $|\eta|$ region

(f) Forward $|\eta|$ region

Figure 7.28: Comparison of muon reconstruction scale factors evaluated using $J/\psi \to \mu\mu$ and $Z \to \mu\mu$ events with respect to the p_T of the probe, for the five $|\eta|$ regions using all 2011 data.

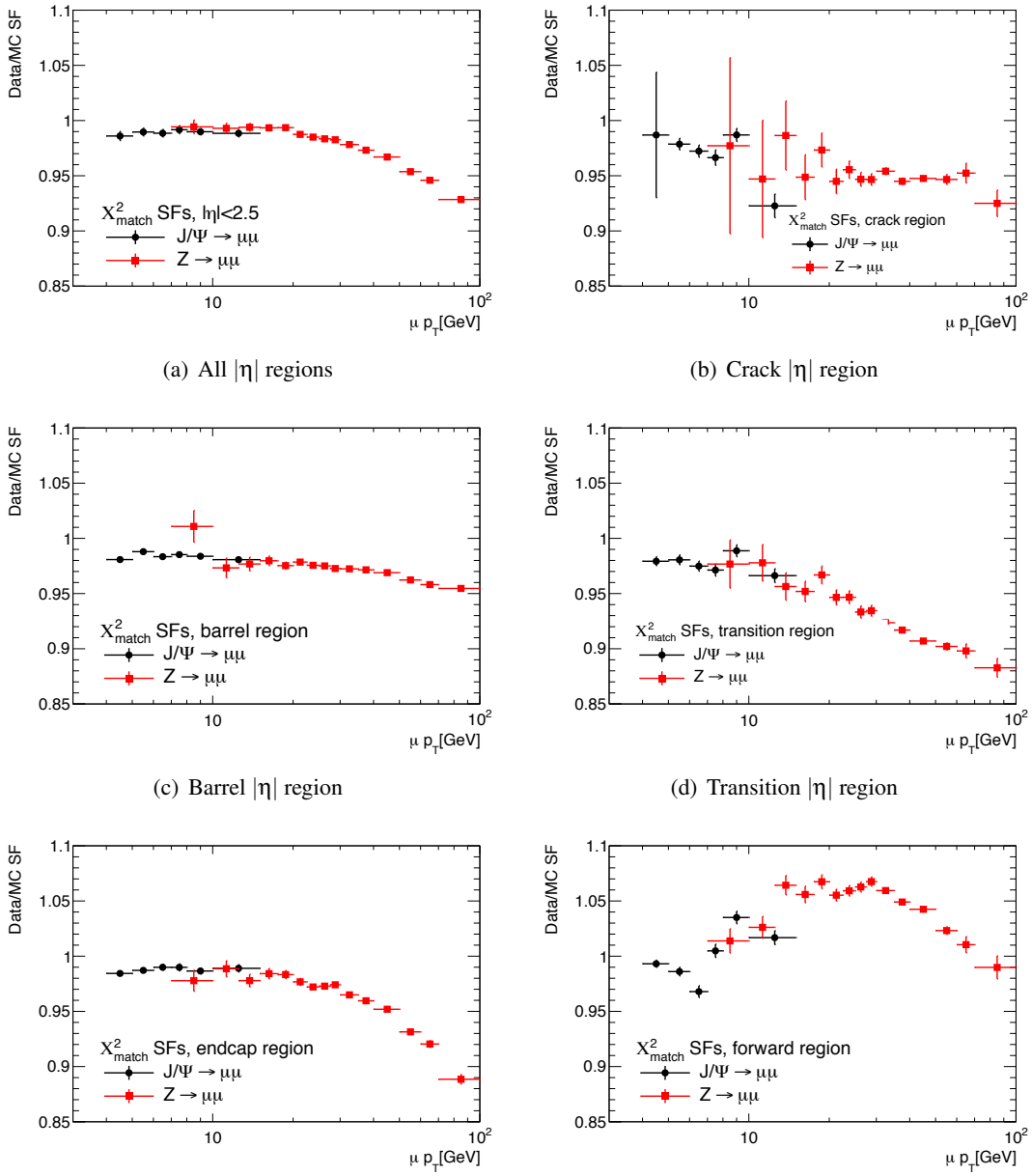

(a) All $|\eta|$ regions

(b) Crack $|\eta|$ region

(c) Barrel $|\eta|$ region

(d) Transition $|\eta|$ region

(e) Endcap $|\eta|$ region

(f) Forward $|\eta|$ region

Figure 7.29: Comparison of χ^2_{match} based soft muon tagger scale factors evaluated using $J/\psi \to \mu\mu$ and $Z \to \mu\mu$ [1] events with respect to the p_T of the probe, for the five $|\eta|$ regions using all 2011 data.

7.3 Kinematic Dependence of the SMT Mistag Rate, in Collision Data

A brief overview of work on the mistag rate is given, containing work performed by other members of the RHUL-QMUL SMT group [1] as mentioned in the Preface.

The mistag rate for the χ^2_{match} based soft muon tagger is defined as the fraction of jets originating from light flavour quarks (u,d and s) which are tagged by the SMT algorithm. This category includes decays in flight of light hadrons such as π and K mesons. Detector effects also contribute to the mistag rate, such as hadronic punch-through as mentioned in Section 6.4, and the interaction of jets with the calorimeter material, creating high p_{T} muon tracks in the MS. The mistag measurement presented here includes all these sources.

Since the mistag rate depends on the kinematics of the jet under consideration, the measurement is performed in bins of jet p_{T} and jet η : 20 GeV $< p_{\text{T}} <$ 30 GeV, 30 GeV $< p_{\text{T}} <$ 60 GeV, $p_{\text{T}} >$ 60 GeV for jet transverse momentum; $|\eta| < 1.2$ and $1.2 < |\eta| < 2.5$ for the jet pseudorapidity.

The mistag rate is measured directly from collision data using an inclusive sample of dijet events, and compared with expectations from studies on simulated data. In order to reduce Heavy Flavour (HF) contributions like $b\bar{b}$ and $c\bar{c}$, the mistag rate is extracted from the combination of two calibration samples defined using the information of a lifetime based flavour tagger [70]. One sample includes events where one of the two jets is required not to be tagged by the lifetime tagger; in the second sample the requirement is that neither jet be tagged by the lifetime tagger. The HF contribution in the latter sample is strongly suppressed ($< 1\%$). A systematic uncertainty is assigned to account for the effect of the residual contribution by varying the HF fractions in the simulation.

The mistag rate is studied as a function of the jet kinematics and no dependence is observed as can be seen in Figure 7.30. A single scale factor, SF = 1.44 $\pm$ 0.20 (stat. $\oplus$ syst.), is sufficient to describe the differences between data and simulation. The systematic uncertainty includes contributions from muon momentum corrections in the simulation, the uncertainty on the calibration of the lifetime tagger and the effect of a bias from the method with respect to the true mistag rate in simulation, observed at low jet p_{T}.

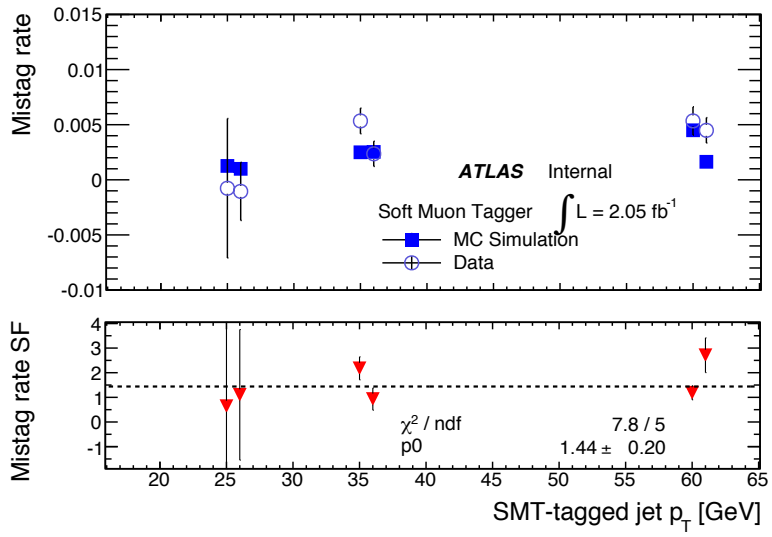

Figure 7.30: Mistag rate and data/simulation scale factor of the SMT algorithm as a function of the jet p_T. The filled squares show the expected rate in MC simulation, the circles show the observations from collision data. For graphics purposes, in each p_T bin the left most point is for central pseudorapidities, the rightmost for forward jets. The scale factor of the mistag rate is defined as the ratio of rates in data and simulation. The values are fitted with a constant function and the fit parameters are also provided [2].

The SF is applied to all true light flavour jets in simulated data. While initial studies have shown that the mistag rate is not dependent on pile-up (the effect of multiple pp interactions per event), this conclusion is limited by available statistics.

SMT muon distributions for signal and background events in the e+jets and μ+jets channels are shown in Figure 7.31 [1]. Both the multijet and W+jets distributions are taken from data and are normalised to their respective estimates. The distributions of the $p_{\text{T}}^{\text{rel}}$ of soft muons (used as the discriminating variable for the $p_{\text{T}}^{\text{rel}}$ based tagger) are also shown in Figure 7.31 for completeness. It is noted that the χ^2_{match} distributions for data and simulation are shifted in both channels, however the integrals of the data and Monte Carlo distributions below $\chi^2_{\text{match}} = 3.2$ are found to agree within uncertainties. Any mismodelling of the detector geometry in the simulation is accounted for by the χ^2_{match} scale factors. The χ^2_{match} of a muon is particularly sensitive to detector material, and so slight inaccuracies in the simulated model of the detector will have an effect on the χ^2_{match} distribution in Monte Carlo as opposed to collision data. Performance between the χ^2_{match} and the $p_{\text{T}}^{\text{rel}}$ taggers is seen to be equivalent in terms of b-tagging efficiency and mistag rate [81].

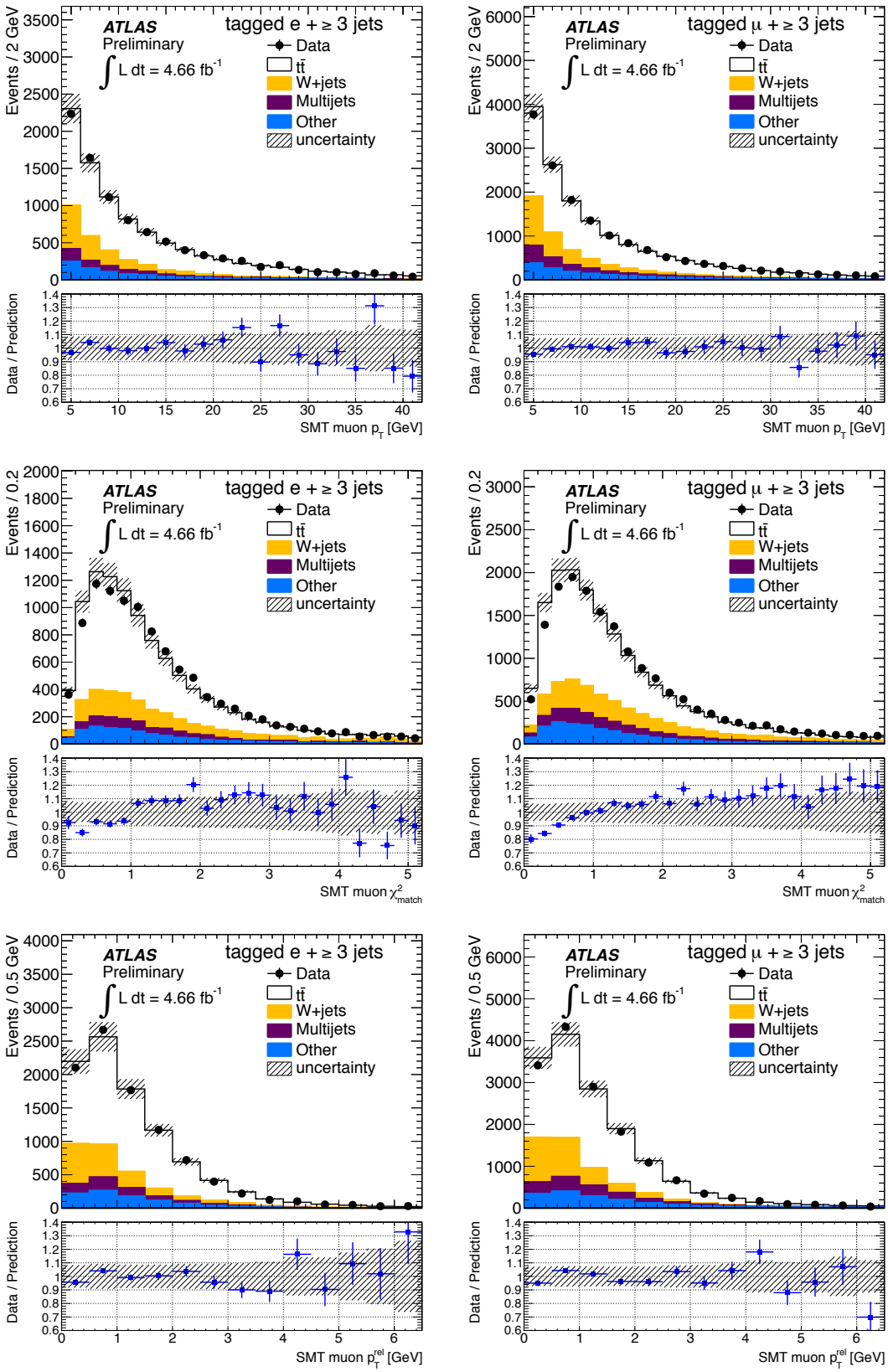

Figure 7.31: From the top left to the bottom right, the p_{T}, the χ^2_{match} (note that the cut is applied at $\chi^2_{\text{match}} < 3.2$) and the p_{T} relative to the jet axis ($p_{\text{T}}^{\text{rel}}$) of the soft muons in the e+jets channel (left) and μ+jets channel (right). Uncertainties include statistical and systematic contributions [1].

Chapter 8

The $\chi^2_{\mathbf{match}}$ based SMT $t\bar{t}$ Cross Section Analysis

This chapter contains a brief summary of a $t\bar{t}$ cross section measurement in the lepton+jets channel, conducted by the joint RHUL-QMUL SMT group [2, 3] as mentioned in the Preface.

8.1 The $\chi^2_{\mathbf{match}}$ based SMT Data/MC Scale Factors

The calibrations in data described in Chapter 7 are used in a measurement of the $t\bar{t}$ cross section in the lepton+jets channel [2]. The purpose of the data/MC scale factors for the χ^2_{match} based SMT is to refine the estimate of the performance of the SMT in simulated data to better reflect the actual performance in collision data. In this analysis, in all simulated data where the SMT is used, the truth flavour of the jet which is tagged is found. In the event that the source of the tagged jet is of heavy flavour (originating from a b or c quark), the kinematics of the tagged muon are used to select the appropriate χ^2_{match} tagging scale factor. If the truth flavour of the tagged jet is not heavy flavour (i.e. the jet has been mistagged) then the mistag scale factor is applied.

The purpose of performing this measurement using the χ^2_{match} based soft muon tagger is to probe the semileptonic b decay channel of top quark pairs. It is also a useful proof that soft muon tagging can be used for b-tagging in such a measurement, and allows the benefits of the tagger to be quantified, both in terms of the signal to background ratio achievable using this method,

and the systematic uncertainties which are unique to the tagger.

The cross section measurement is performed on data recorded by ATLAS from March to November 2011 (periods B-M, as defined in Table 4.1). After the requirements on the status of the detector and beam and the data quality have been satisfied, this dataset has an integrated luminosity of 4.7 fb^{-1} [41]. The cross section is calculated using Equation 8.1.

$$\sigma_{t\bar{t}} = \frac{N_{\text{data}} - N_{\text{bkg}}}{\int Ldt \cdot \varepsilon \cdot BR(\text{noFullHad})} \tag{8.1}$$

N_{data} and N_{bkg} are the data and background yields respectively and $BR(\text{noFullHad}) = 0.543$ is the lepton+jets and dilepton total branching ratio (BR), obtained from simulation [1]. The background yields are calculated using a combination of simulation and data driven methods.

The signal efficiency, ε, can be defined as the ratio of the number of $t\bar{t}$ events which pass all cuts to all generated $t\bar{t}$ events. The signal efficiency includes the geometric acceptance of the detector, the trigger efficiency and the event selection efficiency. This is calculated from simulation, and as such includes the tagging efficiency of the χ^2_{match} based soft muon tagger. In the calculation of ε, therefore, a data/simulation scale factor found in Section 7 is applied to any muon selected by the algorithm.

8.2 Object and Event Selection

The event selection for the $t\bar{t}$ cross section analysis is outlined in Section 6.1 for the μ+jets channel. The e+jets event selection is similar, except that exactly one good electron and no good muons are required.

The "good" electrons and muons are reconstructed electron and muon candidates with $E_{\text{T}} >$ 25 GeV for electrons, and $p_{\text{T}} > 20$ GeV for muons. These requirements are put in place to reduce the contribution from background processes producing low p_{T} leptons. Electrons are also required to have $|\eta| < 2.47$ and not be in the "crack" region between the barrel and the end-cap calorimeters ($1.37 < |\eta| < 1.52$). They must satisfy the "tight" selection using calorimeter, tracking and combined variables [2] [82]. Muons must be combined muons (as defined in Sec-

[1] The $BR(\text{noFullHad})$ includes the dilepton channel as the signal Monte Carlo sample used to obtain the efficiency includes the dilepton events. Any dilepton events that pass event selection are included in the signal (N_{data}), however the selection efficiency for dilepton events is negligible [3].

[2] The definitions of the quality cuts for electrons and muons can be found in Appendix C.

tion 5.3.1) passing the "tight" selection [83], and be found within the $|\eta| < 2.5$ range. Overlap removal in both channels is performed by removing events in which a selected electron and muon share the same reconstructed track in the detector.

If the lepton has been produced by the decay of a W boson it is expected to be isolated, and so a requirement is made that the leptons have etcone20$<$ 4 GeV and ptcone30$<$ 2.5 GeV (these isolation variables are defined in Section 6.1.1), and that the muons be separated from any jet with $p_T > 25$ GeV and jet vertex fraction > 0.75 by at least $\Delta R = 0.4$. The Υ and Z invariant mass vetoes mentioned in Section 6.1 are also applied.

Also the e+jets analysis requires that $\not{E}_T > 30$ GeV (missing transverse energy, indicating the presence of a neutrino) and that the transverse W mass (m_{TW}) > 30 GeV [3]. The μ+jets analysis requires that $\not{E}_T > 20$ GeV and that the sum of $\not{E}_T + m_{TW}$ be > 60 GeV [2].

The analysis requires that events passing the above event selection also have at least three good jets, of which at least one must be tagged by the SMT. Referring to Figure 8.1, it can be seen that with idealised jet reconstruction, this will select the lepton+jets channel but not the all-hadronic or dilepton channels.

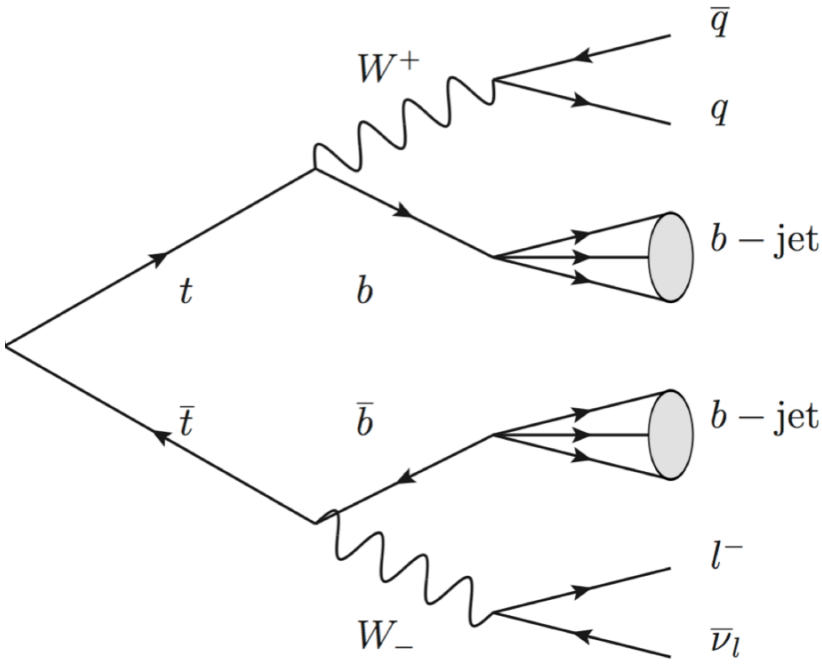

Figure 8.1: A Feynman diagram of the decay of a pair of top quarks via the lepton+jets channel.

[3]The missing transverse energy and the lepton p_{T} can be combined to produce a value of the transverse mass of the W, defined in $W \to \ell\nu$ decays as $M^2_{TW} = 2E_{T\nu}E_{T\ell} - 2p_{T\nu} \cdot p_{T\ell}$ [84, 85].

8.3 Data Driven Background Determination

The background processes with the largest contributions are the W+jets and the QCD multijet backgrounds, and these are estimated using data driven (DD) methods.

8.3.1 W+jets Background

The W+jets background signature contains a real lepton and $\not{E}_T$, indicating a neutrino. This is very similar to the lepton+jets signal. Two methods are used to estimate the W+jets contribution; the W charge asymmetry method, and the Berends-Giele scaling method to verify the results from the first method. Brief overviews of these methods are given here, and detailed explanations can be found in [2] and [3].

W Charge Asymmetry Method

At the LHC, the rate of W^++jets is expected to be higher than that of W^-+jets, due to the excess of u valence quarks as opposed to d quarks. The ratio of positively to negatively charged W bosons is predicted with far smaller theoretical uncertainty than that of the W+jets cross section. Consequently, the ratio can be used to find the overall normalisation of the W+jets background in the sample of events passing the event selection, before the SMT is applied (the "pretag" event selection).

To find the contribution from W+jets to the tagged sample, the tagging rate is used - this is the probability to tag a heavy or light flavour event with n-jets ($R^{n-\text{jets}}_{\text{tag},HF}$ and $R^{n-\text{jets}}_{\text{tag},LF}$ respectively). The tagging rates are derived from simulated data, and either the χ^2_{match} SMT scale factor or mistag rate scale factor is applied to any tagged jet, and used as shown in Equation 8.2. The ratios of $Wb\bar{b}$+jets, $Wc\bar{c}$+jets and Wc+jets out of all W+jets events are set to those observed in data using the tag counting method [86].

$$W^{n-\text{jets}}_{\text{tag}} = R^{n-\text{jets}}_{\text{tag},LF} \cdot W^{n-\text{jets}}_{\text{pretag},LF} + \sum_{HF}^{HF=c,c\bar{c},b\bar{b}} \left(R^{n-\text{jets}}_{\text{tag},HF} \cdot W^{n-\text{jets}}_{\text{pretag},HF} \right) \tag{8.2}$$

The yields of heavy and light flavour contributions to the total background in the e+jets and μ+jets channels are shown in Table 8.1.

Table 8.1: W+jets background estimation in the ≥ 3 jet bin, for the e+jets and μ+jets channels. The combined systematic and statistical uncertainties are shown.

Channel	Pretag events	Tagged events
e+jets	59300±5400	1640±330
μ+jets	117200±9300	2900±500

Berends-Giele Scaling Method

The Berends-Giele scaling states that the ratio of the number of $W+n$ jets to $W+n+1$ jets is approximately constant as a function of n [87]. Therefore the W+jets yield is found in the 1 and 2-jet control regions before tagging by subtracting all other background contributions from the data, and the ratio between the yields in these regions is used to estimate the expected yield in the ≥ 3-jet (signal) regions.

In order to find the W+jets contribution after tagging, the tagging rate in the signal region is estimated by multiplying the tagging rate in the 2-jet region by a factor estimated from simulation, which accounts for the expected difference in the heavy flavour composition between the control and signal regions.

The estimates for the W+jets contribution in the tagged signal region are found to be 1990 and 3410 events for the e and μ+jets channels respectively. Referring to Table 8.1, these values can be seen to agree within uncertainty with the estimates from the charge asymmetry method.

8.3.2 QCD Multijet Background

The multijet background processes can contaminate the signal region in the μ+jets channel by producing muons, both real and fake, which can be falsely identified as being from the decay of $W \to \mu\bar{\nu}_\mu$. Multijet processes can produce fake muons from decays in flight of light hadrons and hadronic punch-through, and the semileptonic decay of heavy flavour jets can produce real muons which can pass the event selection cuts. The multijet background in the e+jets channel contains both real and fake electrons, where the fakes can be produced by photon conversion within the detector, and the misidentification of jets with high EM fractions.

The QCD multijet background in both channels is estimated using the matrix method, shown in Equation 8.3. The fraction of real leptons (either e or μ) in the loose selection that also pass the standard selection is represented by r, and the fraction of fake leptons passing the loose selection

which also pass the standard selection is f. This implies that if N^{loose} and N^{std} are measured, and r and f are known, the number of events containing fake leptons can be found [3].

$$\begin{aligned} N^{\text{loose}} &= N^{\text{loose}}_{\text{real}} + N^{\text{loose}}_{\text{fake}} \\ N^{\text{std}} &= rN^{\text{loose}}_{\text{real}} + fN^{\text{loose}}_{\text{fake}} \end{aligned} \tag{8.3}$$

The fractions r and f are found using control samples of collision data which are enriched in either real or fake leptons (different control samples are used for the two lepton channels, full details of which can be found in [2]). The resultant yields in the two lepton+jets channels are shown in Table 8.2. "Pretag" includes all events passing the event selection, and "tagged" events are those identified by the SMT algorithm as coming from a semileptonic b decay.

Table 8.2: QCD multijet background estimation in the ≥ 3 jet bin, for the e+jets and μ+jets channels. The combined systematic and statistical uncertainties are shown.

Channel	Pretag events	Tagged events
e+jets	16170±8085	620±311
μ+jets	26952 ± 5390	1310 ± 345

8.4 Measured b-tagging Efficiencies

The b-tagging efficiency found in simulated data as a function of the b-jet p_{T} is further adjusted to account for differences between data and simulation [4]. The BRs of the semileptonic b decay, producing soft muons, are adjusted to the world average values [6], for direct ($b \to \mu$) and also sequential decays ($b \to c \to \mu^+$, $b \to \bar{c} \to \mu^-$ and $b \to \tau \to \mu$) as described in Section 6.2. The jet energy is corrected to better reflect the results observed in data (as mentioned in Section 6.3.3), and an ad-hoc correction is applied to account for the momenta of the neutrino and muon in the semileptonic b decays, as there is not a jet energy scale yet available which accounts for the unique kinematics of the semileptonic b-jets. This has little effect on the results of the $t\bar{t}$ cross section analysis as the only jet p_{T} requirement is that the p_{T} is above the minimum threshold of 25 GeV, but it has a large effect when looking at the dependence of the performance of the SMT on the jet p_{T} as investigated in Section 6.3.2.

Any remaining differences between the data and simulation descriptions of the fragmentation and hadronisation stages of the soft muon production are accounted for by an ad-hoc systematic uncertainty on the b-tagging efficiencies. The adjusted b-tagging efficiency is termed the "uncalibrated" efficiency. The efficiency is then scaled using the χ^2_{match} tagging and mistag scale factors to produce the "data-calibrated" efficiency. The data-calibrated efficiency should therefore reproduce the b-tagging efficiency observed in collision data. The comparison between the calibrated and uncalibrated efficiencies is shown in Figure 8.2, along with an overall b-tagging scale factor between the two. This efficiency can be seen to be similar to that in Figure 6.5, as both describe the b-tagging efficiency found in simulated data as a function of the b-jet p_{T}, albeit with and without corrections from collision data.

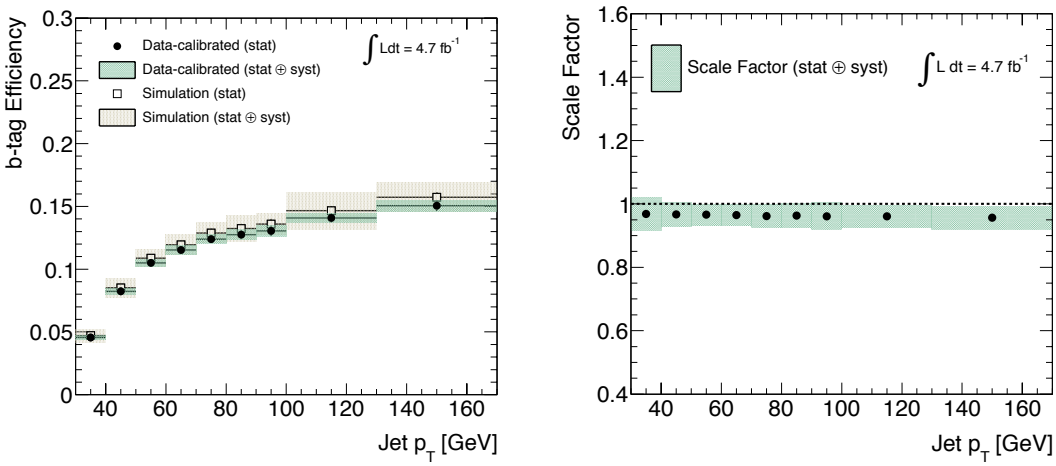

(a) b-jet tagging efficiency, data-calibrated and uncalibrated

(b) b-jet tagging efficiency scale factor (data-calibrated/uncalibrated)

Figure 8.2: Data-calibrated and uncalibrated b-jet tagging efficiencies and scale factor, with respect to the p_{T} of the b-jet. Produced from simulation and calibrated using collision data [4].

8.5 Systematic Uncertainties

The SMT calibration contributes to a b-tagging systematic uncertainty which is unique to this analysis, being a combination of the uncertainties on the χ^2_{match} efficiency and also the SMT mistag rate. The contributions to the total systematic uncertainty on the cross section measurement for each source of uncertainty are found by calculating the cross section using the maximum and minimum values of each contributing factor individually. The yields for the e+jets

and μ+jets channels are resummed for each contribution to the total systematic uncertainty, to account for any correlation between the channels.

Table 8.3: Summary of individual relative systematic uncertainty contributions to the cross section measurement, in percent.

	Relative cross section uncertainty [%]		
Source ($\geq$ 3 Jets)	e+jets	μ+jets	Combined
Statistical Uncertainty	$\pm$1.5	$\pm$1.3	$\pm$1.0
Object Selection			
Lepton Energy Resolution	+0.4 /-0.3	+0.2 /-0.01	+0.2 /-0.1
Lepton Reco, ID, trigger	+2.4 /-2.5	+1.5 /-1.5	+1.7 /-1.8
Jet Energy Scale	+3.8 /-4.3	+3.2 /-3.6	+3.5 /-3.8
Jet Energy Resolution	$\pm$0.2	$\pm$0.5	$\pm$0.2
Jet Reconstruction Efficiency	$\pm$0.06	$\pm$0.06	$\pm$0.06
Jet Vertex Fraction	+1.2 /-1.4	+1.2 /-1.4	+1.2 /-1.4
$\not{E}_T$ Uncertainty	$\pm$0.06	$\pm$0.08	$\pm$0.07
SMT Calibration			
SMT Muon Reco, ID	$\pm$1.3	$\pm$ 1.3	$\pm$1.3
SMT Muon χ^2_{match}Efficiency	$\pm$0.6	$\pm$0.6	$\pm$0.6
Background Estimates			
Multijet Normalisation	$\pm$ 5.2	$\pm$ 3.9	$\pm$ 4.4
W+jet Normalisation	$\pm$ 5.2	$\pm$ 5.7	$\pm$ 5.5
Other Bkg Normalisation	$\pm$ 0.2	$\pm$ 0.2	$\pm$ 0.1
Other Bkg Systematics	+1.6 /-1.5	+2.5 /-2.0	+2.2 /-1.8
Signal Simulation			
$b \to \mu X$ Branching Ratio	+2.9 /-3.0	+2.9 /-3.1	+2.9 /-3.1
ISR/FSR	$\pm$ 2.4	$\pm$ 0.9	$\pm$ 1.5
PDF	$\pm$ 3.2	$\pm$ 3.0	$\pm$ 3.1
NLO Generator	$\pm$ 3.2	$\pm$ 3.2	$\pm$ 3.2
Parton Shower	$\pm$ 2.2	$\pm$ 2.2	$\pm$ 2.2
Total Systematics	+11.1 /-11.3	+10.2 /-10.3	+10.5 /-10.6
Integrated Luminosity	$\pm$ 1.8	$\pm$ 1.8	$\pm$ 1.8

Table 8.3 shows the full list of systematic uncertainties on the cross section measurement, and the total contribution from all the systematics. The uncertainty on the jet energy scale is found using the calorimeter response to isolated single hadrons in collision data, pion test beam measurements, uncertainties on the modelling of the material of the ATLAS detector and the Monte Carlo modelling used in producing the simulated data. The JES uncertainty has a large impact on the $t\bar{t}$ cross section measurement,contributing $^{+3.5\%}_{-3.8\%}$ to the total systematic uncertainty.

Comparison of SMT uncertainty with the SV0 and JetProb methods

The SMT data/MC scale factors contribute a unique uncertainty to the cross section measurement, the impact of which is found by varying the applied scale factors to their maximum and minimum values, and recalculating the calculated cross section using these values. The SMT calibration contributes $\pm 1.4\%$ to the overall systematic uncertainty on the cross section measurement, but the BR systematic should also be included as it is unique to this tagger, bringing the unique systematic up to $^{+3.2\%}_{-3.4\%}$. This compares favourably to the systematic uncertainties inherent in lifetime based taggers, for example the SV0 and JetProb taggers used in the $t\bar{t}$ cross section measurement in the lepton+jets channel [88] which have a b-tagging calibration uncertainty of $^{+7.5\%}_{-6.3\%}$.

It has been shown that, for operating points of 50% b-tagging efficiency for both SV0 and JetProb, an average mistag rate (across all jet p_{T} and η) of approximately 0.5% is found [89]. The analysis in [88] also uses an SV0 operating point of 50% b-tagging efficiency, and achieves a mistag rate of $< 0.4\%$. This b-tagging efficiency is significantly larger than that achievable by the SMT, however the BR of semileptonic b decays is not taken into account as mentioned in Section 5.4.2. The mistag rate of the SMT is found from Monte Carlo to be between 0.1% and 0.5%, depending on the p_{T} of the tagged jet as shown in Section 7.3 [2]. The signal to background ratios achieved are shown in Table 8.4 - the signal to background ratio is found by dividing the number of expected $t\bar{t}$ events (found from Monte Carlo simulation) by the total estimated background contributions for the pretag and tagged samples (found using both MC and DD methods).

Table 8.4: Comparison of signal to background ratios (S/B) for $t\bar{t}$ cross section measurements performed using SMT and JetProb+SV0 b-tagging algorithms.

	χ^2_{match} based SMT		JetProb+SV0	
Channel	Pretag S/B	Tagged S/B	Pretag S/B	Tagged S/B
e+Jets	0.35 ± 0.16	1.87 ± 0.35	0.24 ± 0.07	4.38 ± 1.83
μ+jets	0.32 ± 0.11	1.51 ± 0.26	0.15 ± 0.05	2.84 ± 0.77

8.6 Results and Conclusion

As mentioned in Section 8.2, the analysis accepts events that have at least three good jets, of which at least one must be SMT tagged. Table 8.5 shows the yield of events passing event selection, containing three or more jets, for all data and all background sources determined using simulation only, as well as the contribution from QCD and W+jets, which is determined using data driven methods described in Section 8.3.

The signal selection efficiencies, found by applying the full selection described above on the simulated $t\bar{t}$ signal sample (which includes both dilepton and lepton+jets events), are $1.42 \pm 0.02\%$ in the e+jets channel and $2.15 \pm 0.02\%$ in the μ+jets channel [2]. The fully hadronic acceptance is negligible and consequently is not quoted.

Table 8.5: Observed event yields in the pretag and tagged ≥ 3 jet bin and background estimates with the quadrature sum of the statistical and systematic uncertainties. The multijet and W+jets backgrounds are evaluated with data driven techniques whilst all other backgrounds are evaluated with Monte Carlo simulation [2]. The signal to background ratio is given to show the background rejection power of the χ^2_{match} based soft muon tagger.

	e+jets		**μ+jets**	
Sample	**Pretag**	**Tagged**	**Pretag**	**Tagged**
Data(4.66 fb^{-1})	124424	9165	227318	14940
$t\bar{t}$ MC	31900±1300	5980±350	52100±1600	9100±500
W+jets DD	59300±5400	1640±330	117200±9300	2900±500
Multijet DD	16200±8100	620±310	27000±5400	1310±350
Z+jets MC	9900^{+2500}_{-1400}	$270\pm^{+40}_{-30}$	11500^{+2400}_{-1600}	780^{+140}_{-100}
Single top MC	4300±400	630±60	7200±600	980±80
DiBoson MC	1190^{+220}_{-180}	40±10	2030^{+350}_{-300}	60±10
$t\bar{t}$ MC + Backgrounds	123000±10000	9200±600	217000±12000	15100±800
Measured $t\bar{t}$		6000±500		8900±600
Signal/Background	0.35 ± 0.16	1.87 ± 0.35	0.32 ± 0.11	1.51 ± 0.26

8.6.1 The $t\bar{t}$ Cross Section Measurement

The e+jets and μ+jets analyses are combined by summing the event yields for the data, signal and background MC. The systematic uncertainty assigned to the combined result is evaluated

for each systematic uncertainty individually so as to take into account any correlations.

In a sample of 4.7fb^{-1}, corresponding to the 2011 dataset, the $t\bar{t}$ production cross section has been measured, using semileptonic b decays, with an inclusive cross section [4] of

$$\sigma_{t\bar{t}} = 165 \pm 2(\text{stat.}) \pm 17(\text{syst.}) \pm 3(\text{lumi.}) \text{ pb}.$$

The method used to identify semileptonic b decays is to require a well reconstructed muon inside at least one reconstructed jet within the event (Soft Muon Tagging), with the χ^2_{match} of the match between ID and MS used as a discriminant by which to choose the muons. The soft muon tagger is calibrated using data samples corresponding to the full 2011 dataset. The analysis is done in the lepton+jets $t\bar{t}$ decay channel using electrons and muons, and the most important backgrounds are estimated using data-driven methods. The kinematic properties of the selected events are consistent with SM $t\bar{t}$ production. The final result is compatible with the theoretical prediction of $\sigma_{t\bar{t}} = 165^{+11}_{-16}$ pb in simulated data, and with published ATLAS and CMS measurements using b-tagging in the lepton+jets channel:

$$\begin{aligned} \text{ATLAS [88]:} \quad & \sigma_{t\bar{t}} = 186 \pm 10(\text{stat.})^{+20}_{-21}(\text{syst.}) \pm 6(\text{lumi.}) \text{ pb} \\ \text{CMS [90]:} \quad & \sigma_{t\bar{t}} = 164.4 \pm 2.8(\text{stat.}) \pm 11.9(\text{syst.}) \pm 7.4(\text{lumi.}) \text{ pb} \end{aligned}$$

The total uncertainty is systematics-dominated, coming mainly from the background estimates and the jet energy scale. The b-tagging uncertainty is smaller than the calibration uncertainty with lifetime based taggers - the SV0 and JetProb taggers used in the cross section measurement in the lepton+jets channel [88] have a b-tagging calibration uncertainty of $^{+7.5\%}_{-6.3\%}$, compared to the $\pm 1.4\%$ systematic uncertainty from the SMT calibration ($^{+3.2\%}_{-3.4\%}$ including the BR reweighting uncertainty). The uncertainties and the performance of the SMT algorithm are unaffected by the pile-up conditions present in the 2011 dataset.

[4] The "stat." uncertainty is the statistical uncertainty on the measurement, "syst." represents the quadrature sum of all systematic uncertainties and "lumi." is the uncertainty on the ATLAS luminosity measurement - these uncertainties are listed as percentages in Table 8.3.

Chapter 9

Conclusions

A new method for identifying b-jets has been presented, which uses the quality of the match between tracks left in the inner detector and muon spectrometer of the ATLAS detector (χ^2_{match}) to find muons of low, or "soft", transverse momentum which are likely to have been produced by the decay of B hadrons within the jets. The performance of this Soft Muon Tagger (SMT) has been shown to be comparable to that of another method which makes use of the relative transverse momentum of a muon to the axis of the jet within which it is found.

The χ^2_{match} based SMT has been characterised in simulated data, and found to be capable of tagging jets of heavy flavour with acceptable efficiency, and the sources of incorrectly tagged jets have been understood. In order to use the tagger on collision data, the efficiency of the tagger with respect to the kinematics of the soft muon has been investigated, and appropriate collision/simulated data scale factors have been produced which can be applied to tagged muons in the sample of collision data. The tagger has been used to identify the semileptonic b decay signature of top quark decays, for a measurement of the top quark pair production cross section ($\sigma_{t\bar{t}}$) in the lepton+jets decay channel in 2011 data.

The use of the χ^2_{match} based SMT contributes a unique systematic uncertainty to the overall uncertainty on the cross section measurement, and this is found to have a $^{+3.2\%}_{-3.4\%}$ effect on the total cross section. The cross section is found to be

$$\sigma_{t\bar{t}} = 165 \pm 2(\text{stat.}) \pm 17(\text{syst.}) \pm 3(\text{lumi.})\ \text{pb}$$

and good agreement is observed between the e+jets and μ+jets channels. This cross section

measurement is consistent with theoretical predictions, and with other $t\bar{t}$ cross section measurements which make use of b-tagging in the lepton+jets channel, both in ATLAS [88] and CMS [90].

It has been demonstrated that the χ^2_{match} based SMT can be used for heavy flavour tagging in collision data, and that it has a low contribution to the systematic uncertainty while providing a good signal to background ratio. As such, it could be used in Higgs searches in the $H \to b\bar{b}$ decay channel, which has a branching ratio of $56.1 \pm 1.9\%$ for a Higgs boson of mass 126.0 GeV (the mass of the Higgs boson as discovered by ATLAS [14]). The production of $t\bar{t}H$ at ATLAS is likely to result in four b-jets ($t\bar{t}H \to WbWbbb$) so the probability of there being at least one semileptonic b-decay containing a muon is therefore approximately 59.0% [1], meaning that a b-tagging algorithm with low systematic uncertainties and a high signal to background ratio can be of great use in establishing the cross section of $t\bar{t}H$ production.

The SMT could also be of use in any top analysis which has limited precision due to systematic uncertainties. It is also possible to make use of the semileptonic b decays to perform a top mass measurement, by finding the invariant mass of the muons produced in the W and b decays [91]. This mass will be correlated with the top mass but not sensitive to the jet energy scale calibration.

[1] $1-(1-\text{BR}(b \to \mu\nu X))^4$

Appendix A

CP Violation

CP symmetry proposes that, the amplitude (M) of a process $a \to b$ must be the same as the amplitude ($\bar{M}$) of the process $\bar{a} \to \bar{b}$ involving the corresponding antiparticles. The amplitudes can be separated into magnitude and phase as $M = |M|e^{i\theta}$, and a phase term from the CKM matrix can be introduced as $e^{i\phi}$. In the event that there is only one possible route for the process $a \to b$, then the measured rate of the process $|M|^2$ does not differ from $|\bar{M}|^2$ as shown in Equation A.1.

$$\begin{aligned} |M|^2 &= |M|e^{i\theta}e^{i\phi} \cdot |M|e^{-i\theta}e^{-i\phi} &= |M|^2 \\ |\bar{M}|^2 &= |\bar{M}|e^{i\theta}e^{-i\phi} \cdot |\bar{M}|e^{-i\theta}e^{i\phi} &= |M|^2 \\ |M|^2 - |\bar{M}|^2 &= 0 \end{aligned} \tag{A.1}$$

However, if there are two routes for the process $a \to b$, the amplitudes are as shown in Equation A.2, and the rates of the processes are not identical as shown in Equation A.3. This shows that a complex phase results in different rates for processes involving particles and their antiparticles, thereby violating CP symmetry.

$$\begin{aligned} M &= |M_1|e^{i\theta_1}e^{i\phi_1} + |M_2|e^{i\theta_2}e^{i\phi_2} \\ \bar{M} &= |M_1|e^{i\theta_1}e^{-i\phi_1} + |M_2|e^{i\theta_2}e^{-i\phi_2} \end{aligned} \tag{A.2}$$

$$\begin{aligned} |M|^2 &= |M_1|^2 + |M_2|^2 + |M_1||M_2|(e^{i(-\theta_1-\phi_1+\theta_2+\phi_2)} + e^{-i(-\theta_1-\phi_1+\theta_2+\phi_2)}) \\ |\bar{M}|^2 &= |M_1|^2 + |M_2|^2 + |M_1||M_2|(e^{i(-\theta_1+\phi_1+\theta_2-\phi_2)} + e^{-i(-\theta_1+\phi_1+\theta_2-\phi_2)}) \\ |M|^2 - |\bar{M}|^2 &= -4sin(\theta_1-\theta_2)sin(\phi_1-\phi_2) \end{aligned} \tag{A.3}$$

Appendix B

Covariance Matrices

The covariance matrix between track parameters in the ID and MS of ATLAS is given by

$$\mathbf{C}_{ij} = (T_i - \langle T_i \rangle)(T_i - \langle T_j \rangle)$$

where T_i are the elements of the vector $\mathbf{T}$, which contains five track parameters, $T_i = \eta, \phi, p_{\mathrm{T}}, d_0$ or z_0 [72]. $\langle T_j \rangle$ is the expected value of T_i. The measurement uncertainty on these is $\Delta T_i = T_i - \langle T_i \rangle$. The limited resolution of the detector components is the source of these measurement uncertainties. Equation B.1 shows the expanded form of $\mathbf{C}_{\mathrm{X}}$, representing either $\mathbf{C}_{\mathrm{MS}}$ or $\mathbf{C}_{\mathrm{ID}}$, and the covariance term from Equation 5.1 is shown in Equation B.2. The covariance matrices are symmetric, as the uncertainties on the measured values commute.

$$\mathbf{C}_{\mathrm{X}} = \begin{pmatrix} (\Delta\eta\Delta\eta)_{\mathrm{X}} & (\Delta\eta\Delta\phi)_{\mathrm{X}} & (\Delta\eta\Delta p_{\mathrm{T}})_{\mathrm{X}} & (\Delta\eta\Delta d_0)_{\mathrm{X}} & (\Delta\eta\Delta z_0)_{\mathrm{X}} \\ (\Delta\phi\Delta\eta)_{\mathrm{X}} & (\Delta\phi\Delta\phi)_{\mathrm{X}} & (\Delta\phi\Delta p_{\mathrm{T}})_{\mathrm{X}} & (\Delta\phi\Delta d_0)_{\mathrm{X}} & (\Delta\phi\Delta z_0)_{\mathrm{X}} \\ (\Delta p_{\mathrm{T}}\Delta\eta)_{\mathrm{X}} & (\Delta p_{\mathrm{T}}\Delta\phi)_{\mathrm{X}} & (\Delta p_{\mathrm{T}}\Delta p_{\mathrm{T}})_{\mathrm{X}} & (\Delta p_{\mathrm{T}}\Delta d_0)_{\mathrm{X}} & (\Delta p_{\mathrm{T}}\Delta z_0)_{\mathrm{X}} \\ (\Delta d_0\Delta\eta)_{\mathrm{X}} & (\Delta d_0\Delta\phi)_{\mathrm{X}} & (\Delta d_0\Delta p_{\mathrm{T}})_{\mathrm{X}} & (\Delta d_0\Delta d_0)_{\mathrm{X}} & (\Delta d_0\Delta z_0)_{\mathrm{X}} \\ (\Delta z_0\Delta\eta)_{\mathrm{X}} & (\Delta z_0\Delta\phi)_{\mathrm{X}} & (\Delta z_0\Delta p_{\mathrm{T}})_{\mathrm{X}} & (\Delta z_0\Delta d_0)_{\mathrm{X}} & (\Delta z_0\Delta z_0)_{\mathrm{X}} \end{pmatrix} \tag{B.1}$$

$$\mathbf{C}_{\mathrm{MS}} + \mathbf{C}_{\mathrm{ID}} = \begin{pmatrix} (\Delta\eta\Delta\eta)_{\mathrm{MS}} + (\Delta\eta\Delta\eta)_{\mathrm{ID}} & (\Delta\eta\Delta\phi)_{\mathrm{MS}} + (\Delta\eta\Delta\phi)_{\mathrm{ID}} & \cdots & (\Delta\eta\Delta z_0)_{\mathrm{MS}} + (\Delta\eta\Delta z_0)_{\mathrm{ID}} \\ (\Delta\phi\Delta\eta)_{\mathrm{MS}} + (\Delta\phi\Delta\eta)_{\mathrm{ID}} & (\Delta\phi\Delta\phi)_{\mathrm{MS}} + (\Delta\phi\Delta\phi)_{\mathrm{ID}} & \cdots & (\Delta\phi\Delta z_0)_{\mathrm{MS}} + (\Delta\phi\Delta z_0)_{\mathrm{ID}} \\ \vdots & \vdots & \ddots & \vdots \\ (\Delta z_0\Delta\eta)_{\mathrm{MS}} + (\Delta z_0\Delta\eta)_{\mathrm{ID}} & (\Delta z_0\Delta\phi)_{\mathrm{MS}} + (\Delta z_0\Delta\phi)_{\mathrm{ID}} & \cdots & (\Delta z_0\Delta z_0)_{\mathrm{MS}} + (\Delta z_0\Delta z_0)_{\mathrm{ID}} \end{pmatrix} \tag{B.2}$$

Appendix C

Muon and Electron Quality Definitions

The definitions of the muon quality cuts for both Muid and STACO muons are given in Table C.1 [83]. The definitions of the electron identification cuts are shown in Table C.2 [92].

Table C.1: Definition of loose, medium and tight muon identification cuts, for the Muid and STACO muon reconstruction algorithms.

Description	Quality Word
Muid	
Muid has found a combined muon	tight
Muid has found a standalone muon with at least three hits in the MDT and CSC	tight
Reconstructed using MuGirl with an extended track and ≥ 2 MDT and CSC hits	tight
Reconstructed using MuGirl with an extended track OR $\lvert\eta\rvert < 0.2$ OR ≥ 2 muon track segments	medium
MuTagIMO at $\lvert\eta\rvert < 0.2$ OR ≥ 2 muon track segments	medium
MuGirl OR MuTagIMO OR MuidStandalone (These identify muons based on ID info. only)	loose
STACO	
All STACO candidates (STACO tracks are combined MS/ID tracks or pure MS tracks when $\lvert\eta\rvert < 2.5$	tight

Table C.2: Definition of variables used for loose, medium and tight electron identification cuts for the central region of the detector ($|\eta| < 2.47$).

Type	Description	Variable name
Loose cuts		
Detector acceptance	· $|\eta| < 2.47$	
Hadronic leakage	· Ratio of ET in the first layer of the hadronic calorimeter to ET of the EM cluster (used over the range $|\eta| < 0.8$ and $|\eta| > 1.37$) · Ratio of ET in the hadronic calorimeter to ET of the EM cluster (used over the range $0.8 < |\eta| < 1.37$)	R_{had1} R_{had}
Second layer of EM calorimeter	· Ratio in η of cell energies in 3×7 versus 7×7 cells. · Lateral width of the shower.	R_η w_{η^2}
Medium cuts (includes Loose)		
First layer of EM calorimeter.	· Total shower width. · Ratio of the energy difference associated with the largest and second largest energy deposit over the sum of these energies	w_{stot} E_{ratio}
Track quality	· Number of hits in the Pixel detector (1) · Number of hits in the Pixels and SCT (7) · Transverse impact parameter (< 5 mm)	d_0
Track matching	· $\Delta\eta$ between the cluster and the track (< 0.01)	$\Delta\eta_1$
Tight cuts (includes Medium)		
b-layer	· Number of hits in the b-layer (1)	
Track matching	· $\Delta\phi$ between the cluster and the track (< 0.02) · Ratio of the cluster energy to the track momentum · Tighter $\Delta\eta$ cut (< 0.005)	$\Delta\phi_2$ E/p $\Delta\eta_1$
Track quality	· Tighter transverse impact parameter cut (< 1 mm)	d_0
TRT	· Total number of hits in the TRT · Ratio of the number of high-threshold hits to the total number of hits in the TRT	
Conversions	· Electron candidates matching to reconstructed photon conversions are rejected	

Appendix D

Jet Flavour Truth Labelling

There is a reconstruction algorithm used in ATLAS simulated data which attempts to match jets to their originating process, after which jets within the simulated sample are tagged as having a "truth flavour". This flavour corresponds to the PDG ID [1] of the quark from which they are thought to have been produced. A reconstructed jet would be said to have a truth flavour of 5 if there were a b quark within $\Delta R < 0.3$ of the jet. If this algorithm has a high efficiency, a high proportion of jets with truth flavour of 5 will be matched to true b quarks, and vice versa. It should be noted that the jets tested here are all "good" jets [2], and so any jets which do not meet the requirements of being a good jet are excluded from the matching, meaning that the overall efficiency of matching the jets to b quarks cannot be 100%. To test this matching, the plots in Figure D.1 and D.2 were produced. The former shows the ΔR between each true b quark from $t \to b$ and the nearest jet of truth flavour 5 (if there is any such jet present), and the corresponding percentage of b quarks where this $\Delta R(b, \text{jet}) < 0.4$. Figure D.2 shows the ΔR between the jet and the nearest true b quark. The largest value of ΔR between the jet and the nearest true b quark is 0.3, as expected from the definition of truth flavour tagged jets mentioned above - if the nearest b quark were over $\Delta R = 0.3$ from the jet axis, then the jet would not have truth flavour of 5. There is no such absolute cutoff seen in the ΔR distribution when the $t \to b$ quark is taken as the origin point - the nearest jet of truth flavour 5 may be more than $\Delta R = 0.3$ away, meaning that the particular b quark was not discovered by the flavour tagging algorithm, and either a closer b quark (maybe not from a $t \to b$ decay) caused the jet to be labelled as truth flavour 5, or it was

[1] The PDG ID is a number ascribed to a particular Monte Carlo simulated particle, with each Fermion, Boson and hadron given a unique number - b and c quarks are numbered 4 and 5 respectively [6].

[2] Jet $p_{\mathrm{T}} > 25$ GeV, JVF > 0.75.

labelled incorrectly.

There is a clear dependence observed on the p_{T} of the denominator of the efficiency (Figure D.1(b)). Jets near high momentum b quarks are far more likely to be matched correctly, with an efficiency approaching 100% for b quarks of $p_{\mathrm{T}} > 60$ GeV. The efficiency of each muon cut within the χ^2_{match} based soft muon tagger is investigated with respect to the p_{T} of all jets with truth flavour of 5, as was done in Section 6.3.1 for b quarks and all jets matched to these quarks, but with no matching of reconstructed entities to truth information beyond the truth flavour labelling of the jet. The resultant distributions, shown in Figure D.3, are similar to those found using all reconstructed jets matched to the b quark, (Figure 6.6(a) in Section 6.3.1) but the efficiencies are systematically higher as would be expected before the matching of the SMT muon to truth muons from $t \to b \to \mu$.

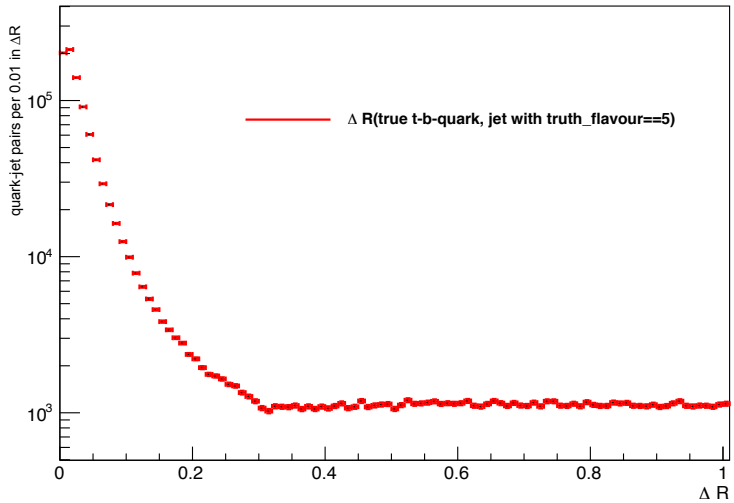

(a) Distribution of ΔR between a true b quark from $t \to b$ and the nearest jet of truth flavour 5.

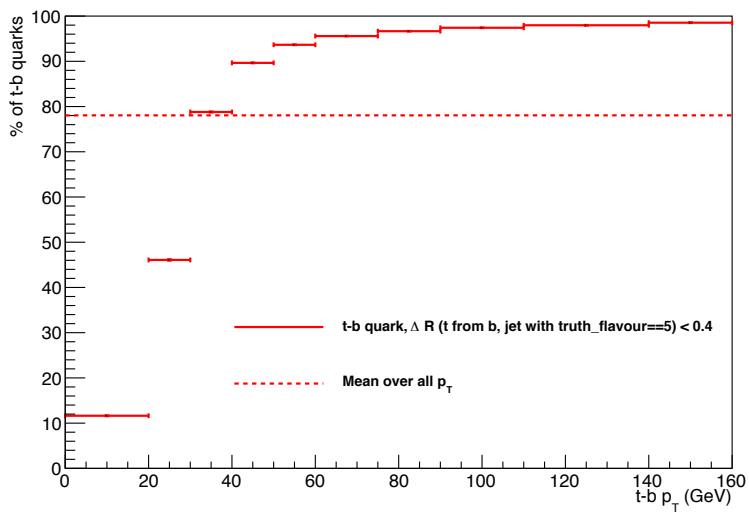

(b) Efficiency of matching true b quarks from $t \to b$ to jets with truth flavour 5. The dashed lines represent the mean values across all p_{T}.

Figure D.1: Efficiency of matching true b quarks from $t \to b$ and jets of truth flavour 5.

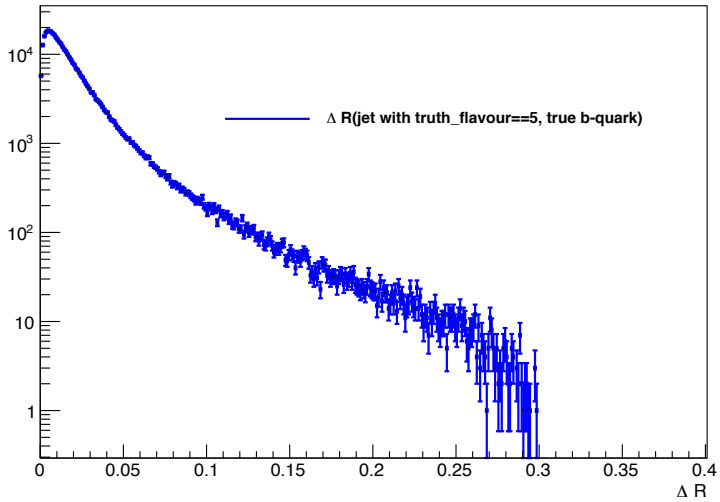

Figure D.2: Distribution of ΔR between a jet of truth flavour 5 and the nearest true b quark

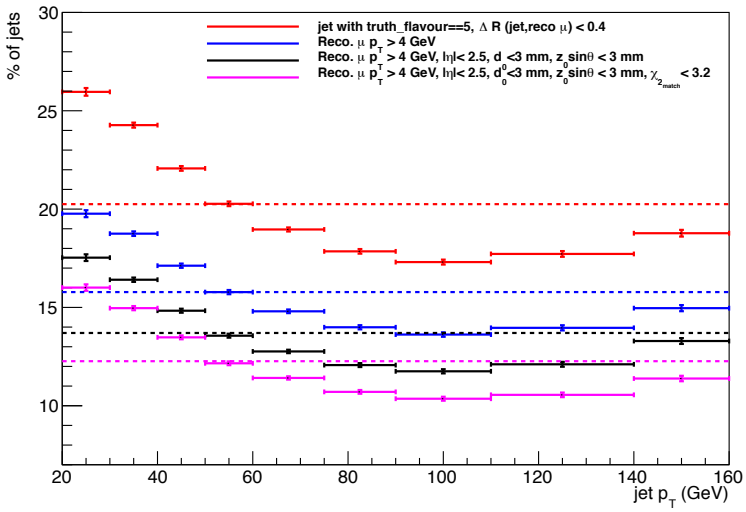

Figure D.3: Inclusive ε_b^{μ} with respect to jets labelled as truth flavour 5, matched to the reconstructed muon. The dashed lines represent the mean values across all p_{T}.

Appendix E

Decay Chains of “Fake” Muons

Section 6.4 describes an investigation of the true sources of muons which have been incorrectly identified as resulting from a $t \to b \to \mu$ decay by the χ^2_{match} based soft muon tagger, when running on simulated data. The decay chains of a random sample of these “fakes” are shown in Table E.1. The quark content of each hadron in the decay chain is shown, and the dashed arrows ($\dashrightarrow$) refer to the fragmentation and hadronisation stage.

Table E.1: The full decay chains of a sample of muons incorrectly tagged as originating from a $t \to b \to \mu$ decay.

Channel	Decay Chain
$t \to W \to X_c \to \mu$	$p \to g \to \bar{t} \to W^- \to \bar{c} \dashrightarrow D_{s1}(H)^-[s\bar{c}] \to \bar{D}^*(2007)^0[u\bar{c}] \to \bar{D}^0[u\bar{c}] \to \mu^-$
	$p \to u \to t \to W^+ \to c \dashrightarrow D_{s2}^{*+}[c\bar{s}] \to D^*(2010)^+[c\bar{d}] \to D^+[c\bar{d}] \to \mu^+$
	$p \to g \to \bar{t} \to W^- \to \bar{c} \to c \dashrightarrow D^*(2010)^+[c\bar{d}] \to D^0[c\bar{u}] \to \mu^+$
	$p \to g \to \bar{t} \to W^- \to \bar{c} \dashrightarrow D_1(2420)^0[u\bar{c}] \to D^-[d\bar{c}] \to \mu^-$
	$p \to \bar{d} \to \bar{t} \to W^- \to \bar{c} \dashrightarrow \bar{D}^*(2007)^0[u\bar{c}] \to \bar{D}^0[u\bar{c}] \to \mu^-$
	$u \to t \to W^+ \to c \dashrightarrow D^*(2010)^+[c\bar{d}] \to D^+[c\bar{d}] \to \mu^+$
	$p \to g \to \bar{t} \to W^- \to \bar{c} \dashrightarrow D_s^{*-}[s\bar{c}] \to D_s^-[s\bar{c}] \to \mu^-$
	$p \to g \to t \to W^+ \to c \dashrightarrow \Lambda_c^+[udc] \to \mu^+$
	$p \to d \to t \to W^+ \to c \dashrightarrow D^+[c\bar{d}] \to \mu^+$
	$p \to g \to \bar{t} \to W^- \to \bar{c} \dashrightarrow D^-[d\bar{c}] \to \mu^-$
	$p \to g \to t \to W^+ \to c \dashrightarrow D^0[c\bar{u}] \to \mu^+$
$t \to W \to \mu$	$p \to d \to \bar{t} \to W^- \to \tau^- \to \mu^-$
	$p \to g \to t \to W^+ \to \mu^+$
	$p \to g \to \bar{t} \to W^- \to \mu^-$
$t \to X_c \to \mu$	$p \to \bar{u} \to t \to g \to c \dashrightarrow D^*(2007)^0[c\bar{u}] \to D^0[c\bar{u}] \to \mu^+$
	$p \to g \to t \to c \dashrightarrow D^*(2010)^+[c\bar{d}] \to D^+[c\bar{d}] \to \mu^+$
	$g \to \bar{t} \to g \to \bar{c} \dashrightarrow D_2^*(2460)^0[c\bar{u}] \to \bar{D}^0[u\bar{c}] \to \mu^-$
$X_c \to \mu$	$p \to \bar{u} \to g \to c \dashrightarrow \Sigma_c^{*++}[uuc] \to \Lambda_c^+[udc] \to \mu^+$
	$p \to g \to \bar{c} \dashrightarrow D^*(2010)^+[c\bar{d}] \to \bar{D}^0[u\bar{c}] \to \mu^-$
	$p \to g \to \bar{c} \dashrightarrow \bar{D}^0[u\bar{c}] \to \mu^-$
$X_b \to \mu$	$p \to g \to \bar{b} \to b \dashrightarrow \bar{B}_1(H)^+[u\bar{b}] \to B^{*-}[b\bar{u}] \to B^-[b\bar{u}] \to \tau^- \to \mu^-$
	$p \to g \to b \dashrightarrow \bar{B}_s^0[s\bar{b}] \to B_s^0[b\bar{s}] \to \mu^+$
	$g \to b \dashrightarrow B^{*-}[b\bar{u}] \to B^-[b\bar{u}] \to \mu^-$
$X_b \to X_c \to \mu$	$p \to g \to \bar{b} \dashrightarrow B^{*+} \to B^+ \to \bar{b} \to \bar{c} \dashrightarrow \bar{D}^0[u\bar{c}] \to \mu^-$
	$g \to b \dashrightarrow \bar{B}^0 \to D_1(2420)^+[c\bar{d}] \to D^0[c\bar{u}] \to \mu^+$
	$g \to b \dashrightarrow \bar{B}^0 \to b \to c \dashrightarrow D^+[c\bar{d}] \to \mu^+$

Appendix F

Uncertainties on Efficiency values

Table F.1: Muon reconstruction efficiencies for the Crack region ($0.0 < \eta < 0.1$) of side A of the ATLAS detector, using periods B2-M of 2011 collision data. The separate statistical, background and fit uncertainties, as well as the quadrature sum of these uncertainties are shown.

Probe μ	N_σ	Reconstruction	Uncertainty			
p_T [GeV]		Efficiency (ε)	stat.	$\lvert\varepsilon_{bkgmax} - \varepsilon_{bkgmin}\rvert$	$\lvert\varepsilon_{5\sigma} - \varepsilon_{3\sigma}\rvert$	Total
4-5	3	0.52669	0.00870	0.00424	0.00120	0.00976
4-5	5	0.52789	0.00869	0.00441	0.00120	0.00983
5-6	3	0.59721	0.01020	0.00347	0.00061	0.01080
5-6	5	0.59783	0.01019	0.00357	0.00061	0.01082
6-7	3	0.59563	0.01187	0.00307	0.00021	0.01226
6-7	5	0.59583	0.01186	0.00312	0.00021	0.01226
7-8	3	0.56456	0.01390	0.00891	0.00052	0.01652
7-8	5	0.56403	0.01388	0.00909	0.00052	0.01660
8-10	3	0.55709	0.01213	0.03993	0.00048	0.04174
8-10	5	0.55661	0.01212	0.04053	0.00048	0.04230
10-12	3	0.61274	0.01595	0.00388	0.00098	0.01644
10-12	5	0.61371	0.01592	0.00397	0.00098	0.01644
10-12	3	0.61274	0.01595	0.00388	0.00098	0.01644
10-12	5	0.61371	0.01592	0.00397	0.00098	0.01644

Table F.2: χ^2_{match} efficiencies for the Crack region ($-0.1 < \eta < 0.0$) of side A of the ATLAS detector, using periods B2-M of 2011 collision data. The separate statistical, background and fit uncertainties, as well as the quadrature sum of these uncertainties are shown.

Probe μ p_T [GeV]	N_σ	χ^2_{match} Efficiency (ε)	Uncertainty stat.	$\lvert\varepsilon_{\text{bkgmax}} - \varepsilon_{\text{bkgmin}}\rvert$	$\lvert\varepsilon_{5\sigma} - \varepsilon_{3\sigma}\rvert$	Total
4-5	3	0.93709	0.00583	0.00657	0.00189	0.00899
4-5	5	0.93520	0.00590	0.00680	0.00189	0.00921
5-6	3	0.94532	0.00612	0.00200	0.00060	0.00647
5-6	5	0.94472	0.00614	0.00215	0.00060	0.00653
6-7	3	0.94396	0.00720	0.00075	0.00023	0.00726
6-7	5	0.94374	0.00721	0.00077	0.00023	0.00725
7-8	3	0.93464	0.00921	0.00091	0.00227	0.00953
7-8	5	0.93690	0.00907	0.00096	0.00227	0.00938
8-10	3	0.94586	0.00740	0.00072	0.00133	0.00755
8-10	5	0.94729	0.00731	0.00074	0.00133	0.00746
10-12	3	0.88479	0.01336	0.00047	0.00133	0.01343
10-12	5	0.88346	0.01339	0.00050	0.00133	0.01347
10-12	3	0.88478	0.01336	0.00047	0.00133	0.01343
10-12	5	0.88346	0.01339	0.00050	0.00133	0.01347

Bibliography

[1] J. Blanco, V. Boisvert, L. Cerrito, N. Cooper-Smith, J. D. Morris, M. Rose, G. Salamanna, G. Snidero, and M. Vanadia, *Calibration of the χ^2_{match}-based Soft Muon Tagger algorithm*, ATL-COM-PHYS-2012-008, CERN, Geneva, Jan, 2012.

[2] J. Blanco, V. Boisvert, L. Cerrito, N. Cooper-Smith, J. D. Morris, M. Rose, G. Salamanna, G. Snidero, and M. Vanadia, *Measurement of the top quark pair production cross-section with ATLAS in pp collisions at $\sqrt{s} = 7$ TeV in the single-lepton channel with semileptonic b decays*, ATLAS-COM-CONF-2012-056, CERN, Geneva, Mar, 2012.

[3] J. Blanco, V. Boisvert, L. Cerrito, N. Cooper-Smith, B. Cooper, J. D. Morris, M. Rose, G. Salamanna, G. Snidero, and M. Vanadia, *Measurement of the top quark pair production cross-section with ATLAS in pp collisions at $\sqrt{s}$=7 TeV in the single-lepton channel with semileptonic b decays*, ATL-COM-PHYS-2012-218, CERN, Geneva, Jan, 2012.

[4] ATLAS Collaboration, *The Identification of b-Jets with the ATLAS Detector*, ATL-PERF-2012-04, CERN, Geneva, 2012. To be submitted to the Journal of Instrumentation.

[5] ATLAS Collaboration, *B tagging for Top Physics*, ATL-COM-PHYS-2010-846, CERN, Geneva, 2010.

[6] K. Nakamura et al., *(Particle Data Group)*, J. Phys. **G** (2010) no. 37, 075021. and 2011 partial update for the 2012 edition.

[7] CDF Collaboration, F. Abe et al., *Observation of Top Quark Production in $p\bar{p}$ Collisions with the Collider Detector at Fermilab*, Phys. Rev. Lett. **74** (1995) no. 14, 2626–2631.

[8] G. Aad et al., *Measurement of the top quark-pair production cross section with ATLAS in pp collisions at* $\sqrt{s} = 7$ TeV, The European Physical Journal C - Particles and Fields **71** (2011) 1–36.

[9] CDF Collaboration, T. Aaltonen et al., *Search for Charged Higgs Bosons in Decays of Top Quarks in* $p\overline{p}$ *Collisions at* $\sqrt{s} = 1.96$ TeV, Phys. Rev. Lett. **103** (2009) 101803. http://link.aps.org/doi/10.1103/PhysRevLett.103.101803.

[10] J. J. Aubert, U. Becker, P. J. Biggs, J. Burger, M. Chen, G. Everhart, P. Goldhagen, J. Leong, T. McCorriston, T. G. Rhoades, M. Rohde, S. C. C. Ting, S. L. Wu, and Y. Y. Lee, *Experimental Observation of a Heavy Particle J*, Phys. Rev. Lett. **33** (1974) 1404–1406. http://link.aps.org/doi/10.1103/PhysRevLett.33.1404.

[11] E. D. Bloom, D. H. Coward, H. DeStaebler, J. Drees, G. Miller, L. W. Mo, R. E. Taylor, M. Breidenbach, J. I. Friedman, G. C. Hartmann, and H. W. Kendall, *High-Energy Inelastic* $e-p$ *Scattering at* 6° *and* 10°, Phys. Rev. Lett. **23** (1969) 930–934. http://link.aps.org/doi/10.1103/PhysRevLett.23.930.

[12] M. Breidenbach, J. I. Friedman, H. W. Kendall, E. D. Bloom, D. H. Coward, H. DeStaebler, J. Drees, L. W. Mo, and R. E. Taylor, *Observed Behavior of Highly Inelastic Electron-Proton Scattering*, Phys. Rev. Lett. **23** (1969) 935–939. http://link.aps.org/doi/10.1103/PhysRevLett.23.935.

[13] D. Griffiths, *Introduction to Elementary Particles*. Physics textbook. Wiley, 2008. http://books.google.co.uk/books?id=Wb9DYrjcoKAC.

[14] G. Aad et al., *Observation of a new particle in the search for the Standard Model Higgs boson with the ATLAS detector at the LHC*, Physics Letters B **716** (2012) no. 1, 1 – 29. http://www.sciencedirect.com/science/article/pii/S037026931200857X.

[15] N. Cabibbo, *Unitary Symmetry and Leptonic Decays*, Phys. Rev. Lett. **10** (1963) 531–533. http://link.aps.org/doi/10.1103/PhysRevLett.10.531.

[16] M. Kobayashi and T. Maskawa, *CP-Violation in the Renormalizable Theory of Weak Interaction*, Progress of Theoretical Physics **49** (1973) no. 2, 652–657.

[17] J. H. Christenson, J. W. Cronin, V. L. Fitch, and R. Turlay, *Evidence for the* 2π *Decay of the* K_2^0 *Meson*, Phys. Rev. Lett. **13** (1964) 138–140.

[18] S. L. Glashow, *Partial-symmetries of weak interactions*, Nuclear Physics **22** (1961) no. 4, 579 – 588. http://www.sciencedirect.com/science/article/pii/0029558261904692.

[19] S. Weinberg, *A Model of Leptons*, Phys. Rev. Lett. **19** (1967) 1264–1266. http://link.aps.org/doi/10.1103/PhysRevLett.19.1264.

[20] A. Salam, *Weak and electromagnetic interactions*, Eighth Nobel Symposium on Elementary particle theory, relativistic groups and analyticity (1968) 367.

[21] *Experimental observation of isolated large transverse energy electrons with associated missing energy at s=540 GeV*, Physics Letters B **122** (1983) no. 1, 103 – 116. http://www.sciencedirect.com/science/article/pii/0370269383911772.

[22] P. W. Higgs, *Broken Symmetries and the Masses of Gauge Bosons*, Phys. Rev. Lett. **13** (1964) 508–509. http://link.aps.org/doi/10.1103/PhysRevLett.13.508.

[23] D. H. Perkins, *Introduction to High Energy Physics*. Cambridge University Press, 2000.

[24] S. L. Glashow and S. Weinberg Phys. Rev. D (1977) no. 15, 1958.

[25] J. F. Donoghue and L. F. Li Phys. Rev. D (1979) no. 19, 945.

[26] CMS Collaboration Collaboration, S. Chatrchyan et al., *Observation of a new boson at a mass of 125 GeV with the CMS experiment at the LHC*, Phys.Lett. **B716** (2012) 30–61, arXiv:1207.7235 [hep-ex].

[27] M. L. Perl et al., *Evidence for Anomalous Lepton Production in* $e^+ - e^-$ *Annihilation*, Phys. Rev. Lett. **35** (1975) no. 22, 1489–1492.

[28] S. W. Herb et al., *Observation of a Dimuon Resonance at 9.5 GeV in 400-GeV Proton-Nucleus Collisions*, Phys. Rev. Lett. **39** (1977) no. 5, 252–255.

[29] D. Binosi and L. Theul, *JaxoDraw: A graphical user interface for drawing Feynman diagrams*, Computer Physics Communications **161** (2004) no. 12, 76 – 86.

[30] M. Alviggi, *Standard model constraints on M_{Top} and M_{Higgs} from the LEP experiments*, in *XXXth Rencontres de Moriond, QCD and High Energy Interactions*. 1995.

[31] CDF Collaboration, T. Aaltonen et al., *Observation of Electroweak Single Top-Quark Production*, Phys. Rev. Lett. **103** (2009) 092002.

[32] D0 Collaboration Collaboration, V. M. Abazov et al., *Observation of Single Top-Quark Production*, Phys. Rev. Lett. **103** (2009) 092001.

[33] ATLAS Collaboration, *Measurement of the t-channel single top-quark production cross section in pp collisions at $\sqrt{s} = 7$ TeV with the ATLAS detector*, . `https://atlas.web.cern.ch/Atlas/GROUPS/PHYSICS/PAPERS/TOPQ-2011-14/`.

[34] *ATLAS Physics Summary Plots*, Available online. `http://twiki.cern.ch/twiki/bin/view/AtlasPublic/CombinedSummaryPlots`.

[35] *Statistical combination of top quark pair production cross-section measurements using dilepton, single-lepton, and all-hadronic final states at s = 7 TeV with the ATLAS detector*, ATLAS-CONF-2012-024, CERN, Geneva, Mar, 2012.

[36] M. Gosselink, *Top quark pair cross section measurement at ATLAS*, `arXiv:0810.3677 [hep-ex]`.

[37] O. Brüning, P. Collier, P. Lebrun, S. Myers, R. Ostojic, J. Poole, and P. Proudlock, *LHC Design Report*, CERN-2004-003-V-1, 2004. `http://cdsweb.cern.ch/record/782076`.

[38] L. Evans and P. Bryant, *LHC Machine*, Journal of Instrumentation **3** (2008) 8001.

[39] *LHC Project Illustrations*, Available online. `http://cdsweb.cern.ch/record/842700`.

[40] *The Accelerator Complex*, Available online. `http://public.web.cern.ch/public/en/Research/AccelComplex-en.html`.

[41] *Luminosity Determination in pp Collisions at sqrt(s) = 7 TeV using the ATLAS Detector in 2011*, ATLAS-CONF-2011-116, CERN, Geneva, Aug, 2011.

[42] ATLAS Collaboration, G. Aad et al., *The ATLAS Experiment at the CERN Large Hadron Collider*, Journal of Instrumentation **3** (2008) no. 08, S08003.

[43] *Luminosity Public Results*, Available online. http://twiki.cern.ch/twiki/bin/view/AtlasPublic/LuminosityPublicResults.

[44] *Summary of the analysis of the 19 September 2008 incident at the LHC. Résumé de l'analyse de l'incident survenu le 19 septembre 2008 au LHC*, Press release, Oct, 2008.

[45] CDF and D0 Collaboration, M.-A. Pleier, *Top quark physics at the Tevatron*, Acta Phys.Polon.Supp. **1** (2008) 237–244, arXiv:0709.2665 [hep-ex].

[46] Obtained using the ATLAS run query tool, May, 2012. http://atlas-runquery.cern.ch/.

[47] Obtained using the ATLAS luminosity calculator, May, 2012. http://atlas-lumicalc.cern.ch/.

[48] *CERN announces LHC to run in 2012*, Press release, Jan, 2011.

[49] *ATLAS TDR*, Available from the ATLAS Technical Design Report web page. http://atlas.web.cern.ch/Atlas/GROUPS/PHYSICS/TDR/access.html.

[50] J. Schmitz, *The Microstrip Gas Counter and its application in the ATLAS inner tracker*. PhD thesis, Nikhef, 1994.

[51] F. Hügging, *The ATLAS Pixel Insertable B-layer (IBL)*, Nuclear Instruments and Methods in Physics Research Section A: Accelerators, Spectrometers, Detectors and Associated Equipment **650** (2011) no. 1, 45 – 49. International Workshop on Semiconductor Pixel Detectors for Particles and Imaging 2010.

[52] H. Pernegger, *ATLAS Insertable B-Layer Construction*, Cern detector seminar, January, 2012.

[53] ATLAS Collaboration, G. Aad et al., *Performance of the ATLAS Detector using First Collision Data*, J. High Energy Phys. **09** (2010) no. CERN-PH-EP-2010-015, 056. 65 p, arXiv:1005.5254 [hep-ex].

[54] G. Aad et al., *Expected performance of the ATLAS experiment: detector, trigger and physics*. CERN, Geneva, 2009.

[55] A. Gesualdi-Mello et al., *Overview of the High-Level Trigger Electron and Photon Selection for the ATLAS Experiment at the LHC*, ATL-DAQ-CONF-2006-011. ATL-COM-DAQ-2005-024. CERN-ATL-COM-DAQ-2005-024, CERN, Geneva, Jun, 2005.

[56] M. A. Dobbs et al., *Les Houches Guidebook to Monte Carlo Generators for Hadron Collider Physics*, ArXiv High Energy Physics - Phenomenology e-prints (2004) , `arXiv:0403045 [hep-ph]`.

[57] A. Schaelicke, T. Gleisberg, S. Hoeche, S. Schumann, J. Winter, et al., *Event generator for particle production in high-energy collisions*, Prog.Part.Nucl.Phys. **53** (2004) 329–338, `asXiv:0311270 [hep-ph]`.

[58] S. Frixione and B.R. Webber, *Matching NLO QCD computations and parton shower simulations*, JHEP **06** (2002), 029 , `arXiv:0204244 [hep-ph]`.

[59] S. Frixione, P. Nason and B.R. Webber, *Matching NLO QCD and parton showers in heavy flavour production*, JHEP **08** (2003), 007 , `arXiv:0305252 [hep-ph]`.

[60] G. Corcella et al., *Herwig 6.5: an event generator for Hadron Emission Reactions With Interfering Gluons (including supersymmetric processes)*, JHEP **01** (2001), 010 , `arXiv:0011363 [hep-ph]`.

[61] J. Butterworth, J. Forshaw, and M. Seymour, *Multiparton interactions in photoproduction at HERA*, Z. Phys. **C72** (1996), 637-646 , `arXiv:9601371 [hep-ph]`.

[62] T. Sjöstrand, S. Mrenna, and P. Skands, *PYTHIA 6.4 physics and manual*, Journal of High Energy Physics **2006** (2006) no. 05, 026.

[63] GEANT4 Collaboration, GEANT4 - *a simulation toolkit*, Nuclear Instruments and Methods in Physics Research Section A: Accelerators, Spectrometers, Detectors and Associated Equipment **506** (2003) no. 3, 250 – 303. `http://www.sciencedirect.com/science/article/pii/S0168900203013688`.

[64] T. Goepfert, *Tagging b-jets in ATLAS*, ATL-PHYS-PROC-2010-014, CERN, Geneva, Feb, 2010.

[65] H. Cheung and T. Pratt, *Lepton and Photon Interactions at High Energies: Proceedings of the XXI International Symposium : Fermi National Accelerator Laboratory, USA, 11-16 August 2003*. World Scientific, 2004.

[66] M. Cacciari, G. P. Salam, and G. Soyez, *The anti-k_t jet clustering algorithm*, Journal of High Energy Physics **2008** (2008) no. 04, 063. http://stacks.iop.org/1126-6708/2008/i=04/a=063.

[67] W. Lampl et al., *Calorimeter clustering algorithms: Description and performance*, ATL-LARG-PUB-2008-002, ATL-COM-LARG-2008-003, 2008.

[68] B. Acharya et al., *Object selection and calibration, background estimations and MC samples for the Winter 2012 Top Quark analyses with 2011 data*, ATL-COM-PHYS-2012-224, CERN, Geneva, 2012.

[69] A. Meyer, *Heavy Quark Production at HERA*. PhD thesis, University of Hamburg, 2005.

[70] *Commissioning of the ATLAS high-performance b-tagging algorithms in the 7 TeV collision data*, ATLAS-CONF-2011-102, CERN, Geneva, Jul, 2011.

[71] V. Boisvert, L. Cerrito, B. Cooper, R. Goncalo, A. J. Poll, and M. Rose, *Extension of the ATLAS Soft Muon Tagging Algorithm to use Muon Reconstruction Quality Criteria*, ATL-COM-PHYS-2010-335, CERN, Geneva, Jun, 2010.

[72] E. Lund, L. Bugge, I. Gavrilenko, and A. Strandlie, *Transport of covariance matrices in the inhomogeneous magnetic field of the ATLAS experiment by the application of a semi-analytical method*, Journal of Instrumentation **4** (2009) no. 04, P04016. http://stacks.iop.org/1748-0221/4/i=04/a=P04016.

[73] *MCP Guidelines for Analyses of 2011 Data in Release 17*, available via ATLAS TWiki, November, 2011. https://twiki.cern.ch/twiki/bin/view/AtlasProtected/MCPAnalysisGuidelinesRel17MC11a#AnchorSelections.

[74] M. J. Woudstra and the ATLAS muon collaboration, *Commissioning of the muon track reconstruction in the ATLAS experiment*, Journal of Physics: Conference Series **219** (2010) no. 3, 032026. http://stacks.iop.org/1742-6596/219/i=3/a=032026.

[75] A. Shibata et al., *Understanding Monte Carlo Generators for Top Physics*, ATL-COM-PHYS-2009-334, CERN, Geneva, Jun, 2009.

[76] *TopCommonObjects*, available via ATLAS TWiki, August, 2012. `https://twiki.cern.ch/twiki/bin/viewauth/AtlasProtected/TopCommonObjects2011`.

[77] ATLAS Collaboration, *Jet energy measurement with the ATLAS detector in proton-proton collisions at* $\sqrt{s} = 7$ TeV, Eur. Phys. J. C , `arXiv:1112.6426v1 [hep-ex]`.

[78] K. Bachas et al., *A measurement of the ATLAS muon reconstruction and trigger efficiency using* J/ψ *decays*, ATLAS-CONF-2011-021, CERN, Geneva, Mar, 2011.

[79] *Trigger Menu Convention*, available via ATLAS TWiki, July, 2012. `https://twiki.cern.ch/twiki/bin/viewauth/Atlas/TriggerMenuConvention`.

[80] CMS Collaboration, *Prompt and non-prompt* J/ψ *production in pp collisions* $\sqrt{s} = 7$ *TeV*, The European Physical Journal C - Particles and Fields **71** (2011) 1–26.

[81] *Measurement of the b-tag Efficiency in a Sample of Jets Containing Muons with 5* fb^{-1} *of Data from the ATLAS Detector*, ATLAS-CONF-2012-043, CERN, Geneva, Mar, 2012.

[82] ATLAS Collaboration, *Electron performance measurements with the ATLAS detector using the 2010 LHC proton-proton collision data*, Eur. Phys. J. C (2012) , `arXiv:1110.3174v1 [hep-ex]`.

[83] W. Liebig, *MuonCombinedQualityDocumentation*, available via ATLAS TWiki, August, 2012. `https://twiki.cern.ch/twiki/bin/view/AtlasProtected/MuonCombinedQualityDocumentation`.

[84] D. J. Summers, *Transverse mass as a means of measuring the W width at the Tevatron*, Phys. Lett. B **392** (1996) no. hep-ph/9608332. CERN-TH-96-205, 216–222. 13 p. `oai:cds.cern.ch:308850`.

[85] A. J. Barr and C. G. Lester, *A review of the mass measurement techniques proposed for the Large Hadron Collider*, Journal of Physics G: Nuclear and Particle Physics **37** (2010) no. 12, 123001. `http://stacks.iop.org/0954-3899/37/i=12/a=123001`.

[86] ATLAS Collaboration, *Observation of t Channel Single Top-Quark Production in pp Collisions at $\sqrt{s} = 7$ TeV with the ATLAS detector*, ATLAS-CONF-2011-088,. http://cdsweb.cern.ch/record/1356197.

[87] F. A. Berends, H. Kuijf, B. Tausk and W. T. Giele, *On the production of a W and jets at hadron colliders*, Nucl. Phys. B **357** (1991) no. 1, 32.

[88] *Measurement of the top quark-pair cross-section with ATLAS in pp collisions at $\sqrt{s} = 7$ TeV in the single-lepton channel using b-tagging*, ATLAS-CONF-2011-035, CERN, Geneva, Mar, 2011.

[89] *Calibrating the b-Tag Efficiency and Mistag Rate in $35pb^{-1}$ of Data with the ATLAS Detector*, ATLAS-CONF-2011-089, CERN, Geneva, 2011.

[90] CMS Collaboration, *Measurement of $t\bar{t}$ Pair Production Cross Section at $\sqrt{s} = 7$ TeV using b-quark Jet Identification Techniques in Lepton + Jet Events*, CMS-PAS-TOP-11-003. http://cdsweb.cern.ch/record/1386709.

[91] CDF Collaboration Collaboration, T. Aaltonen et al., *Measurement of the top quark mass using the invariant mass of lepton pairs in soft muon b-tagged events*, Phys. Rev. D **80** (2009) 051104. http://link.aps.org/doi/10.1103/PhysRevD.80.051104.

[92] *Expected electron performance in the ATLAS experiment*, ATL-PHYS-PUB-2011-006, CERN, Geneva, Apr, 2011.